Sinc Function-Based Vibration-Reducing Profilers for Agile Attitude Control of Flexible Spacecraft

(Sinc関数を用いた振動抑制型プロファイラによる柔軟衛星の高速姿勢変更制御の研究)

by

Toshio Kamiya

Submitted to the Space and Astronautical Science
in partial fulfillment of the requirements for the degree of

Doctor of Philosophy

at the

GRADUATE UNIVERSITY FOR ADVANCED STUDIES
(SOKENDAI)

September 2014

Author .....
Space and Astronautical Science
December 19, 2014

Certified by .....
Shin-ichiro Sakai
Associate Professor
Thesis Supervisor

Accepted by .....
Hideo Matsuhara
Chairman, Department Committee on Graduate Theses

Sinc Function-Based Vibration-Reducing Profilers for Agile Attitude Control of Flexible Spacecraft

(Sinc関数を用いた振動抑制型プロファイラによる柔軟衛星の高速姿勢変更制御の研究)

by

Toshio Kamiya

Submitted to the Space and Astronautical Science
on December 19, 2014, in partial fulfillment of the
requirements for the degree of
Doctor of Philosophy

Abstract

In this thesis, a feedforward controller which performs agile attitude control of flexible spacecraft reducing the residual vibration at the end of maneuver is proposed and evaluated first. The feedforward controller is a preshaping profiler composed of a pair of sinc functions which generates a system input command profile. The sinc function has an ideal attenuation performance in frequency domain. Therefore, the combined pair of sinc functions still have a good attenuation at high frequencies region. Then, improvements for longer maneuver distance are attempted. The modified sinc function-based profilers show better performances from a viewpoint of longer maneuver distances, i.e. agility, at the minimum cost of residual vibrations.

Thesis Supervisor: Shin-ichiro Sakai
Title: Associate Professor

Acknowledgments

First and foremost, I would like to express my deepest and sincere gratitude to my supervisor Professor Sakai for his continuous support and his many constructive advices during my studies. Thanks to the members of the committee, Professor Kawakatsu, Professor Tsuchiya, Professor Minesugi, Professor Matsunaga, and Professor Kojima for taking their time to read this work and provide insightful comments and constructive advices to improve the overall quality of this thesis.

I also wish to thank Mr. Maeda, and Mr. Ogura at NEC Corporation for their support, advices, and helpful discussions at the first stage of my study during ASTRO-G program. This work was supported in part by all the members of Astro-G team in JAXA-ISAS and NEC Corporation.

Finally, I would like to extend special gratitude to my wife Rieko, my son Ryota, and my parents for their patience and understanding throughout a period of my study.

Contents

List of Figures

THIS PAGE INTENTIONALLY LEFT BLANK

List of Tables

Chapter 1

Introduction

1.1 Motivations

The recent evolution of advanced space missions such as deep space observation, earth observation, or disaster monitoring has been forwarded to higher "pointing accuracy" and higher "agility" in contradiction to the complexity of the structural design of the mission equipment required for the highly functionalized mission. The basic features which allow an efficient attitude maneuver are the spacecraft "pointing accuracy" and "agility". Pointing accuracy represents the attitude stability after the maneuver. Fine pointing accuracy is realized by reducing the residual vibration where the vibration is induced during the maneuver motion and some remains after the maneuver. Thus the fine pointing accuracy can be rephrased as low residual vibration. Agility represents the rotational motion of the spacecraft with the fastest angular rate or shortest maneuver duration. The rotational motion is realized by attitude control actuators which are dimensioned according to the spacecraft's inertia and required maneuver performance etc. However every spacecraft has some limited resources, i.e. dimensional capability or mass capability or power consumption capability. Therefore the agility, meaning the flexibility and the ability to quickly move the satellite, becomes constantly constraint of the mission. The pointing accuracy and agility would sometimes be contrary requirements. If an agile motion is realized, then flexible structural modes of the spacecraft tend to be excited after the maneuver motion, and vice versa.

Considering current situation of the needs for highly functionalized scientific observations, global environmental issues, or international security affairs, the demands for fine pointing and high agility will be getting stronger in the future. On the other hand, structural design for such the high-performance observation equipment tends to be complicated, e.g. large deployable antenna, large extendable telescope, or synthetic aperture radar (SAR). Thus, in contradiction to structural design being more complicated, demands for higher performances on pointing accuracy and agility are getting stronger and stronger for recent space applications. Nevertheless, looking around the conventional control algorithms, it is difficult to find the optimal control algorithm which realizes fine pointing and high agility when applied to spacecraft with complicated flexible structures. That is why this thesis deals with flexible spacecraft rest-to-rest maneuver in fine pointing accuracy and agile motion.

The difficulties in applying the conventional methods to an actual flexible satellite are as follows:

- Satellite with large flexible structures contains many structural modes with various mode shapes.
- It is difficult to predict high-mode frequencies.

Therefore, not only multi-mode system but also the presence of unknown high-order flexible modes should be considered in high-accuracy controller design for actual satellite application.

The methods presented in this thesis are control algorithms of flexible spacecraft especially for high-speed rest-to-rest maneuver with minimal residual vibration at the end of maneuver. The controllers are feedforward controllers composed of sinc functions as the base function. It is demonstrated that these controllers show the highest performances among conventional controllers concerning the balanced performance of pointing accuracy and agility when applied to flexible spacecraft rest-to-rest maneuver. The feature of the sinc function-based feedforward controller is that the sinc function itself has an ideal attenuation above a certain boundary frequency. Therefore when it is applied as the base function of a controller, the characteristic frequencies

of the flexible structures and the controller can be designed well separately. The concept of sinc function-based controller is a new one, therefore the original sinc function-based profiler is patented in Japan [1], North America [2, 3, 4], and European countries [5, 6].

As previous satellite programs, World View-1 and 2 (US), and Pleiades (France, Fig. 1-1, [7, 8, 9]) are heritage satellites which perform high-speed rest-to-rest maneuvers. Those satellites have relatively rigid structures, therefore major effects of pointing performance degradation by structural flexible modes are not expected unless extremely high pointing accuracy is required after the end of maneuvers. Looking at domestic programs, ETS-VI and ETS-VIII (Fig. 1-2, [10, 11, 12, 13]) has been launched and being used for experimental on-orbit evaluation of attitude controllers for flexible spacecraft. The main purpose of the experiment is evaluation of modern control theory such as H-infinity or gain-scheduling. ASTRO-G (Fig. 1-3, [14, 15, 16, 17, 18, 19]) was a satellite planned to perform high-speed rest-to-rest maneuvers with control moment gyros (CMGs), unfortunately the ASTRO-G program was terminated due to the deployable antenna's technical feasibility reason during critical design phase. One of the methods presented in this thesis, nil-mode-exciting profiler (NME profiler), is a controller developed for the ASTRO-G mission.

Brief explanations why feedforward (not feedback), smooth (not on-off), and sinc function (not other trigonometric function or polynomial expression)-based profilers are proposed in this thesis for flexible spacecraft rest-to-rest maneuvers are shown hereafter.

- Why feedforward (not feedback) ?

  Letting Laplace transform of the plant be $P(s)$ and the feedback controller be $C(s)$, a block diagram of the feedback control system is shown in Fig. 1-4 and the transfer function of its input-output relation is given as $X = \frac{PC}{1+PC}R$, where $R(s)$ is input and $X(s)$ is output. On the other hand, block diagram of a feedforward control system representing the feedforward controller as $C(s)$ is shown in Fig. 1-5 and the transfer function is given as $X = PCR$. There is only a difference of the $1 + PC$ in the denominator. However control stability

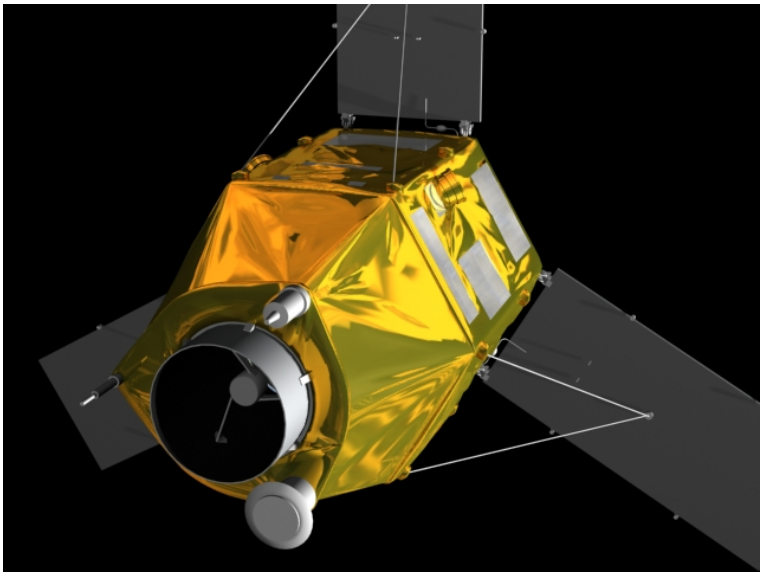

Figure 1-1: Pleiades.

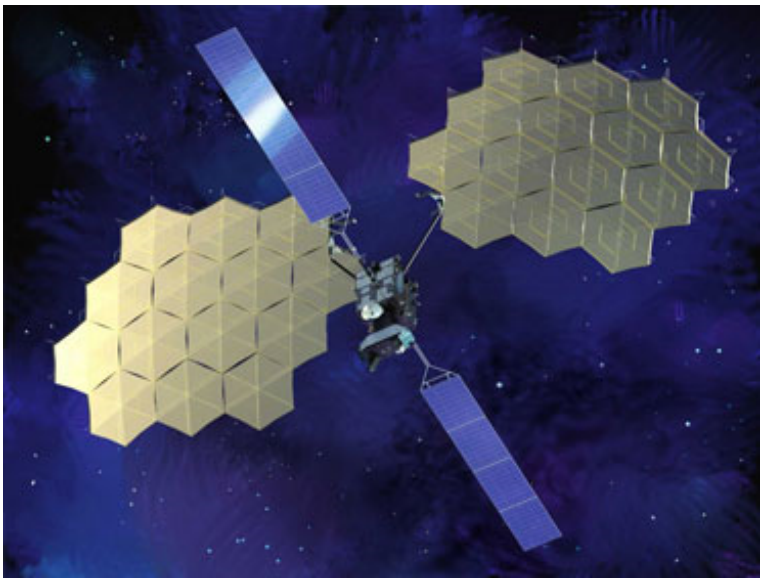

Figure 1-2: ETS-VIII.

Figure 1-3: ASTRO-G.

is always required for a stable control of a closed-loop control system, so the feedback controller must be designed to meet the control stability. The control stability usually limits the controller's highest frequency. Theoretically, there is no upper limit on characteristic frequency of a feedforward control system. Based on such the reason, feedforward controllers have been chosen in this thesis for better frequency characteristics, i.e. for faster responses.

Note that an outer loop feedback controller would be also required for an actual application for feedforward controllers because of the existence of modeling errors and/or disturbances as shown in Fig. 1-6 where $C_2(s)$ is the outer feedback controller and $T(s)$ is a disturbance torque.

- Why smooth (not on-off) ?

  If a control target is known and there is no modeling error, then on-off type controllers such as ZV or ZVD shaper or convolution of the input shapers will be optimal solutions for fine pointing accuracy and high agility. However actual applications have some modeling errors and have some unknown high-order flexible modes. The smooth type controllers presented in this thesis have higher robustness against the modeling errors in frequency domain and the existences of unknown high-order flexible modes, though the numerical expression of smooth type tends to be more complicated compared to on-off type.

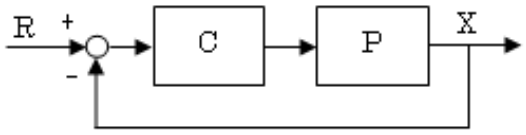

Figure 1-4: Feedback controller.

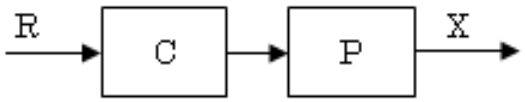

Figure 1-5: Feedforward controller.

Note that the force commands generated by the methods presented in this thesis are smoothly shaped; hence, these methods cannot be used for on-off actuator moves such as thruster moves, but can be used for smooth actuator moves such as reaction wheel (RW) or control moment gyro (CMG) moves.

- Why sinc function (not trigonometric function or polynomial expression) ?
  As mentioned above, the sinc function has been selected because it has an ideal low-pass filter shaped frequency characteristic.

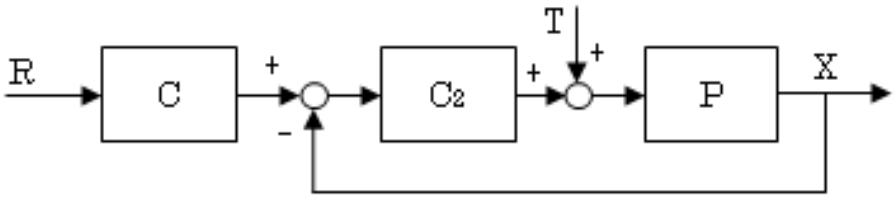

Figure 1-6: Feedforward controller with outer loop for modeling error.

1.2 Literature Review and Discussion

Many researchers have studied this subject, and all the proposed feedforward control algorithms can be categorized, on the basis of the shape of the input command waveform, as either on-off or smooth. The algorithm presented in this thesis is a smooth-type controller in which the duration is relatively longer than that of conventional algorithms, but the residual vibration is much smaller. Therefore, this new algorithm is especially suitable for a mission that requires very high pointing accuracy at the end of maneuvers, but does not require rapid motion. For example, this algorithm is suitable for a satellite carrying a scientific telescope because such a satellite is often required to establish a fine and stable attitude for performing scientific observations immediately after attitude maneuvers.

Input commands are usually given in terms of physical quantities such as force (torque) or position (angle); the method presented here uses force (torque) input. The on-off controller for rest-to-rest maneuvers is implemented by convolving a sequence of impulses (an input shaper) with a step function. The input shaper consists of a series of impulses such that the vibration caused by the first impulse will be cancelled by that caused by the second or later impulses, so there will be no residual vibration at the end of the input command [20, 21, 22] as shown in Fig. 1-7. The earliest appearance of an input shaper which meets the constraints of the zero vibration (ZV) shaper was in the method of posicast control developed by O. J. M. Smith in the late 1950s [20, 21]. Various methods for incorporating robustness against modeling errors have been presented [22, 23, 24, 25, 26, 27, 28, 29]. At least a couple of forces, one for acceleration and the other for deceleration, are required for a rest-to-rest motion, but conventional input shapers only include positive impulses; therefore, time-optimal controllers with force input commands for rest-to-rest motions have been developed [30, 31, 32]. Smooth controllers are implemented by a smooth curve of trigonometric functions or polynomial expressions as input commands [33, 34, 35, 36, 37, 38, 39, 40, 41].

Various comparisons have been made between on-off and smooth controllers [33,

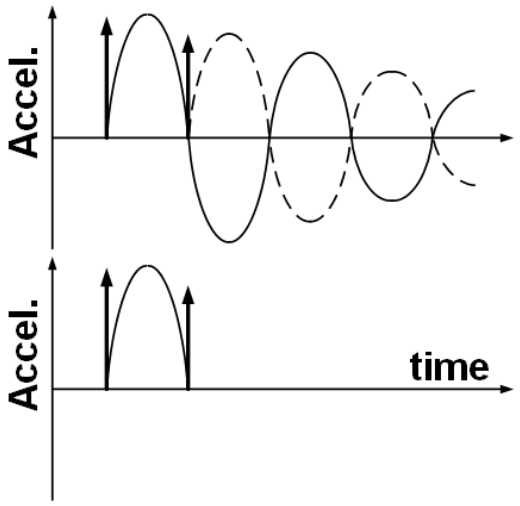

Figure 1-7: Concept of ZV shaper.

34, 39, 42, 43, 44]. Hybrid-type controller which is generated by a convolution of an on-off and a smooth, e.g. S-curve smoothed on-off command convolved with input shaper, has been proposed for multimode systems [44, 45, 46]. The most difficult aspect in establishing a suitable algorithm for rest-to-rest maneuvers of a satellite with flexible structures is to achieve maneuvers with minimum excitation of structural vibrations. If the target system contains only a few flexible modes, without any modeling errors in structural frequency and damping ratio, a conventional algorithm such as a zero-vibration (ZV) shaper will be the best solution since it achieves the maneuver with the minimum residual vibration and in the shortest time [20, 21, 22]. However, actual satellite systems with large flexible structures, such as solar array paddles or large deployable antennas, contain many structural modes with various mode shapes. Generally, low-mode frequencies are easy to predict by structural analysis, but high-mode frequencies are difficult to predict, especially when the flexible appendage has a complicated shape like a solar array paddle or deployable antenna. Table 1.1 shows examples of analyzed frequencies and coupling vectors of major flexible modes with modal masses larger than 1% of the total mass or total moment of inertia (MOI) of a solar array paddle. In such cases, input shapers that eliminate these modes can be built by convolving multiple input shapers. However, the modeling errors

Table 1.1: Flexible parameters of a solar array paddle. The masses larger than 1% are indicated by boldface.

Mode No.	Mode Description	Frequency (Hz)	Modal Mass for Translational Motion (%)			Modal Mass for Rotational Motion (%)		
			X	Y	Z	RX	RY	RZ
1	1st out-of-plane	0.270	**62.28**	0.00	0.00	0.00	0.00	**97.67**
2	1st in-plane	0.797	0.00	0.00	**72.19**	**100.00**	0.03	0.00
3	2nd out-of-plane	1.656	**19.85**	0.00	0.00	0.00	0.00	**2.04**
4	1st torsional	2.552	0.00	0.00	0.00	0.00	**82.08**	0.00
5	3rd out-of-plane	4.534	**7.15**	0.05	0.00	0.00	0.00	0.21
6	2nd torsional	7.177	0.06	0.02	0.00	0.00	**14.53**	0.00
7	-	7.609	**4.93**	**2.24**	0.00	0.00	0.13	0.07
8	-	11.619	0.00	0.18	0.09	0.00	**2.92**	0.00
9	-	13.544	0.11	**66.69**	**1.54**	0.00	0.01	0.00
19	-	45.474	0.04	**10.16**	**9.58**	0.00	0.00	0.00
		Total	95.491	82.054	85.616	99.999	99.947	99.997

of high-order flexible modes, which are usually larger than modeling errors of low-order modes, might cause excitation of residual vibrations, even though the mass of high-order modes is relatively small (Table 1.1). Therefore, if the target satellite is equipped with a large flexible structure, and the satellite mission requires highly accurate pointing performance at the end of maneuvers, vibration reduction of high-order modes, especially in the presence of unknown higher modes, is a key factor in high-accuracy controller design.

The characteristics of the conventional profilers can be summarized as follows. Input shaper for single-mode systems can be expanded to multi-mode systems using convolution, but, not effective for systems with unknown flexible modes. Optimal smooth profilers like strict solution for a simple system or minimizing weighted function profiler would be effective for a given system which includes specific number of modes, i.e. relatively simple system, but, not effective for multi-mode systems like actual satellite or system with unknown flexible modes. Low-pass filter shaped smooth profilers like smooth curve of trigonometric functions would be effective and robust for multi-mode systems or systems with unknown flexible modes. Note that ramped sinusoidal is used as typical smooth profiler in this thesis because it shows better attenuation as shown in Fig. 1-8 and 1-9. Figure 1-8 shows time profiles of a ramped sinusoidal command and a versine command. Figure 1-9 shows fast Fourier transforms (FFT) of those commands. The characteristics of those conventional profilers

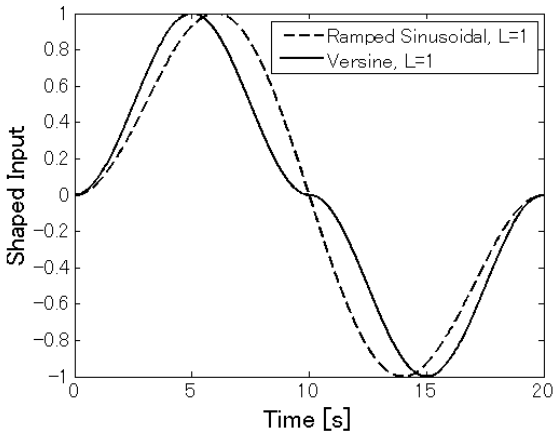

Figure 1-8: Ramped sine and versine.

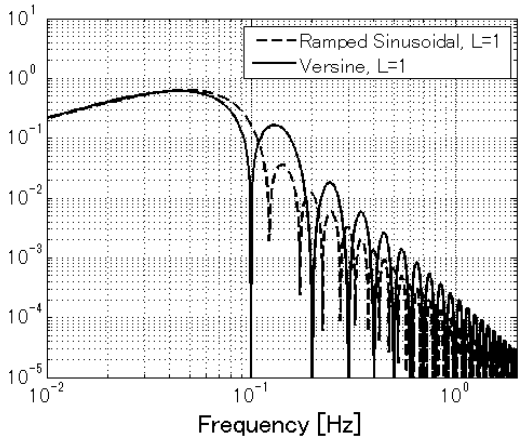

Figure 1-9: FFTs, ramped sine and versine.

Table 1.2: Comparison of input shapers and smooth profilers.

	Type of system		
Type of profiler	Single-mode system	Multi-mode system	System with unknown mode
Input shapers	Good	Good	No good
Optimal smooth profilers	Good	No good	No good
LPF shaped smooth profilers	Good	Good	Good

are summarized in Table 1.2.

1.3 Overview of Thesis

The following is a brief account of the rest of the contents of this thesis. Chapter 2 provides definitions of dynamics model simplified for the evaluation of the essence of the proposed methods and boundary conditions required for rest-to-rest maneuvers. Chapter 3 introduces the original sinc function-based profiler and its characteristics in frequency domain. The approach taken here is to generate smooth force profiles that have been shaped to reduce excitation energy at the frequency above a certain threshold level corresponding to the system's lowest structural mode. By suppressing the energy at frequencies above the lowest structural mode, all the structural modes will not be excited during and after the maneuver. Chapter 4 compares command shaping

techniques for controlling residual vibration after the end of maneuver with single-mode systems. Some typical on-off type input shapers and smooth type profilers are applied as conventional methods. It is demonstrated that the sinc function-based profiler shows the second smallest residual vibration among the methods. Chapter 5 provides comparison with two-mode systems which include unknown high-order mode. The feature of the sinc function-based profiler presented in this thesis is higher attenuation level compared to the conventional methods. Therefore, in the presence of unknown higher modes, the original sinc function-based profiler shows the smallest residual vibrations compared to all other profilers

Chapter 6 introduces a new performance index, i.e. maneuver distance. Agility can be quantified once the input torque is restricted to some upper limit. Then comparison of agility performances of each conventional method discussed in the previous chapters is made in this chapter. Then Chapter 7 proposes new sinc function-based profilers for high-agility rest-to-rest maneuvers. Instead of relaxing the attenuation ability in higher frequency region, well balanced performance of agility and residual vibration can be obtained.

Chapter 8 presents an example of application of the proposed method to actual satellite program called ASTRO-G for which the NME profiler has been originally developed. Experimental test to verify the effectiveness of the proposed NME profiler is introduced in Appendix D.

THIS PAGE INTENTIONALLY LEFT BLANK

Chapter 2

Problem Statement

2.1 Single-Mode System

To study the problem of reducing residual vibrations of rest-to-rest maneuvers, a two mass, one spring model is used here as a simple representation of the dynamic system (Fig. 2-1). The lumped masses represent the inertias of the moving parts, while the spring represents the stiffness of the structure and transmission elements.

$$\begin{aligned} m_1\ddot{x}_1 &= -k\left(x_1 - x_2\right) + u \\ m_2\ddot{x}_2 &= k\left(x_1 - x_2\right) \end{aligned} \tag{2.1}$$

where x_1 and x_2 are the positions of body 1 and body 2, respectively, and u is the input force (torque) applied to body 1. This system can also be represented in the state-space form as

$$\begin{aligned} \dot{x}(t) &= Ax(t) + Bu(t) \\ y(t) &= Cx(t) \end{aligned} \tag{2.2}$$

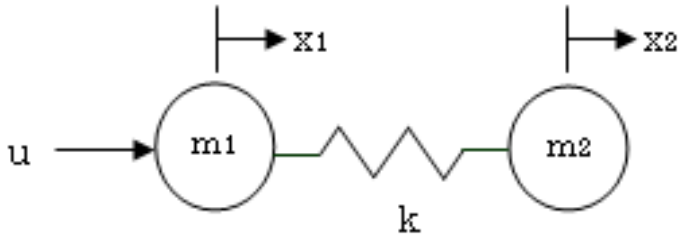

Figure 2-1: Single-mode system composed of two masses and one spring in which an input force u is applied to mass 1.

where

$$x = \begin{bmatrix} x_1 & x_2 & \dot{x}_1 & \dot{x}_2 \end{bmatrix}^T$$

$$A = \begin{bmatrix} 0 & 0 & 1 & 0 \\ 0 & 0 & 0 & 1 \\ -k/m_1 & k/m_1 & 0 & 0 \\ k/m_2 & -k/m_2 & 0 & 0 \end{bmatrix}, \quad B = \begin{bmatrix} 0 \\ 0 \\ 1/m_1 \\ 0 \end{bmatrix}$$

$$C = \begin{bmatrix} 1 & 0 & 0 & 0 \end{bmatrix}$$

The natural frequency of the free-free system is given as

$$\omega = \sqrt{\frac{k}{m_1} + \frac{k}{m_2}} \tag{2.3}$$

Boundary conditions of rest-to-rest maneuver are given as

$$\begin{aligned} x_1(0) &= x_2(0) = 0 \\ \dot{x}_1(0) &= \dot{x}_2(0) = 0 \\ x_1(t_f) &= x_2(t_f) = 1 \\ \dot{x}_1(t_f) &= \dot{x}_2(t_f) = 0 \end{aligned} \tag{2.4}$$

where t_f is the time at the end of the maneuver.

2.2 Two-Mode System

A three-mass, two-spring model is used here as a simple representation of the dynamic system under study (Fig. 2-2). The lumped masses represent the inertias of moving parts, while the springs represent the stiffness of the structure and transmission elements. Generally, a satellite, which contains multiple flexible modes, consists of known lower modes and unknown higher modes. Therefore, a two-mode system (three-mass, two-spring model) can be useful for simplifying the problem. The equations of motion for this two-mode system are

$$\begin{aligned} m_1\ddot{x}_1 &= k_1(x_2 - x_1) - k_2(x_1 - x_3) + u \\ m_2\ddot{x}_2 &= -k_1(x_2 - x_1) \\ m_3\ddot{x}_3 &= k_2(x_1 - x_3) \end{aligned} \tag{2.5}$$

where x_1, x_2, and x_3 are the positions of body 1, body 2, and body 3, respectively, and u is an input force (torque) applied to body 1. This system can also be represented in the state-space form as

$$\begin{aligned} \dot{x}(t) &= \bar{A}x(t) + \bar{B}u(t) \\ y(t) &= \bar{C}x(t) \end{aligned} \tag{2.6}$$

where

$$x = \begin{bmatrix} x_1 & x_2 & x_3 & \dot{x}_1 & \dot{x}_2 & \dot{x}_3 \end{bmatrix}^T$$

$$\bar{A} = \begin{bmatrix} 0 & 0 & 0 & 1 & 0 & 0 \\ 0 & 0 & 0 & 0 & 1 & 0 \\ 0 & 0 & 0 & 0 & 0 & 1 \\ -\dfrac{k_1+k_2}{m_1} & \dfrac{k_1}{m_1} & \dfrac{k_2}{m_1} & 0 & 0 & 0 \\ \dfrac{k_1}{m_2} & -\dfrac{k_1}{m_2} & 0 & 0 & 0 & 0 \\ \dfrac{k_2}{m_3} & 0 & -\dfrac{k_2}{m_3} & 0 & 0 & 0 \end{bmatrix}, \quad \bar{B} = \begin{bmatrix} 0 \\ 0 \\ 0 \\ \dfrac{1}{m_1} \\ 0 \\ 0 \end{bmatrix}$$

$$\bar{C} = \begin{bmatrix} 1 & 0 & 0 & 0 & 0 & 0 \\ 0 & 0 & 1 & 0 & 0 & 0 \end{bmatrix}$$

The natural frequencies of the free-free system are given by

$$\begin{aligned} \omega_L &= \sqrt{\frac{b - \sqrt{b^2 - 4c}}{2}} \quad : \text{Low} - \text{modefrequency} \\ \omega_H &= \sqrt{\frac{b + \sqrt{b^2 - 4c}}{2}} \quad : \text{High} - \text{modefrequency} \end{aligned} \tag{2.7}$$

where

$$\begin{aligned} b &= \frac{k_1 + k_2}{m_1} + \frac{k_1}{m_2} + \frac{k_2}{m_3} \\ c &= \left(\frac{1}{m_1 m_2} + \frac{1}{m_2 m_3} + \frac{1}{m_3 m_1} \right) k_1 k_2 \end{aligned}$$

In the following chapters, the high-mode natural frequency ω_H is assumed to be unknown. Boundary conditions for a rest-to-rest maneuver are

$$\begin{aligned} x_1(0) &= x_2(0) = x_3(0) = 0 \\ \dot{x}_1(0) &= \dot{x}_2(0) = \dot{x}_3(0) = 0 \\ x_1(t_{mnv}) &= x_2(t_{mnv}) = x_3(t_{mnv}) = 1 \\ \dot{x}_1(t_{mnv}) &= \dot{x}_2(t_{mnv}) = \dot{x}_3(t_{mnv}) = 0 \end{aligned} \tag{2.8}$$

where t_{mnv} is the time at the end of the maneuver, i.e., the duration of the maneuver.

The displacement vector $\begin{bmatrix} x_1 & x_2 & x_3 \end{bmatrix}^T := \tilde{x}(t)$ in (2.5) can be transformed into decoupled modal coordinates $\begin{bmatrix} \eta_1 & \eta_2 & \eta_3 \end{bmatrix}^T := \eta(t)$, as follows

$$\tilde{x}(t) = \Phi \eta(t) \tag{2.9}$$

where Φ is the modal matrix formed by stacking the mass-orthonormalized eigenvectors as columns, and $\eta(t)$ is the vector of modal amplitudes $\eta_i(t)$. Thus, the equations of motion (2.5) are transformed to the mass-normalized modal equations of motion, as follows

$$\begin{aligned} \ddot{\eta}_1 &= C_1 u \\ \ddot{\eta}_2 + \omega_L^2 \eta_2 &= C_2 u \\ \ddot{\eta}_3 + \omega_H^2 \eta_3 &= C_3 u \end{aligned} \tag{2.10}$$

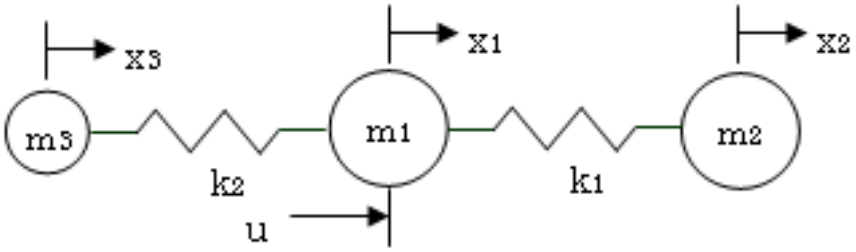

Figure 2-2: Two-mode system composed of three masses and two springs in which an input force u is applied to mass 1.

where C_1, C_2, and C_3 are constants, given by

$$\begin{bmatrix} C_1 \\ C_2 \\ C_3 \end{bmatrix} = \Phi^T \begin{bmatrix} 1 \\ 0 \\ 0 \end{bmatrix} \tag{2.11}$$

Unless otherwise indicated, the following studies are based on the assumption of nominal system with unit mass ($m_1 = m_2 = 1$); unit stiffness for the low mode ($k_1 = 1$); an unknown high mode having mass $m_3 = 0.1$; and the nominal stiffness of the unknown high mode k_2 is set to 0.67; it corresponds to ratios of the high-mode and low-mode frequencies (ω_H/ω_L) of 2.0, where ω_L is 1.37 rad/s (0.218 Hz) and ω_H is 2.74 rad/s (0.436 Hz). This value is chosen because a ratio between the range of 2.0 and 3.0 is a kind of typical one of the ratio of 2nd-mode to 1st-mode frequencies of an actual flexible structure and the ratio of 2.0 induces a typical and easy-to-understand results of conventional input shapers.

THIS PAGE INTENTIONALLY LEFT BLANK

Chapter 3

A New Preshaping Profiler (NME Profiler)

3.1 Introduction

This chapter presents a feedforward input-torque profiler for a single-axis rest-to-rest maneuver of a spacecraft. Using this profiler, a torque profile can be generated for the spacecraft to achieve a rest-to-rest maneuver with reduced residual vibration at the end of the maneuver. This preshaping profiler is called a nil-mode-exciting (NME) profiler [47].

Compared to other algorithms, the algorithm presented here proposes a better solution in terms of roll-off performance in the frequency domain. Therefore, this algorithm shows high robustness against frequency errors in the presence of unknown high modes at the expense of maneuver duration. A recent paper [44] has shown that, in a comparison between input shapers (input-shaped step commands) and S-curves (a kind of smooth command), "S-curves are poor alternatives for applications requiring rapid motion." That is true, but if mild motion or slow motion would be acceptable for the application, a smooth controller might be a better alternative to input shapers. The smooth controller presented in this chapter proposes a slow motion but fine pointing accuracy with smaller residual vibrations in the presence of unknown high modes compared to other algorithms having identical durations; this is

demonstrated in Chapter 5. The recent paper [44] has also shown that "only systems with a wide range of problematic and uncertain high modes should be driven with input-shaped S-curve commands. In the absence of such special conditions, an input-shaped step command can eliminate vibration much faster than an S-curve." This special case exactly corresponds to the target system assumed in this thesis; that is, "a satellite with large flexible structures with unknown higher modes requiring highly accurate pointing performance at the end of maneuvers" is assumed to be a suitable system to which this new algorithm should be applied.

3.2 A Sinc Function-Based Preshaping Profiler

The *sinc function* is defined by

$$\mathrm{sinc}\left(\omega_s t\right) = \frac{\sin\left(\omega_s t\right)}{\omega_s t} = \frac{\sin\left(\frac{2\pi}{T_s}t\right)}{\left(\frac{2\pi}{T_s}t\right)} \tag{3.1}$$

Theoretically, this function itself has no frequency response above frequency ω_s. The continuous Fourier transform of the sinc function is rectangular:

$$\int_{-\infty}^{\infty} \frac{\sin\left(\omega_s t\right)}{\omega_s t} e^{-i\omega_s t} dt = \mathrm{rect}(f_s) \tag{3.2}$$

where

$$f_s = \omega_s / 2\pi = 1/T_s$$

The time profile of a sinc function is shown in Fig. 3-1, and its fast Fourier transform (FFT) appears in Fig. 3-2.

If a controller is composed of the sinc function, the frequency responses of the controller and the frequencies of the spacecraft's flexible structural modes can be separated in the frequency domain by setting ω_s to a value sufficiently lower than that of the lowest flexible mode:

$$\omega_s < \omega_L \tag{3.3}$$

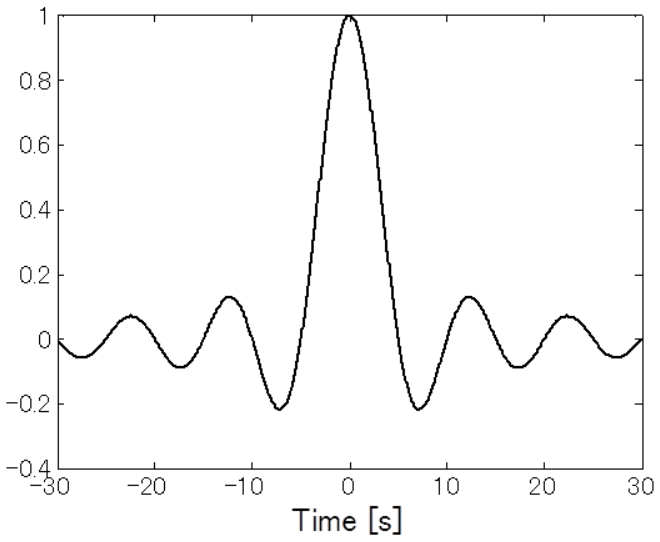

Figure 3-1: Sinc function (3.1) in the time domain with T_s= 10 s.

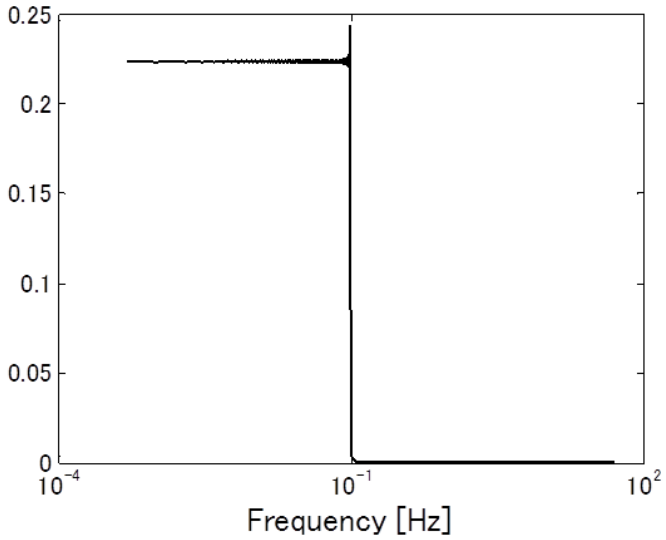

Figure 3-2: Sinc function (3.1) in FFT with T_s= 10 s.

Here, the right-hand term ω_L is the lowest flexible structural mode of the spacecraft. The following input-torque profiler is proposed:

$$u(t) = A \cdot w(t) \cdot f(t) \tag{3.4}$$

where $f(t)$ is expressed as a pair of sinc functions:

$$f(t) = \text{sinc}\left(\omega_s t - \pi\right) - \text{sinc}\left(\omega_s t - 3\pi\right) \tag{3.5}$$

The sinc function's characteristic frequency ω_s is expressed by

$$\omega_s = \frac{2\pi}{\left(t_{mnv}/2\right)} \quad \left(= \frac{2\pi}{T_s}\right) \tag{3.6}$$

In (3.4), A is a constant that is calculated from a required maneuver angle. The window function $w(t)$ is the Hamming window, which is expressed as

$$w(t) = \begin{cases} 0.54 + 0.46\cos\left\{\dfrac{2\pi}{t_{mnv}}\left(t - \dfrac{t_{mnv}}{2}\right)\right\} & \text{for} \quad 0 \le t \le t_{mnv} \\ 0 & \text{for} \quad t < 0, t_{mnv} < t \end{cases} \tag{3.7}$$

In Fig. 3-3, the upper panel shows the pair of sinc functions with 2π offset and reversed signs, as expressed by the first-term and the second-term of (3.5). The middle panel shows the window function used to truncate the summed sinc functions (3.7), and the lower panel shows the summed sinc functions multiplied by the window function (3.4). The Hamming window is chosen because of its better balance of low sidelobe level and high frequency resolution, compared to other conventional window functions.

The conversion of the function $f(t)$ in (3.5) to the Laplace domain yields

$$\begin{aligned} F(s) &= \text{sinc}(s)\left(e^{-0.5Ts} - e^{-1.5Ts}\right) \\ &= \text{sinc}(s) \cdot e^{-0.5Ts}\left(1 - e^{-Ts}\right) \end{aligned} \tag{3.8}$$

Equation (3.8) can be interpreted as the product of three functions—a sinc function, a delay of half a period, and a negative ZV shaper—for an undamped system [20, 21, 22, 24]. In the time domain, this product represents the convolution of the baseline function, $\text{sinc}(\omega_s t)$, with a sequence of impulses, $i(t)$, given by

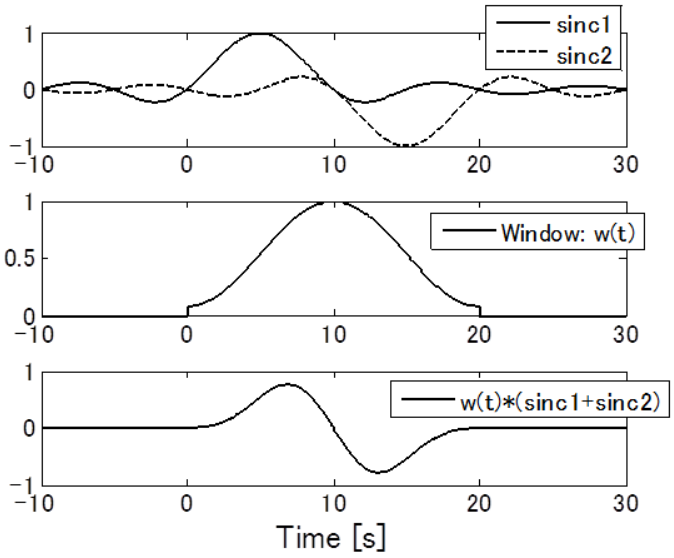

Figure 3-3: NME profiler for T_s= 10 s. Top: Pair of sinc functions with 2π offset and reversed signs (3.5). Middle: Window function (3.7) used to truncate the summed sinc functions. Bottom: Summed sinc functions multiplied by the window function (3.4).

$$\text{sinc}(\omega_s t) = \frac{\sin(\omega_s t)}{\omega_s t} \tag{3.9}$$

and

$$i(t) = \delta(t - 0.5T_s) - \delta(t - 1.5T_s) \tag{3.10}$$

Figure 3-4 shows this convolution. It is clear that this smooth profile can be considered as an input-shaped function in which the baseline function is $\text{sinc}(\omega_s t)$ and the input shaper is

$$\begin{bmatrix} A_j \\ t_j \end{bmatrix} = \begin{bmatrix} 0 & 1 & -1 \\ 0 & 0.5T_s & 1.5T_s \end{bmatrix} \tag{3.11}$$

It is noted that although a ZV shaper is usually designed for a system whose vibration period is equal to the value of T_s used to form the command, the command duration for this method is determined in a different way and it is explained later in this chapter.

Figure 3-5 shows the magnitudes of the Fourier transforms of $\text{sinc}(\omega_s t)$, $i(t)$, and $f(t)$, scaled for display purposes. This provides a general interpretation of the convolution process of the two functions $\text{sinc}(\omega_s t)$ and $i(t)$. Figure 3-6 shows the magnitudes

of the Fourier transforms of $f(t)$ in (3.5) and $u(t)$ in (3.4), illustrating the effect of window functioning.

This profiler is a smooth input-torque profiler of a sinc function convolved with a negative ZV shaper and multiplied by a window function. The sinc function has low-pass filter characteristics with a roll-off frequency $f_s(= 1/T_s)$, while the negative ZV shaper is a multinotch filter with a cut-off frequency $f_s(= 1/T_s)$ and its harmonics, so the frequency characteristic of the convolved smooth curve appears as in Fig. 3-5. Because of the truncation by the window function with time length $\pm 1.5T_s$, the frequency characteristic of the applied sinc function is slightly rounded from an ideal rectangular shape.

Note that Figs. 3-5 and 3-6 represent the FFT of a force (torque) input command, not a position (angle) command. Therefore, in those figures, there is no energy at 0 Hz because the accumulated acceleration forces for a rest-to-rest motion will always be cancelled by an equivalent amount of accumulated deceleration forces at the end of the motion.

The boundary frequency cycle of the sinc functions $T_s(= 2\pi/\omega_s)$ is determined as half period of a maneuver duration t_{mnv}, and t_{mnv} should be determined considering the relation between the frequency of the lowest structural frequency mode ω_L and the boundary frequency of this profiler. The boundary frequency of this profiler, when T_s is 10 s (i.e., maneuver duration is 20 s), is shifted from the boundary frequency of the sinc functions itself (0.1 Hz) to 0.174 Hz (period of 5.747 s) because of the truncation effect by the window function as shown in Fig. 3-6. Therefore, t_{mnv} in relation to the frequency cycle of the lowest structural mode T_L should be determined as

$$t_{mnv}\,(= 2T_s) \geq \frac{20}{5.747} T_L \cong 3.48 T_L \tag{3.12}$$

where T_L is the vibration cycle of the lowest flexible structural mode, and is given by

$$T_L = \frac{2\pi}{\omega_L}$$

Considering potential effects by the modeling errors of the flexible modes, t_{mnv} used in this study will be set to four times the lowest mode vibration cycle,

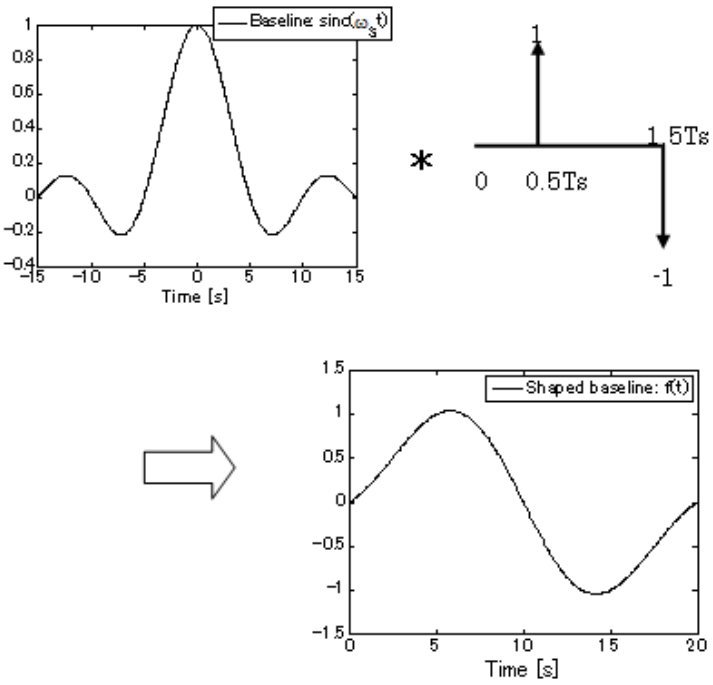

Figure 3-4: Convolution of a sinc function (3.9) (T_s=10 s) with a series of impulses (3.10). Top left is the original sinc function, top right shows the impulses, and bottom right is the convolution.

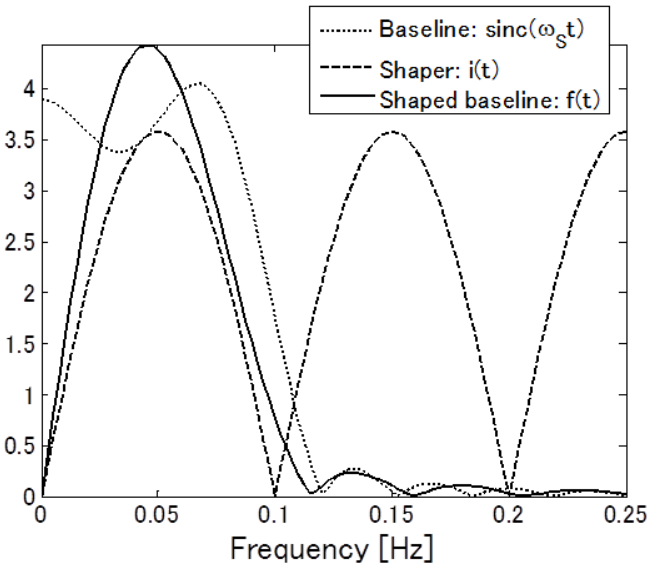

Figure 3-5: FFT of the baseline sinc function (dotted line), the sequence of impulses used as the shaper (dashed line), and the resulting shaped baseline (solid line) (T_s=10 s).

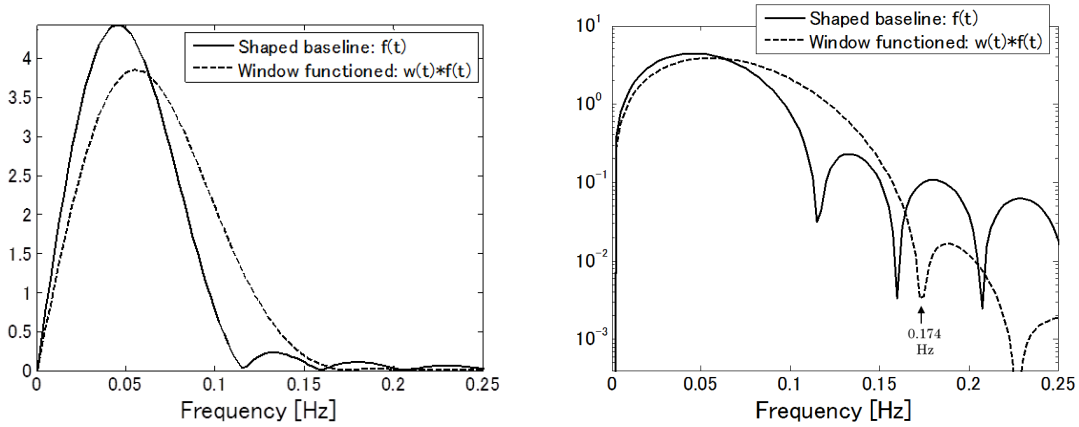

(a) Linear (b) Semilog

Figure 3-6: FFTs of the shaped baseline (solid line) and the window functioned result (dashed line) (T_s=10 s).

$$t_{mnv} \, (= 2T_s) \equiv 4T_L \tag{3.13}$$

For example, if the lowest structural mode ω_L is 0.4π rad/s (so the vibration cycle T_L is 5 s), the maneuver duration t_{mnv} will be 20 s (four times the vibration cycle of 5 s).

Chapter 4

Comparison of Preshaping Profilers for Single-Mode Systems

4.1 Introduction

Three criteria will be used here to evaluate command shaping profilers [42]. First, the profiler duration will be compared. The time required for the system to move depends on the duration of the profiler and the duration of the profiler is a lower bound on the maneuvering time. Second, the residual vibration resulting from a filtered step command will be compared. Finally, the robustness of the preshaping profilers to uncertainties in the system model will be examined. Each of the preshaping profilers will be used to shape the input to a simple harmonic oscillator shown in Fig. 2-1. In order to evaluate the second and third performance criteria, three step responses (here, rest-to-rest maneuver responses) will be determined for each profiler. One is the response when the system model is perfect. The other two are the responses when k, spring constant of the model, is varied from the nominal value of 1.0 to 0.8 and 0.6. All the systems will have no damping so that two quantities can clearly be observed: the time at which the profiler finishes and the residual vibration amplitude. The design parameters used to generate the preshaping profilers in this comparison consist of the system frequency and, in case of EI shapers, the limit on the tolerable level of residual vibration, V, and, in case of low-pass filters, the stopband, the passband, the

passband ripple, the stopband attenuation, and the filter number. For each of the following profilers, it is attempted to select the design parameters so that the best possible performance is obtained.

4.2 Minimum Time Control for Rigid Body

For a "rigidized" model of the nominal system shown in Fig. 2-1, the equation of motion is simply

$$(m_1 + m_2)\,\ddot{x} = u \tag{4.1}$$

The boundary conditions for a rest-to-rest maneuver are given as

$$\begin{aligned} x(0) &= 0 \\ x(t_f) &= 1 \end{aligned} \tag{4.2}$$

Solving the rest-to-rest, time-optimal control problem of rigid body with boundary conditions of (4.2) and applying the symmetry about $t_2(= t_f/2)$, the time-optimal bang-bang control input is given as

$$u(t) = u_s(t) - 2u_s(t - 1.41421) + u_s(t - 2.82843) \tag{4.3}$$

Figure 4-1 shows input command and responses of the rigid-body minimum time controller. The input command is applied as input force of u in Fig. 2-1 and vertical axis of the responses represents position of m_1 mass. The time duration is short (2.828s) but residual vibration is significant because no vibration reduction is considered.

4.3 ZV/ZVD Time-Optimal Shaper

Smith [20, 21] proposed an input shaper, zero vibration (ZV) shaper which was derived from constraint equations of multi-impulse responses. Singer and Seering [22, 48]

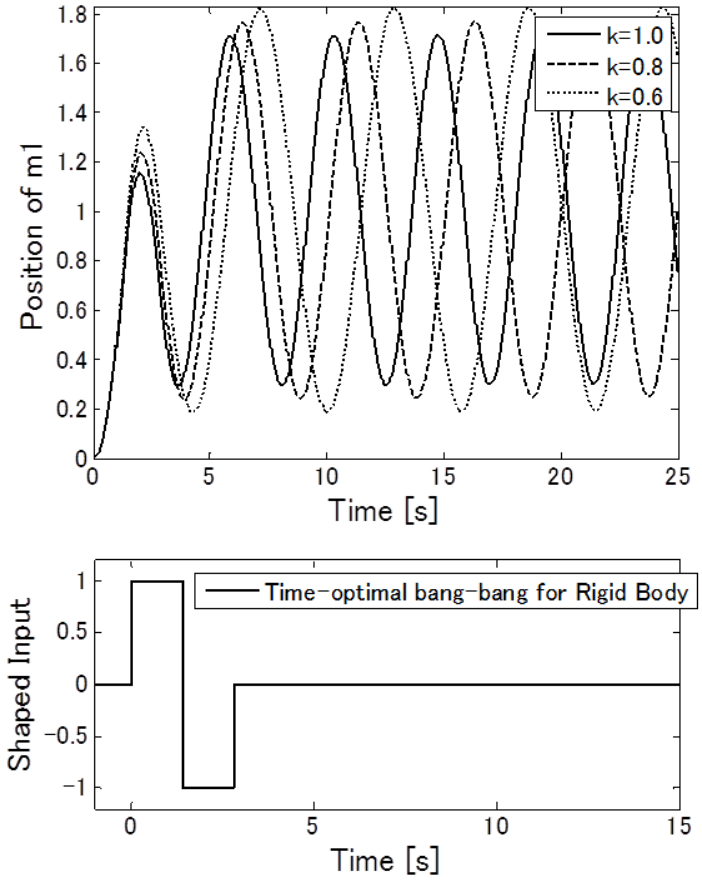

Figure 4-1: Shaped command and responses of Minimum time controller for Rigid Body

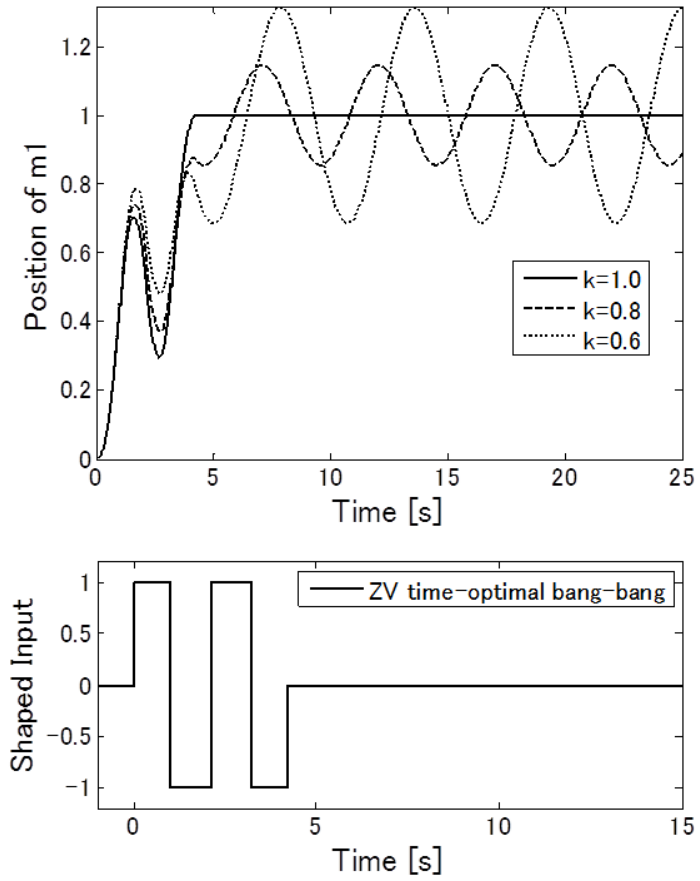

Figure 4-2: Shaped command and responses of ZV Time-Optimal shaper

proposed an input shaper, zero vibration and derivative (ZVD) shaper with robustness to modeling errors of the system frequency by adding a new constraint regarding the system natural frequency. The input shapers like ZV or ZVD shaper consist of a series of impulses, so the input shaper itself cannot be applied to an actual system if the system's input command is defined as forcing input. Liu and Wie proposed an approach for computing time-optimal control inputs for uncertain flexible spacecraft's rest-to-rest maneuver with constant-force actuators based on ZV and ZVD shaper techniques [30, 31]. Figures 4-2 and 4-3 show input commands and responses of the ZV time-optimal controller and the ZVD time-optimal controller, respectively. The residual vibration is reduced in the ZVD time-optimal controller (5.866s) responses compared to the ZV time-optimal controller (4.218s) at a cost of time duration.

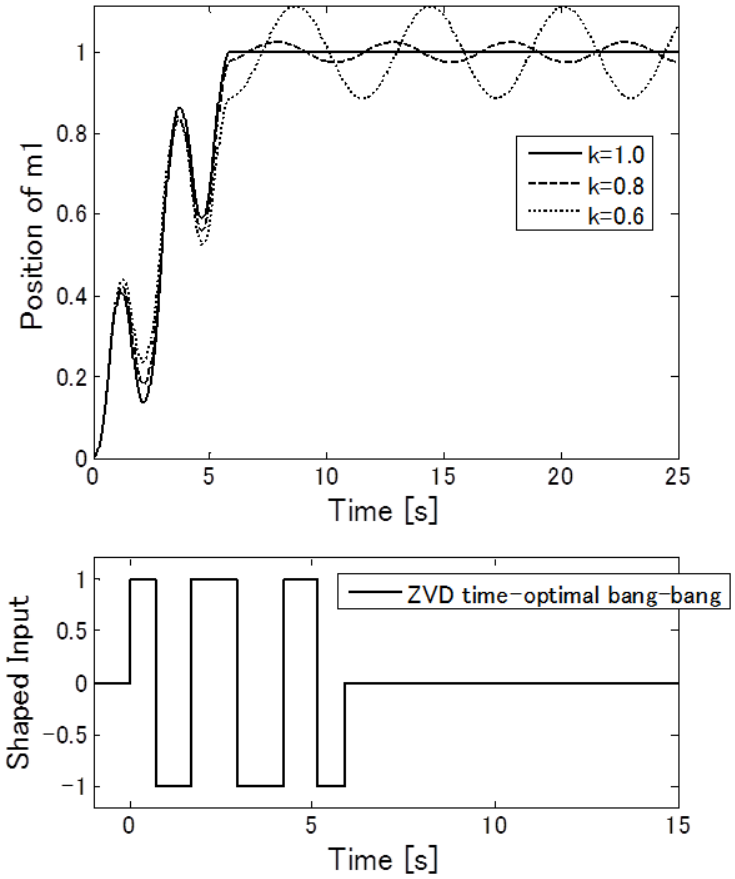

Figure 4-3: Shaped command and responses of ZVD Time-Optimal shaper

4.4 One-hump/Two-hump EI Time-Optimal Shaper

Singhose et al. [23] proposed an alternate robustness constraint which generates more insensitivity by abandoning the requirement of zero residual vibration at the modeling frequency i.e. $\omega/\omega_0 = 1$. By limiting the residual vibration to some small value, V, rather than forcing it to zero, the robustness can be improved without increasing the shaper duration. Shapers designed with this approach are called extra-insensitive (EI) shaper. Singhose et al. [32] proposed an approach for computing time-optimal control inputs for uncertain flexible spacecraft's rest-to-rest maneuver with constant-force actuators based on EI shaper techniques. Figures 4-4 and 4-5 show input commands and responses of the one-hump EI time-optimal controller (V=5%) and two-hump EI time-optimal controller (V=5%), respectively. The time durations of ZVD time-optimal (5.866s) and one-hump EI time-optimal (5.902s) are nearly equivalent, but the residual vibration in frequency error case is smaller in one-hump EI time-optimal than ZVD time-optimal at a cost of residual vibration in exact case, i.e. $k = 1$. The residual vibration is reduced in two-hump EI time-optimal controller (7.770s) responses compared to one-hump EI time-optimal controller at a cost of time duration. The degree of freedoms of the constraint conditions for ZVD shaper and one-hump EI shaper are the same, hence the time durations are nearly equivalent between those shapers. The same relationship can happen between ZVDD and two-hump EI or ZVDDD and three-hump EI.

4.5 Input-shaped Rigid Body Commands with ZV/ZVD/One-hump EI shapers

Smith [20, 21] proposed an input shaper, the zero-vibration (ZV) shaper, which was derived from constraint equations of multi-impulse responses, as follows.

$$\begin{bmatrix} A_j \\ t_j \end{bmatrix} = \begin{bmatrix} 0.5 & 0.5 \\ 0 & 0.5T \end{bmatrix} \tag{4.4}$$

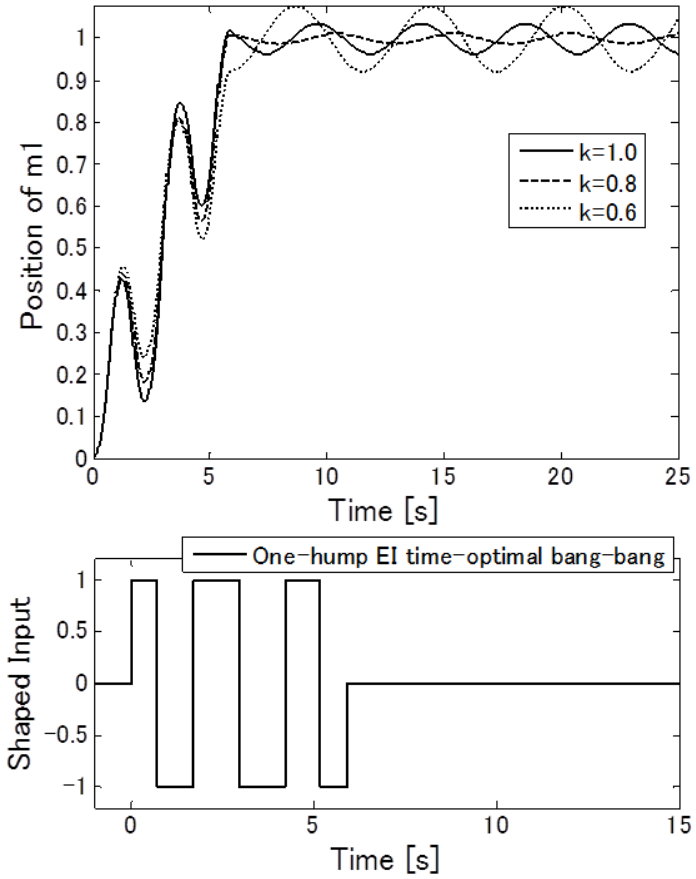

Figure 4-4: Shaped command and responses of One-Hump EI Time-Optimal shaper

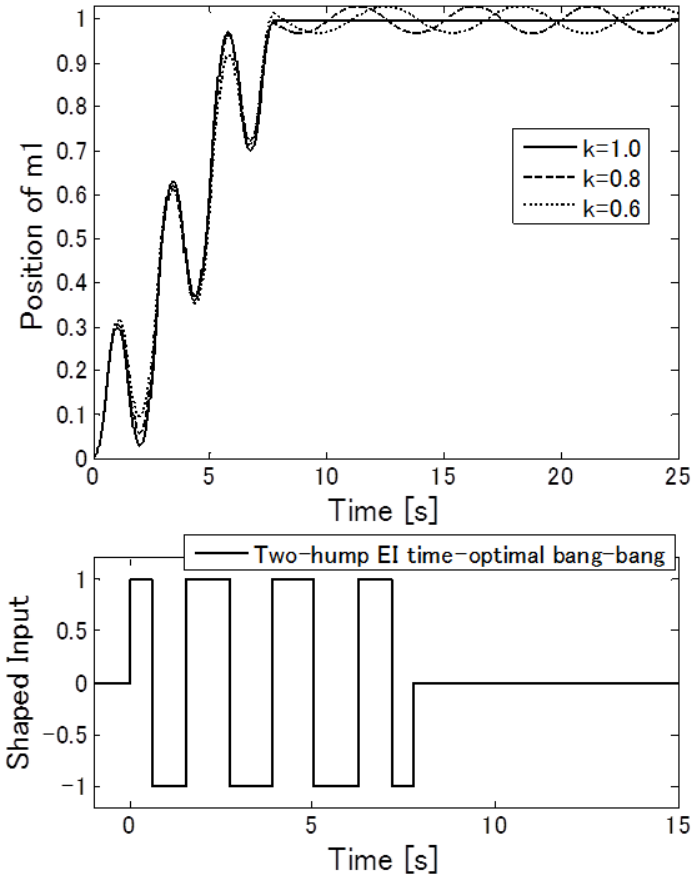

Figure 4-5: Shaped command and responses of Two-Hump EI Time-Optimal shaper

where

$$T = \frac{2\pi}{\omega}$$

is the period of the undamped vibration ($\omega = \sqrt{2}$ from (2.3)).

Singer and Seering [22, 48] proposed an input shaper, ZVD shaper with robustness to modeling errors of the system frequency by adding a new constraint regarding the system natural frequency as follows.

$$\begin{bmatrix} A_j \\ t_j \end{bmatrix} = \begin{bmatrix} 0.25 & 0.5 & 0.25 \\ 0 & 0.5T & T \end{bmatrix} \tag{4.5}$$

Singhose et al. [23] proposed an alternate robustness constraint that generates more insensitivity by abandoning the requirement of zero residual vibration at the modeling frequency, i.e., $\omega/\omega_0 = 1$. By limiting the residual vibration to a small value V, rather than forcing it to zero, robustness can be improved without increasing the shaper duration. Shapers designed with this approach are called extra-insensitive (EI) shapers. A one-hump EI shaper is given as follows.

$$\begin{bmatrix} A_j \\ t_j \end{bmatrix} = \begin{bmatrix} \frac{1+V}{4} & \frac{1-V}{2} & \frac{1+V}{4} \\ 0 & 0.5T & T \end{bmatrix} \tag{4.6}$$

Input shapers like ZV, ZVD, and EI consist of a series of impulses, so the input shaper itself is not suitable for actual system use. The rigid-body minimum-time commands given in (4.3) convolved with ZV, ZVD, or EI shapers are used here as input-force commands.

Figures 4-6, 4-7, and 4-8 show input commands and responses of the rigid-body minimum time commands (4.3) shaped with ZV, ZVD and EI shapers (V=5%), respectively. Durations of each controller are slightly longer than the same type time-optimal controllers, but residual vibrations are slightly smaller than the same type time-optimal controllers.

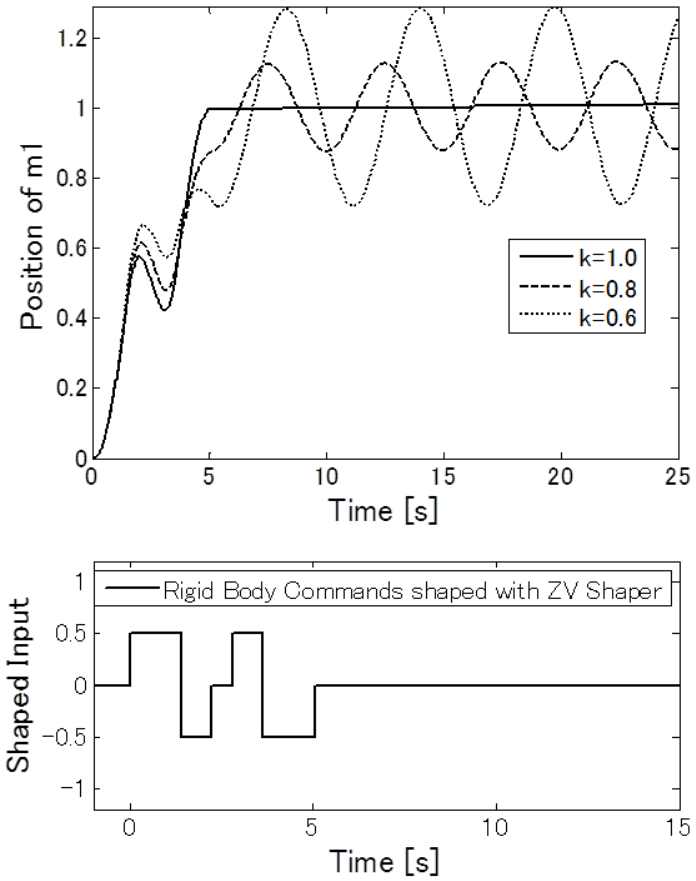

Figure 4-6: Shaped command and responses of Rigid Body command shaped with ZV shaper

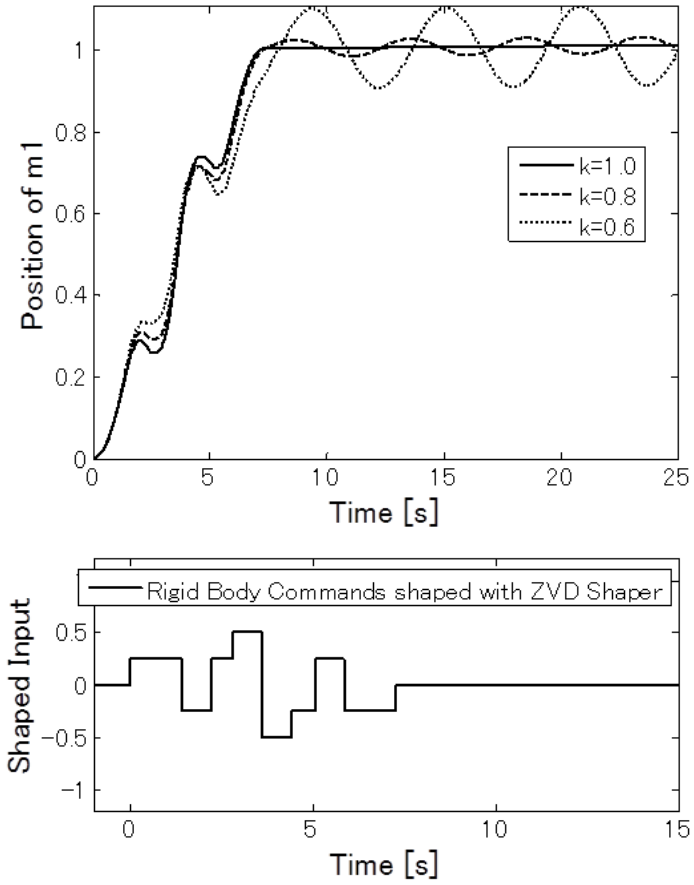

Figure 4-7: Shaped command and responses of Rigid Body command shaped with ZVD shaper

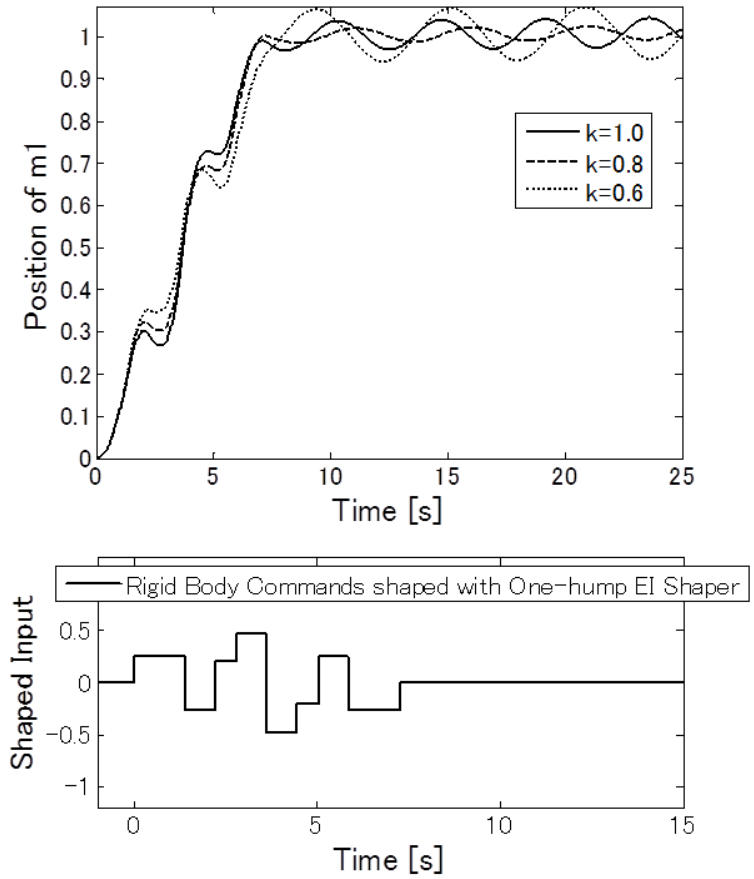

Figure 4-8: Shaped command and responses of Rigid Body command shaped with One-hump EI shaper

4.6 Input-shaped Rigid Body Commands with ZVDDD/Three-hump EI/ZVDDDDDD shapers

Expanding the constraint equations of multi-impulse responses of ZVD shaper and one-hump EI shaper by adding the higher order derivatives regarding the system natural frequency, ZVDDD shaper, three-hump EI shaper and ZVDDDDDD are given [22, 25]. Figures 4-9, 4-10, and 4-11 show input commands and responses of the rigid-body minimum time commands (4.3) shaped with ZVDDD, three-hump EI shapers (V=5%) and ZVDDDDDD, respectively. Durations of ZVDDD and three-hump EI are twice or more than ZVD type or one-hump EI type controller, but residual vibrations are less than half of ZVD type or one hump EI type controller. The duration of ZVDDDDDD is 18.379 s, but the residual vibration is significantly smaller than others.

4.7 Elliptic Low-pass Filter

So far, the durations of the profilers are evaluated as maneuver durations, but regarding Infinite Impulse Response (IIR) low-pass filter, the filtered command will continue infinitely so the duration to settle within 2% of its steady state value (2%, 0-to-peak) is evaluated as the maneuver duration. The elliptic filter was designed with a passband at 50% of the anticipated natural frequency, and 1 dB ripple and 40 dB attenuation in the stopband. The elliptic filter is applied to the rigid body command. Figure 4-12 shows responses of the elliptic filter.

4.8 Ramped Sinusoidal

Meckl and Seering proposed smooth input functions from either versine functions or ramped sinusoids [35, 36, 37]. A ramped sinusoidal curve can be used as a characteristic function for a rest-to-rest maneuver since the smooth transitions in slope at the beginning and end tend to reduce excitation energy at higher frequencies. To achieve

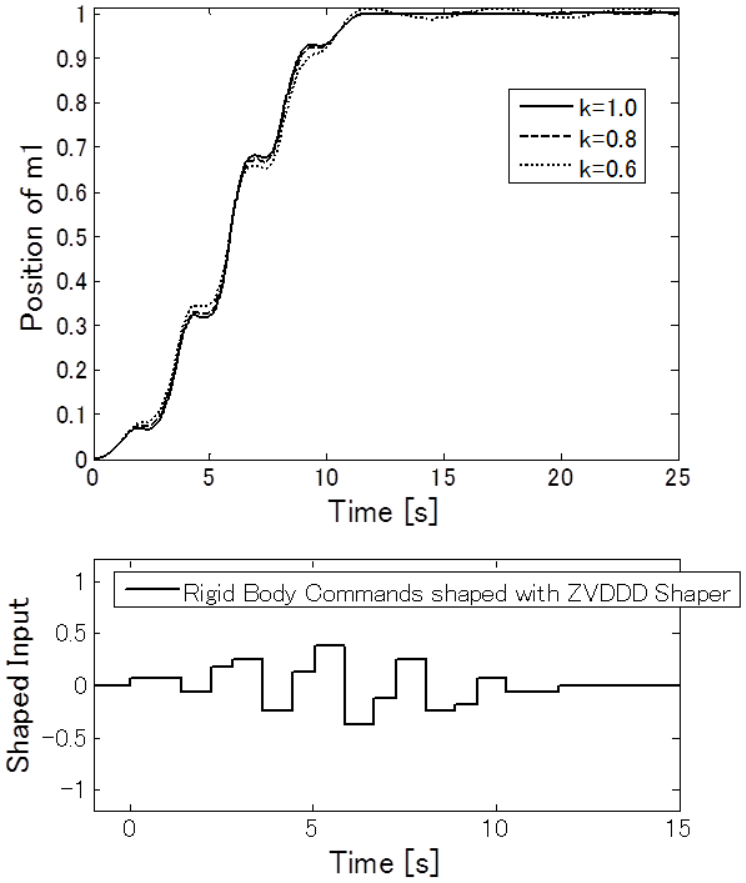

Figure 4-9: Shaped command and responses of Rigid Body command shaped with ZVDDD shaper

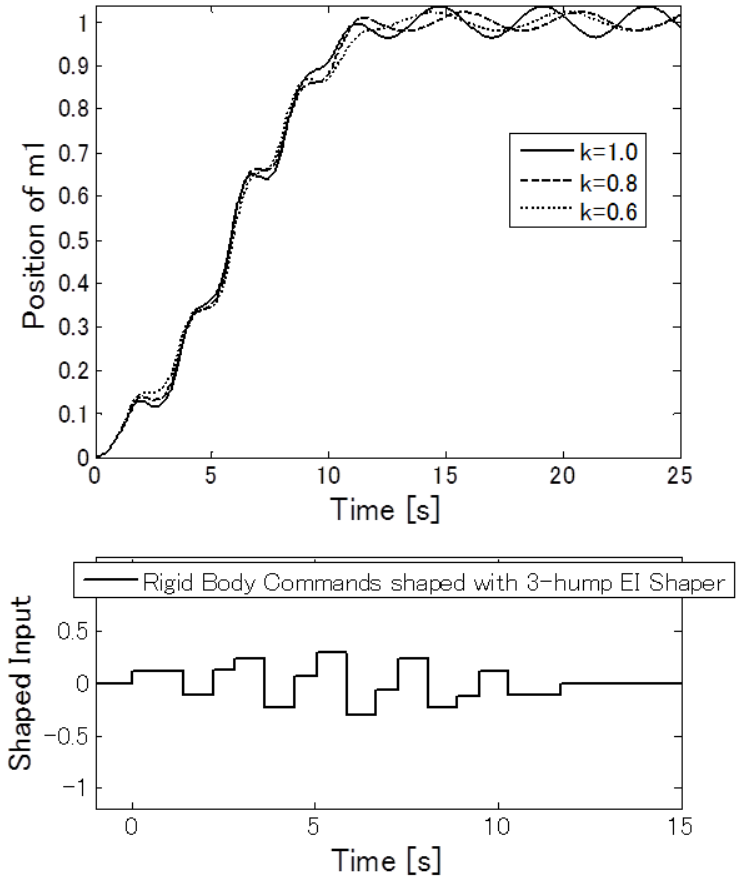

Figure 4-10: Shaped command and responses of Rigid Body command shaped with Three-hump EI shaper

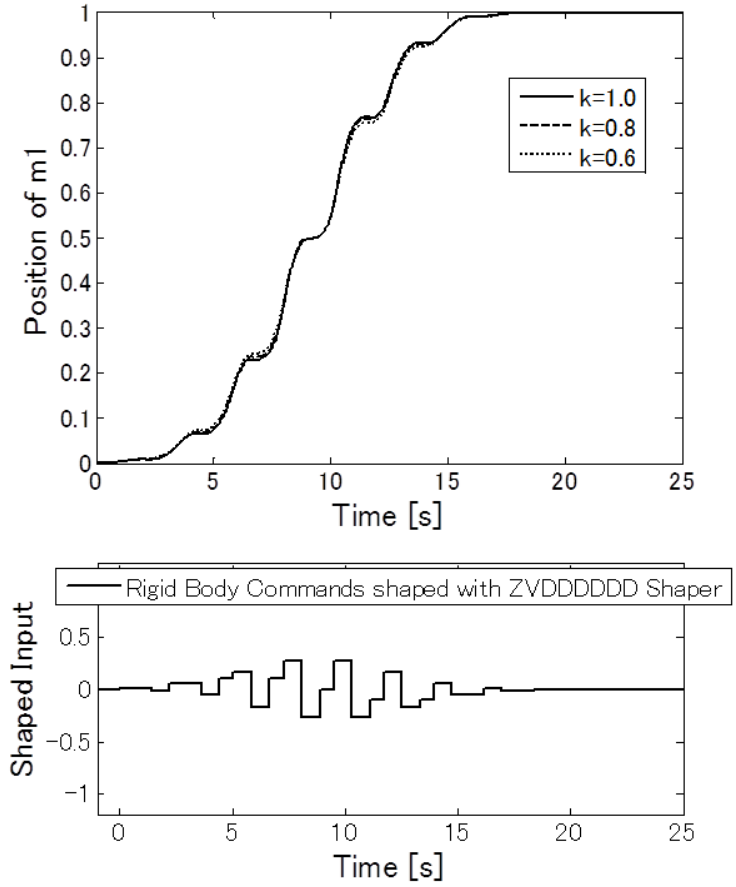

Figure 4-11: Shaped command and responses of Rigid Body command shaped with ZVDDDDDD shaper

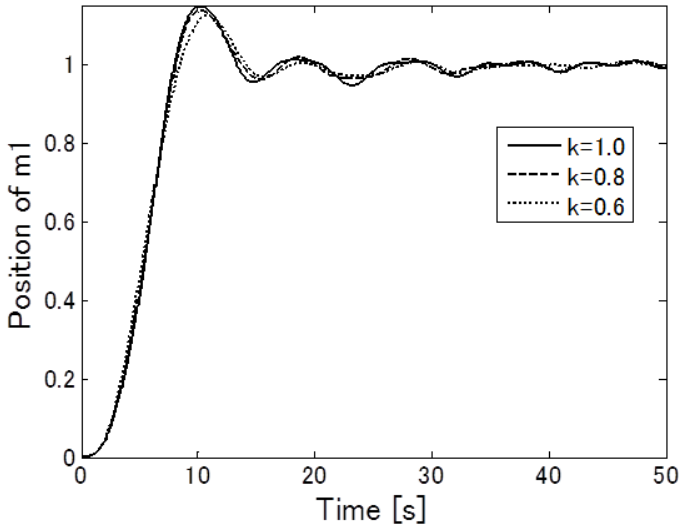

Figure 4-12: Responses of Elliptic Low-pass filter

a swift maneuver, the fundamental ramped sinusoidal function and its harmonics are selectively added to approximate a square wave [36, 37]. The input commands of a 15-term series of ramped sinusoidal curves and the responses are shown in Figs. 4-13 and 4-14.

4.9 NME Profiler

Figure 4-15 shows input commands and responses of the NME profiler which was proposed in the Chapter 3. The duration is approximately 18 s, but the residual vibration is very small.

4.10 Discussion on Single-Mode System

Table 4.1 lists the duration, residual vibration (peak-to-peak) of exact model, and residual vibration (peak-to-peak) of model with k=0.6 (frequency lowered by 22.54%) for each of the shapers and filters discussed. Figure 4-16 shows comparison of durations versus residual vibrations at k=0.6.

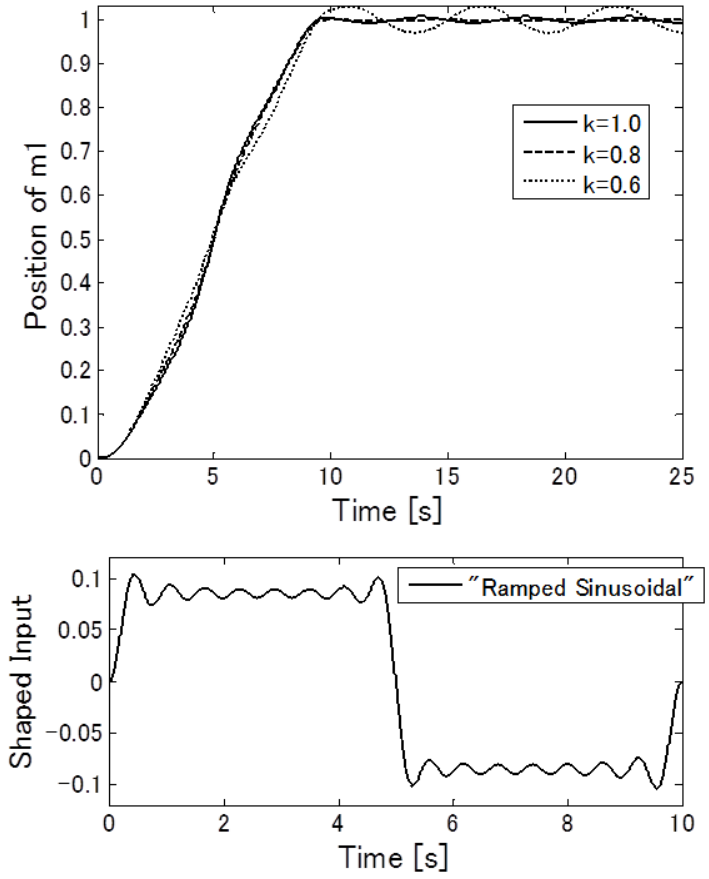

Figure 4-13: Shaped command and responses of Ramped Sinusoidal (L=15, t_{mnv}=10 s)

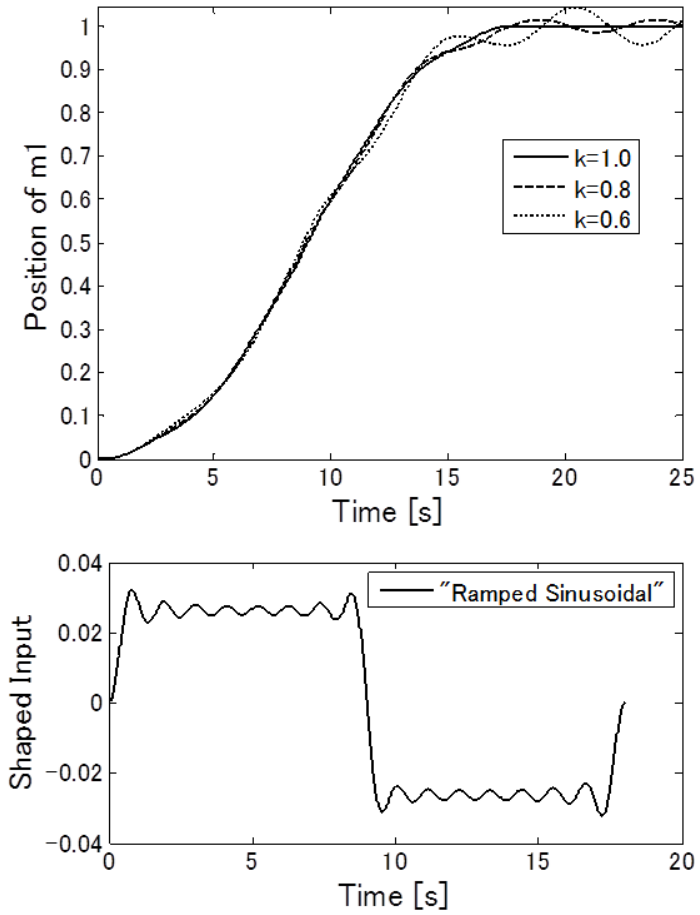

Figure 4-14: Shaped command and responses of Ramped Sinusoidal (L=15, t_{mnv}=18 s)

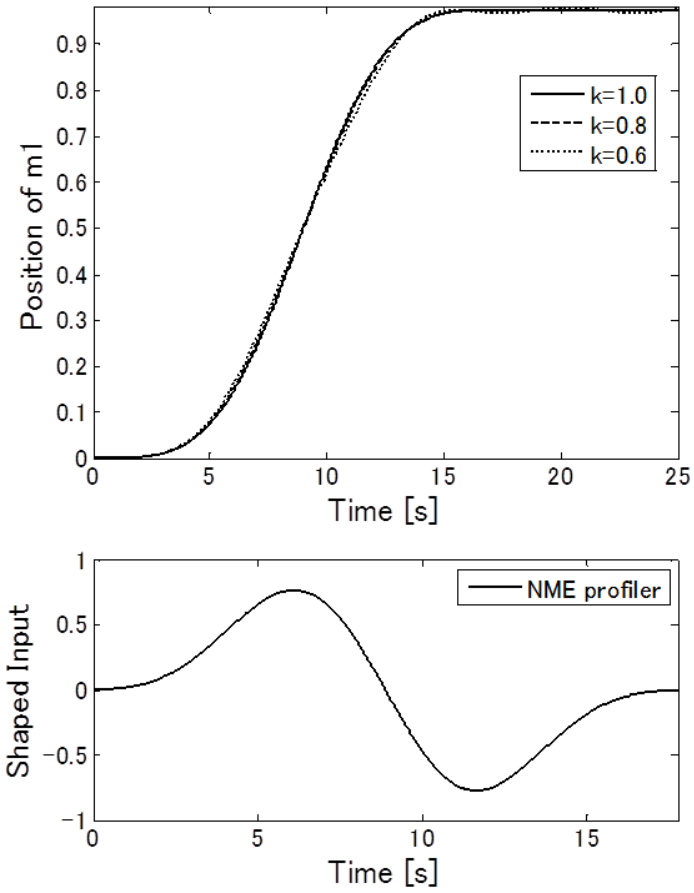

Figure 4-15: Shaped command and responses of NME profiler (T_s=8.886 s)

Table 4.1: Simulation results for comparison (Single-Mode System)

	Duration	Vibration of m_1 (peak-to-peak)	
		Exact	k=0.6 (22.5% Low)
On-off type			
Minimum time for rigid body	2.828s	141.5%	163.0%
ZV time-optimal	4.218s	0.0%	62.8%
ZVD time-optimal	5.866s	0.0%	22.7%
One-hump EI time-optimal	5.902s	7.2%	15.5%
Two-hump EI time-optimal	7.770s	0.0%	6.2%
Rigid body cmd shaped with ZV shaper	5.050s	0.0%	56.4%
Rigid body cmd shaped with ZVD shaper	7.271s	0.0%	19.5%
Rigid body cmd shaped with 1-hump EI shaper	7.271s	7.0%	12.3%
Rigid body cmd shaped with ZVDDD shaper	11.714s	0.0%	2.3%
Rigid body cmd shaped with 3-hump EI shaper	11.714s	7.1%	4.2%
Rigid body cmd shaped with ZVDDDDDD shaper	18.379s	0.0%	0.1%
Smooth type			
Elliptic low-pass filter	41.034s	2.8%	1.7%
Ramped sinusoidal (L=15, t_{rmv}=10s)	10.000s	1.3%	6.2%
Ramped sinusoidal (L=15, t_{rmv}=18s)	18.000s	0.0%	8.8%
NME (T_s=8.886s)	17.772s	0.1%	1.4%

Note: All the EI shapers are based on V=5%.

ZVDDDDDD shaper shows the smallest residual vibrations among all the profilers compared, although maneuver distance will be turned out to be very short in Chapter 6. The NME profiler shows the second smallest residual vibrations among the profilers. This chapter assumed a known single-mode system which represents a simple system rather than complicated systems that this thesis deal with, so two-mode system with known lower mode and unknown higher mode, which represents the most simplified complicated system, will be introduced in the next chapter.

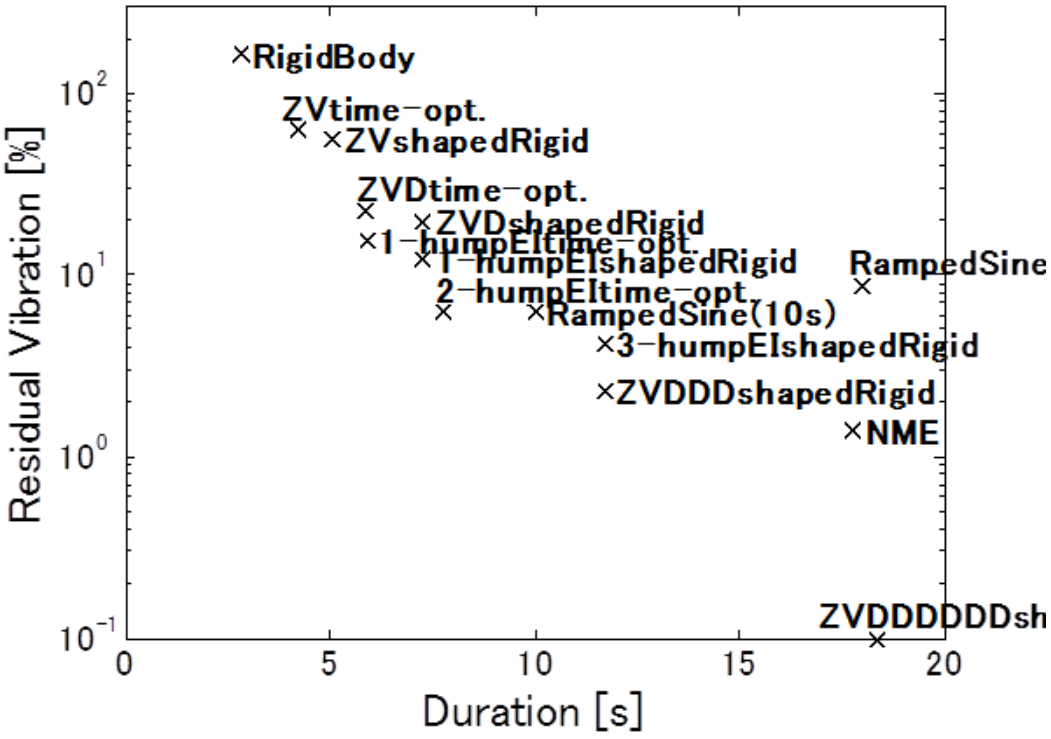

Figure 4-16: Comparison of durations vs. residual vibrations (k=0.6) (Single-Mode System)

Chapter 5

Comparison of Preshaping Profilers for Two-Mode Systems with an Unknown High Mode

5.1 Introduction

The previous chapter assumed a known single-mode system which represents a simple system rather than complicated systems that this thesis deal with, so two-mode system with known lower mode and unknown higher mode, which represents the most simplified complicated system, is introduced in this chapter.

The same criteria introduced in Chapter 4 will be used here to evaluate command-shaping profilers, where residual vibrations of the mass of the body (m_1) are evaluated as the residual vibrations.

Each preshaping profiler will be used to generate input-force commands to the two-mode harmonic oscillator shown in Fig. 2-2. The two-mode system consists of unit masses ($m_1 = m_2 = 1$); unit stiffness for the low mode ($k_1 = 1$); and an unknown high mode having mass $m_3 = 0.1$, which is 10% of the low-mode mass m_2. The assumption of the unknown high-mode mass m_3 being 0.1 (10%) is suggested from Table 1.1. The effective mass of the lowest mode of x-axis translational motion is 62.28% of a total

mass, and the effective masses of the higher modes are 19.85% (32% of the lowest-mode mass), 7.15% (11% of the lowest-mode mass), 4.93% (8% of the lowest-mode mass), etc. Therefore, it is realistic to assume that the unknown high-mode mass will be 10% of the low-mode mass. The low-mode frequency ω_L is known, but the high-mode frequency ω_H is assumed to be unknown here; therefore, preshaping profilers compared in this chapter are designed only to eliminate the low-mode vibration.

To evaluate the second and third performance criteria, three shaped-command responses will be determined for each profiler. The three cases will be the responses when the stiffness of the unknown high mode k_2 is set to 0.67, 1.54, and 2.76; these correspond to ratios of the high-mode and low-mode frequencies (ω_H/ω_L) of 2.0, 3.0, and 4.0, respectively. The low-mode and high-mode frequencies are given by (2.7) as 0.21811 Hz and 0.43563 Hz when k_2 is 0.67, 0.21924 Hz and 0.65703 Hz when k_2 is 1.54, and 0.21955 Hz and 0.87834 Hz when k_2 is 2.76. None of the systems will have damping; hence, two quantities can clearly be observed: the time at which the profiler finishes and the amplitudes of residual vibrations.

The design parameters used to generate the preshaping profilers in this comparison consist of the system frequency, and in the case of EI shapers, the limit on the tolerable level of residual vibration *V,* and in the case of ramped sinusoidal profilers, maneuver duration and the number of harmonics of the fundamental ramped sinusoidal function. For each of the following profilers, the design parameters are selected such that the best possible performance is obtained.

5.2 Minimum Time Control for Rigid Body

Ignoring the unknown high-mode mass m_3 in Fig. 2-2 and considering a "rigidized" model of a two-mass one-spring system, the equation of motion is simply

$$(m_1 + m_2)\,\ddot{x} = u \tag{5.1}$$

The boundary conditions for a rest-to-rest maneuver are

$$\begin{aligned} x(0) &= 0 \\ x(t_{mnv}) &= 1 \end{aligned} \tag{5.2}$$

Solving the rest-to-rest, time-optimal control problem of a rigid body with the boundary conditions in (5.2), and applying symmetry about $t(= t_{mnv}/2)$, the time-optimal bang-bang control input is

$$u(t) = u_s(t) - 2u_s(t - 1.41421) + u_s(t - 2.82843) \tag{5.3}$$

Figure 5-1 shows the input command and command responses of the rigid-body minimum-time controller applying the input command (5.3). The input command is applied as the input force u in Fig. 2-2, and the vertical axes in Fig. 5-1 represent the positions of mass m_1 and mass m_3, scaled for display purposes. The duration is short (2.828 s); but, residual vibrations are significant because no vibration reduction is applied.

5.3 Input-shaped Rigid Body Commands with ZV/ZVD/One-hump EI shapers

The ZV, ZVD, and EI shapers used for the convolution are designed to eliminate low-mode vibrations. Figures 5-2, 5-3, and 5-4 show the input commands and responses of the rigid-body minimum-time commands (5.3) shaped with ZV, ZVD, and one-hump EI shapers ($V = 5\%$), respectively.

Residual vibrations occur when ω_H/ω_L is 2.0 and 4.0. This result can be explained by the sensitivity curves of residual vibration versus normalized system frequency [22] shown in Figs. 5-5 and 5-6. Figures 5-5 and 5-6 show the sensitivity curves of ZV, ZVD, and higher-order ZVD-type shapers on different horizontal scales. The shapers will cause no vibration when the modeling frequency is correct ($\omega/\omega_0 = 1$). If this frequency deviates from the low mode by a factor of 2.0 or 4.0, then the shaper will induce considerable high-mode vibrations. The same discussion can be applied

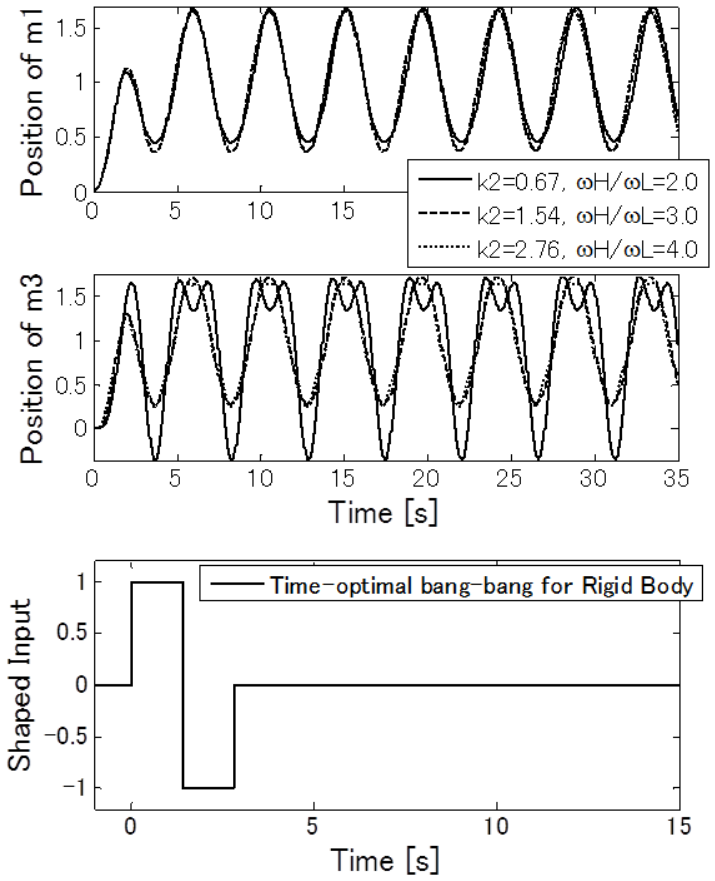

Figure 5-1: Shaped-command responses of a minimum-time controller for a rigid body (5.1) at three values of stiffness k_2 of the unknown high-frequency mode. Top: positions of mass m_1. Middle: positions of mass m_3. Bottom: shaped input command (5.3).

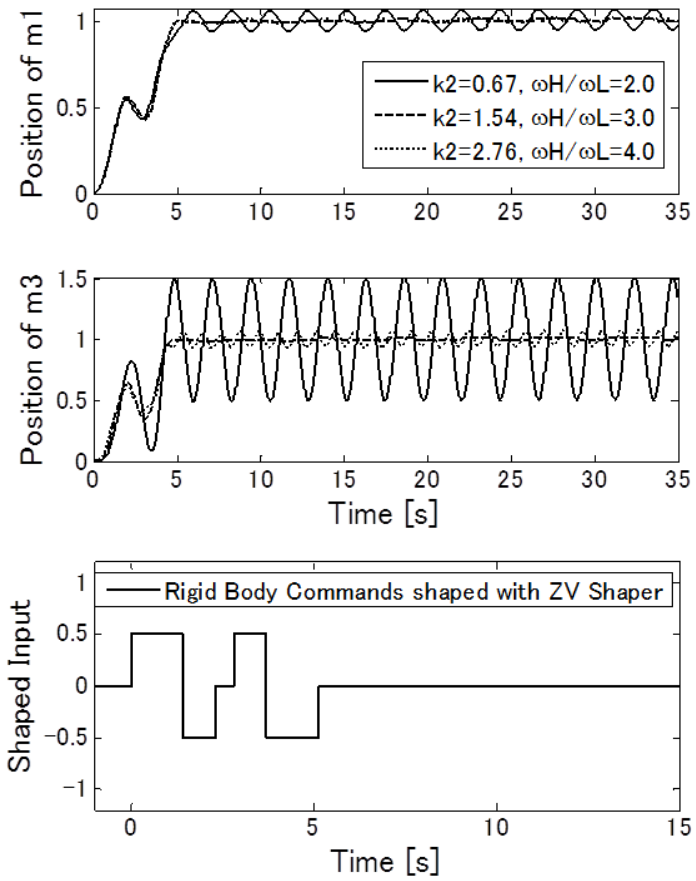

Figure 5-2: Shaped-command responses of a rigid-body command shaped with a ZV shaper at three values of stiffness k_2 of the unknown high-frequency mode. Key to panels as in Fig. 5-1.

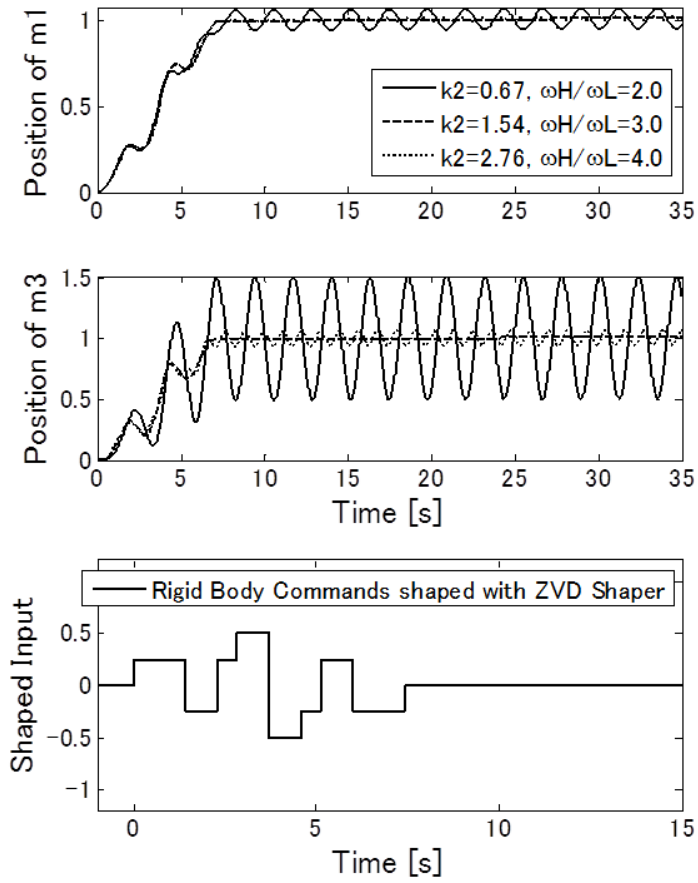

Figure 5-3: Shaped-command responses of a rigid-body command shaped with a ZVD shaper at three values of stiffness k_2 of the unknown high-frequency mode. Key to panels as in Fig. 5-1.

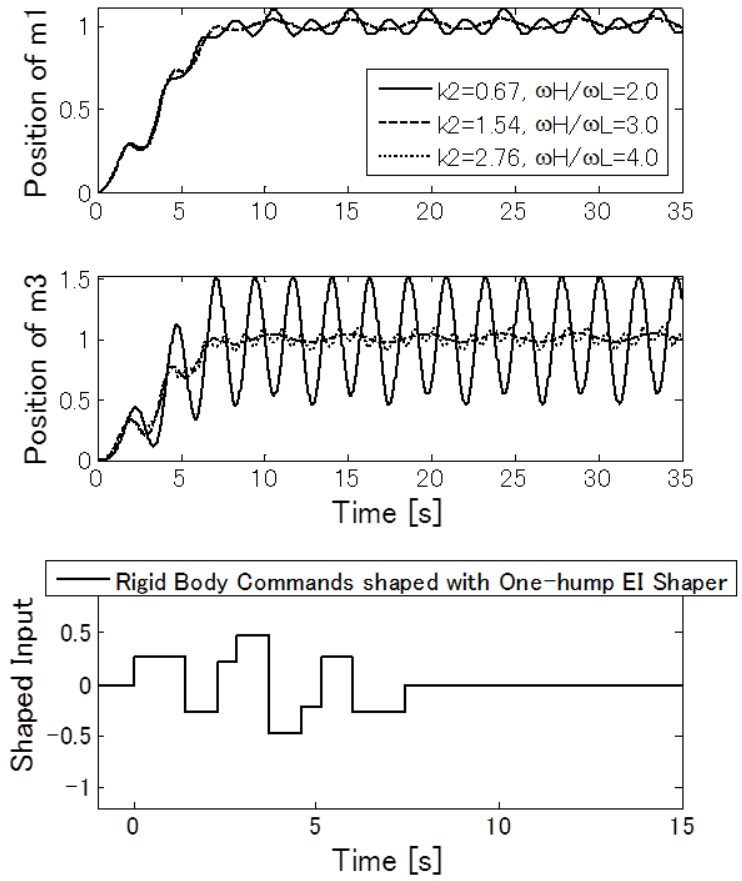

Figure 5-4: Shaped-command responses of a rigid-body command shaped with a one-hump EI shaper at three values of stiffness k_2 of the unknown high-frequency mode. Key to panels as in Fig. 5-1.

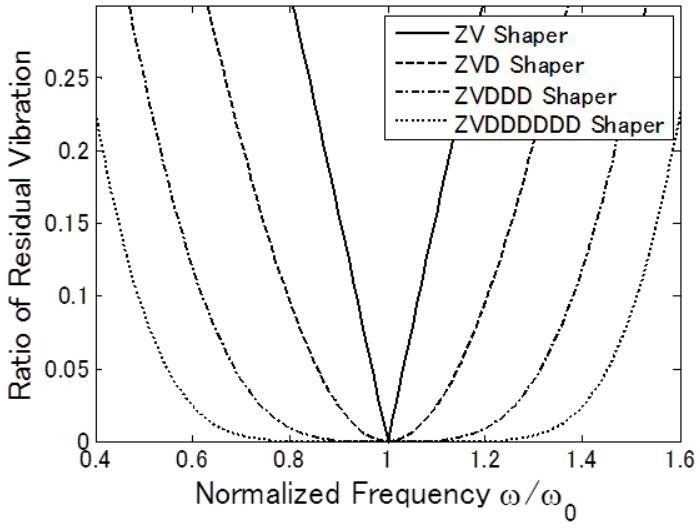

Figure 5-5: Small residual vibrations as functions of normalized system frequency for ZV, ZVD, and higher-order ZVD-type shapers.

to the unknown high-mode frequency. The EI shaper generates more insensitivity to frequency errors by allowing residual vibrations at the modeling frequency and its harmonics, i.e., at $\omega/\omega_0 = 1, 2, 3, \cdots$ etc.; therefore, the responses show higher residual vibrations compared to the ZV and ZVD shapers. The lower frequency vibration contains higher energy; therefore, the residual vibrations are higher at $\omega_H/\omega_L = 2.0$ than at 4.0.

5.4 Input-shaped Rigid Body Commands with ZVDDD/Three-hump EI/ZVDDDDDD shapers

By adding higher-order derivatives of the system's natural frequency, the constraint equations of multi-impulse responses of the ZVD shaper and the one-hump EI shaper can be expanded to obtain the ZVDDD, three-hump EI, and ZVDDDDDD shapers [22, 25]. The ZVDDDDDD shaper is selected here for comparisons because its duration is nearly equivalent to that of the NME profiler. Figures 5-7, 5-8, and 5-9 show input commands and responses of the rigid-body minimum-time commands

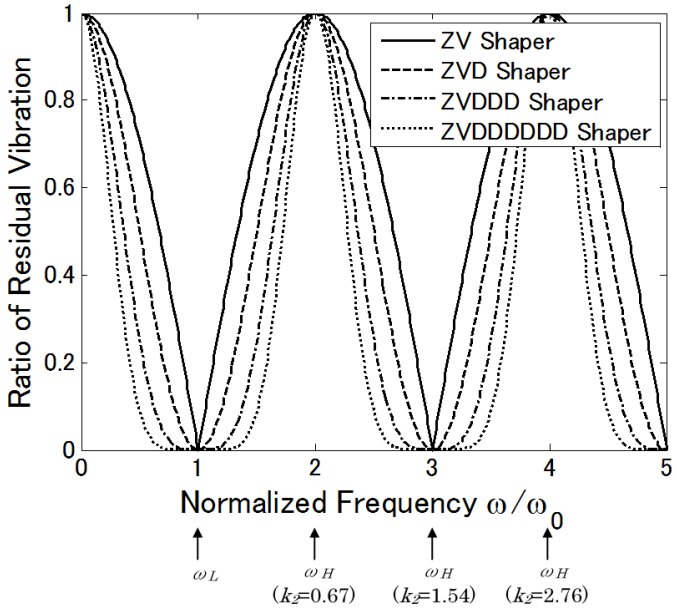

Figure 5-6: Full residual vibrations as functions of normalized system frequency for ZV, ZVD, and higher-order ZVD-type shapers.

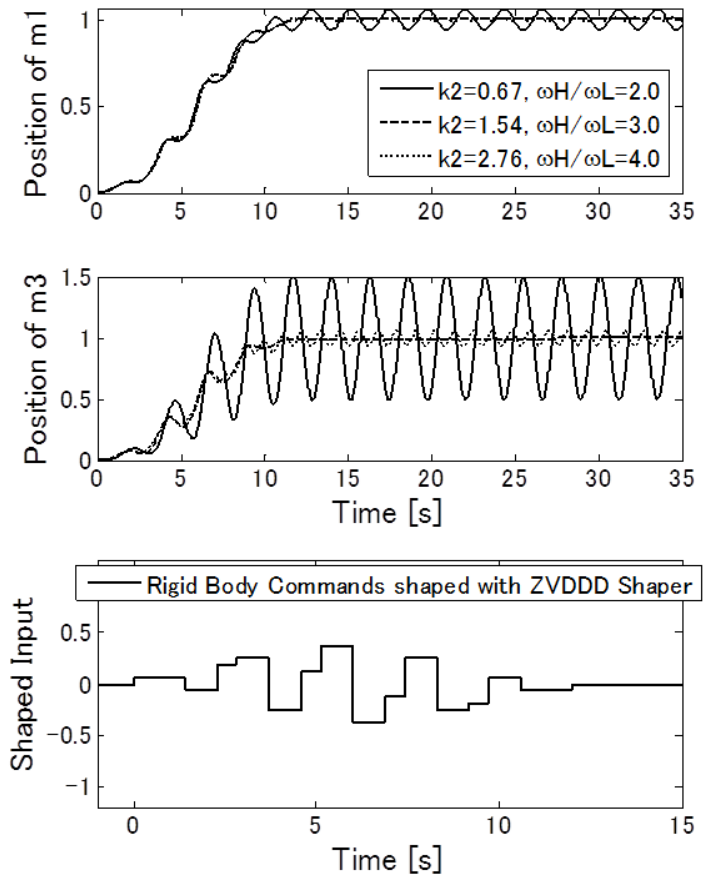

Figure 5-7: Shaped-command responses of a rigid-body command shaped with a ZVDDD shaper at three values of stiffness k_2 of the unknown high-frequency mode. Key to panels as in Fig. 5-1.

(5.3) shaped with ZVDDD, three-hump EI ($V = 5\%$), and ZVDDDDDD shapers, respectively. The ZVDDD- and ZVDDDDDD-shaped command responses show reductions in residual vibrations similar to those of ZVD-shaped command responses. This is because, according to the sensitivity curves shown in Fig. 5-6, the residual vibrations at $\omega_H/\omega_L = 2.0$, 3.0, and 4.0 are equally reduced among ZV, ZVD, and higher-order ZVD-type shapers. The same results are found for one-hump EI and higher-order EI shapers.

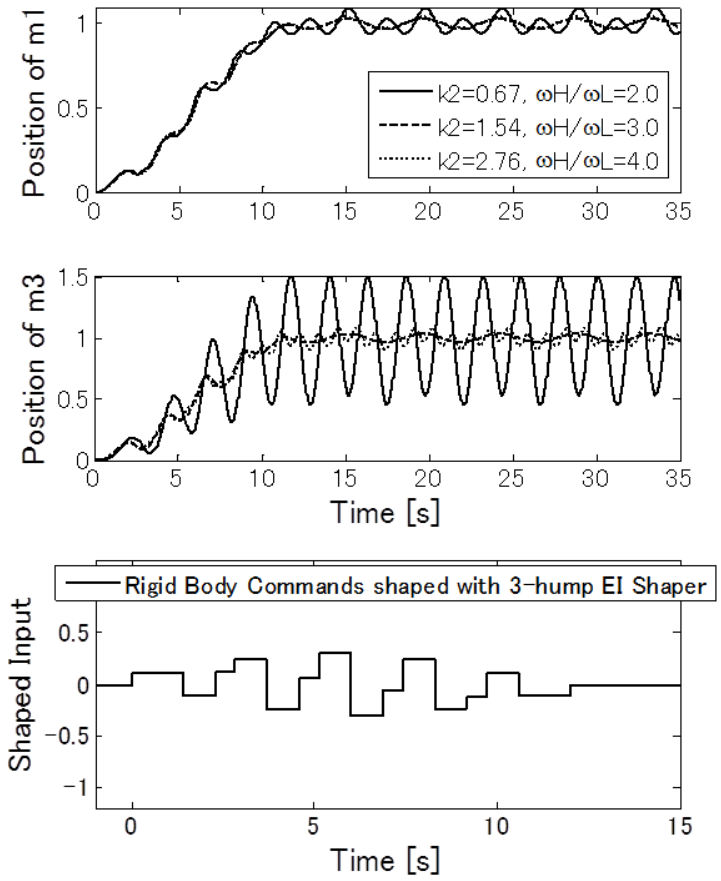

Figure 5-8: Shaped-command responses of a rigid-body command shaped with a three-hump EI shaper at three values of stiffness k_2 of the unknown high-frequency mode. Key to panels as in Fig. 5-1.

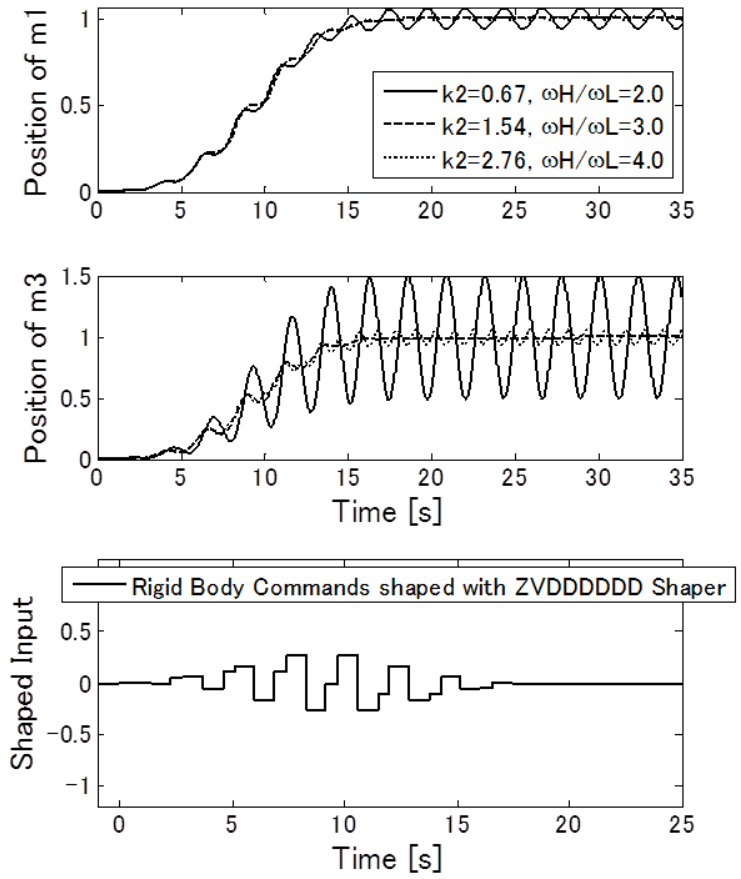

Figure 5-9: Shaped-command responses of a rigid-body command shaped with a ZVDDDDDD shaper at three values of stiffness k_2 of the unknown high-frequency mode. Key to panels as in Fig. 5-1.

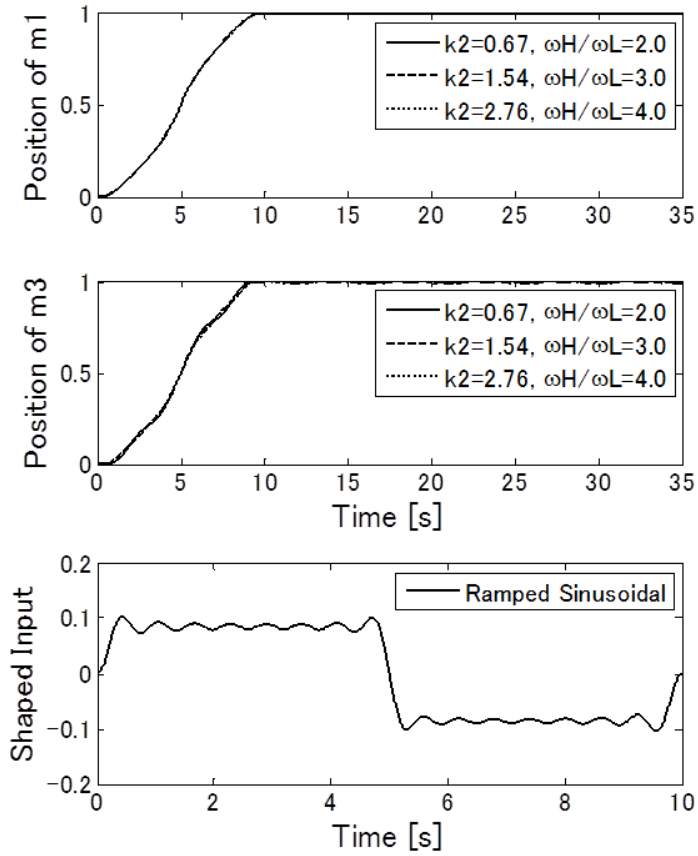

Figure 5-10: Shaped-command responses of a ramped sinusoidal (L=15, t_{mnv}=10 s) at three values of stiffness k_2 of the unknown high-frequency mode. Key to panels as in Fig. 5-1.

5.5 Ramped Sinusoidal

The input commands of a 15-term series of ramped sinusoidal curves and the responses are shown in Fig. 5-10 when the duration is 10 s and in Fig. 5-11 when the duration is 18 s. Residual vibrations of 0.5% to 0.7% are found in the 10 s case and 0.4% in the 18 s case.

5.6 NME Profiler

Figure 5-12 shows input commands and responses of the NME profiler that was proposed in Chapter 3. Figure 5-13 shows an enlargement of the responses. The

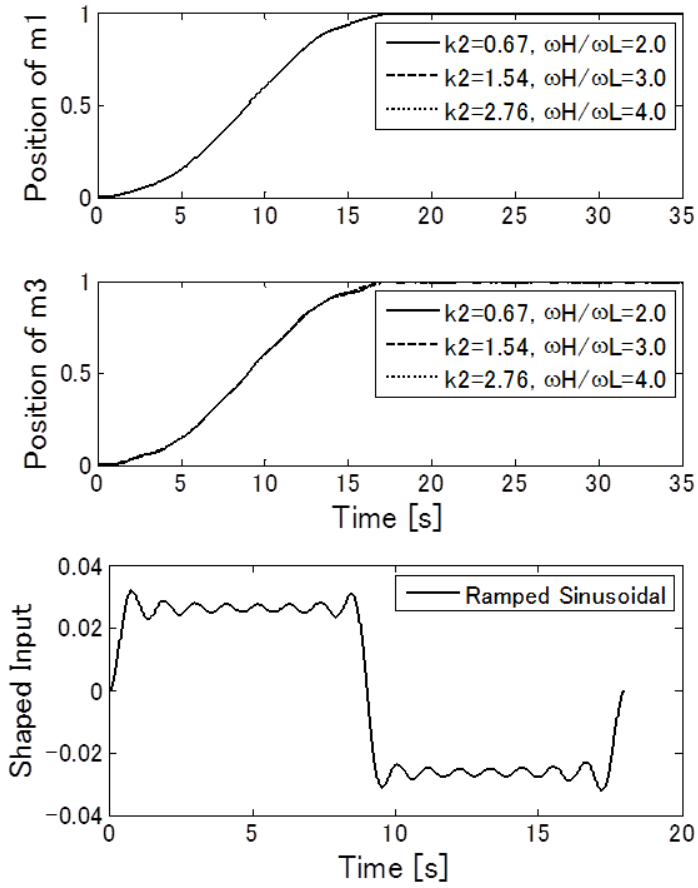

Figure 5-11: Shaped-command responses of a ramped sinusoidal (L=15, t_{mnv}=18 s) at three values of stiffness k_2 of the unknown high-frequency mode. Key to panels as in Fig. 5-1.

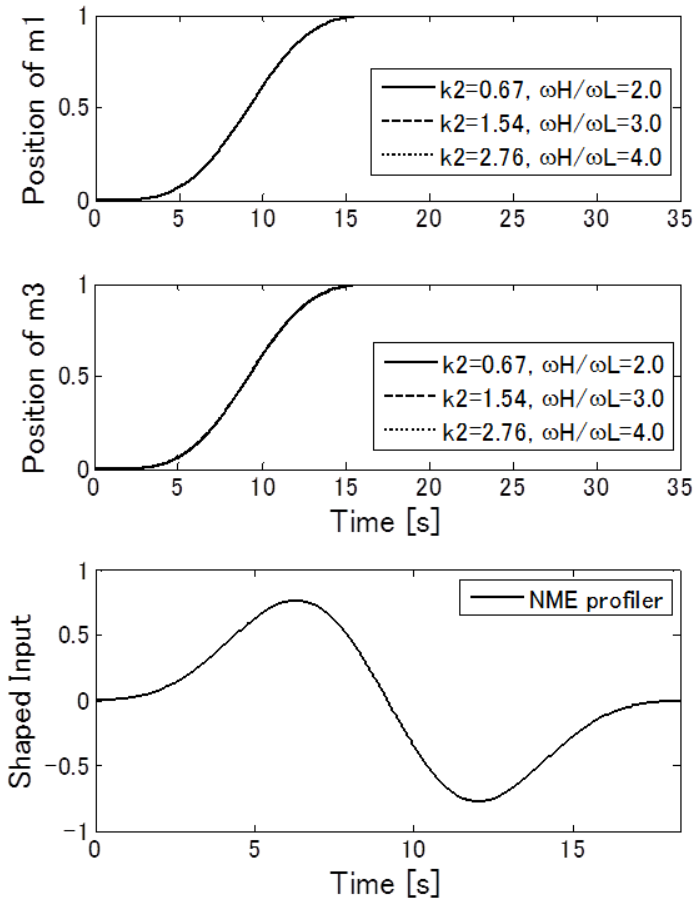

Figure 5-12: Shaped-command responses of the NME profiler (T_s=9.170 s) at three values of stiffness k_2 of the unknown high-frequency mode. Key to panels as in Fig. 5-1.

duration is 18.340 s, but the residual vibrations are very small (0.1%) for all cases. The period of the residual vibration is approximately 4.6 s; hence, it is found that the NME profiler does not excite the high-mode frequency, but only the low-mode frequency.

5.7 Ramped Sinusoidal (Additional Cases)

Although the NME profiler has shown slightly better results, additional cases are considered because the results for the ramped sinusoidal profiler and the NME profiler have not shown major differences. Two cases are considered here: when the stiffness

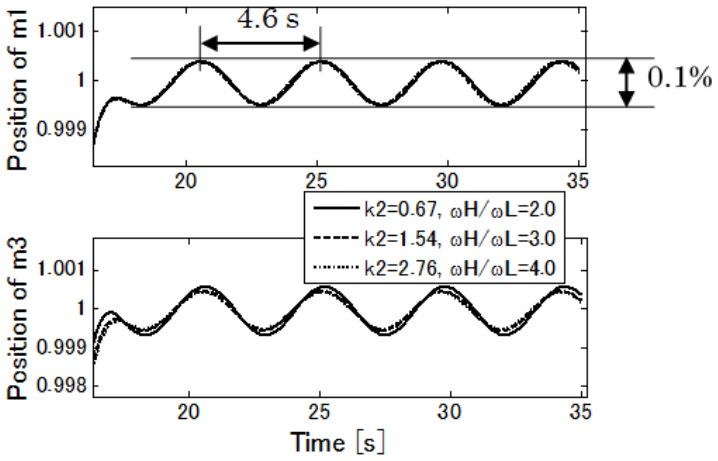

Figure 5-13: Enlargement; shaped-command responses of the NME profiler (T_s=9.170 s) at three values of stiffness k_2 of the unknown high-frequency mode. Top: positions of mass m_1. Bottom: positions of mass m_3.

of the unknown high mode k_2 is set to 0.310 and 0.270. These correspond to the frequency of the third harmonics of the fundamental ramped sinusoidal function when t_{mnv} is 10 s, and to the fifth harmonics when t_{mnv} is 18 s. The frequencies of the i-th harmonics of the ramped sinusoids have been evaluated by FFT. Figures 5-14 and 5-15 show input commands and responses of the ramped sinusoidal curves when t_{mnv} is 10 s and 18 s, respectively. The residual vibrations are 4.1% to 4.7% with t_{mnv} = 10 s and 1.6% to 2.3% with t_{mnv} =18 s. In contrast, the NME profiler still shows residual vibrations of 0.1%.

5.8 Smoothed Rigid-Body Commands convolved with ZVD Shapers (Hybrid Type)

Singhose et al. [44] suggested that "a reasonable approach for some special types of multimode systems is to combine input shaping and command smoothing." This kind of on-off and smooth hybrid-type profiler might be an effective alternative. The time-optimal bang-bang command (5.3) is smoothed by an S-curve with a unit rise, and is described by

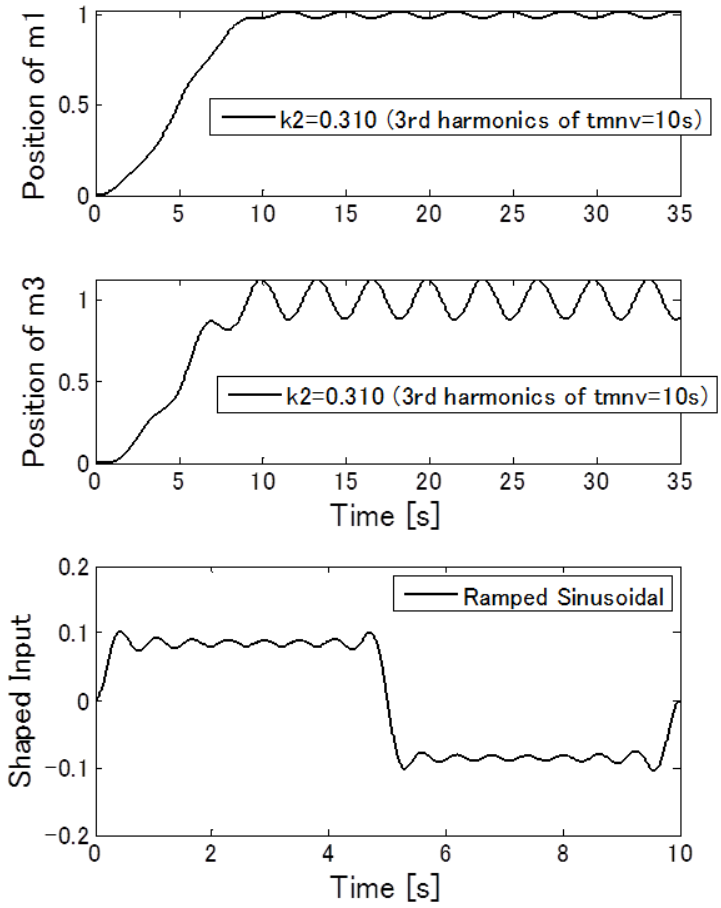

Figure 5-14: Shaped-command responses of a ramped sinusoidal (L=15, t_{mnv}=10 s, third harmonics) at three values of stiffness k_2 of the unknown high-frequency mode. Key to panels as in Fig. 5-1.

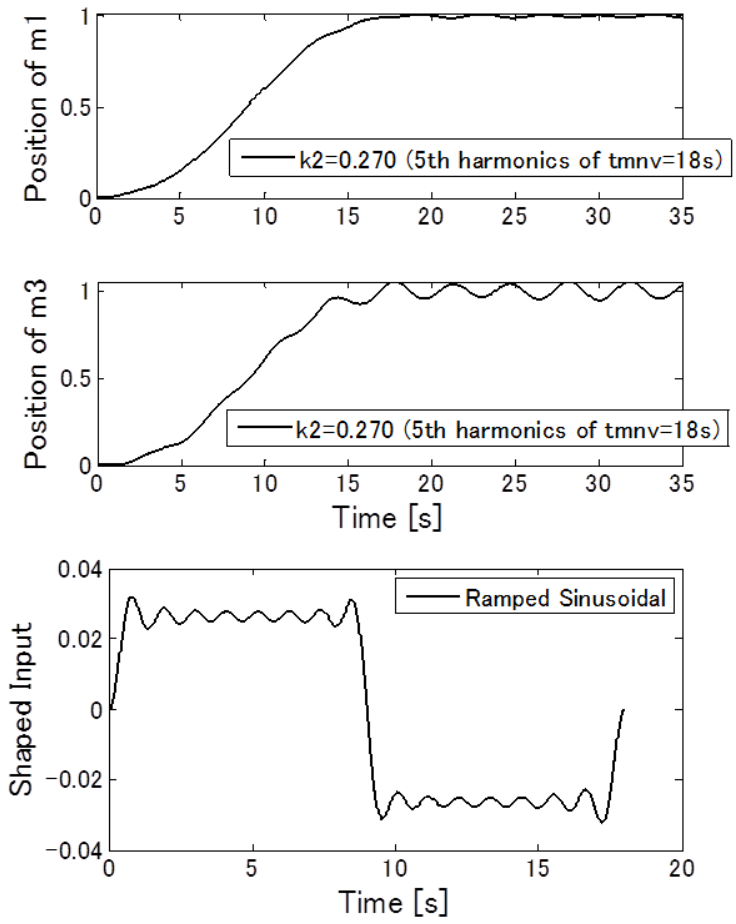

Figure 5-15: Shaped-command responses of a ramped sinusoidal (L=15, t_{mnv}=18 s, fifth harmonics) at three values of stiffness k_2 of the unknown high-frequency mode. Key to panels as in Fig. 5-1.

$$r(t) = \begin{cases} 2\left(t/R_C\right)^2 & \text{for} \quad 0 \le t < \frac{R_C}{2} \\ -2\left(t/R_C\right)^2 + 4\left(t/R_C\right) - 1 & \text{for} \quad \frac{R_C}{2} \le t < R_C \\ 1 & \text{for} \quad R_C \le t \end{cases} \tag{5.4}$$

where R_C is the rise time of the S-curve. The input commands and the responses when R_C is 1 s are shown in Fig. 5-16. The residual vibrations are smaller than those of unsmoothed rigid body command shaped with ZVD shaper, but still larger than NME profiler. Therefore, the duration of bang-bang command is lengthened so as to be nearly equivalent to that of the NME profiler, and is given as

$$u(t) = u_s(t) - 2u_s(t - 6.5) + u_s(t - 13.0) \tag{5.5}$$

Smoothing this lengthened bang-bang command by the S-curve (5.4) with R_C is 1 s, the input commands and the responses are shown in Fig. 5-17. The residual vibrations for all the k_2 cases are significantly reduced to equivalent levels of those of NME profilers.

5.9 Discussion on Two-Mode System

For each shaper discussed in this chapter, Table 5.1 lists the duration and residual vibration (peak-to-peak) of the model for $k_2 = 0.67$, 1.54, and 2.76. The maximum forces used in the input commands are also shown in the table just for references. The maximum force information can be used to check if the input commands do not exceed a force limit of the actuator, if any. Each controller for the simulations is designed under the condition of k_2 being 0.67, where the low-mode frequency ω_L is known but the high-mode frequency ω_H is unknown. However, because the low-mode natural frequency of the free-free system, given by (2.7), is determined not only by k_1 but also k_2, even if m_1, m_2, m_3, and k_1 are fixed, the low-mode frequency ω_L is slightly changed from 0.21811 Hz to 0.21924 Hz and 0.21955 Hz according to k_2. Therefore, the ratios of the high-mode and "designed" low-mode frequencies are not exactly 3.0 and 4.0 for k_2 being 1.54 and 2.76, respectively. This results in the residual vibration of

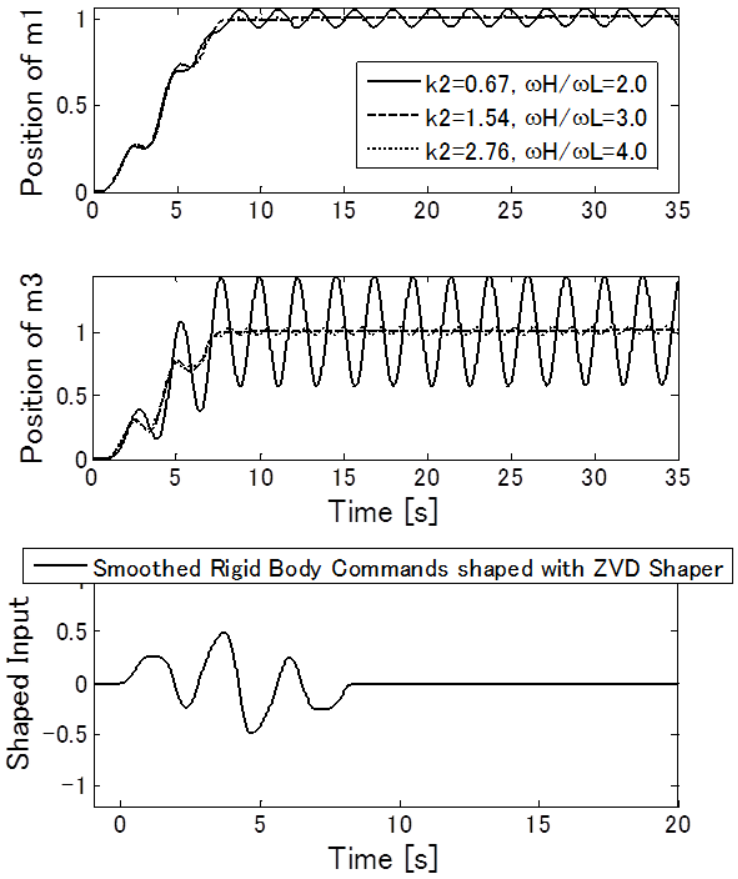

Figure 5-16: Shaped-command responses of a smoothed rigid-body command (time-optimal, R_C=1 s) shaped with a ZVD shaper at three values of stiffness k_2 of the unknown high-frequency mode. Key to panels as in Fig. 5-1.

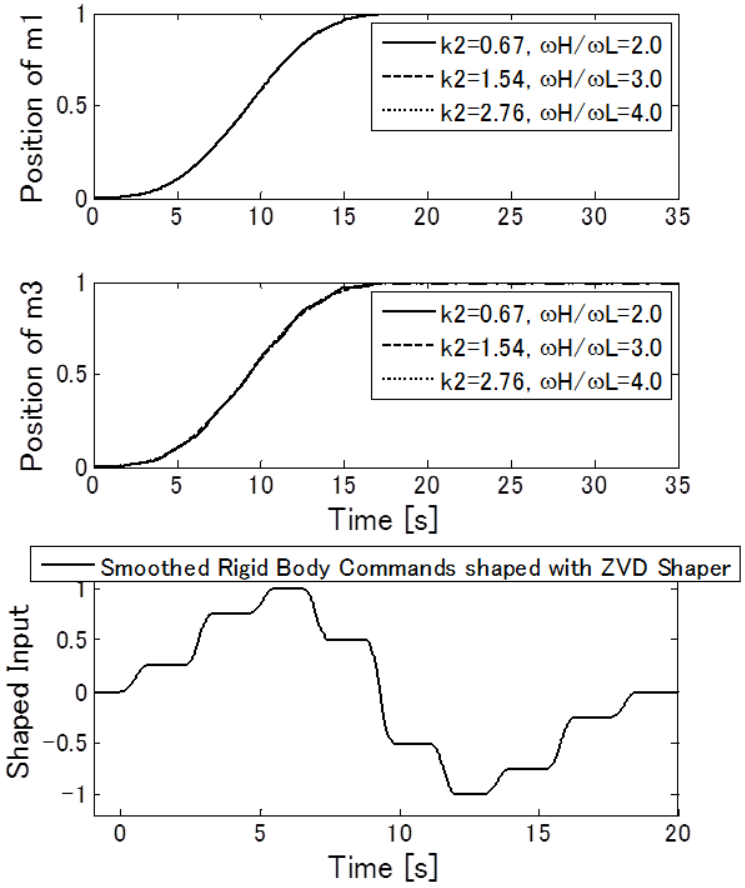

Figure 5-17: Shaped-command responses of a smoothed rigid-body command (lengthened, R_C=1 s) shaped with a ZVD shaper at three values of stiffness k_2 of the unknown high-frequency mode. Key to panels as in Fig. 5-1.

1.0% for the ZV shaper when k_2 is 1.54, because the ZV shaper is frequency sensitive (Fig. 5-5). The ZVD and higher-order ZVD-type shapers show nearly equivalent residual vibrations because of their frequency robustnesses. The EI shapers show higher residual vibrations compared to the same-order ZVD-type shapers because of their characteristics. Figure 5-18 compares durations versus residual vibrations at k_2 = 0.67. Because of their low-pass filtering characteristics, the smooth-type shapers produce smaller vibrations than the on-off shapers, especially when k_2 is 0.67 or 2.76.

Because Table 5.1 does not show major differences between the smooth-type profilers, additional cases were considered. Table 5.2 shows the same evaluation for the additional cases involving only smooth-type (and hybrid-type) profilers. The NME profiler produces smaller vibrations compared to the ramped sinusoidal profilers.

The on-off and smooth hybrid-type profiler: the smoothed bang-bang commands shaped with ZVD shaper shows small residual vibrations comparable with NME profiler when the duration of the bang-bang command is lengthened to be nearly identical to NME profiler. In the presence of unknown higher modes, the NME profiler or the hybrid profiler show the smallest residual vibrations compared to all other profilers, even when the comparisons are between profilers having nearly equivalent durations. The assumed two-mode system represents the most simplified system with complicated structures, so the same results can be expected for systems equipped with more complicated flexible structures.

The effectiveness of the NME profiler can be summarized as follows:
NME profiler is suitable for

1. system with unknown high-order flexible modes[1].

2. either distributed parameter system (DPS) or lumped parameter system (LPS) where most of large flexible structures should be considered as DPS[2].

NME profiler is not suitable for

3. system with flexible modes which have given nominal frequencies and a certain amount of frequency errors.

NME profiler might not be suitable for

4. system with unknown high-order flexible modes when the ratio of unknown mode mass to spacecraft total mass is too small[1].

The behaviors when NME profiler is applied to the system of 3 or 4 can be presumed by the comparison on single-mode system shown in Chapter 4, because single-mode system is the most simplified system of 3.

[1] The ratio of unknown mode mass to total mass discussed in this thesis is about 5% ($\simeq m_3/(m_1+m_2+m_3)\times 100$).

[2] In actual design, a DPS which consists of infinite modes is truncated and approximated by LPS with finite modes, then the existence of unknown modes are inevitable. In this sense, advantage of the methods presented in this thesis might be confirmed.

This chapter assumed that there is no limitation on the actuator torquing capability, so agility comparison could not be made. Therefore the discussion will be expanded to the agility region in the next chapter for more practical performance improvement.

Table 5.1: Comparison of simulation results for maneuver durations and vibrations of mass m_1 for on-off and smooth controllers (Two-Mode System).

	Duration	Vibration of m_1 (peak-to-peak)			Max. force
		$k_2 = 0.67$ (ω_H/ω_r =2.0)	$k_2 = 1.54$ (ω_H/ω_r =3.0)	$k_2 = 2.76$ (ω_H/ω_r =4.0)	
On-off type					
Minimum time for rigid body	2.828 s	122.0%	127.9%	129.1%	1.050
Rigid body cmd. shaped with ZV shaper	5.121 s	11.9%	1.0%	2.4%	0.525
Rigid body cmd. shaped with ZVD shaper	7.413 s	11.9%	0.0%	1.3%	0.525
Rigid body cmd. shaped with 1-hump EI shaper	7.413 s	15.2%	6.3%	6.9%	0.499
Rigid body cmd. shaped with ZVDDD shaper	11.998 s	12.0%	0.0%	1.3%	0.394
Rigid body cmd. shaped with 3-hump EI shaper	11.998 s	15.3%	6.4%	7.0%	0.315
Rigid body cmd. shaped with ZVDDDDDD shaper	18.876 s	12.0%	0.0%	1.3%	0.287
Smooth type					
Ramped sinusoidal (L=15, t_{mnv} =10s)	10.000 s	0.5%	0.7%	0.7%	0.109
Ramped sinusoidal (L=15, t_{mnv} =18s)	18.000 s	0.4%	0.4%	0.4%	0.034
NME (T_s =9.170s)	18.340 s	0.1%	0.1%	0.1%	0.071
Hybrid type					
Smoothed rigid body cmd. shaped with ZVD shaper	8.413 s	10.2%	0.0%	0.7%	0.519
Smoothed cmd. (*1) shaped with ZVD shaper	18.585 s	0.1%	0.0%	0.0%	0.050

Note: All the EI shapers are based on $V = 5\%$.
*1: The duration bang-bang command is adjusted to 13 s so as to be total duration of around 18 s.

Table 5.2: Comparison of simulation results for maneuver durations and vibrations of mass m_1 for additional cases for smooth controllers (Two-Mode System).

	Duration	Vibration of m_1 (peak-to-peak)	
		$k_2 = 0.310$ (3rd harmonics of t_{mnv} =10s)	$k_2 = 0.270$ (5th harmonics of t_{mnv} =18s)
Smooth type			
Ramped sinusoidal (L=15, t_{mnv} =10s)	10.000 s	4.1%	4.7%
Ramped sinusoidal (L=15, t_{mnv} =18s)	18.000 s	1.6%	2.3%
NME (T_s =9.349/9.434s)	18.698/18.869 s	0.0%	0.1%
Hybrid type			
Smoothed cmd. (*1) shaped with ZVD shaper	18.675/18.717 s	0.0%	0.2%

Note:
The durations of NME are 18.698 s when k_2 is 0.310 and 18.869 s when k_2 is 0.270.
The durations of Hybrid profiler are 18.675 s when k_2 is 0.310 and 18.717 s when k_2 is 0.270.
*1: The duration bang-bang command is adjusted to 13 s so as to be total duration of around 18 s.

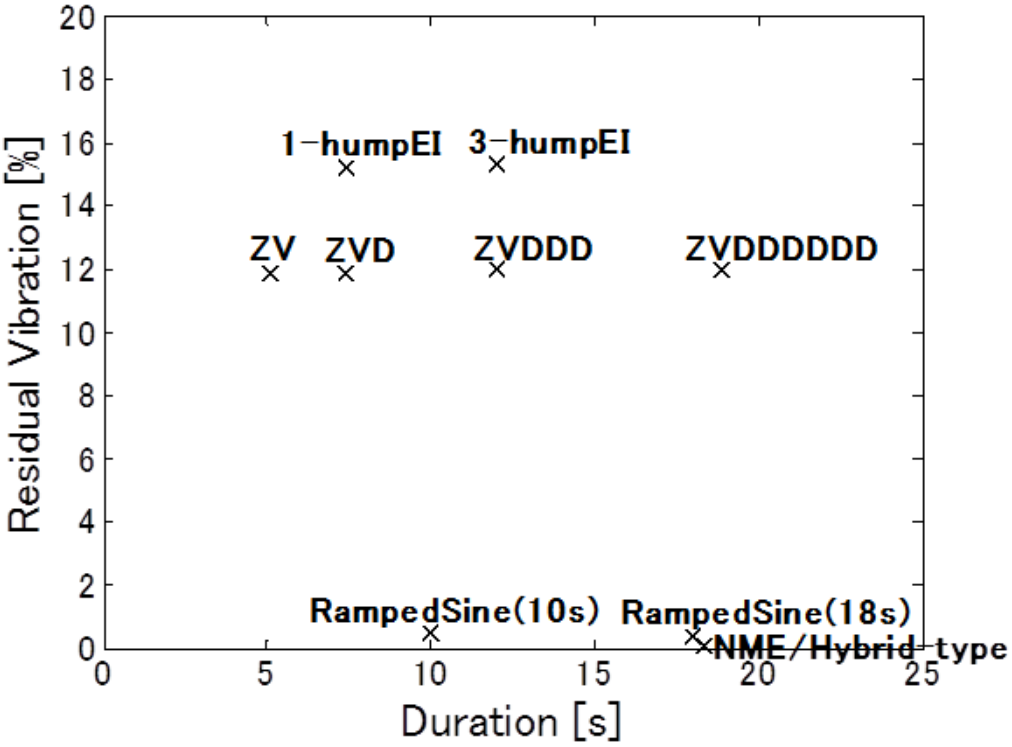

Figure 5-18: Correlation of duration and residual vibration for on-off, smooth, and hybrid controllers at $k_2 = 0.67$ (Two-Mode System).

THIS PAGE INTENTIONALLY LEFT BLANK

Chapter 6

Agility Comparison

6.1 Introduction to Agility Discussion

So far, maneuver duration, residual vibration, and robustness to modeling error for linear time-invariant (LTI) system have been evaluated in which input force is used as input and maneuver distance is used as output of the LTI system. For the LTI system, maneuver distance can be arbitrarily changed by amplifying the input without changing the shape of waveform. Therefore agility discussion does not appear so far. However, it is necessary for actual space applications to discuss the agility because there is always a limitation of actuator maximum output torque which is mainly determined by resource reasons like mass, dimension, and power consumption. If agility performance is low, then mission capability with regard to the spatial range of observations is restricted accordingly. In this sense, agility can be directly connected to performance measure of the mission success. Thus, agility discussion is introduced hereafter by limiting the actuator output torque.

6.2 Definition of Agility in This Study

Assuming that, there is three parameters which characterize agility performance:

- Maximum force ($\max|u|$)
- Duration
- Distance ($|y|$)

Here, the maximum force means the largest force which is used during the maneuver, the duration means the required time to complete the maneuver, and the distance means the maneuver length realized by the maneuver. Regarding force related parameters, energy consumption is occasionally used as performance measure but this thesis applies the maximum force as the force related performance measure.

Then, three ways to evaluate the agility are conceivable as shown in Table 6.1.

Table 6.1: Given conditions and objectives for agility evaluations

	Given conditions	Objective	Remarks
(1)	Max force & Duration	$\Rightarrow$ Longer distance (Maneuverability)	Major issue in Chap. 7
(2)	Max force & Distance	$\Rightarrow$ Shorter duration (Speed of response)	Partly discussed in Sec. 7.2
(3)	Duration & Distance	$\Rightarrow$ Smaller max force ($\equiv$Maneuverability)	Same result as (1) [*]

Note [*]
Because the system discussed in this work is LTI system, for any inputs $u_1, ..., u_m$ and scalars $a_1, ..., a_m$, the following equality holds: $y = f(a_1u_1 + \cdots + a_mu_m) = a_1f(u_1) + \cdots + a_mf(u_m)$. For example, if a set of $\max|u| = 1$ and a certain duration gives distance of $y = \alpha$, then the set of distance $y = 1$ and the same duration gives $\max|u| = 1/\alpha$, this means that the profiler which shows the longest distance in evaluation (1) must win the smallest max force in evaluation (3) i.e. the evaluations of (1) and (3) generate equivalent results.

In general, once a profiler is chosen, the shortest duration will be automatically determined according to the frequencies of the flexible structures. Therefore the evaluation (2) shown in Table 6.1 will be "partly" discussed in Section 7.2 for the LTI system as the coefficients of input shaper durations to modal cycle summarized in Table 7.1 which imply the shortest maneuver durations by each profiler. Here the

"partly" is used because the maximum force and distance are given in (2) and the shortest duration is determined by the choice of profiler as mentioned above, so if the maneuver distance realized by the given maximum force and the profiler's shortest duration is shorter than the required distance then the duration should be set longer, and such cases are not discussed in this thesis.

6.3 New Constraint and New Criteria

In the previous chapters, a sinc function-based profiler, called a nil-mode-exciting (NME) profiler, was proposed and it was shown that, in the presence of an unknown high-order flexible mode and for a unit distance rest-to-rest maneuvers, the NME profiler generates the smallest residual vibrations compared with conventionally designed on-off input shapers or smooth profilers, when identical durations are used. Only a hybrid-type controller [44], which is made by convolution of a smooth controller and an on-off controller, has shown small residual vibrations comparable with the NME profiler. The evaluations were made based on performance criteria of "profiler duration," "ratio of residual vibration amplitude to a unit distance maneuver," and "robustness to uncertainty in system frequency." Because the model is linear time-invariant, the ratio of resultant residual vibration amplitude to a unit distance maneuver can also be applied to an arbitrary maneuver distance, then a residual vibration for the arbitrary maneuver distance can be evaluated by applying the ratio. However, most of actual space applications have restriction of control actuators' output torques (e.g. maximum reaction wheel torque or maximum control moment gyro torque), thus there must be a maximum maneuver distance for a "given maneuver duration" and a "given maximum torque." Actually, the maneuver distance (i.e. agility performance) is an important performance criterion for a satellite with scientific observation mission which is required a long maneuver distance with a limited actuators' torque. Thus, this chapter introduces a new constraint condition and a new performance criterion as follows:

Constraint conditions :

(1) A given maneuver duration

(2) A given maximum actuator torque [New]

Performance criteria :

(1) Residual vibrations after the maneuvers

(2) Robustness to uncertainty in system frequency

(3) Maneuver distances [New]

By this new constraint condition, it becomes necessary to discuss how to realize an efficient use of high frequency components. If there is no limitation of actuators' torque, a required maneuver distance can be obtained just by amplifying the amplitude of the input torque without changing the shape of the input profile. This means that the profilers realize any required maneuver distances without changing the frequency responses if there is no limitation of actuators' torque. However, if there is a limitation of actuators' torque, an effective use of high-frequency region of the controller becomes necessary because the profilers which have shown the best performances in the Chapter 5 (the NME profiler and the hybrid controller) have low-pass filter shaped frequency responses, i.e. high frequency is not used. The main technical contribution of the following chapter beyond the previous chapters is to discuss such the effective use of high-frequency region of the controller which has not been discussed sufficiently in conventional papers or our previous work.

The following chapter proposes two kinds of new sinc function-based profilers, the first one achieves "longer maneuver distances with the smallest residual vibrations" compared with conventional smooth profilers and the second one achieves "the longest maneuver distances with comparable residual vibrations," compared with conventional smooth profilers.

6.4 Comparison of Agilities

For an agility comparison among the NME profiler and conventional on-off and smooth profilers discussed in Chapter 5, maneuver durations and maneuver distances, i.e. positions of m_1 at the end of maneuvers, are shown in Table 6.2, under the con-

dition of maximum input torque, u, given by

$$\max |u| = 1 \tag{6.1}$$

All the maneuver durations are set to be four times as long as the low-mode period $T_L (= 2\pi/\omega_L)$, i.e. $4T_L =$ 18.340 s. Actual forcing actuator has some upper limit for output torque, therefore the condition (6.1) is realistic for the agility comparison of each profiler. Regarding on-off profilers, the longest maneuver distance is 40.04 by full acceleration and deceleration, although the largest residual vibration is assumed to appear. The second longest maneuver distance among the on-off profilers is 30.66 by acceleration and deceleration command convolved with a zero-vibration (ZV) shaper [20, 21, 22]. Then, the higher-order ZVD-type shaped commands [22] generate shorter distances down to 2.29 by ZVDDDDDD shaped command. Figure 6-1 shows the input command and the command responses of the ZVDDDDDD shaped commands at three values of stiffness k_2 of the unknown high-frequency mode, and the maneuver distance is 2.29. Regarding the smooth profilers, Figure 6-2 shows the input command and the command responses of the first-order ($L = 1$) ramped sinusoids [36, 37] and the maneuver distance is 19.09. Figure 6-3 shows those of the fifteenth-order ($L = 15$) ramped sinusoids and the maneuver distance is 30.89. The above mentioned sinc function-based profiler (NME profiler) [47, 14] generates the maneuver distance of 14.01 as shown in Fig. 6-4. The hybrid-type profiler [44, 47] for the case of the S-curve rise time $R_C = 1$ s generates the maneuver distance of 19.37 as shown in Fig. 6-5.

Here, the maneuver distance by ZVDDDDDD shaped command, 2.29, might be shorter than expectation although it is an on-off type profiler which is generally assumed to generate agile motion compared to smooth type, but it is reasonable because the ZVDDDDDD shaped command, shown in Fig. 6-1, has much more switches than smooth profilers. To verify the assumption that more switches would cause shorter maneuver distance, two types of input command are considered as shown in Fig. 6-6. Both commands have same durations, same peak forces, and the total durations of

Table 6.2: Comparison of simulation results for maneuver durations and distances for on-off and smooth controllers for three-mass two-spring model (Two-Mode System, $m_1 = m_2 = k_1 = 1$, $m_3 = 0.1$, $k_2 = 0.67$).

	Maneuver duration	Maneuver distance
On-off type		
Full acceleration and deceleration	18.340 s	40.04
Rigid body cmd. shaped with ZV shaper (*1)	18.340 s	30.66
Rigid body cmd. shaped with ZVD shaper (*1)	18.340 s	22.53
Rigid body cmd. shaped with ZVDDDDDD shaper (*1)	18.340 s	2.29
Smooth type		
Ramped sinusoids (L=1, t_{mnv} =18.340 s)	18.340 s	19.09
Ramped sinusoids (L=5, t_{mnv} =18.340 s)	18.340 s	27.73
Ramped sinusoids (L=11, t_{mnv} =18.340 s)	18.340 s	30.24
Ramped sinusoids (L=15, t_{mnv} =18.340 s)	18.340 s	30.89
NME (T_c =9.170 s)	18.340 s	14.01
Hybrid type		
Smoothed cmd. shaped with ZVD shaper (Rc=1s) (*1)	18.340 s	19.37

Note:
- L is the number of harmonics for ramped sinusoids.
- The rigid body commands for shapers marked (*1) are bang-bang commands adjusted for duration of 18.340 s.

accelerations and decelerations are also same. The maneuver time is equally divided into A, B, C, and D. The first command accelerates at A and B then decelerates at C and D, the second command accelerates at A and C, decelerates at B and D. Considering maneuver distances by the second-order integral of both the commands, it is clear that the first command generates longer maneuver distance, actually it is twice as long as the second command.

6.5 Concept for Higher Agility

The energy of the input force, which is transmitted by an input command, corresponds to the area of the spectrum of the input command. The more the energy of the input force is, the longer the maneuver distance will be.

The FFT of the NME profiler shows that the NME profiler has a good attenuation above a certain frequency as shown in Fig. 6-7. In other words, a longer maneuver

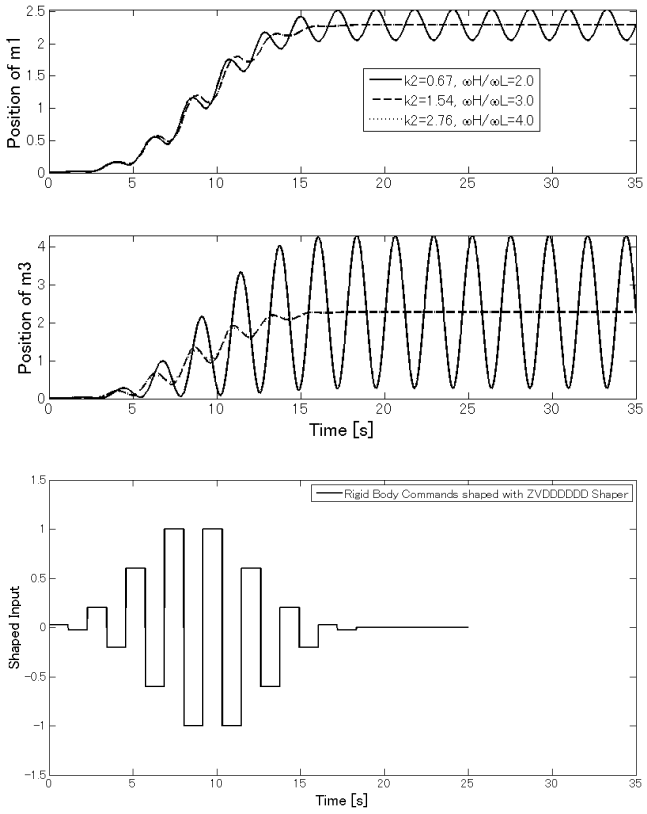

Figure 6-1: Shaped-command responses of a rigid-body command shaped with a ZVDDDDDD shaper at three values of stiffness k_2 of the unknown high-frequency mode. Key to panels as in Fig. 5-1.

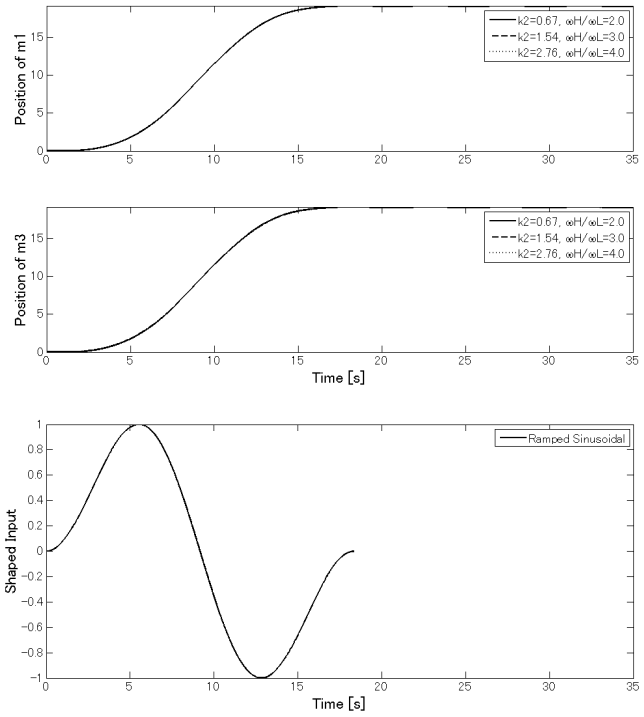

Figure 6-2: Shaped-command responses of the ramped sinusoidal ($L = 1$, $t_{mnv} = 4T_L$) at three values of stiffness k_2 of the unknown high-frequency mode. Key to panels as in Fig. 5-1.

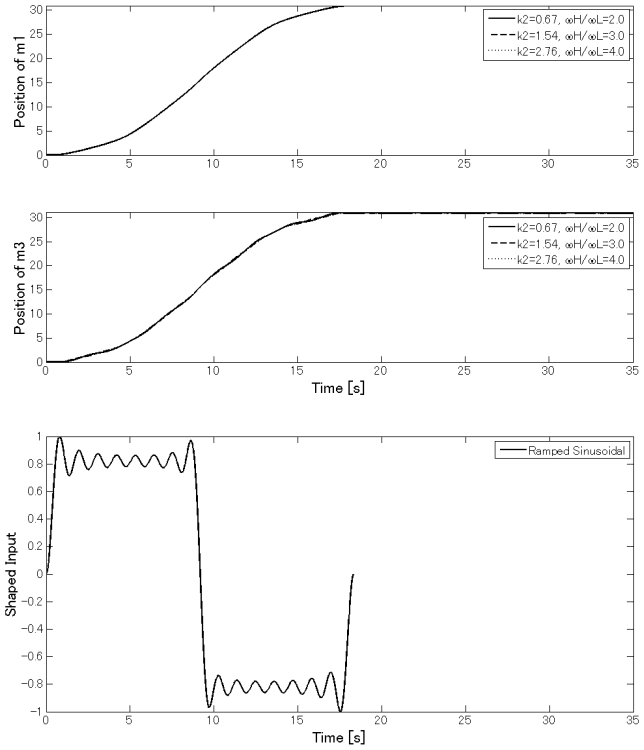

Figure 6-3: Shaped-command responses of the ramped sinusoidal ($L = 15$, $t_{mnv} = 4T_L$) at three values of stiffness k_2 of the unknown high-frequency mode. Key to panels as in Fig. 5-1.

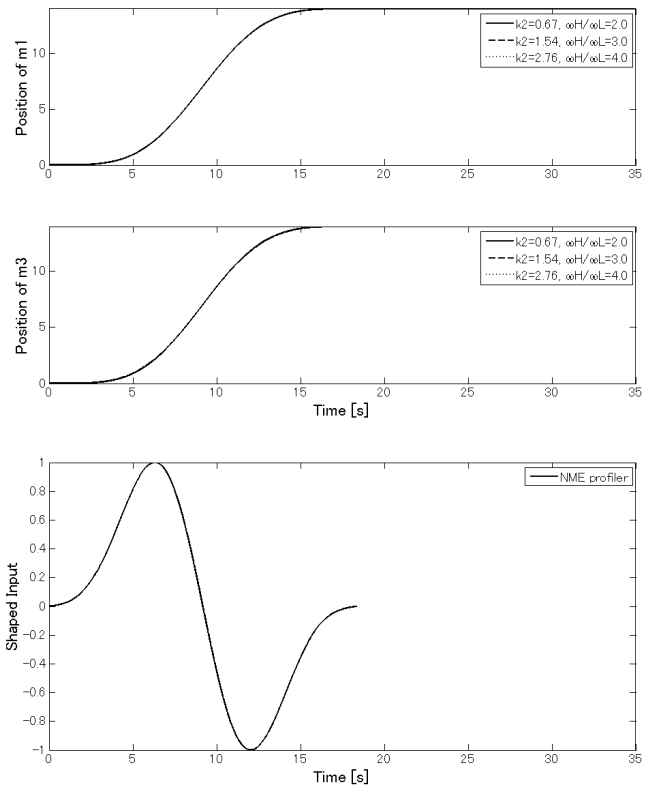

Figure 6-4: Shaped-command responses of the NME profiler (T_s=9.170 s, $t_{mnv} = 4T_L$) at three values of stiffness k_2 of the unknown high-frequency mode. Key to panels as in Fig. 5-1.

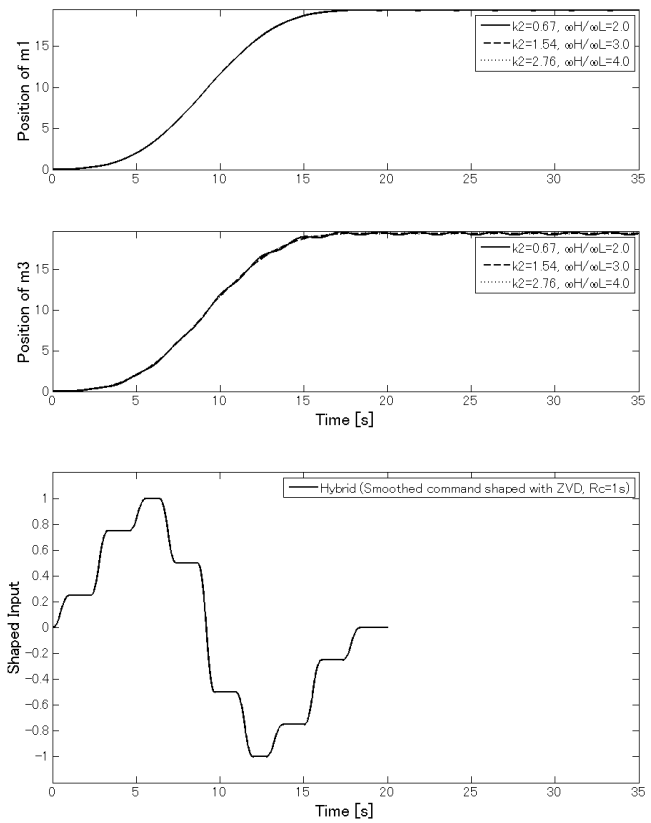

Figure 6-5: Shaped-command responses of the hybrid profiler (smoothed command shaped with ZVD shaper, R_C=1 s, $t_{mnv} = 4T_L$) at three values of stiffness k_2 of the unknown high-frequency mode. Key to panels as in Fig. 5-1.

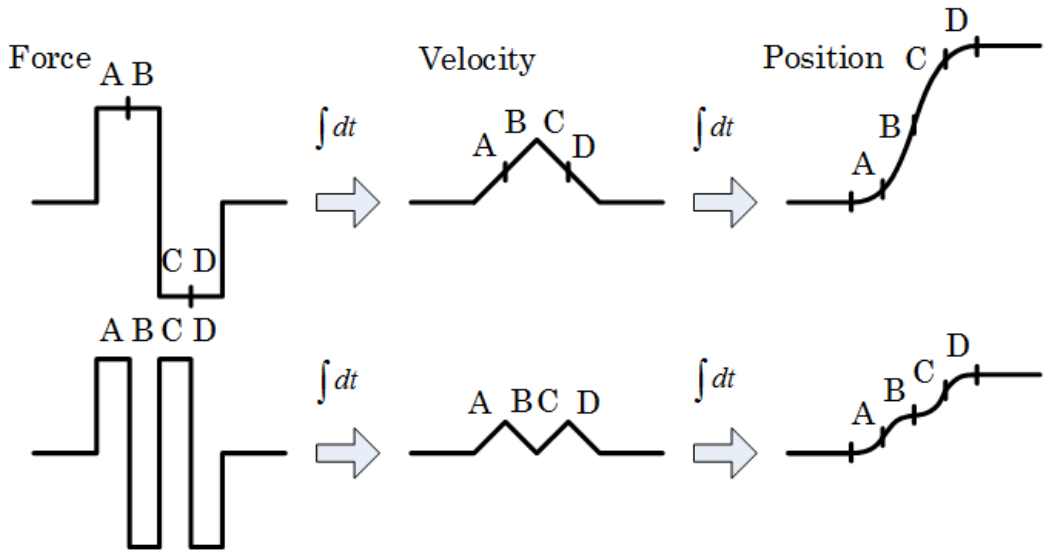

Figure 6-6: Comparison of agility between 1-swith and 3-switches

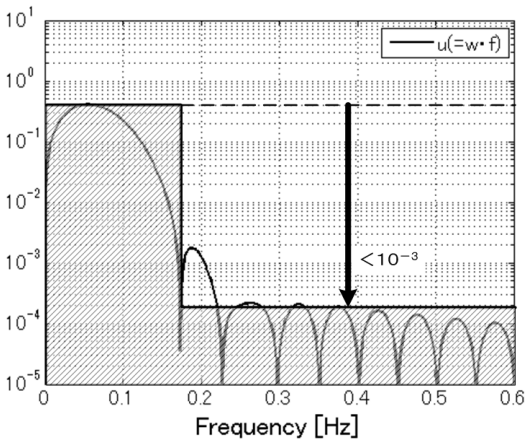

Figure 6-7: FFT of NME profiler

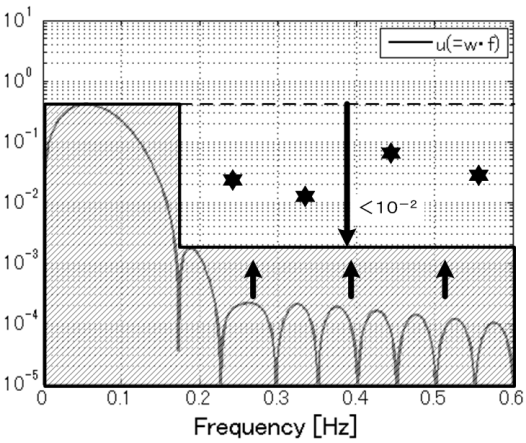

Figure 6-8: Concept for high agility

distance can be realized by increasing the energy of input force by relaxing the attenuation level, from less than 10^{-3} to e.g. less than 10^{-2}, at frequencies higher than the lowest mode as shown in Fig. 6-8. Here, the unknown high mode can exist at any frequency higher than the low mode, so the relaxed attenuation level should be a flat or an inclined line. Level and slope of the line can be calculated from the required pointing accuracy (See the future work in Section 9.2).

THIS PAGE INTENTIONALLY LEFT BLANK

Chapter 7

Modified Sinc Function-Based Preshaping Profilers for High Agility

7.1 Introduction

To realize longer maneuver distances, three kinds of modified sinc function based profilers are proposed in this chapter as follows.

1: NME profiler convolved with input shapers [49]

2: Sinc function convolved with step function

3: Sinc function with weighted harmonics

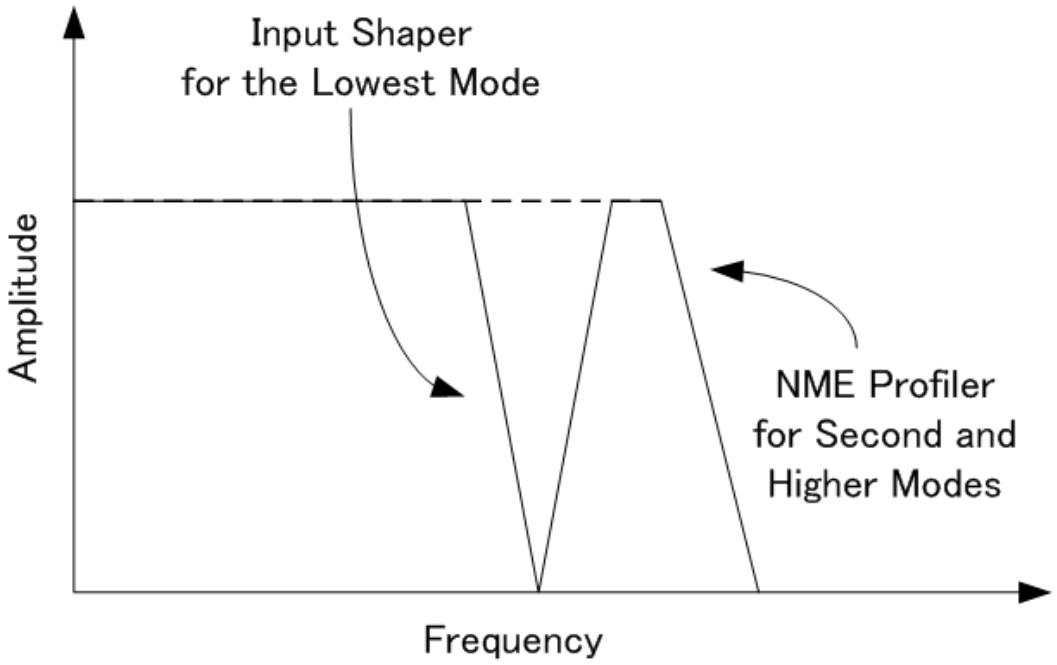

Figure 7-1: FFT - Concept of the NME profiler convolved with input shaper

7.2 NME Profiler Convolved with Input Shaper

Convolving two waveforms in the time domain equals to multiplying their spectra (i.e. frequency content) in the frequency domain. Using this nature of convolution, higher agility comparing to the original NME profiler can be achieved by the profiler convolving an "input shaper designed for the lowest mode" and an "NME profiler designed for the second lowest mode." This idea has been proposed in the previous works [44, 50, 49], and the concept is shown in Fig. 7-1. However this idea will not always work when better balanced performance of short maneuver duration and fine pointing accuracy is required. This section proposes a formula which clarifies a region in which this convolution technique presents better performance compared to the original profiler.

The duration of the NME profiler is given as

$$T_{nme} = n_{nme} T_L \tag{7.1}$$

where

T_L: Cycle of the lowest mode [s]

n_{nme}: Coefficient of NME profiler duration to modal cycle

and in my previous work [47], it is recommended that n_{nme} should be 4, where some modeling error margin for the nominal value $n_{nme} = 3.48$ is considered (refer to (4.1) and (4.2)).

The duration of the above mentioned profiler given by convolving an input shaper designed for the lowest mode and an NME profiler designed for the second lowest mode is given as

$$T_{shaped} = n_{shaper} T_L + n_{nme} T_H \tag{7.2}$$

where

T_H: Cycle of the second lowest mode [s]

n_{shaper}: Coefficient of input shaper duration to modal cycle

and n_{shaper} is 0.5 for ZV shaper, 1.0 for ZVD shaper, and 1.5 for ZVDD shaper, according to the order of the constraint conditions, as shown in Table 7.1.

Table 7.1: Coefficients of input shapers and smooth profilers

Type	$n_{shaper}(n_{nme})$
ZV shaper	0.5
ZVD shaper	1.0
ZVDD shaper	1.5
ZVDDD shaper	2.0
ZVDDDD shaper	2.5
ZVDDDDD shaper	3.0
ZVDDDDDD shaper	3.5
Ramped sinusoids	>1.50 + 1.0L, (L=1,3,5, ...)
NME profiler	>3.48
Sinc function convolved with step (*1)	>2.70
Sinc function with weighted harmonics (*2)	>1.30 + 1.0L, (L=1,3,5, ...)

Note:
*1: Introduced in Section 7.3
*2: Introduced in Section 7.4

If the relation between the lowest mode frequency ω_L and the second lowest mode

frequency ω_H is given as

$$p = \frac{\omega_H}{\omega_L} \qquad (> 1) \tag{7.3}$$

Then the periodical cycle of the lowest mode T_L and the second lowest mode T_H is give as

$$T_H = \frac{1}{p} T_L \tag{7.4}$$

Here, the relation p is determined by structural parameters and it is out of scope of this thesis. Just for reference, Table 1.1 shows that the ratios of the flexible mode frequencies next to each other which correspond to the p are mostly distributed to the range of 2 to 3.

Substituting (7.4) into (7.2) gives

$$T_{shaped} = \left(n_{shaper} + \frac{n_{nme}}{p} \right) T_L \tag{7.5}$$

To realize shorter maneuver duration by this convolution technique, the required condition is given as

$$T_{nme} > T_{shaped} \tag{7.6}$$

Substituting (7.1) and (7.5) into (7.6) gives

$$n_{nme} > n_{shaper} + \frac{n_{nme}}{p} \tag{7.7}$$

where both sides is divided by $n_{nme}(> 0)$, then the following equation is obtained.

$$\frac{n_{shaper}}{n_{nme}} < 1 - \frac{1}{p} \quad , \quad (p > 1) \tag{7.8}$$

Since the left-hand side of (7.8) is positive, the shaded area of Fig. 7-2 shows the area of $\frac{n_{shaper}}{n_{nme}}$ which satisfies (7.8).

For example, assuming p of the system being 3, then (7.8) will be $\frac{n_{shaper}}{n_{nme}} < \frac{2}{3}$. Here if n_{nme} is selected as 4, $n_{shaper} < \frac{8}{3} (\approx 2.667)$ is required to obtain a shorter duration by the convolved profiler. According to Table 7.1, this means that the order of input shaper should be not greater than 2.5, i.e. ZVD-type shaper with equal or

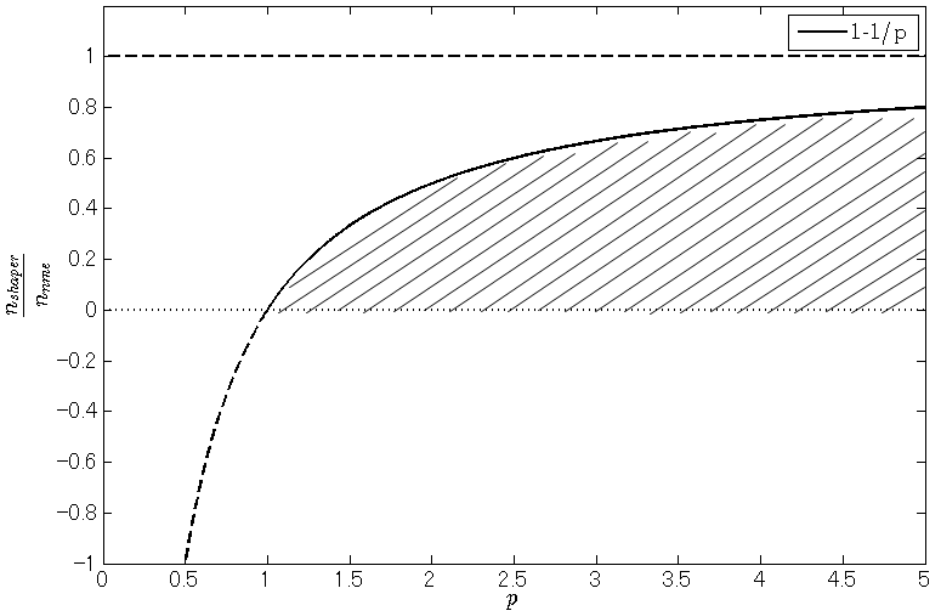

Figure 7-2: Condition for shorter duration.

lower order than ZVDDDD shaper would realize shorter duration when convolved with NME profiler designed for the second lowest mode compared to the duration of NME profiler designed for the lowest mode.

The same discussion can be applied to other types of smooth profilers such as ramped sinusoids or S-curve. Once the coefficient n of the smooth profiler is determined, then (7.8) replacing n_{nme} with n will be the required condition for shorter maneuver duration. The coefficient for each input shaper and smooth profiler is shown in Table 7.1.

7.3 Sinc Function Convolved with Step

The profiler proposed in this section is formed by convolving a windowed sinc function, which has duration of a single period, with a step function as shown in Fig. 7-3. The convolved command is used as positioning input. Because the convolution does not shift the frequency characteristic of the original function, the boundary frequency of the convolved positioning input would be the frequency corresponds to the single period of the maneuver duration although the previously proposed sinc function-based profiler (NME profiler) requires two periods of sinc functions: one period for acceleration and the other period for deceleration. This implies the new profiler has lower boundary frequency compared with the NME profiler when the same maneuver durations are used, or the new profiler would generate faster maneuver compared with the NME profiler when the same boundary frequencies are used. Input-torque command, hereinafter referred to as "sinc function convolved with step" or "sinc convolved with step", is given by the second order differential of the positioning input given as

$$u(t) = A \cdot \frac{d^2}{dt^2} \left\{ (w(t) \cdot f(t)) * g(t) \right\} \tag{7.9}$$

where $X * Y$ is the convolution of X and Y, and

$$f(t) = \mathrm{sinc}\left(\omega_s t - \pi\right) \tag{7.10}$$

$$w(t) = \begin{cases} 0.54 + 0.46 \cos\left\{ \dfrac{2\pi}{t_{mnv}} \left(t - \dfrac{t_{mnv}}{2} \right) \right\} & \text{for} \quad 0 \le t \le t_{mnv} \\ 0 & \text{for} \quad t < 0, t_{mnv} < t \end{cases} \tag{7.11}$$

$$g(t) = \begin{cases} 0 & \text{for} \quad t < 0 \\ 1 & \text{for} \quad 0 \le t \end{cases} \tag{7.12}$$

where $t_{mnv} = T_s = 2\pi/\omega_s$. It is noted that the required duration of this profiler is half as long as the one of the previously proposed sinc function-based profiler (NME profiler). Figure 7-3 shows the step function (7.12) at the top, the windowed sinc

function at the middle, and the convolved positioning input at the bottom.

Here, the Laplace transform of the step function $g(t)$ is 1/s, and the convolution theorem is given as

$$\mathcal{L}\left[h(t) * g(t)\right] = \mathcal{L}\left[h(t)\right]\mathcal{L}\left[g(t)\right] = H(s)G(s) \tag{7.13}$$

Therefore the convolution of a step function $g(t)$ and a function $h(t)$ is equivalent to the integral of the function $h(t)$. Then (7.9) can be transformed to

$$u(t) = A \cdot \frac{d^2}{dt^2}\left\{\int_0^{T_f} w(t) \cdot f(t)dt\right\} = A \cdot \frac{d}{dt}\left\{w(t) \cdot f(t)\right\} \tag{7.14}$$

The time profile of (7.9) (or (7.14)) with T_s=10 s is shown in Fig. 7-4, and its fast Fourier transform (FFT) appears in Fig. 7-5. The FFTs of the NME profiler with T_s=10 s is also shown in Fig. 7-5 as dashed line. Maneuver durations are 10 s for the new profiler, 20 s for the NME profiler. The boundary frequency of the spectrum of the new profiler is higher than that of the NME profiler with duration of 20 s, i.e. 0.174Hz. The frequency of the new profiler has been shifted from the frequency of the original sinc function, i.e. 0.1Hz, or the frequency of the NME profiler, 0.174Hz. This is because the width of window function has been changed from 20 s for the NME profiler to 10 s for this profiler. The inclination of the sidelobe of the spectrum is –20 dB/dec for the new profiler while –40 dB/dec for the NME profiler. This is because the new profiler applies the sinc function as rating input while the NME profiler applies the sinc function as forcing input. Therefore the difference in Laplace transform's s-domain between the NME profiler and the new profiler is "s" and the sidelobe of the new profiler inclines more moderate by –20 dB/dec compared with the sidelobe of the NME profiler. If the duration of the new profiler is set to be same as the NME profiler with duration of 20 s, the FFT is given as Fig. 7-6. Both the maneuver durations are the same (20 s) but the boundary frequency is lower in the new profiler (0.135Hz) than the NME profiler (0.174Hz). The sidelobe level of the new profiler is higher than the NME profiler but it is under 10^{-2}, thus significant vibration reductions can be expected in high frequency region.

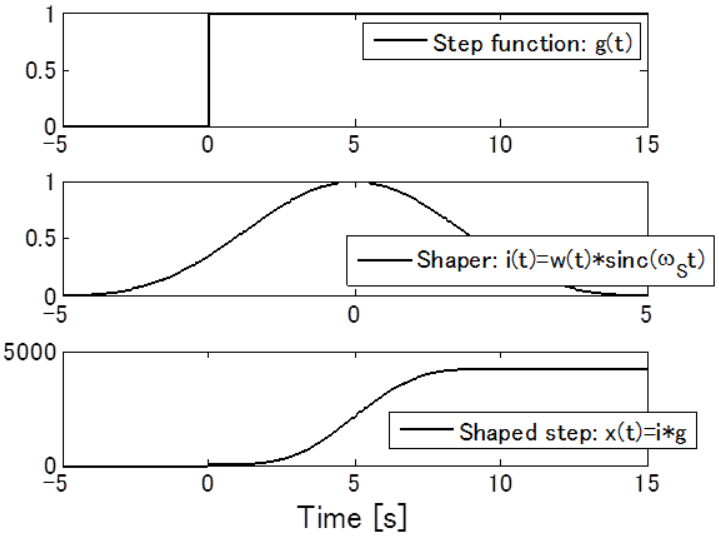

Figure 7-3: Convolution (T_s=10 s)

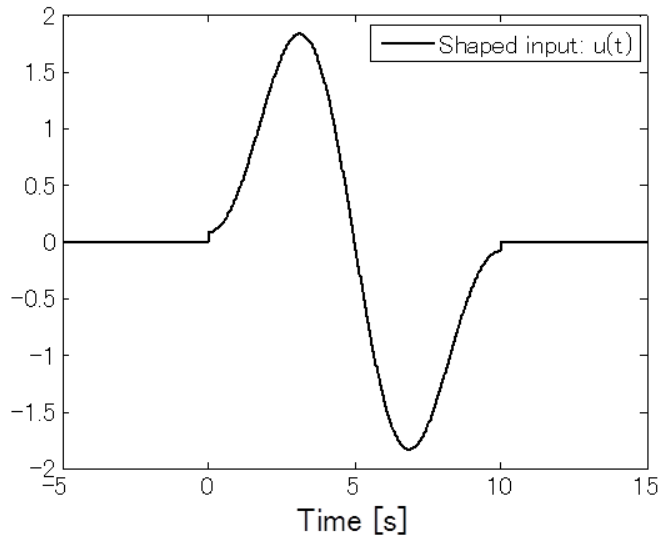

Figure 7-4: Input command (T_s=10 s)

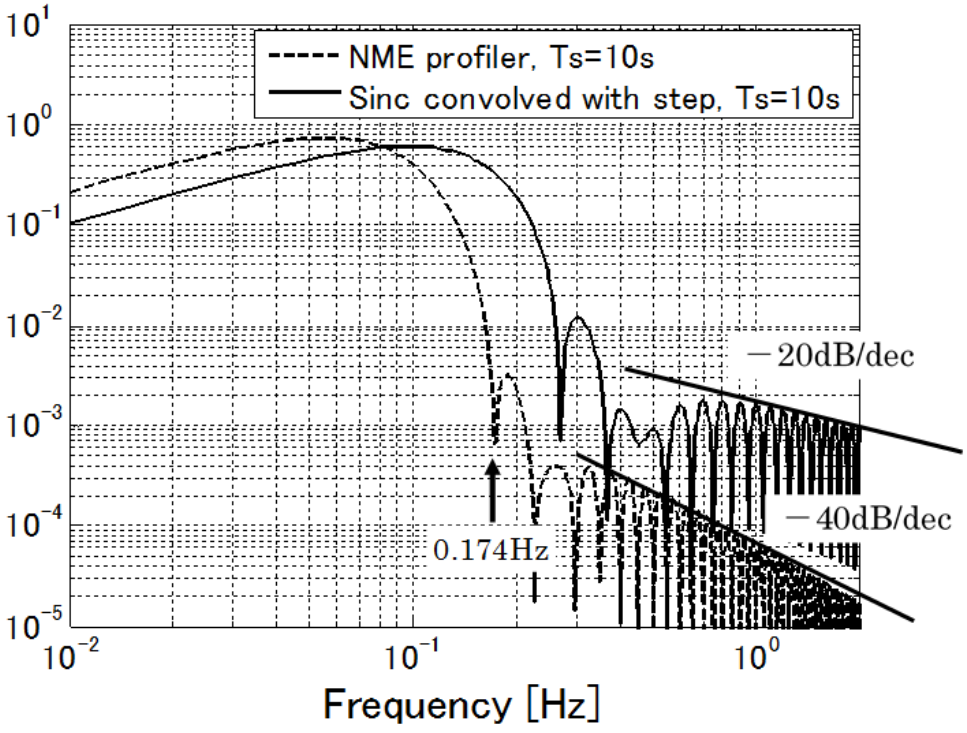

Figure 7-5: FFTs of NME profiler (T_s=10 s) and sinc function convolved with step (T_s=10 s)

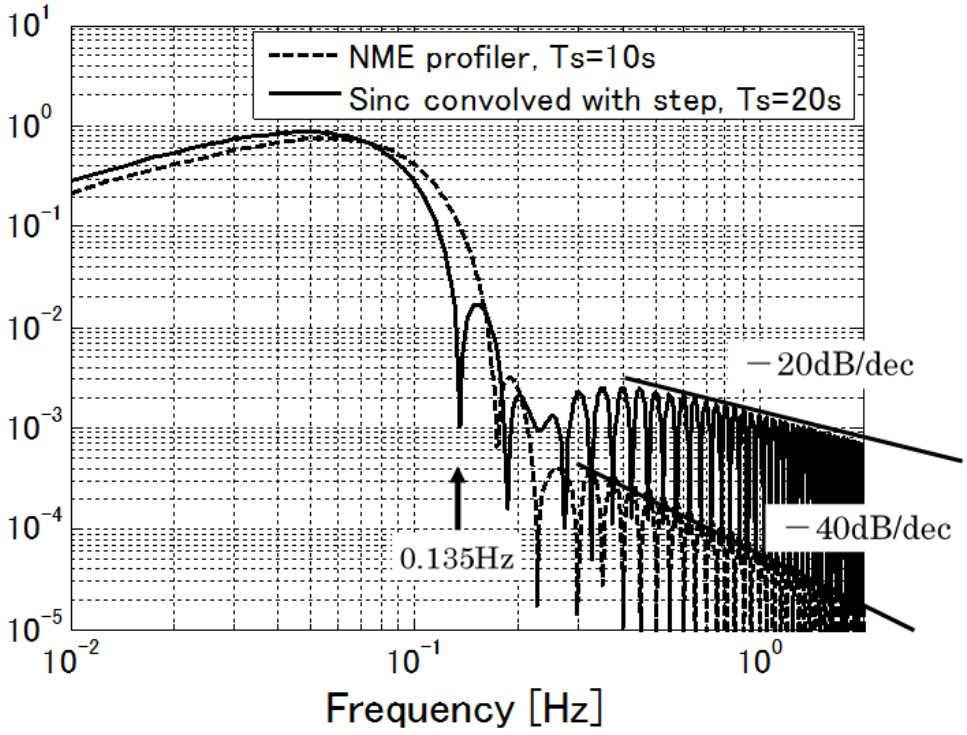

Figure 7-6: FFTs of NME profiler (T_s=10 s) and sinc function convolved with step (T_s=20 s)

Figure 7-7 shows the input command and command responses of the new sinc function-based profiler applying the input command (7.9) where the constant A is chosen so as to satisfy the peak force condition (6.1). The input command is applied as the input force u in Fig. 2-2, and the vertical axes in Fig. 7-7 represent the positions of mass m_1 and mass m_3. Maneuver distances and residual vibrations after rest-to-rest maneuvers by the sinc function-based profilers, the ramped sinusoids [36, 37], and the hybrid-type profilers [44, 47] are shown in Table 7.2 (two-mode system) and Table 7.3 (single-mode system) when the peak force condition (6.1) is applied. The maneuver durations of all the profilers are set to be identical; it is four times as long as period of the low-order flexible mode, i.e. $t_{mnv} = 4T_L = 8\pi/\omega_L$. Table 7.2 shows maneuver distances and residual vibrations of each profiler for frequency error cases of the unknown high-order flexible mode in two-mode system. Five shaped-command responses will be determined for each profiler. The first three cases will be the responses when the stiffness of the unknown high mode k_2 is set to 0.67 (nominal), 1.54, and 2.76; these correspond to ratios of the high-mode and low-mode frequencies (ω_H/ω_L) of 2.0, 3.0, and 4.0, respectively. Additional two cases: k_2 is 0.237 (ω_H is 0.27Hz) and 0.544 (ω_H is 0.39Hz) which are determined by peak frequencies of the FFT of the hybrid controller as shown in Fig. 7-10, are considered because the residual vibrations for the hybrid controllers and the proposed profiler (sinc function convolved with step) have not shown major differences.

The maneuver distances of the new profiler, 18.64, for the same peak force condition, are increased by 33% from the NME profiler, 14.01. The residual vibrations are nearly equivalent among the new sinc function-based profilers, the NME profiler, and the hybrid controller (ZVD, $R_C = 5$ s), and those are smaller than the residual vibrations of other profilers. The maneuver distance of the new profiler (sinc function convolved with step) is the longest among those three profilers. Table 7.3 shows the same evaluations for frequency error cases in single-mode system for references. Similar results are observed in the frequency error cases of single-mode system putting $m_3 = 0$. These results can be confirmed from a different aspect. Figure 7-8 shows the FFTs of ramped sinusoids ($L = 1$, solid line) and sinc function convolved with

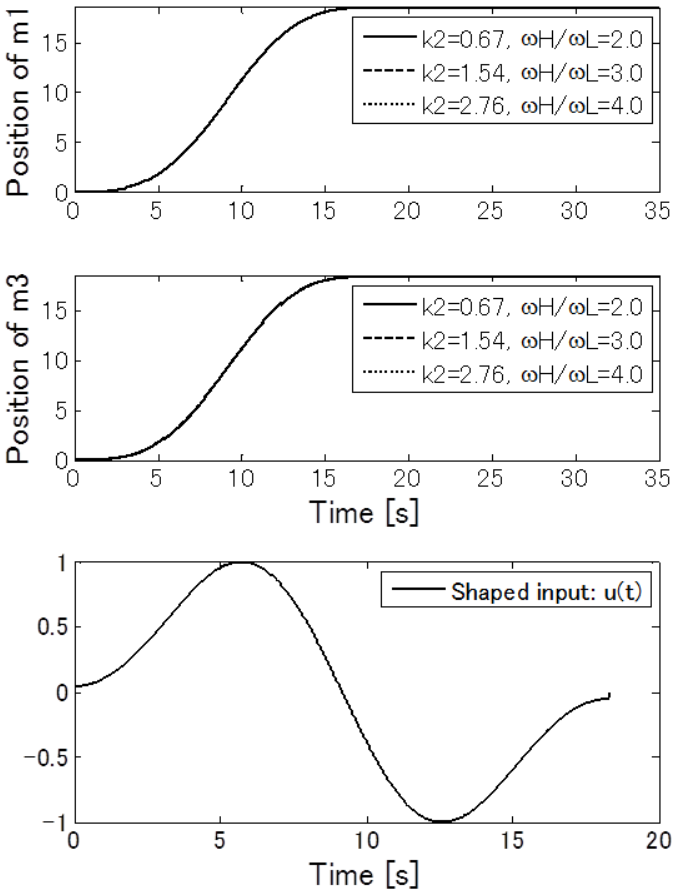

Figure 7-7: Shaped-command responses of the sinc function convolved with step ($t_{mnv} = T_s = 4T_L$) at three values of stiffness k2 of the unknown high-frequency mode. Key to panels as in Fig. 5-1.

Table 7.2: Comparison of simulation results for maneuver distances and residual vibrations of mass m_1 for smooth and hybrid controllers. (Two-Mode System, $m_1 = m_2 = k_1 = 1, m_3 = 0.1$).

	Maneuver distance	Residual vibration of m_1 (peak-to-peak)				
		$k_2 = 0.67$ (ω_H/ω_L =2.0)	$k_2 = 1.54$ (ω_H/ω_L =3.0)	$k_2 = 2.76$ (ω_H/ω_L =4.0)	$k_2 = 0.237$ (ω_H = 0.27Hz)	$k_2 = 0.544$ (ω_H = 0.39Hz)
Ramped sinusoids (L=1, 18.340s)	19.09	**0.5%**	**0.5%**	**0.5%**	**0.4%**	**0.5%**
Ramped sinusoids (L=5, 18.340s)	27.73	**1.1%**	**1.0%**	**1.0%**	**2.6%**	**1.2%**
Ramped sinusoids (L=11, 18.340s)	30.24	**0.3%**	**0.3%**	**0.2%**	**2.5%**	**0.7%**
Hybrid (ZVD, Rc=5s, 18.340s)	14.68	0.0%	0.0%	0.0%	0.1%	0.0%
Hybrid (ZVD, Rc=1s, 18.340s)	19.37	**0.2%**	0.0%	0.1%	**0.3%**	**0.7%**
NME (18.340s)	14.01	0.1%	0.1%	0.1%	0.1%	0.1%
Sinc convolved with step (18.340s)	18.64	0.1%	0.1%	0.1%	0.0%	0.1%

Note: The residual vibrations larger than 0.1% are indicated by boldface.

step (dashed line). The spectrum of the ramped sinusoids has some higher peaks in the range of 0.1 to 0.4 Hz. These peaks may cause larger residual vibrations because higher spectrum causes higher response. Figure 7-9 shows the FFTs of hybrid controller (ZVD, $R_C = 5$ s, solid line) and sinc function convolved with step (dashed line). The envelope of the spectrum of hybrid controller is similar or rather partly lower than that of sinc function convolved with step, however too much low spectrum may cause shorter maneuver distance. Actually the residual vibration of the hybrid controller (ZVD, $R_C = 5$ s) is very small, but the maneuver distance, i.e. 14.68 is shorter than that of sinc function convolved with step, i.e. 18.64. Figure 7-10 shows the FFTs of hybrid controller (ZVD, $R_C = 1$ s, solid line) and sinc function convolved with step (dashed line). The spectrum of the hybrid controller has some higher peaks in the range of 0.2 to 1.3 Hz, thus there might be larger residual vibrations if the frequency of the unknown high-order flexible mode exists around the frequency range.

As a conclusion of this section, the proposed new sinc function-based profiler generates the longest maneuver distance with the smallest residual vibration under the same peak force condition, compared with the previously proposed sinc function-based profiler (NME profiler) or other conventional profilers.

Table 7.3: Comparison of simulation results for maneuver distances and residual vibrations of mass m_1 for smooth and hybrid controllers. (Single-Mode System, $m_1 = m_2 = 1$).

	Maneuver distance	Vibration of m_1 (peak-to-peak)		
		Exact (k_1=1)	k_1=0.8 (10.6% Low)	k_1=0.6 (22.5% Low)
Ramped sinusoids (L=1, 17.772s)	18.82	**0.6%**	**0.3%**	**1.6%**
Ramped sinusoids (L=5, 17.772s)	27.33	**1.4%**	**6.3%**	**9.7%**
Ramped sinusoids (L=11, 17.772s)	29.81	**0.3%**	**4.2%**	**9.2%**
Hybrid (ZVD, Rc=5s, 17.772s)	14.34	0.0%	0.1%	**1.4%**
Hybrid (ZVD, Rc=1s, 17.772s)	19.00	0.0%	**0.2%**	0.1%
NME (L=1, 17.772 s)	13.82	0.1%	0.1%	**1.4%**
Sinc convolved with step (17.772 s)	18.38	0.1%	0.1%	**0.7%**

Note: The residual vibrations larger than 0.1% are indicated by boldface.

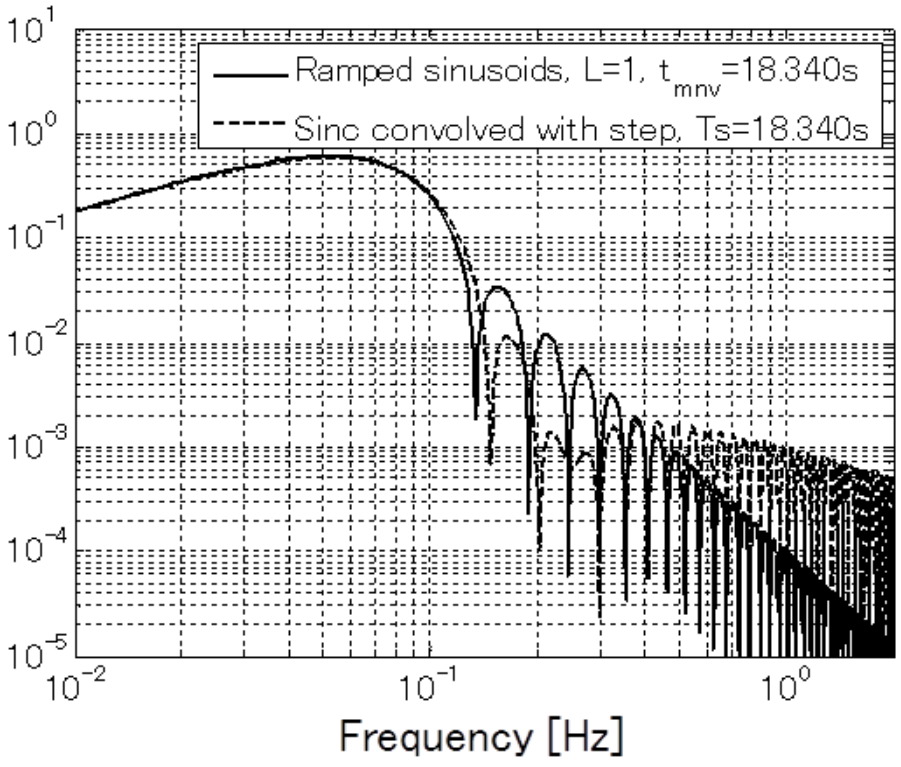

Figure 7-8: FFTs of ramped sinusoids (L=1) and sinc function convolved with step.

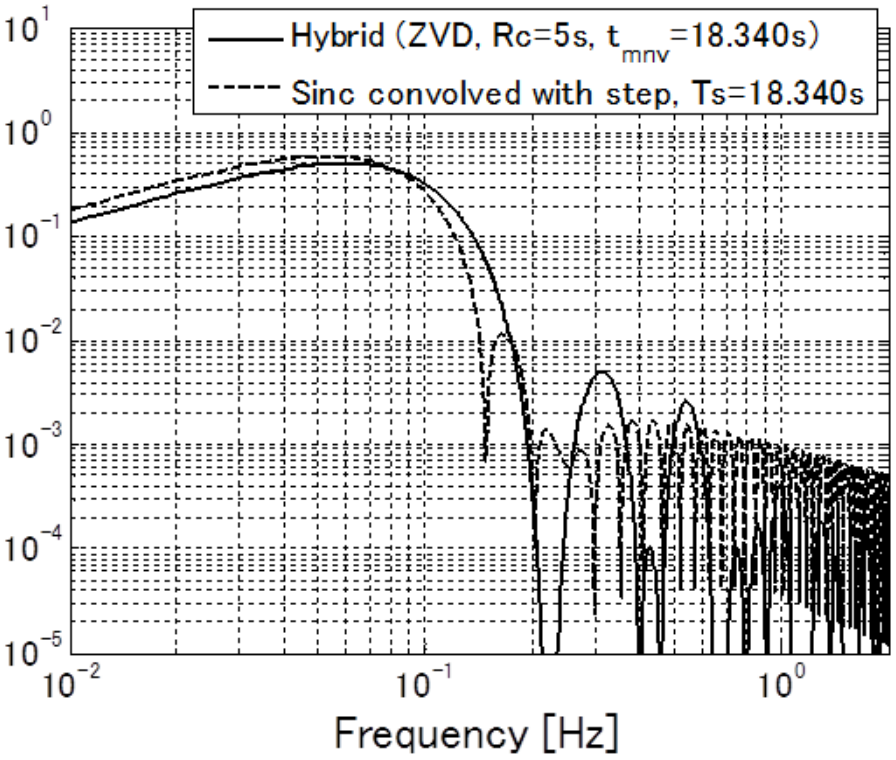

Figure 7-9: FFTs of hybrid controller (ZVD, Rc = 5 s) and sinc function convolved with step.

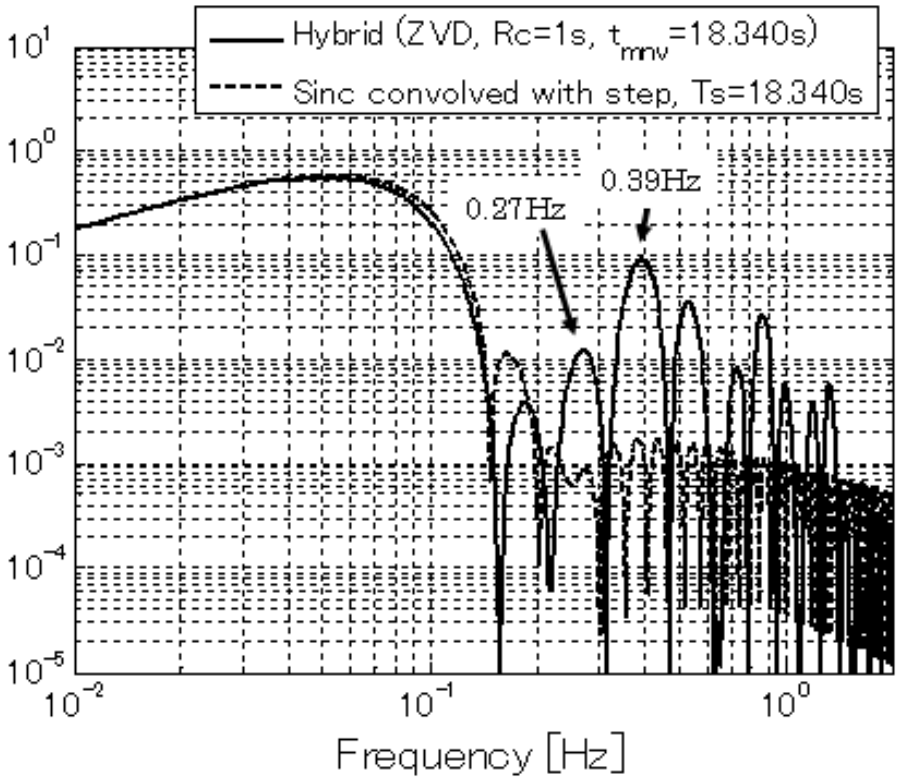

Figure 7-10: FFTs of hybrid controller (ZVD, Rc = 1 s) and sinc function convolved with step.

7.4 Sinc Function with Weighted Harmonics

The NME profiler uses a pair of sinc functions as a forcing function, given by

$$f(t) = \text{sinc}\,(\omega_s t - \pi) - \text{sinc}\,(\omega_s t - 3\pi) \tag{7.15}$$

where time domain is defined as $t = [0,\ 2T_s]$**:** twice as long as the period of the boundary frequency of the sinc function, $T_s(= 2\pi/\omega_s)$**.** Assuming (7.15) as fundamental function, j-th harmonics is given by compressing more waveforms into the same time interval as

$$f_j(t) = \sum_{m=1}^{2j} \left\{ (-1)^{m-1} \frac{\sin\left(j\omega_s t - (2m-1)\,\pi\right)}{j\omega_s t - (2m-1)\,\pi} \right\}\ , \qquad (j = 1,\ 2,\ \cdots) \tag{7.16}$$

Notice that it has odd symmetry about T_s which makes it particularly convenient as a forcing function. The harmonics from 1^{st} to 5^{th} order are shown in Fig. 7-11 when T_s is 10 s. If the harmonics could be added so that the resulting function approximates a square wave, the speed of response would improve considerably, as long as the resultant frequency spectrum does not contain high energies at system resonant frequencies.

A least-squares approximation to the square wave can be constructed by minimizing the square of the error between the desired square wave of height F and a finite sum of weighted harmonics from 1^{st} to L^{th} order. The weighting coefficients A_j can be determined by the minimization problem given as

$$\int_0^{T_f/2} \left[F - \sum_{j=1}^{L} A_j f_j(t) \right]^2 dt + \int_{T_f/2}^{T_f} \left[-F - \sum_{j=1}^{L} A_j f_j(t) \right]^2 dt = \min\,. \tag{7.17}$$

where T_f is a maneuver duration and $T_f = 2T_s$. Differentiating with respect to A_i,

$$\int_0^{T_f/2} \left[F - \sum_{j=1}^{L} A_j f_j(t) \right] f_i(t)dt - \int_{T_f/2}^{T_f} \left[F + \sum_{j=1}^{L} A_j f_j(t) \right] f_i(t)dt = 0\ , \qquad (i = 1,\ 2,\ \cdots,\ L) \tag{7.18}$$

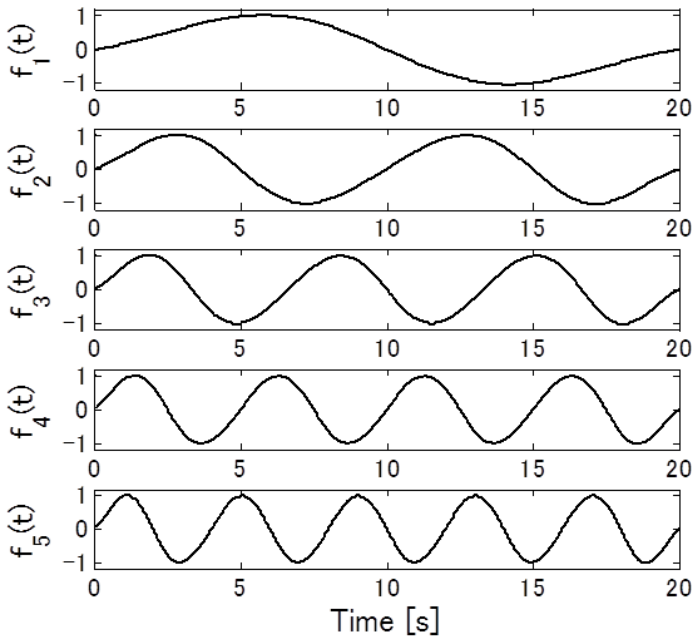

Figure 7-11: Harmonics at $j = 1$ to 5 (T_s=10 s)

and rearranging gives:

$$\sum_{j=1}^{L} A_j \underbrace{\int_0^{T_f} f_j(t) f_i(t) dt}_{I_{ij}} = F \underbrace{\left[\int_0^{T_f/2} f_i(t) dt - \int_{T_f/2}^{T_f} f_i(t) dt \right]}_{I_i}, \qquad (i = 1,\ 2,\ \cdots,\ L) \tag{7.19}$$

The resulting matrix expression to solve for the A_i is

$$\begin{bmatrix} I_{11} & I_{12} & \cdots & I_{1L} \\ I_{21} & I_{22} & \cdots & I_{2L} \\ \vdots & \vdots & & \vdots \\ I_{L1} & I_{L2} & \cdots & I_{LL} \end{bmatrix} \begin{bmatrix} A_1 \\ \vdots \\ \vdots \\ A_L \end{bmatrix} = F \begin{bmatrix} I_1 \\ I_2 \\ \vdots \\ I_L \end{bmatrix} \tag{7.20}$$

where

$$I_{ij} = \int_0^{T_f} \left[\sum_{m=1}^{2j} \left\{ (-1)^{m-1} \frac{\sin\left(j\omega_s t - (2m-1)\,\pi\right)}{j\omega_s t - (2m-1)\,\pi} \right\} \sum_{m=1}^{2i} \left\{ (-1)^{m-1} \frac{\sin\left(i\omega_s t - (2m-1)\,\pi\right)}{i\omega_s t - (2m-1)\,\pi} \right\} \right] dt \tag{7.21}$$

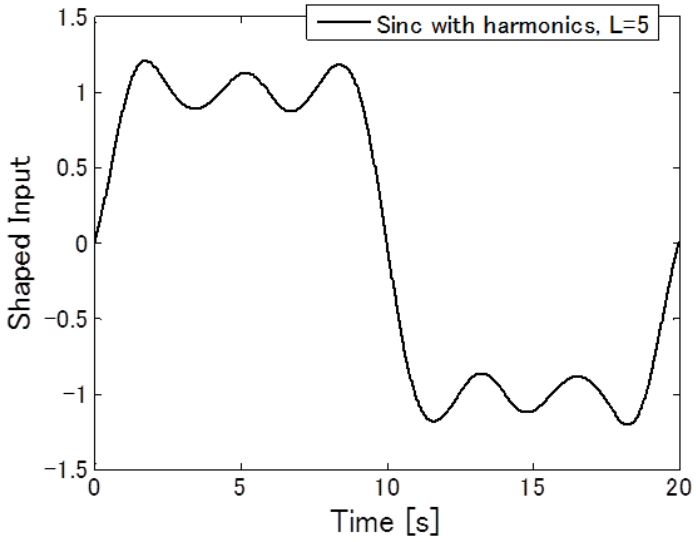

Figure 7-12: Shaped input (T_s=10 s, $L = 5$, $F = 1$)

$$
\begin{aligned}
I_i = &\int_0^{T_f/2} \left[\sum_{m=1}^{2i} \left\{ (-1)^{m-1} \frac{\sin\left(i\omega_s t - (2m-1)\,\pi\right)}{i\omega_s t - (2m-1)\,\pi} \right\} \right] dt \\
&- \int_{T_f/2}^{T_f} \left[\sum_{m=1}^{2i} \left\{ (-1)^{m-1} \frac{\sin\left(i\omega_s t - (2m-1)\,\pi\right)}{i\omega_s t - (2m-1)\,\pi} \right\} \right] dt
\end{aligned}
\tag{7.22}
$$

Thus, the weighting coefficients A_j are given by

$$
[A_j] = F\,[I_{ij}]^{-1}\,[I_i] \tag{7.23}
$$

Input-torque command of the least-square fitted sinc function-based profiler, hereinafter referred to as "sinc function with weighted harmonics" or "sinc with harmonics," is given as

$$
u(t) = \begin{cases} A \sum_{j=1}^{L} A_j \cdot f_j(t) & \text{for} \quad 0 \le t \le t_{mnv} \\ 0 & \text{for} \quad t < 0, t_{mnv} < t \end{cases}
\tag{7.24}
$$

The shapes of the resulting forcing function with L=5 and F=1 is shown in Fig. 7-12. A typical input command and command responses of the two-mode system are shown in Fig. 7-13, where the peak force condition (6.1) is applied.

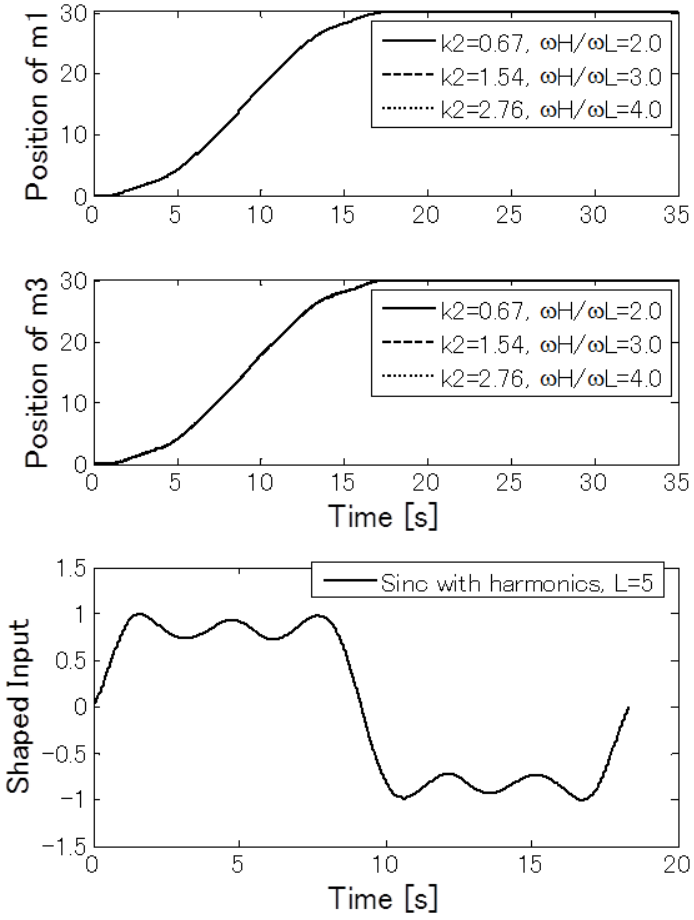

Figure 7-13: Shaped-command responses of the sinc function with weighted harmonics ($L = 5$, $t_{mnv} = 2T_s = 4T_L$) at three values of stiffness k_2 of the unknown high-frequency mode. Key to panels as in Fig. 5-1.

Table 7.4: Comparison of simulation results for maneuver distances and residual vibrations of mass m_1 for smooth and hybrid controllers. (Two-Mode System, $m_1 = m_2 = k_1 = 1, m_3 = 0.1$).

	Maneuver distance	Vibration of m_1 (peak-to-peak)				
		$k_2 = 0.67$ ($\omega_H/\omega_L = 2.0$)	$k_2 = 1.54$ ($\omega_H/\omega_L = 3.0$)	$k_2 = 2.76$ ($\omega_H/\omega_L = 4.0$)	$k_2 = 0.237$ ($\omega_H =$ 0.27Hz)	$k_2 = 0.544$ ($\omega_H =$ 0.39Hz)
Ramped sinusoids (L=1, 18.340s)	19.09	**0.5%**	**0.5%**	**0.5%**	**0.4%**	**0.5%**
Ramped sinusoids (L=5, 18.340s)	27.73	**1.1%**	**1.0%**	**1.0%**	**2.6%**	**1.2%**
Ramped sinusoids (L=11, 18.340s)	30.24	**0.3%**	**0.3%**	**0.2%**	**2.5%**	**0.7%**
Hybrid (ZVD, Rc=5s, 18.340s)	14.68	0.0%	0.0%	0.0%	0.1%	0.0%
Hybrid (ZVD, Rc=1s, 18.340s)	19.37	**0.2%**	0.0%	0.1%	**0.3%**	**0.7%**
Hybrid (ZVD, Rc=0.2s, 18.340s)	21.87	0.0%	0.0%	0.0%	0.1%	**0.5%**
NME (L=1, 18.340s)	14.01	0.1%	0.1%	0.1%	0.1%	0.1%
Sinc convolved with step (18.340s)	18.64	0.1%	0.1%	0.1%	0.0%	0.1%
Sinc with harmonics (L=5, 18.340s)	30.36	**0.2%**	0.1%	0.1%	**2.6%**	**0.3%**
Sinc with harmonics (L=11, 18.340s)	32.01	0.0%	0.0%	0.0%	**2.3%**	**0.5%**

Note: The residual vibrations larger than 0.1% are indicated by boldface.

Maneuver distances and residual vibrations after rest-to-rest maneuvers by the sinc function with weighted harmonics, other smooth profilers, and hybrid profilers, where all the profilers include identical durations, are shown in Table 7.4 (two-mode system) and Table 7.5 (single-mode system) when the peak force condition (6.1) is applied. According to Table 7.4, the longest maneuver distance, 32.01, can be achieved by the proposed sinc function with weighted harmonics (indicated as "Sinc with harmonics" in the Table 7.4 and Table 7.5) with $L = 11$ as shown in Fig. 7-14. The maneuver distances of the sinc function with weighted harmonics with $L = 11$, 32.01, are increased by 128% from the NME profiler, 14.01. The hybrid profiler generates maneuver distance of 21.87 at the most when R_C is 0.2 s as shown in Fig. 7-15, and it is not expected to make any further improvement of the maneuver distance even if the R_C will be shorter. The same observations are made from the Table 7.5 which shows comparison for single-mode system. FFTs of the sinc function with weighted harmonics and the ramped sinusoids with a 5-term ($L = 5$) are shown in Fig. 7-16. The spectrum of the sinc function with weighted harmonics has slightly lower boundary frequencies compared with the ramped sinusoids. The sidelobe of the sinc function with weighted harmonics inclines at –40 dB/dec while the ramped sinusoids inclines at –60 dB/dec.

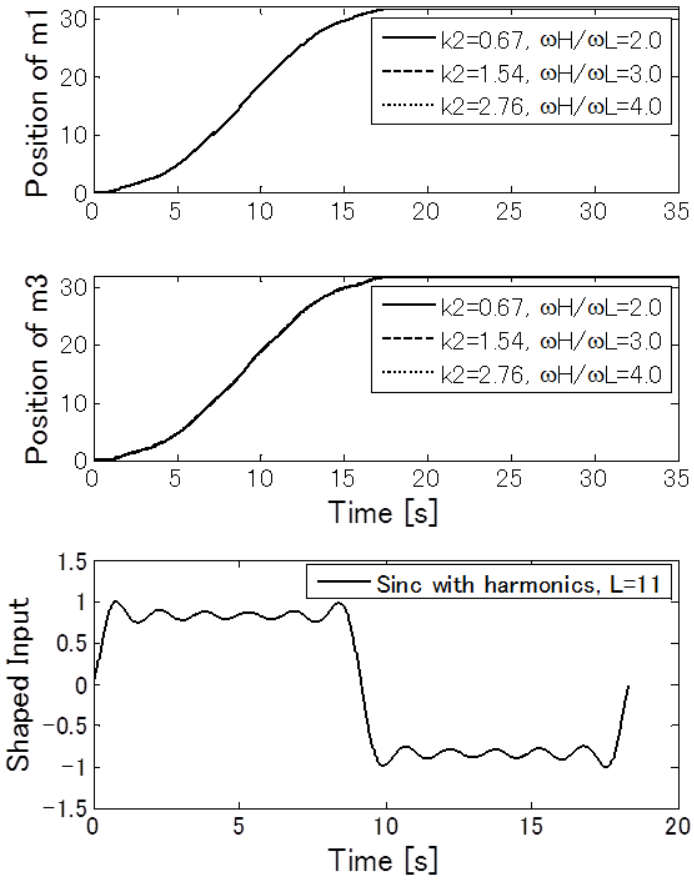

Figure 7-14: Shaped-command responses of the sinc function with weighted harmonics ($L = 11$, $t_{mnv} = 2T_s = 4T_L$) at three values of stiffness k_2 of the unknown high-frequency mode. Key to panels as in Fig. 5-1.

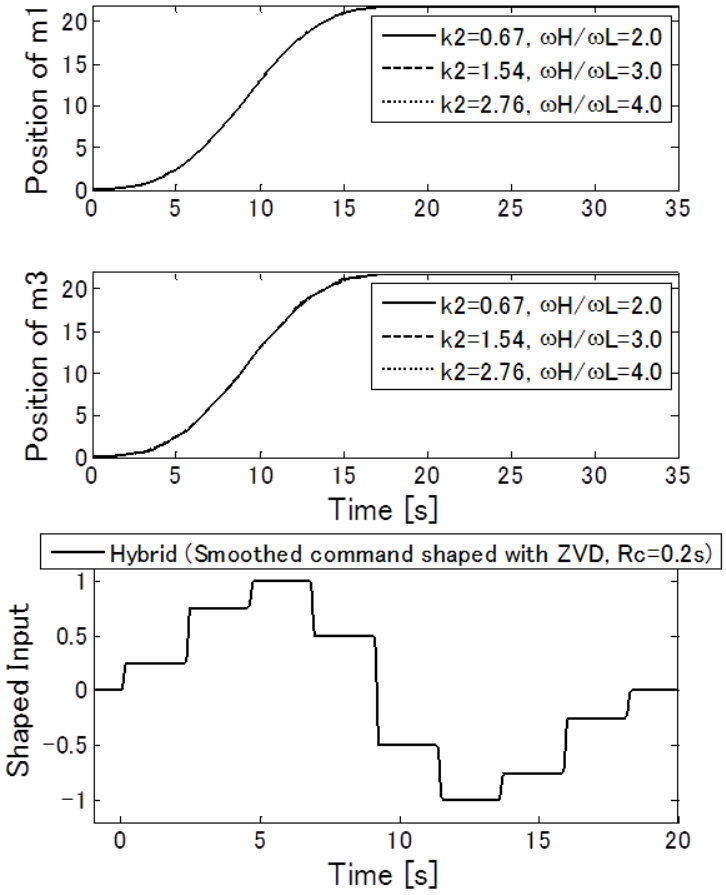

Figure 7-15: Shaped-command responses of the hybrid profiler (smoothed command shaped with ZVD shaper, R_C=0.2 s, $t_{mnv} = 4T_L$) at three values of stiffness k_2 of the unknown high-frequency mode. Key to panels as in Fig. 5-1.

Table 7.5: Comparison of simulation results for maneuver distances and residual vibrations of mass m_1 for smooth and hybrid controllers. (Single-Mode System, $m_1 = m_2 = k_1 = 1$).

	Maneuver distance	Vibration of m_1 (peak-to-peak)		
		Exact (k_1=1)	k_1=0.8 (10.6% Low)	k_1=0.6 (22.5% Low)
Ramped sinusoids (L=1, 17.772s)	18.82	**0.6%**	**0.3%**	**1.6%**
Ramped sinusoids (L=5, 17.772s)	27.33	**1.4%**	**6.3%**	**9.7%**
Ramped sinusoids (L=11, 17.772s)	29.81	**0.3%**	**4.2%**	**9.2%**
Hybrid (ZVD, Rc=5s, 17.772s)	14.34	0.0%	0.1%	**1.4%**
Hybrid (ZVD, Rc=1s, 17.772s)	19.00	0.0%	**0.2%**	0.1%
Hybrid (ZVD, Rc=0.2s, 17.772s)	21.55	0.0%	**0.2%**	**0.4%**
NME (L=1, 17.772 s)	13.82	0.1%	0.1%	**1.4%**
Sinc convolved with step (17.772 s)	18.38	0.1%	0.1%	**0.7%**
Sinc with harmonics (L=5, 17.772 s)	29.92	**0.2%**	**4.5%**	**9.4%**
Sinc with harmonics (L=11, 17.772 s)	31.56	0.0%	**3.3%**	**8.9%**

Note: The residual vibrations larger than 0.1% are indicated by boldface.

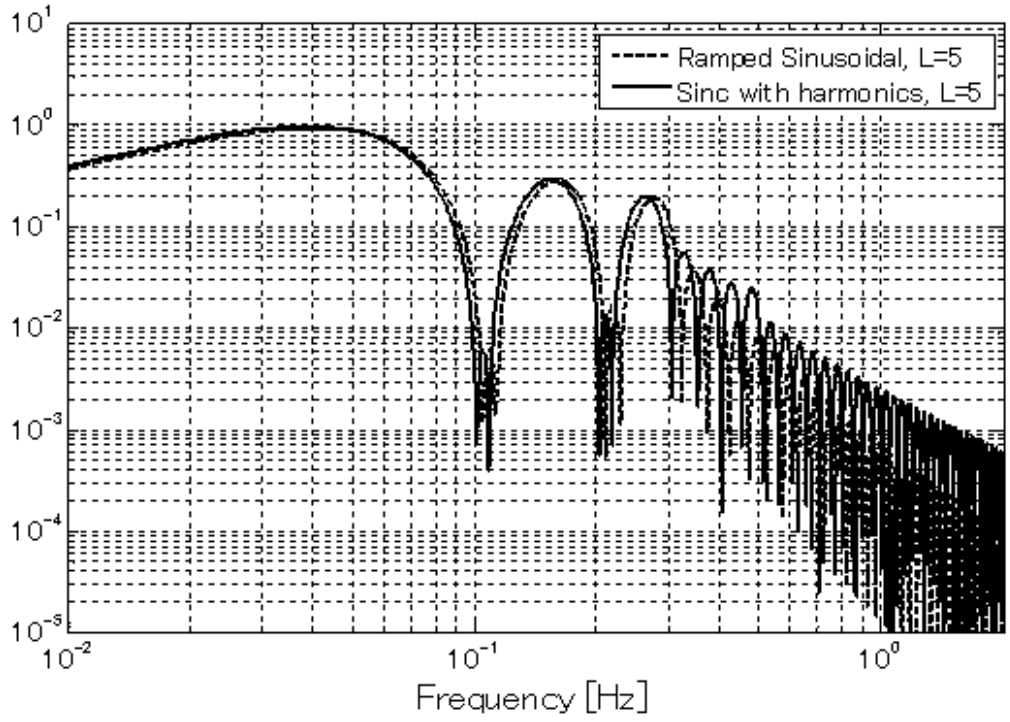

Figure 7-16: FFTs of shaped input of ramped-sinusoids and sinc function with weighted harmonics ($t_{mnv} = 2T_s$=20 s, $L = 5$).

Table 7.6: Comparison of simulation results for maneuver distances for smooth controllers. (Two-Mode System, $m_1 = m_2 = k_1 = 1$, $m_3 = 0.1$).

	Maneuver distance					
	L=1	L=3	L=5	L=7	L=9	L=11
Ramped sinusoids (18.340 s)	19.09	25.36	27.73	28.99	29.74	30.24
Sinc with harmonics (18.340 s)	21.57	28.31	30.36	31.12	31.68	32.01

A further comparison of maneuver distances by the sinc function with weighted harmonics proposed in this section and the ramped sinusoids with identical durations are shown in Table 7.6. The maneuver distances with respect to each number of terms L are shown in Fig. 7-17. The proposed sinc functions with weighted harmonics show longer maneuver distances compared with the ramped sinusoids for each number of terms L. Assuming the distance at L=11 being 100%, percentages of the maneuver distances are shown in Fig. 7-18. The curves converge in an exponential manner and the curve for the proposed profiler becomes 95% with L=5.

Determination of Numbers of Terms (L):

As discussed in the previous work of the ramped sinusoids [37], some directions to decide the number of terms L of the sinc function with weighted harmonics are shown as follows. The higher order harmonics are used, the closer the function approximates a square wave, and the longer the maneuver distance will be. The problem is that higher harmonics introduce excitation at higher frequencies. This may bring excitations of frequencies closer to the system resonances. Preferably, any frequencies excited by the forcing function will lie well below the lowest system resonances. An alternate approach would be to allow excitation frequencies over a wider range, some exceeding system resonance, while making sure that the actual resonant frequencies are not excited. It is conceivable that the latter effect could be achieved if the forcing function has a local minimum excitation at the frequency corresponding to resonance. This requires a trough in the frequency spectrum being at the appropriate frequency. A look at the frequency spectra of sums of harmonics will help an interpretation of the relationship between the spectra and the number of terms

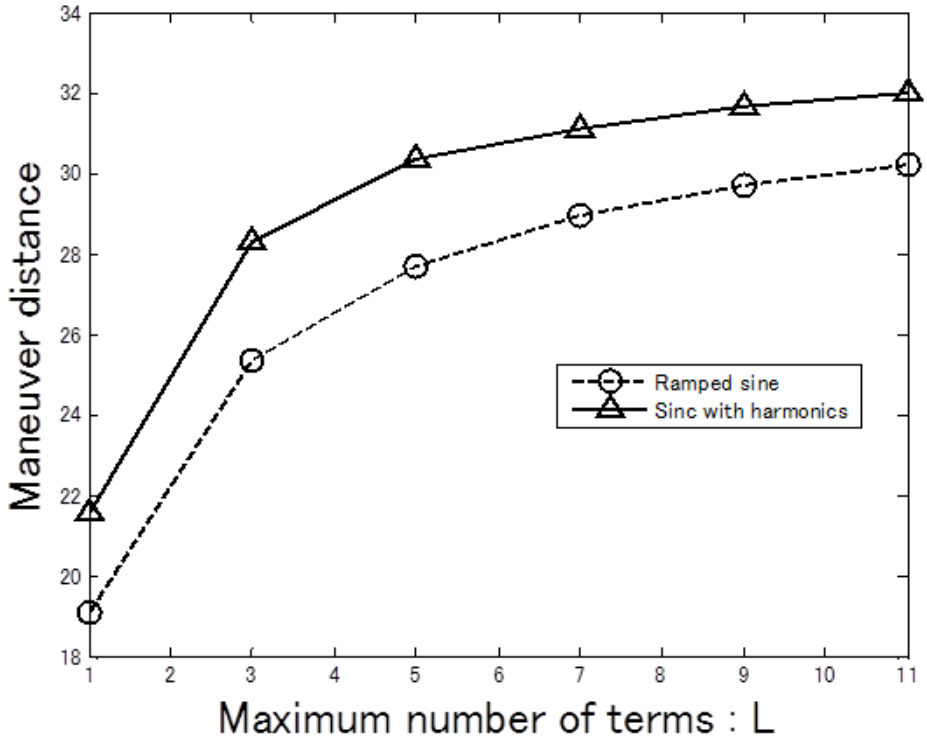

Figure 7-17: Max. number of terms L vs. maneuver distance when t_{mnv} is 18.340 s (Two-Mode System)

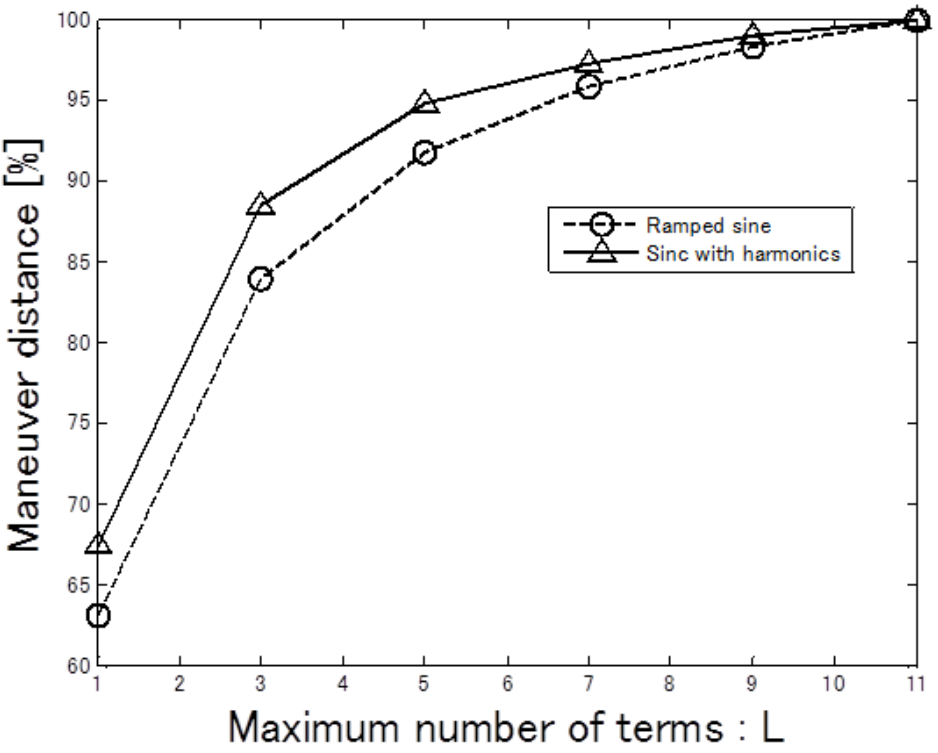

Figure 7-18: Max. number of terms L vs. maneuver distance when t_{mnv} is 18.340 s (Two-Mode System) where the maneuver distance at L=11 corresponds to 100%

(L). A comparison of frequency spectra of three different series of sinc functions with weighted harmonics, the spectra of a 3-term (L=3), a 5-term (L=5), and a 7-term (L=7) with $t_{mnv}(= 2T_s)$ =20 s, are shown in Fig. 7-19. It is clear that series with more terms have trough at nearly the same frequencies as series with fewer terms. Thus, if the system resonant frequency falls in a trough for a series with 3 terms, it will fall equally well into the trough for a series of 5 terms or 7 terms. This suggests that, if the profiler proposed in this section is determined in which the system resonance occurs in a spectral trough, many terms can be added without detrimental effects on residual vibration. When more terms are combined to form the forcing function, more energy can be transferred to the system and the maneuver distance is correspondingly getting longer. As shown in Fig. 7-19, the regions of frequency where excitation is minimal have a finite width; they are not merely a single point. Thus placement of the trough with respect to the system natural frequencies is not critical. The magnitude of the frequency components higher than the frequency of the $(j+1)/2$th trough for the j-term (j=1,3,5,. . .), i.e. the frequency components higher than the second trough (0.2 Hz) for 3-term, the third trough (0.3 Hz) for 5-term, or the fourth trough (0.4 Hz) for 7-term, tapers off by approximately –40 dB/dec as shown in Fig. 7-19.

The foregoing observations lead to a method for determining the appropriate forcing function for a given set of dynamic model, peak force of actuator, and maneuver distance. Considering a relationship between system resonant frequency and forcing function, number of terms L and maneuver duration t_{mnv} are chosen, so that the command response indicates a residual vibration below a certain threshold level.

As a conclusion of this section, the proposed new sinc function-based profiler, i.e. the sinc function with weighted harmonics, has been demonstrated that it generates the longest maneuver distance, compared with the original sinc function-based profiler (NME profiler) or other conventional profilers. If the forcing function has a local minimum excitation at the frequency corresponding to the system resonance, this profiler generates significantly longer maneuver distances with minimal residual vibrations. This profiler is suitable for a satellite with relatively rigid structure; such

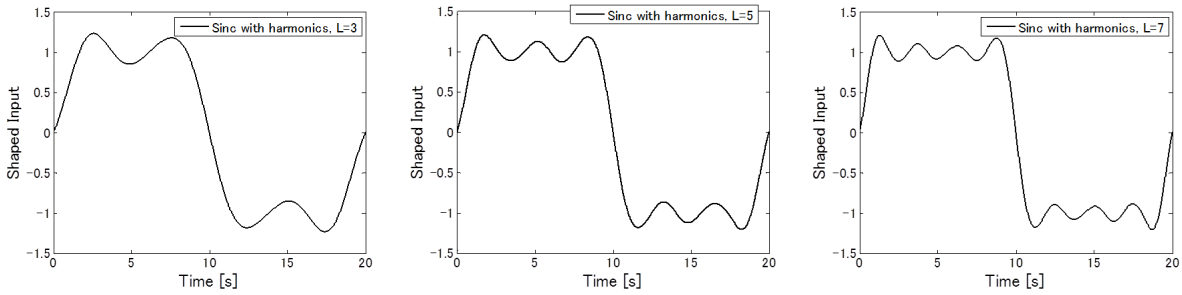

(a) $L = 3$ (b) $L = 5$ (c) $L = 7$

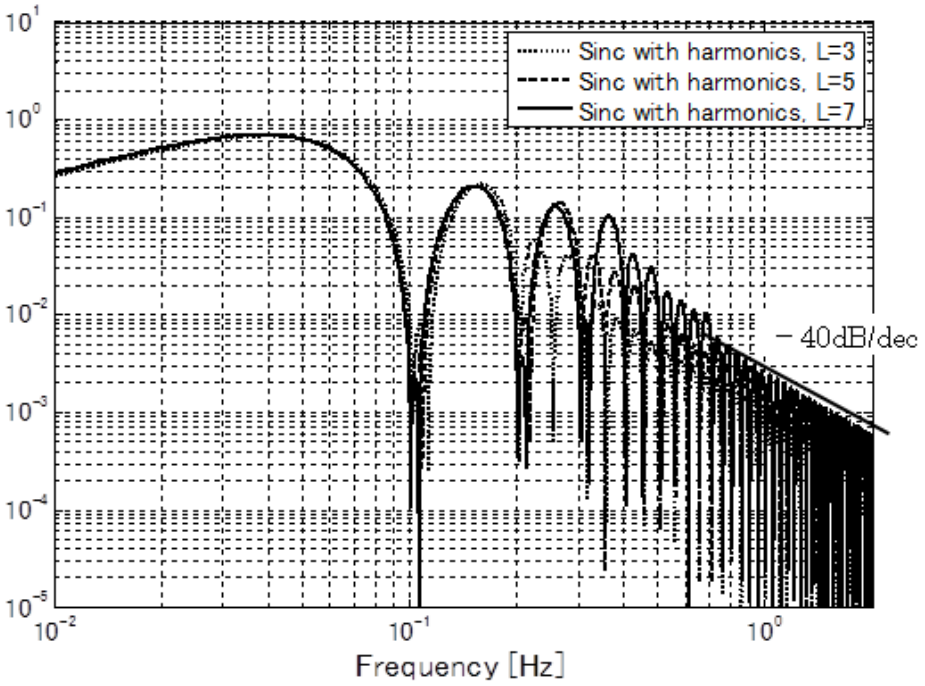

Figure 7-19: Top-left, middle, right: shaped input of the sinc with weighted harmonics, Bottom: FFTs of the sinc with harmonics (L=3, 5, and 7, t_{mnv}=$2T_L$=20 s)

a satellite has fewer critical flexible modes, so that the profiler with the system resonances falling in troughs can be determined easily and a longer maneuver distance is generated with small residual vibration.

7.5 Discussion on Modified Sinc Function-Based Profilers

This chapter proposed two kinds of sinc function-based smooth profilers to achieve higher agility: the sinc function convolved with step and the sinc function with weighted harmonics. Performances of those profilers have been compared with those of the original sinc function-based profiler (NME profiler) and conventional smooth or hybrid profilers. The sinc function convolved with step increased maneuver distance by a factor of 1.33 with the smallest residual vibration under a common peak force condition, compared with the NME profiler. The sinc function convolved with step shows the longest maneuver distances among the profilers with the smallest residual vibrations. The sinc function with weighted harmonics increased maneuver distance by a factor of 2.28 under a common peak force condition, compared with the NME profiler. The sinc function with weighted harmonics shows the longest maneuver distances with comparable or smaller residual vibrations, compared with the ramped sinusoids or hybrid profilers. Both of the newly proposed sinc function-based profilers can be used as effective alternatives for appropriate applications; if there are many unknown high-order flexible modes, the sinc function convolved with step would be suitable, if there are fewer critical high-order modes, the sinc function with weighted harmonics would be suitable.

THIS PAGE INTENTIONALLY LEFT BLANK

Chapter 8

Application to ASTRO-G

8.1 Introduction

So far, two-mode systems with an unknown high-order mode have been used as the most simplified model of flexible spacecraft. In this section, numerical simulations are presented to demonstrate the effectiveness of the proposed profiler (NME profiler) when applied to an actual spacecraft's flexible model, i.e. ASTRO-G model [15, 16]. The preliminary design of ASTRO-G had been successfully completed and planned to be launched based on this controller design. However, unfortunately the program was terminated due to the deployable antenna's technical feasibility reasons during critical design phase in 2011.

8.2 Outline of ASTRO-G Attitude Control Subsystem

In this section, application to ASTRO-G ACS (Attitude Control Subsystem) is introduced. The mission of ASTRO-G was called as VSOP2 (VSOP: VLBI Space Observatory Programme) and the satellite includes 4-single-gimbal CMGs with parallel gimbal arrangement and 4-skewed RWs as actuators. Missions of VSOP2 are performed by way of back and forth rest-to-rest high speed maneuvers (switching maneuvers). The satellite attitude is required to be highly-stable at the end of maneuvers. Figure 8-1 shows on-orbit image of ASTRO-G. This satellite has two kinds of large flexible appendages, one is large deployable antenna, the other is flexible solar panel. For the observation mission, a large deployable flexible mesh antenna is equipped in Astro-G, the antenna's observation axis exists along +Z direction in the satellite body coordinate system. Then satellite +Z-axis needs to be kept on a target celestial body and required a quick rest-to-rest maneuver to change the +Z-axis to another calibration celestial body.

Figure 8-2 shows functional block diagram of ASTRO-G ACS which consists of attiude sensors, control actuators, and attitude control electronics (i.e., ACE). Gyro scopes and optical sensors are used as attitude sensors. CMGs and RWs are used as control actuators. The ACE includes attitude estimator, NME profiler, torque profiler / distributor, CMG gimbal steering law, CMG gimbal controller, RW controller, and RW distributor. These are realized by software.

NME (nil-mode-exciting) profiler is defined as the preshaping input profiler proposed in Chapter 3 and used for computing control inputs (target attitude profile). Torque profiler has the function of computing control torque which is required to perform the target attitude profile. Decoupling torque needed for avoiding cross-coupled disturbances is also computed at the same time. Distributor has the function of distributing the control torque into CMGs and RWs.

Figure 8-3 shows outline of single-gimbal CMG. CMG is a high torque actuator which generates large torque by the effect of gyroscopic torque. CMG output torque

Figure 8-1: ASTRO-G on-orbit image

T_{CMG} is expressed as

$$\begin{aligned} T_{CMG} &= -(\omega_B + \omega_G) \times H_{CMG}^{rotor} \\ &= -\omega_B \times H_{CMG}^{rotor} - \omega_G \times H_{CMG}^{rotor} \end{aligned} \tag{8.1}$$

where H_{CMG}^{rotor} is CMG rotor momentum, ω_G is gimbal rate relative to body coordinate system, and ω_B is body rate defined in inertial reference frame. .

CMG gimbal steering law computes CMGs gimbal angle profiles and gimbal rate profiles which are required to output the control torque distributed. CMG gimbal controller is a controller for minor feedback loop of gimbal angle and gimbal rate. RW controller computes feedback control torque of RWs which is required to perform the satellite motion as target attitude profile and the torque is computed from the current body angle error and the current body rate error. RW distributor distributes the control torque into each RWs. The feature of this system exists in the part of NME profiler that computes optimal profile of feedforward control inputs in which the character frequencies of the flexible appendages are not excited.

The block diagram of controller for ASTRO-G is shown in Fig. 8-4. It consists of a feedforward controller of the nil-mode-exciting (NME) profiler and a feedback controller of C. The input-output relation from the reference signal r and disturbance

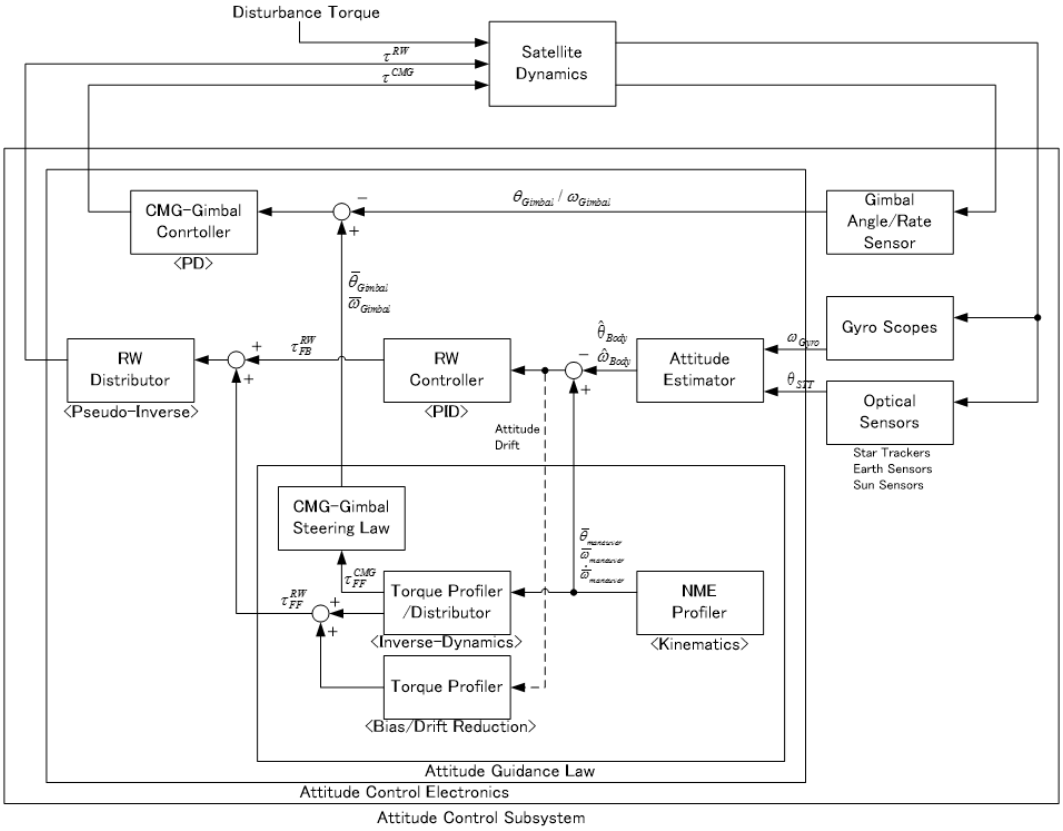

Figure 8-2: ASTRO-G ACS functional block diagram

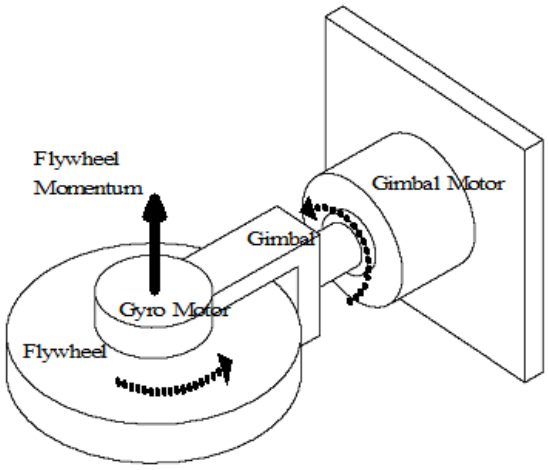

Figure 8-3: Single-gimbal CMG

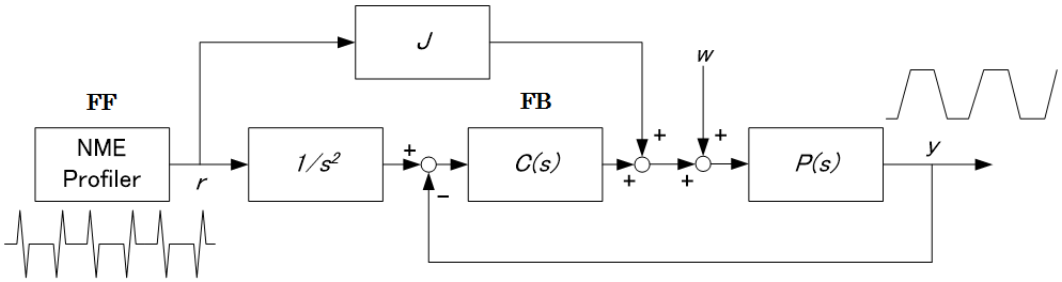

Figure 8-4: Block diagram of Astro-G controller

w to the measurement output y is given by

$$y = G_{yr}r + G_{yw}w \tag{8.2}$$

where

$$G_{yr} = G_{yw}(J + C/s^2), G_{yw} = (I + PC)^{-1}P \tag{8.3}$$

P denotes the plant transfer function. J denotes the spacecraft moment of inertia. C is designed so that the closed-loop system is robustly stable and has disturbance attenuation capability to w. The NME profiler generates feedforward profiles of attitude maneuvers. Figure 8-5 shows the frequency range of each influence factors which consist of frequencies of structural modes and frequencies of controllers. As shown in Fig. 8-5, ASTRO-G ACS is designed to realize frequency separation between flexible-modes and controllers. Figure 8-6 shows maneuver sequence of ASTRO-G. Several times of repeating test maneuvers are performed for model identification prior to observation maneuvers.

All gimbal axes of CMGs are aligned parallel to Z-axis and steered by symmetrical gimbal motion called scissors pair steering law. Figure 8-7 shows outline of the gimbal control. As shown in Fig. 8-7, gimbals are steered by symmetrical motion algorithm. CMG output torque axis will be time-invariant (normal to gimbal home angle) once the gimbal home position is determined. Then a continuous output torque profile along to the axis can be generated.

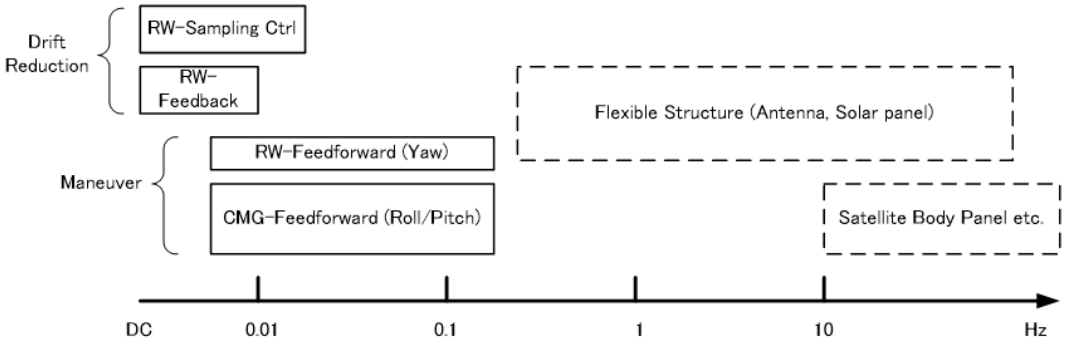

Figure 8-5: Frequency distribution of controllers and structures

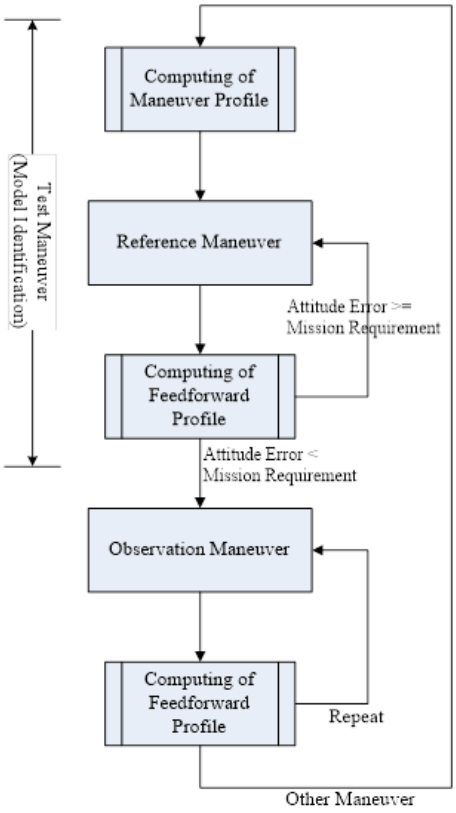

Figure 8-6: ASTRO-G maneuver sequence

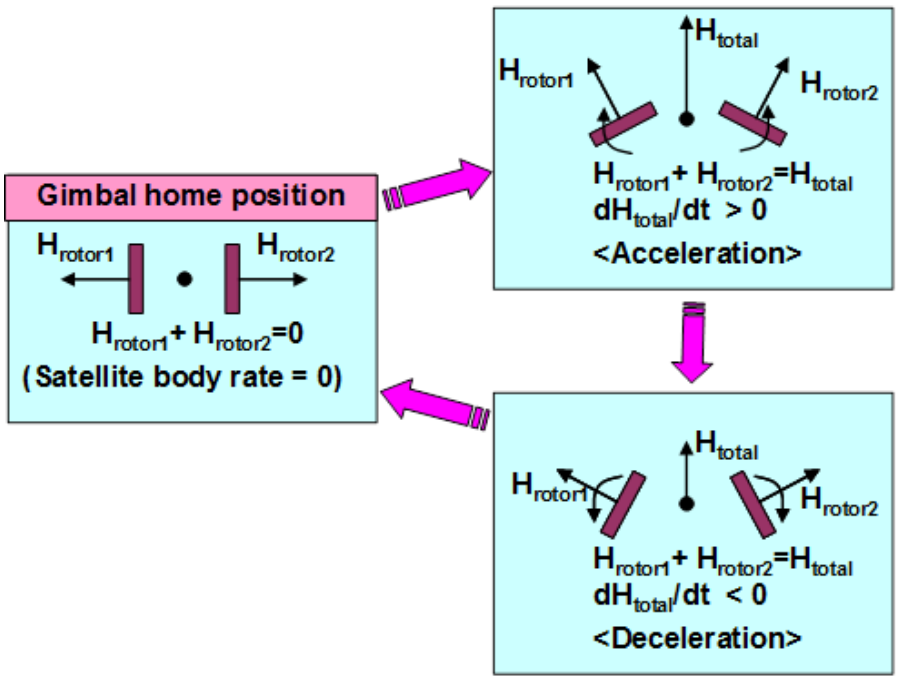

Figure 8-7: Gimbal control by scissors pair steering law

8.3 Feedforward Algorithm of Rest-to-Rest Maneuvers with CMGs Parallel Gimbal Arrangement

8.3.1 Path Planning of Rest-to-Rest Maneuvers with CMGs Parallel Gimbal Arrangement

Fundamental principles of satellite body motion are briefly described based on a rigid spacecraft. Then, path planning of rest-to-rest body motion with CMGs parallel gimbal arrangement is discussed.

A satellite total angular momentum vector consists of the satellite body angular momentum and the internal angular momentum such as momentum of reaction wheels as follows,

$$H = I\omega + H_{int} \tag{8.4}$$

The principle of angular momentum conservation is shown as

$$\frac{dH}{dt} = 0 \tag{8.5}$$

Substituting Eq. (8.4) into (8.5) gives

$$I\dot{\omega} + \dot{H}_{int} + \omega \times H = 0 \tag{8.6}$$

Assuming $\omega \times H$ will be compensated by reaction wheels, so the $\omega \times H$ is not required to be considered for the CMG steering algorithm design, then Eq. (8.6) can be simplified as

$$I\dot{\omega} + \dot{H}_{int} = 0 \tag{8.7}$$

Now a simple equation which represents relation between satellite angular acceleration vector and CMGs output torque vector N_{CMG} is given as

$$\dot{\omega} = I^{-1} N_{CMG} \tag{8.8}$$

Considering the above relationship between CMG torque vector and satellite body rate, gimbal steering algorithm is described hereafter based on gimbal parallel arrangement. The objective here is to find an optimal way to realize a required rest-to-rest maneuver minimizing axial coupling torque to the direction normal to CMGs maneuver axis.

For Astro-G, satellite +Z-axis is required to point at a target celestial body A and a quick maneuver to change the +Z-axis to another target B (= a calibration celestial body) is required by a rest-to-rest motion and attitude around Z-axis is allowed to be free because of ASTRO-G's one-dimensional radio observation.

As CMGs output torque plane is constrained within a 2-DOF plane in gimbal parallel arrangement, here Astro-G's CMGs output torque plane is constrained within satellite X-Y plane because CMG's gimbal axes are parallel to satellite Z-axis. Considering Eq. (8.8), satellite rotational motion is also constrained within an another

2-DOF plane as a mapping plane X'-Y' by Eq. (8.8). Eq. (8.8) is transformed to

$$X' - Y' : \quad \dot{\omega} = I^{-1} N_{CMG} \tag{8.9}$$

Astro-G's CMG gimbal steering algorithm is based on symmetrical gimbal driving algorithm that means CMG output torque keeps a time-invariant direction during a series of rest-to-rest maneuvers. And Eq. (8.9) indicates that if CMG output torque vector is decided in a certain time-invariant direction, satellite rotational axis is also determined in a certain time-invariant direction.

Thus, an optimal direction of time-invariant CMG output torque vector in which satellite can path the way from current +Z direction A to target +Z direction B according to Eq. (8.9) is introduced as follows.

Current +Z direction A and target +Z direction B are given as Fig. 8-8, then define blue broken line as it divides A and B symmetrically, green solid line as satellite rotational axis X'-Y' plane obtained by a mapping from CMG output torque X-Y plane by Eq. (8.9). This is how two intersection points of satellite rotational axis X'-Y' green solid line and blue broken line are given as α and α'. Line $\alpha - \alpha'$ is the only axis which realizes CMG attitude maneuver from current +Z direction A to target +Z direction B without generating axial coupling torque. The violet solid line is the shortest path between A and B (i.e. violet solid line is the maneuver path by the Euler-axis maneuver), however the obtained maneuver around the axis $\alpha - \alpha'$ is passing through black chain line that is longer path than the Euler-axis maneuver but there is no axial coupling.

Phase angle θ of CMG output torque which realizes $\alpha - \alpha'$ axis maneuver without axial coupling can be determined uniquely as follows.

Define g as a rotated direction of satellite +X direction by θ rotation around +Z-axis, then g direction unit vector r_{0g} is given as

$$r_{0g} = [\cos\theta \ \sin\theta \ \ 0]^T \tag{8.10}$$

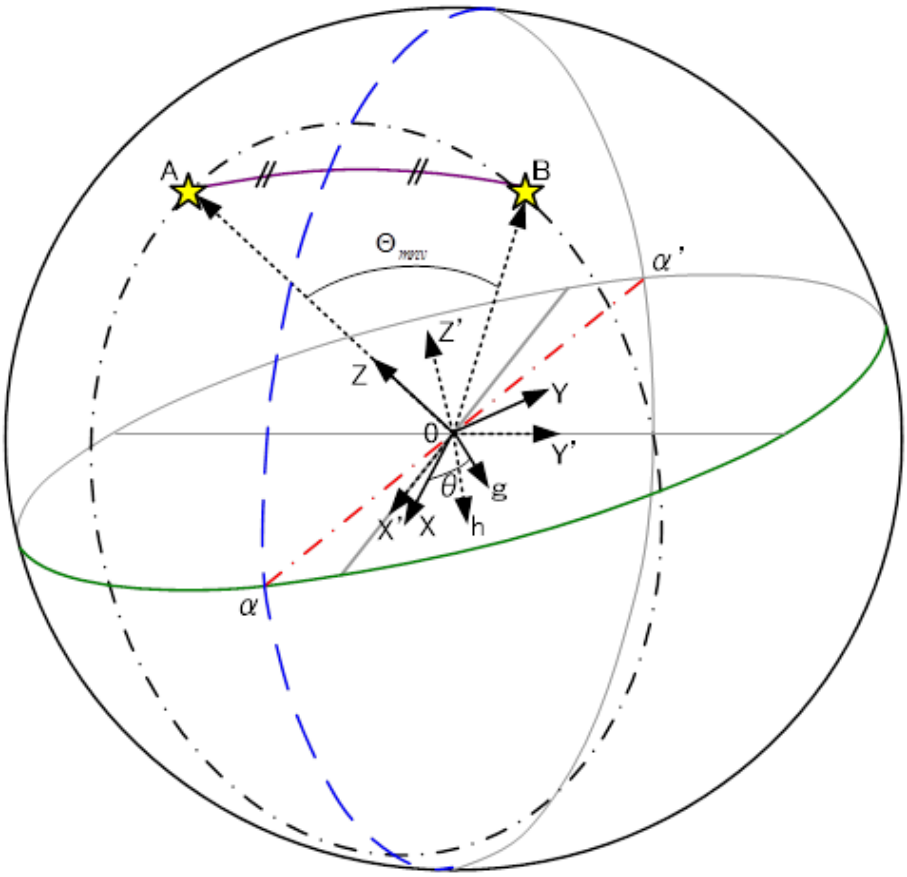

Figure 8-8: CMG Maneuver Surface

Define a vector r_{0h} as a mapped vector from r_{0g} by Eq. (8.9).

$$r_{0h} = I^{-1} r_{0g} \tag{8.11}$$

Define a satellite current +Z unit vector r_{0A} and target +Z unit vector r_{0B} as

$$\begin{aligned} r_{0A} &= [0\ 0\ 1]^T \\ r_{0B} &= R_y(\varphi) R_x(\phi) r_{0A} \\ &= \begin{bmatrix} \cos\varphi & 0 & \sin\varphi \\ 0 & 1 & 0 \\ -\sin\varphi & 0 & \cos\varphi \end{bmatrix} \begin{bmatrix} 1 & 0 & 0 \\ 0 & \cos\phi & -\sin\phi \\ 0 & \sin\phi & \cos\phi \end{bmatrix} \begin{bmatrix} 0 \\ 0 \\ 1 \end{bmatrix} \\ &= \begin{bmatrix} \cos\phi\sin\varphi & -\sin\phi & \cos\phi\cos\varphi \end{bmatrix}^T \end{aligned} \tag{8.12}$$

To align r_{0h} identical to line $\alpha - \alpha'$, length of line segment $|h - A|$ and $|h - B|$ need to be equal, then the following equation is obtained.

$$\begin{aligned} & |r_{hA}| = |r_{hB}| \\ \Leftrightarrow\ & |r_{0A} - r_{0h}| = |r_{0B} - r_{0h}| \end{aligned} \tag{8.13}$$

Substituting Eq. (8.11), (8.12) into Eq. (8.13), equation of θ is obtained. Thus CMG output torque angle θ is solved as

$$\theta = \tan^{-1}\left[\frac{num}{den}\right] \tag{8.14}$$

where

$$\begin{cases} num &= I_{xy}I_{yz} - I_{yy}I_{zx} + (-I_{xy}I_{zz} + I_{yz}I_{zx})\sin\phi \\ &\quad + \left((-I_{xy}I_{yz} + I_{yy}I_{zx})\cos\varphi + \left(I_{yz}^2 - I_{yy}I_{zz}\right)\sin\varphi\right)\cos\phi \\ den &= I_{xx}I_{yz} - I_{xy}I_{zx} + (-I_{xx}I_{zz} + I_{zx}^2)\sin\phi \\ &\quad + ((-I_{xx}I_{yz} + I_{xy}I_{zx})\cos\varphi + (-I_{xy}I_{zz} + I_{yz}I_{zx})\sin\varphi)\cos\phi \end{cases}$$

Then, the maneuver axis r_{0h} identical to $\alpha - \alpha'$ axis is given as follows

$$\begin{aligned} r_{0h} &= I^{-1} r_{0g} \\ &= \frac{1}{I_{xx}I_{yy}I_{zz}+2I_{xy}I_{yz}I_{zx}-I_{xx}I_{yz}^2-I_{yy}I_{zx}^2-I_{zz}I_{xy}^2} \begin{bmatrix} \left(I_{yy}I_{zz} - I_{yz}^2\right)\cos\theta + \left(I_{yz}I_{zx} - I_{xy}I_{zz}\right)\sin\theta \\ \left(I_{yz}I_{zx} - I_{xy}I_{zz}\right)\cos\theta + \left(I_{zz}I_{xx} - I_{zx}^2\right)\sin\theta \\ \left(I_{xy}I_{yz} - I_{yy}I_{zx}\right)\cos\theta + \left(I_{xy}I_{zx} - I_{xx}I_{yz}\right)\sin\theta \end{bmatrix} \end{aligned} \tag{8.15}$$

8.3.2 Preshaping Profiler for ASTRO-G

This section presents a maneuvering profiler of satellite body rotation around the single-axis given in previous section. This profiler is called NME (Nil-Mode-Exciting) profiler presented in Chapter 3.

It is possible to separate frequency characterictic of ACS (Attitude Control Subsystem) and flexible structures completely by means of sampling function. To separate frequency characteristic of controller and flexible structures, put the frequency of sampling function ω_s as

$$\omega_s < \omega_{flex}|_{\text{lowest mode}} \tag{8.16}$$

where right-hand term should be defined as the lowest flexible-mode frequency of the spacecraft.

Angular acceleration profile for back and forth rest-to-rest maneuvers is given as

$$\begin{aligned} f(t) &= A\ \{g_1\left(\text{sinc11} + \text{sinc12}\right) + g_2\left(\text{sinc21} + \text{sinc22}\right)\} \\ &= A\ \left\{ g_1(t)\left(\frac{\sin\left(\omega_s\left(t-t_{11}\right)\right)}{\omega_s\left(t-t_{11}\right)} - \frac{\sin\left(\omega_s\left(t-t_{12}\right)\right)}{\omega_s\left(t-t_{12}\right)}\right)\right. \\ &\quad \left. + g_2(t)\left(-\frac{\sin\left(\omega_s\left(t-t_{21}\right)\right)}{\omega_s\left(t-t_{21}\right)} + \frac{\sin\left(\omega_s\left(t-t_{22}\right)\right)}{\omega_s\left(t-t_{22}\right)}\right)\right\} \end{aligned} \tag{8.17}$$

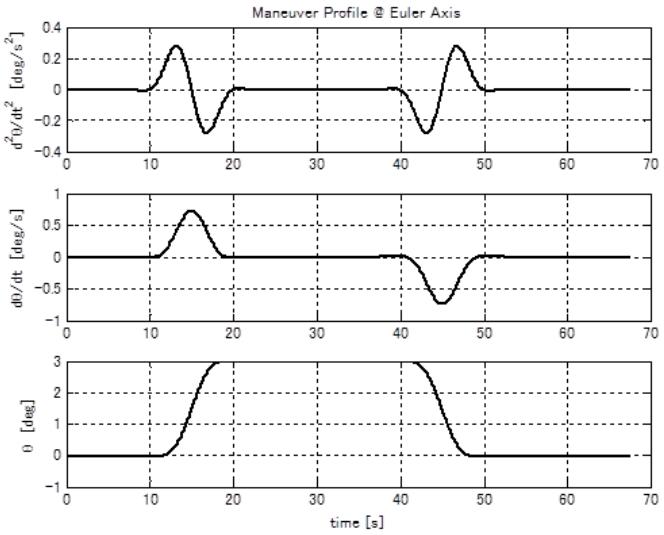

Figure 8-9: Satellite body-angular acceleration (upper), body-rate (middle), body-angle (lower) profiles of a rest-to-rest maneuver

where, the offset time t_{ij} and ω_s are expressed as

$$
\begin{aligned}
t_{11} &= \tfrac{1}{4} t_{mnv} \\
t_{12} &= \tfrac{3}{4} t_{mnv} \\
t_{21} &= t_{mnv} + t_{obs} + \tfrac{1}{4} t_{mnv} \\
t_{22} &= t_{mnv} + t_{obs} + \tfrac{3}{4} t_{mnv} \\
\omega_s &= \frac{2\pi}{\left(t_{mnv}/2 \right)}
\end{aligned}
$$

The window functions g_k are hamming window which is expressed as

$$
g_i(t) = \begin{cases} 0.54 + 0.46 \cos\left(\dfrac{2\pi}{t_{mnv}} \left(t - \dfrac{t_{i1} + t_{i2}}{2} \right) \right) & \text{for} \quad \text{abs}\left(t - \dfrac{t_{i1} + t_{i2}}{2} \right) \leq \dfrac{t_{mnv}}{2} \\ 0 & \text{for} \quad \text{abs}\left(t - \dfrac{t_{i1} + t_{i2}}{2} \right) > \dfrac{t_{mnv}}{2} \end{cases}
$$

$$
i = 1, 2 \tag{8.18}
$$

Figure 8-9 shows one cycle of a back and forth rest-to-rest maneuvering profile computed from Eq. (8.17).

8.3.3 CMGs Gimbal Steering Law in Parallel Gimbal Arrangement

In this section, CMGs gimbal guidance law in parallel gimbal arrangement with NME profiler is introduced. As described in the previous section, $f(t)$ is defined as a time-profile of scalar values of satellite angular acceleration around maneuver axis r_{0h}, satellite angular acceleration vector $\dot{\omega}$ is given as

$$\dot{\omega} = f(t) \cdot \frac{r_{0h}}{|r_{0h}|} \tag{8.19}$$

Combining Eq. (8.9), (8.11) into Eq. (8.19), a equation which shows the relation between NME profile $f(t)$ and CMG output torque vector N_{CMG} is given as

$$N_{CMG} \simeq \frac{f(t)}{|r_{0h}|} \cdot r_{0g} \tag{8.20}$$

Here, CMG total angular momentum vector H_{CMG} is given as

$$H_{CMG} \left(= \begin{bmatrix} H_x \\ H_y \\ H_z \end{bmatrix} \right) = \sum_i h_i(\delta_i) \tag{8.21}$$

Then, CMG output torque vector N_{CMG} is obtained by time derivative of $-H_{CMG}$ as follows

$$\begin{aligned} N_{CMG} &= -\frac{dH_{CMG}}{dt} = -\sum_i \frac{dh_i(\delta_i)}{d\delta_i}\dot{\delta}_i \\ &= -C\dot{\delta} \end{aligned} \tag{8.22}$$

From Eq. (8.22) gimbal angle rate is computed by Singularity Robust Inverse (SR-Inverse) [51] as

$$\dot{\delta} = -C^T \left(CC^T + \rho E\right)^{-1} N_{CMG} \tag{8.23}$$

Combining Eq. (8.20) and Eq. (8.23), we obtain

$$\dot{\delta} = -\frac{f(t)}{|r_{0h}|} \cdot C(t)^T \left(C(t)C(t)^T + \rho E\right)^{-1} r_{0g} \tag{8.24}$$

This is how gimbal angle profile which realizes desired satellite rotational motion profile $\dot{\omega} = f(t) \cdot \frac{r_{0h}}{|r_{0h}|}$ can be obtained, where,

$$\begin{aligned} f(t) = \quad & A \left\{ g_1(t) \left(\frac{\sin\left(\omega_s \left(t - t_{11}\right)\right)}{\omega_s \left(t - t_{11}\right)} - \frac{\sin\left(\omega_s \left(t - t_{12}\right)\right)}{\omega_s \left(t - t_{12}\right)} \right) \right. \\ & \left. + \; g_2(t) \left(-\frac{\sin\left(\omega_s \left(t - t_{21}\right)\right)}{\omega_s \left(t - t_{21}\right)} + \frac{\sin\left(\omega_s \left(t - t_{22}\right)\right)}{\omega_s \left(t - t_{22}\right)} \right) \right\} \\ & t = [\ 0 \text{ to } (2t_{mnv} + 2t_{obs})] \end{aligned} \tag{8.25}$$

where the constant A can be solved as follows. Relation between maneuver angle along the Euler-axis Θ_{mnv} and maneuver angle along the obtained maneuver axis (r_{0h}) Θ'_{mnv} is shown in Fig. 8-10.

$$A = \frac{\Theta'_{mnv}}{\int_0^{t_{mnv}} \int_0^{t_{mnv}} g_1(t) \left(\frac{\sin(\omega_s(t-t_{11}))}{\omega_s(t-t_{11})} - \frac{\sin(\omega_s(t-t_{12}))}{\omega_s(t-t_{12})} \right) dt^2} \tag{8.26}$$

$$\Theta'_{mnv} = \cos^{-1}\left(\frac{\cos\Theta_{mnv} - e_3^2}{1 - e_3^2} \right) \tag{8.27}$$

$$\frac{r_{0h}}{|r_{0h}|} = \begin{bmatrix} e_1 \\ e_2 \\ e_3 \end{bmatrix} \tag{8.28}$$

8.4 Flexible Parameters

ASTRO-G is equipped with three flexible structures: a large deployable flexible mesh antenna called LDR (Large Deployable Reflector), a solar array paddle called SAP, and a Ka-band antenna called KaANT, as shown in Figs. 8-11 and 8-11. Dimensional outline of ASTRO-G is shown in Fig. 8-13.

Table 8.1 shows flexible parameters of the LDR called coupling vector, i.e. translational and rotational modal masses of each flexible mode. Mode shapes of 1st, 2nd, and 3rd mode are shown in Figs. 8-14, 8-15, and 8-16 which correspond to 1st in-plane, 1st out-of-plane, and 1st torsional mode.

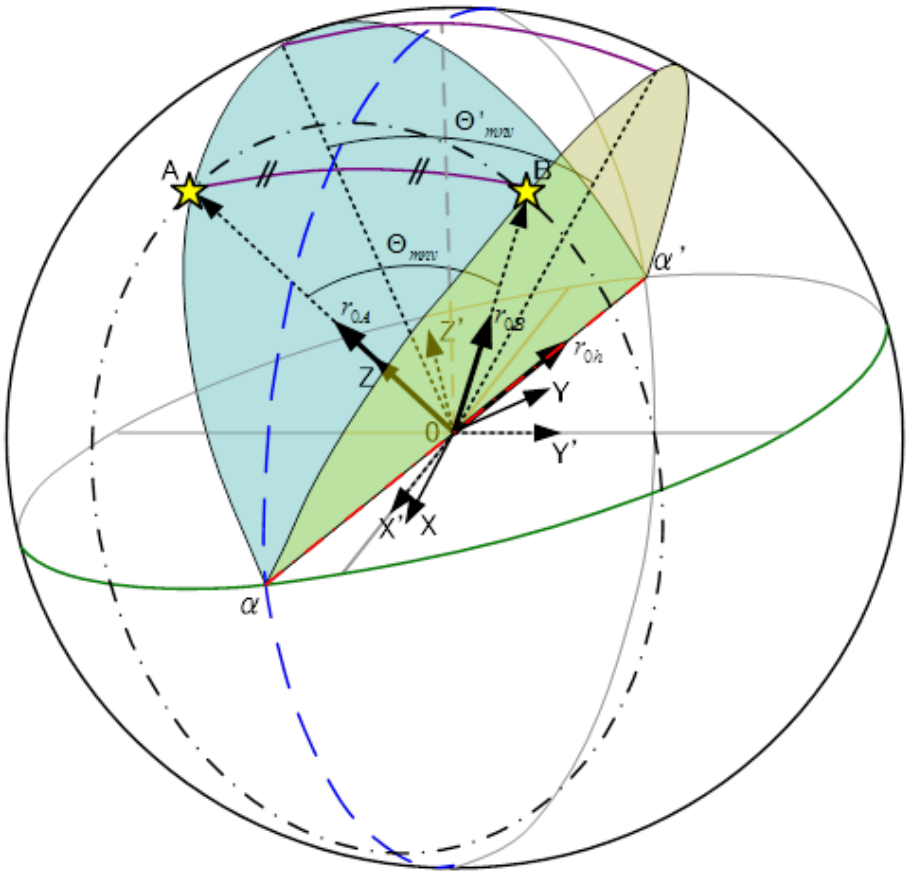

Figure 8-10: CMG Maneuver Surface

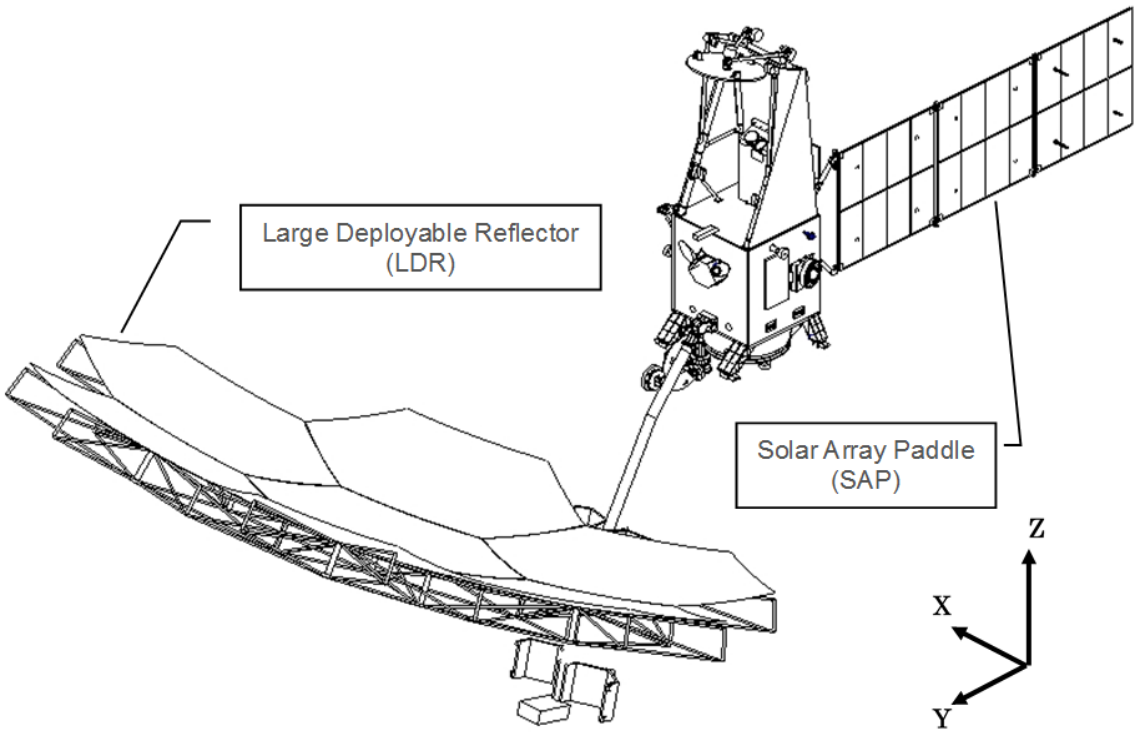

Figure 8-11: Outline of ASTRO-G and flexible structures (1/2)

Table 8.2 shows flexible parameters of the SAP. Mode shapes of 1st to 4th mode are shown in Fig. 8-17 which correspond to 1st out-of-plane, 1st in-plane, 2nd out-of-plane, and 1st torsional mode.

Table 8.3 shows flexible parameters of the KaANT. Mode shapes of 1st mode is shown in Fig. 8-18.

8.5 Numerical Simulation

In this section, an example of Astro-G rest-to-rest maneuver in numerical simulation is shown. Astro-G performs repeating back and forth rest-to-rest maneuvers in which a same couple of target celestial sources are pointed repeatedly. As shown Fig. 8-6, on-orbit test maneuver is conducted first before observation maneuver for the purpose of model identification. The effectiveness of feedforward algorithm introduced in the previous section has been verified by numerical simulations.

Open-loop dynamics simulations using proposed algorithm are performed for 2.82

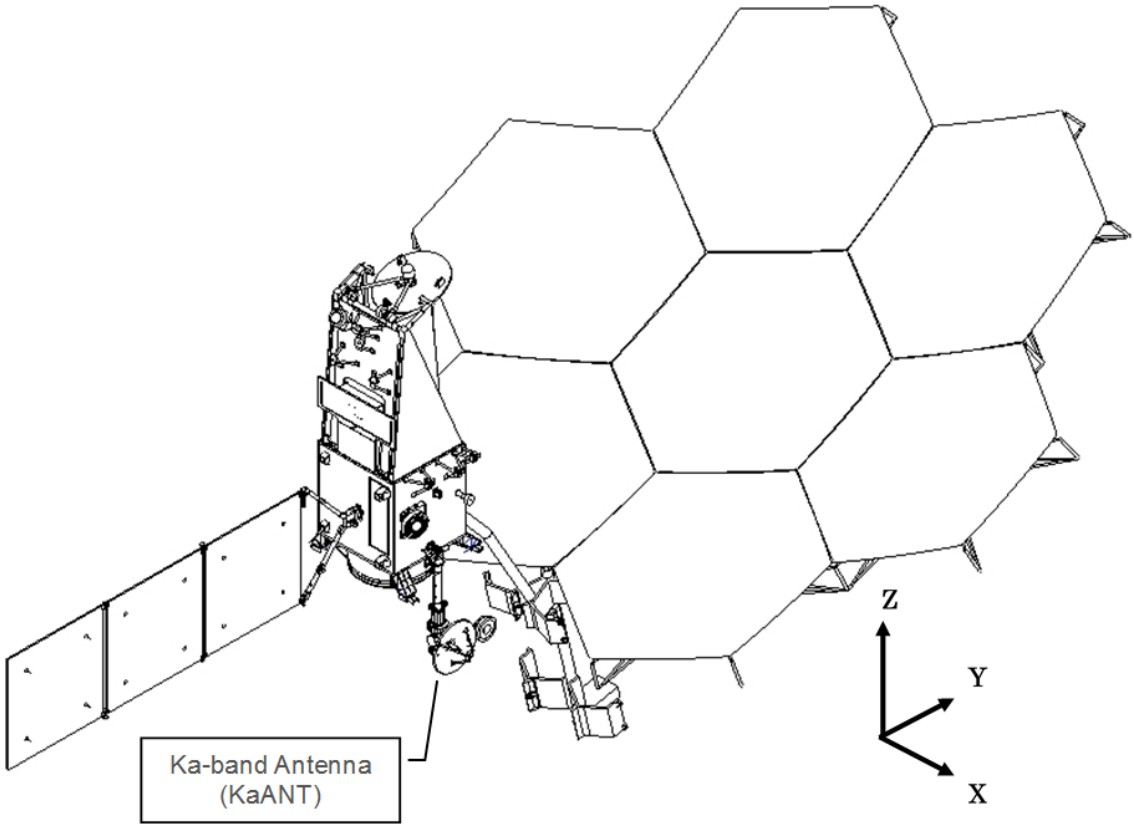

Figure 8-12: Outline of ASTRO-G and flexible structures (2/2)

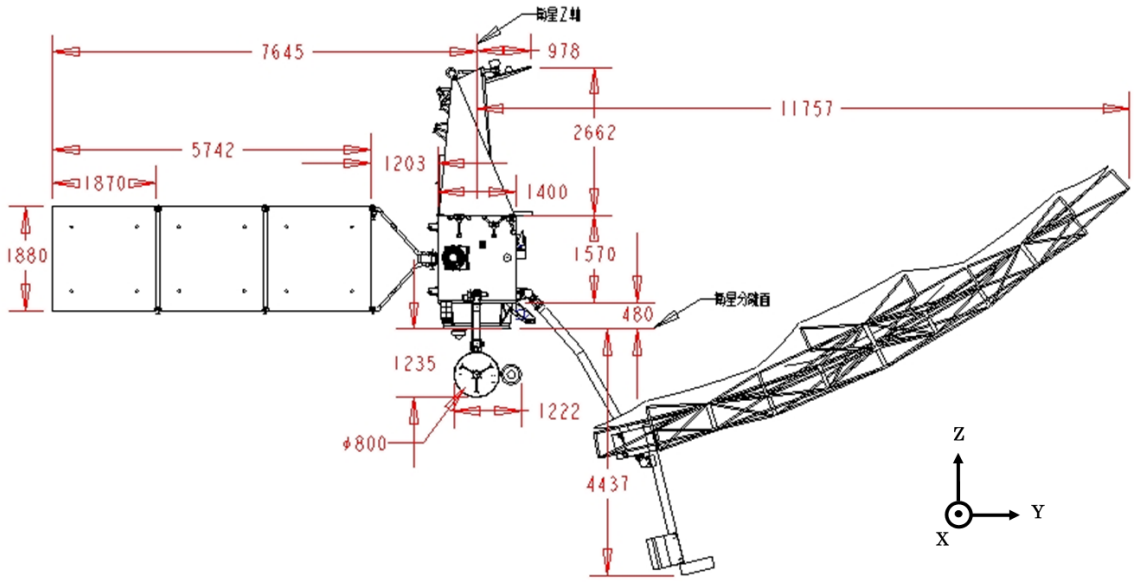

Figure 8-13: Dimensional outline of ASTRO-G

Table 8.1: Flexible parameters of LDR

No.	Mode No.	Frequency f(Hz)	Coupling Vector					
			Xt (√Kg)	Yt (√Kg)	Zt (√Kg)	Xr (√Kg・m)	Yr (√Kg・m)	Zr (√Kg・m)
1	1	2.73E-01	-8.24E+00	3.65E-03	4.95E-03	4.63E-02	-1.51E+00	6.94E+01
2	2	3.48E-01	-5.52E-03	-8.20E-01	-9.51E+00	-7.27E+01	-7.03E-03	3.31E-02
3	3	8.35E-01	-6.79E+00	-1.42E-01	-6.68E-02	-4.04E-01	4.20E+01	2.17E+01
4	4	9.07E-01	1.12E-01	-1.12E+01	-4.55E+00	-2.77E+01	-5.74E-01	-3.24E-01
5	5	1.75E+00	-8.28E+00	-5.20E-02	-6.25E-03	-5.05E-02	1.14E+01	1.25E+01
6	6	3.04E+00	2.90E-02	-5.50E+00	2.23E+00	-1.53E+00	-2.12E-02	-3.00E-02
7	7	3.66E+00	2.34E+00	2.30E-02	-3.32E-02	-1.10E-02	-9.75E-01	-2.90E+00
8	10	7.94E+00	4.33E-03	2.23E+00	-3.69E+00	-7.88E-01	3.37E-03	-8.50E-03
9	15	1.17E+01	-1.40E-02	-1.11E+00	2.90E+00	9.81E-01	8.10E-03	8.99E-03
10	19	1.37E+01	5.27E-02	2.12E+00	-3.20E+00	-6.98E-01	-2.92E-02	-3.75E-02
11	20	1.38E+01	1.05E-01	-1.19E+00	1.77E+00	3.79E-01	-3.40E-02	-1.05E-01
12	36	1.67E+01	-9.44E-03	1.19E+00	-1.80E+00	-3.93E-01	3.53E-03	6.35E-03
13	53	1.79E+01	2.73E-02	1.41E+00	-2.27E+00	-5.19E-01	-1.22E-02	-1.32E-02
14	55	1.81E+01	-4.55E-02	-1.01E+00	1.60E+00	3.63E-01	2.10E-02	2.04E-02
15	57	1.83E+01	2.14E-02	-1.13E+00	1.72E+00	3.76E-01	-1.38E-02	-2.27E-03

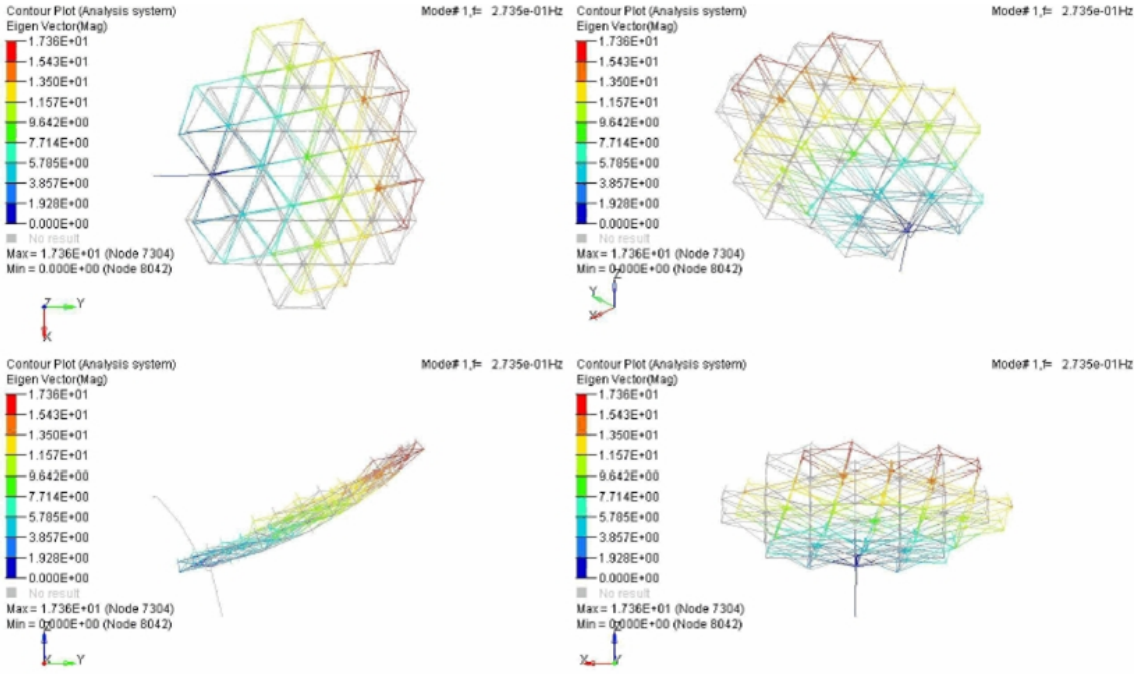

Figure 8-14: Mode shape of LDR (0.273Hz, 1st mode: in-plane 1st)

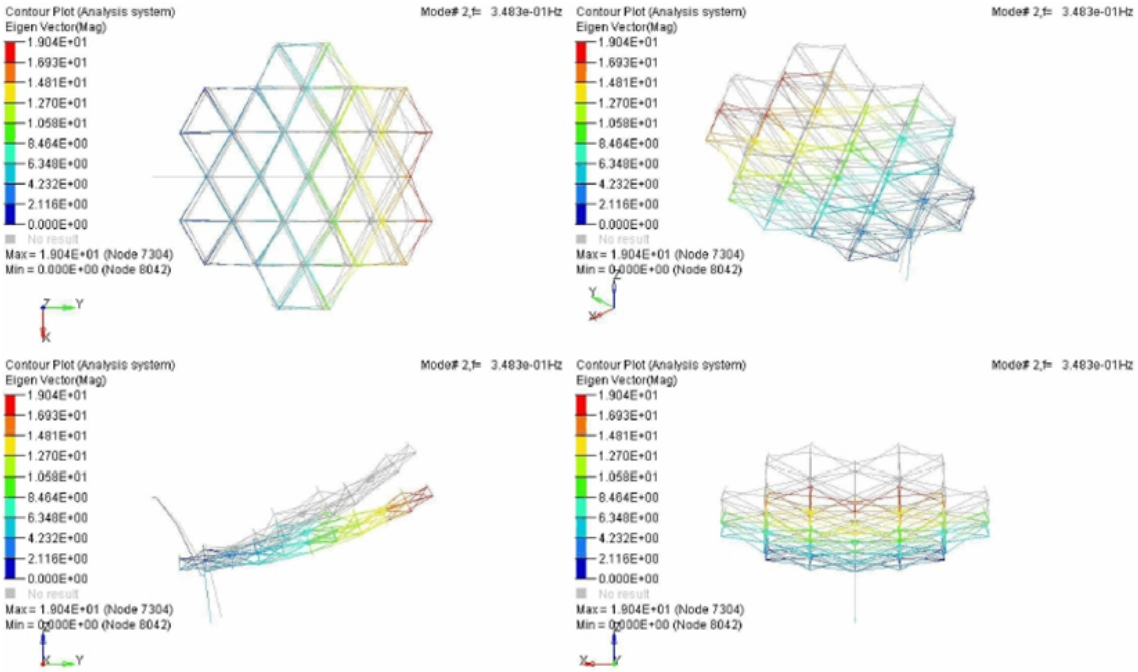

Figure 8-15: Mode shape of LDR (0.348Hz, 2nd mode: out-of-plane 1st)

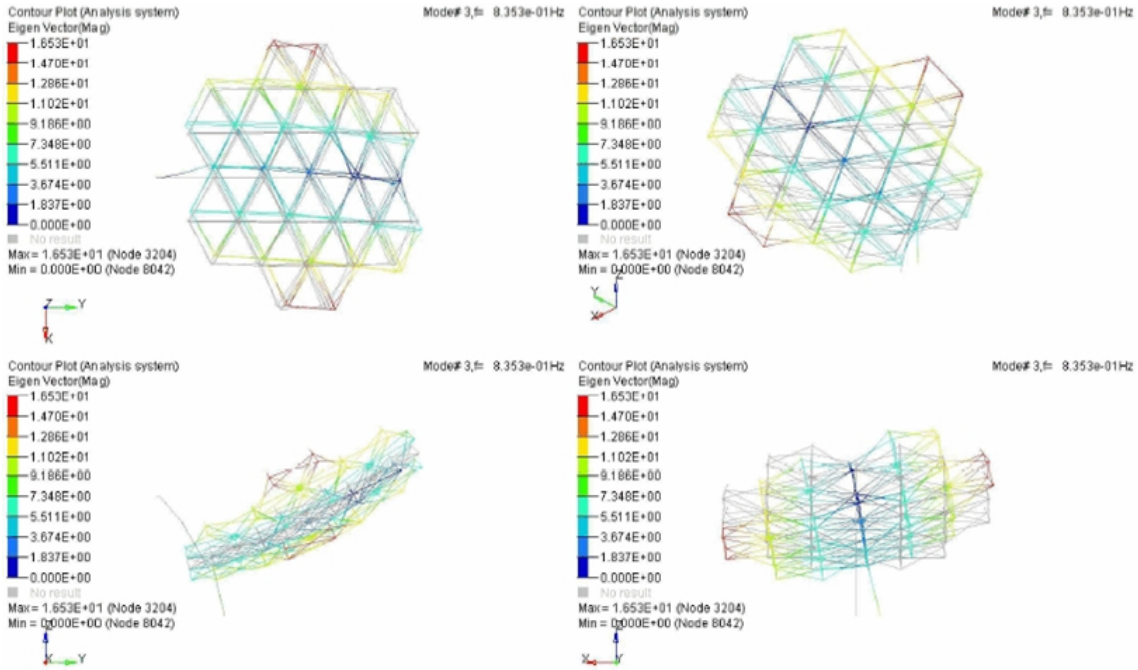

Figure 8-16: Mode shape of LDR (0.835Hz, 3rd mode: torsional 1st)

Table 8.2: Flexible parameters of SAP. The masses larger than 1% are highlighted by yellow.

Mode No. i	Mode description	Frequency fi(Hz)	0th coupling vector ($\sqrt{}$kg)			1st coupling vector ($\sqrt{}$kg・m)		
			δ 0xi	δ 0yi	δ 0zi	δ 1xi	δ 1yi	δ 1zi
1	1st out-of-plane	0.270	6.061	-0.008	0.000	0.000	-0.016	30.107
2	1st in-plane	0.797	0.000	0.021	6.557	-30.790	-0.079	0.000
3	2nd out-of-plane	1.656	-3.422	-0.011	0.000	-0.001	-0.001	-4.349
4	1st torsional	2.552	0.027	0.001	0.007	-0.063	4.059	0.023
5	3rd out-of-plane	4.534	2.054	0.167	0.000	0.003	0.003	1.400
6	2nd torsional	7.177	0.190	0.113	-0.031	0.010	1.708	0.091
7		7.609	1.705	1.150	0.040	0.013	-0.164	0.815
8		11.619	-0.004	-0.323	-0.235	0.031	0.765	-0.005
9		13.544	-0.258	6.272	0.958	0.087	0.035	-0.043
10		16.906	0.006	0.454	-0.210	0.027	0.187	0.003
11		18.923	-0.524	0.334	0.165	0.008	0.017	-0.118
12		26.744	-0.452	-0.069	0.083	0.001	0.004	-0.077
13		29.907	0.013	-0.122	0.202	-0.013	-0.092	0.002
14		34.756	0.154	0.087	-0.050	0.000	-0.004	0.021
15		37.867	-0.220	-0.192	0.150	-0.001	0.004	-0.029
16		39.570	-0.039	0.655	-0.555	0.004	-0.068	-0.004
17		40.363	-0.144	-0.340	0.323	-0.002	0.001	-0.020
18		44.481	-0.162	0.688	-0.712	0.008	-0.007	-0.017
19		45.474	-0.153	2.448	-2.389	0.030	-0.021	-0.017
20		48.345	0.176	-0.449	0.504	-0.008	0.004	0.020
		Sum square	56.332	48.405	50.999	948.065	20.059	928.006

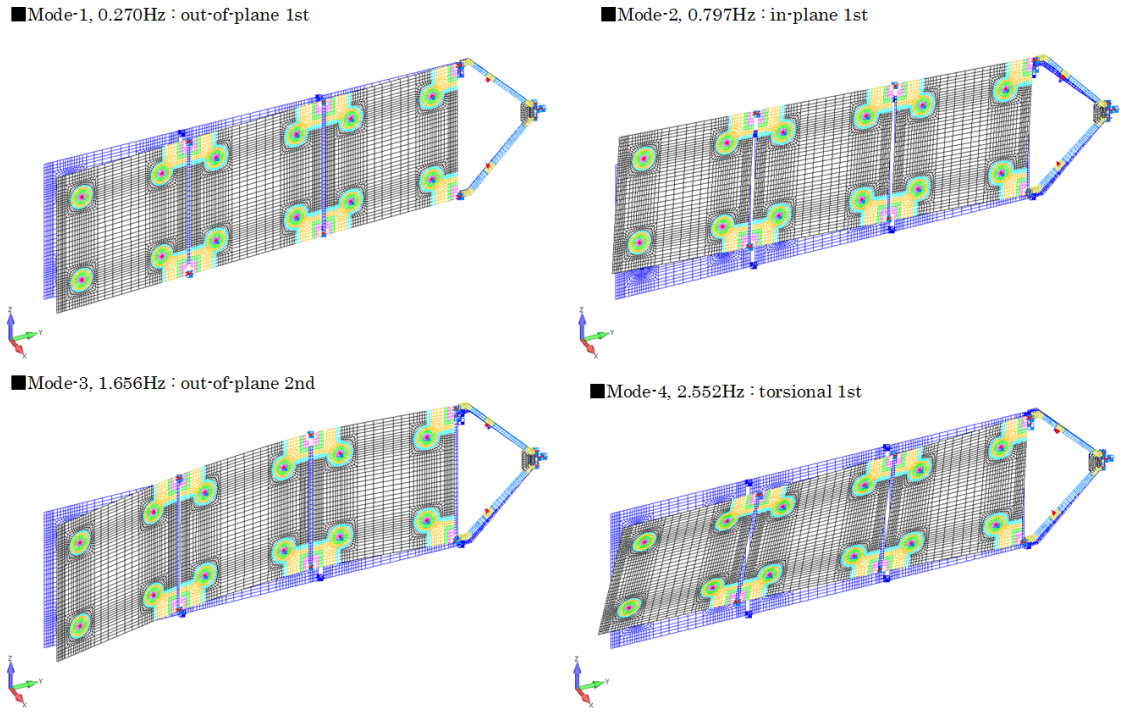

Figure 8-17: Mode shapes of SAP (1st to 4th mode)

Table 8.3: Flexible parameters of KaANT. The masses larger than 10% are highlighted by yellow.

Mode No.	Frequency [Hz]	Translational [√(kg)] Effective mass [%]			Rotational [√(kg·m^2)] Effective mass [%]		
		TX	TY	TZ	RX	RY	RZ
1	4.28	0.31	5.40	0.09	8.44	−0.54	1.97
		0.21	65.33	0.02	90.85	0.35	74.88
2	4.37	−5.27	0.33	−0.97	0.50	8.86	0.15
		62.26	0.24	2.10	0.32	94.39	0.44
3	8.45	−0.01	1.76	−0.02	2.28	0.03	−0.97
		0.00	6.96	0.00	6.63	0.00	18.09
4	11.39	−2.73	−0.08	1.77	−0.06	1.88	−0.02
		16.66	0.01	7.00	0.00	4.26	0.01
5	15.88	0.07	−1.74	−0.03	−1.28	−0.04	−0.38
		0.01	6.75	0.00	2.09	0.00	2.73
6	45.42	−0.41	0.02	−1.40	0.01	0.37	0.01
		0.38	0.00	4.36	0.00	0.17	0.00
7	51.16	0.06	−0.04	0.08	−0.01	−0.03	0.03
		0.01	0.00	0.02	0.00	0.00	0.02
8	61.41	−0.21	−0.61	0.81	−0.18	−0.05	−0.07
		0.09	0.82	1.47	0.04	0.00	0.10
9	62.73	−0.46	0.24	2.38	0.07	−0.20	0.04
		0.47	0.13	12.73	0.01	0.05	0.04
10	84.40	0.02	−0.04	1.65	−0.01	−0.24	−0.01
		0.00	0.00	6.07	0.00	0.07	0.00
11	85.33	0.04	0.03	2.76	0.01	−0.41	0.00
		0.00	0.00	17.10	0.00	0.20	0.00
12	89.05	−0.04	−0.12	−0.50	−0.03	0.08	−0.02
		0.00	0.03	0.56	0.00	0.01	0.01
13	97.17	0.14	−0.05	3.24	−0.01	−0.50	−0.02
		0.04	0.01	23.52	0.00	0.30	0.01

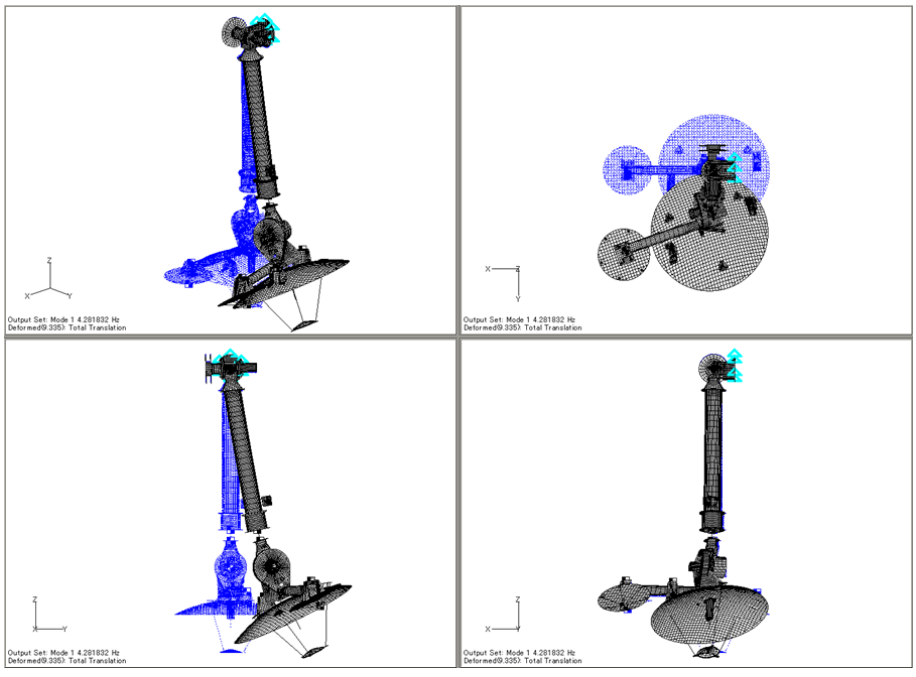

Figure 8-18: Mode shapes of KaANT (4.28Hz, 1st mode)

Table 8.4: Conditions for numerical simulation of repeating rest-to-rest maneuvers

items	conditions
maneuver angle	3 [deg]
maneuver time	15 [s]
observation time	15 [s]
CMG rotor momentum	60 [Nms]
frequency of gimbal controller	30 [Hz]
RW max. torque	FF: 0.5 [Nm], FB: 0.5 [Nm]
RW delay time	200 [ms]
RW FB crossover	0.01 [Hz]

deg per 15 s rest-to-rest maneuvers in which target +Z direction is X/Y 45 deg direction (different from the axis of principle axes of inertia). Open-loop dynamics simulation results are shown in Fig. 8-19. In this case, satellite performs forth maneuver from 0 to 15 s, then performs observation from 15 to 30 s, then performs backward maneuver from 30 to 45 s, then performs observation from 45 to 60 s. As shown in Fig. 8-19, residual vibrations at the end of each maneuver (15 s and 45 s) are reduced to be acceptable small level. If we apply maximum acceleration and maximum deceleration torque to maximize maneuver agility without considering flexible modes excitation [52], longer time to start observation is required until excited flexible-modes will be settle down. Table 8.4 shows the conditions for numerical simulation of repeating rest-to-rest maneuvers. Top of Fig. 8-20 shows the body angle errors of repeating maneuvers. Middle of Fig. 8-20 shows the body rate errors of repeating maneuvers. Bottom of Fig. 8-20 shows the antenna gain-losses which represent the degradation of antenna gain and are calculated as the function of body angle errors and flexible-modes displacements. Each errors are verified within acceptable level. The effectiveness of proposed feedforward algorithm was verified by open-loop dynamics simulations.

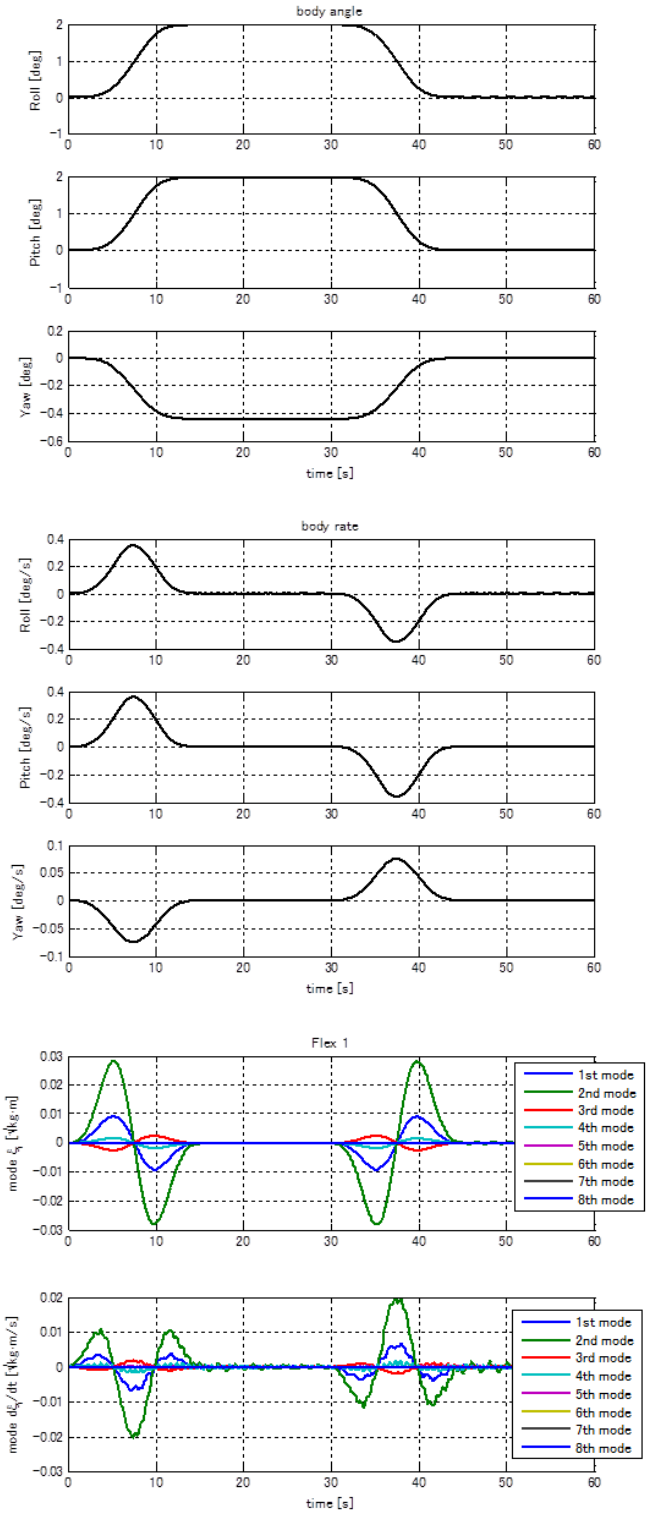

Figure 8-19: Dynamics simulation of rest-to-rest maneuver, top: body angle, middle: body rate, bottom: modal displacement and modal rate

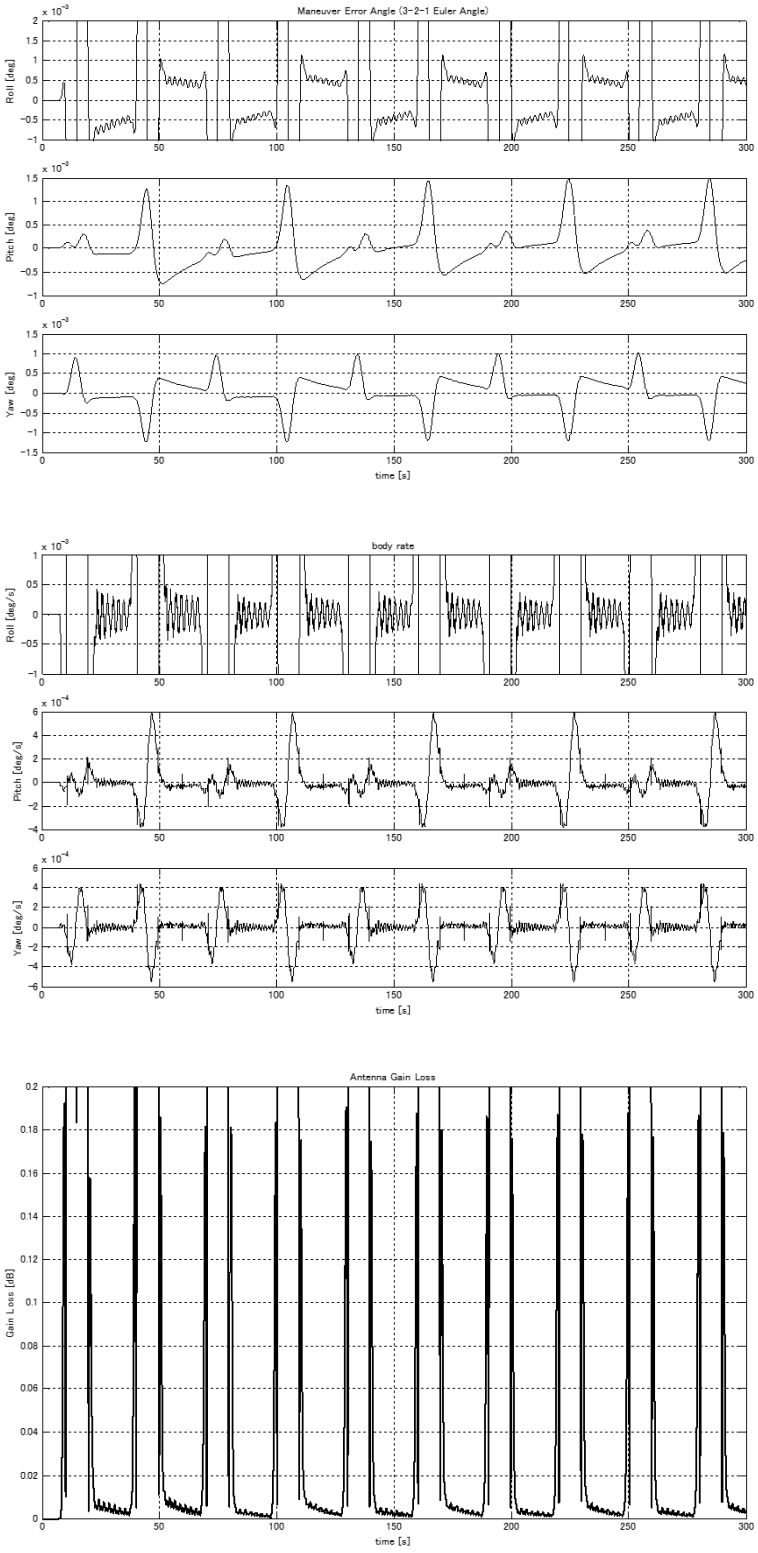

Figure 8-20: Dynamics simulation of repeating rest-to-rest maneuver, top: body angle error, middle: body rate error, bottom: antenna gain loss

8.6 Discussion on ASTRO-G Application

An optimal approach for computing feedforward control inputs for flexible spacecraft 2-DOF rest-to-rest maneuvers with CMG cluster in parallel gimbal arrangement has been investigated based on the proposed profiler approach. The result of numerical simulation has shown the effectiveness of the proposed algorithm. The residual vibration is reduced to be negligible small level as ideal frequency separation has been realized between flexible-modes and feedforward controller. An algorithm in which axial coupling can be avoided has been introduced.

An experimental verification of the NME profiler had been also successfully done with a simplified flexible structure model by Nakamura [49, 50] which is introduced in Appendix D. Effectiveness of the proposed NME profiler for ASTRO-G application has been successfully verified by the combination of the referred tests and numerical simulations. Summary of CMG dynamics characterization test is presented in Appendix E for reference.

Chapter 9

Conclusions and Future Work

9.1 Conclusions

In Chapter 4, comparisons of sinc function-based smooth profilers to conventional input shapers and digital filtering techniques against single-mode system demonstrates that conventionally designed input shapers and frequency domain filters are less effective for command shaping than sinc function-based smooth profilers. The original sinc function-based smooth profiler, i.e. the NME profiler, were shown to offer performance advantage in terms of vibration reduction although rise time is less shorter than conventional input shapers although the ZVDDDDDD shaper shows the smallest residual vibration and the NME shows the second smallest vibration. When large modeling errors exist, the advantage of the sinc function-based smooth profiler is very significant. These performance advantages are achieved because the sinc function-based smooth profiler is designed to eliminate high frequency vibrations with higher attenuation level and have better robustness to modeling errors, compared to conventional input shapers and low-pass filters.

In Chapter 5, performance of the sinc function-based smooth profiler has been compared to those of conventional on-off and smooth profilers using two-mode system including unknown high mode. The comparisons show that, in the presence of an unknown high-order flexible mode, conventionally designed on-off input shapers and smooth profilers are less effective in reducing vibrations than the smooth profiler

based on sinc functions, even when identical durations are used. Only the smoothed bang-bang command shaped with ZVD shaper, i.e., hybrid-type profiler, shows similar level of small residual vibrations comparable with the smooth profiler based on sinc functions. When unknown high-order flexible modes with large mass exist, the advantage of the new smooth profiler is significant (more than an order of magnitude smaller residual vibration). These performance advantages are achieved because, as compared to conventional profilers, the new smooth profiler is specifically designed to eliminate high-frequency vibrations with higher levels of attenuation.

In Chapter 7, three kinds of improved sinc function-based profilers are proposed and evaluated for achieving higher agility. In Section 7.2, the conventional concept of convolution between smooth profiler and input shaper has been introduced and an equation to clarify a range where the convolved shaper has advantage in relation to command duration has been proposed. In Section 7.3, a new sinc function-based smooth profiler to achieve higher agility: the sinc function convolved with step function has been proposed. Performances of the new profiler have been compared with those of the original sinc function-based profiler and conventional smooth/hybrid profilers. The sinc function convolved with step increased maneuver distance by a factor of 1.33 with comparable residual vibration under the same peak force condition, compared with the previously proposed sinc function-based profiler (NME profiler). This profiler shows nearly equivalent maneuver distance but smaller residual vibration, compared with the conventional smooth profiler. In Section 7.4, another new sinc function-based smooth profiler to achieve higher agility: the least-square fitted weighted sinc functions has been proposed. Performances of the new profiler have been compared with those of the sinc function-based profilers mentioned in this thesis and conventional smooth/hybrid profilers. The sinc function-based least-square fitted profiler increased maneuver distance by a factor of 2.28 under the same peak force condition, compared with the NME profiler. This profiler shows the longest maneuver distance and comparable or smaller residual vibration, compared with the ramped sinusoids or hybrid profilers. Both of the newly proposed sinc function-based profilers can be used as effective alternatives for appropriate applications; if there

are many unknown high-order flexible modes, the sinc function convolved with step would be suitable, if there are fewer critical high-order modes, the least-square fitted profiler would be suitable.

In Chapter 8, application of the proposed method to actual satellite program called ASTRO-G for which the NME profiler has been originally developed is presented. The effectiveness of the proposed method is confirmed by numerical simulation using actual designed flexible parameters of deployable antenna and solar array paddle. Experimental verifications to evaluate the effectiveness of the proposed algorithm is also referred in Appendix D. Effectiveness of the proposed NME profiler for ASTRO-G application has been successfully verified.

Thus, the sinc function-based profilers have been evaluated and performances of agility, i.e. maneuver distance, and residual vibration have been measured as shown in Table 9.1, where the criteria are given as follows,

	Agility	Vibration
A :	> 30	$< 0.1\%$
B :	10 to 30	0.1 to 1.0%
C :	< 10	$> 1.0\%$

Table 9.1: Comparison of sinc function-based profilers and conventional profilers

Profiler	Agility	Vibration	Feature
ZVDDDDDD shaper	C-	C-	Conventional
Ramped Sinusoidal	A-	C	Conventional
Hybrid-type	B	B	Conventional
NME profiler	B	A	Chapter 3
Sinc convolved with input shaper	B	B	Section 7.2
Sinc convolved with step	B+	A	Section 7.3
Sinc with harmonics	A	C	Section 7.4

9.2 Future Work

Several additional studies are motivated by this work.

First, a feedback controller around a reference trajectory generated by a feedforward controller is being studied. Combining feedforward and feedback controllers, a robust control system will be established.

Second, as mentioned in Section 6.5, more effective profiler for higher agility and low-residual vibration might be found by determining a level and a slope of an allowable input force spectrum for a pointing accuracy requirement. Concept of this idea is introduced as follows:

Equations of motion of a multi-mode system are given as,

$$\begin{cases} I\ddot{\theta} + \sum_i C_i\ddot{\eta}_i = T \\ \ddot{\eta}_i + 2\zeta_i\omega_i\dot{\eta}_i + \omega_i^2\eta_i + C_i\ddot{\theta} = 0 \\ (i = 1, 2, \cdots) \end{cases} \tag{9.1}$$

(constrained mode model)

Block diagram of this equations are shown in Fig 9-1. Then, transfer function of torque to angle is given as,

$$\frac{\Theta(s)}{T(s)} = \frac{1}{Is^2}\left\{\frac{1}{1 - \frac{1}{I}\sum_i \frac{C_i s^2}{s^2 + 2\zeta_i\omega_i s + \omega_i^2}}\right\} \tag{9.2}$$

Gain of the transfer function is shown in Fig. 9-2. Thus, the effective masses for a two-mode system, for example, are given as,

$$\begin{cases} m_1 + m_2 + m_3 & \text{for} \quad \omega < \omega_L \\ m_1 + m_3 & \text{for} \quad \omega_L < \omega < \omega_H \\ m_1 & \text{for} \quad \omega_H < \omega \end{cases} \tag{9.3}$$

Generalized requirement for pointing stability is given as "Body angle variation at every T [s] shall be within $\Delta\theta$." Assuming a single frequency vibration of a rigid body, the allowable angular amplitude and the resulting allowable input torque amplitude are given in frequency domain as shown in Fig. 9-3 and 9-4 respectively [53]. The allowable input torque for a generalized pointing stability requirement can be approximated as,

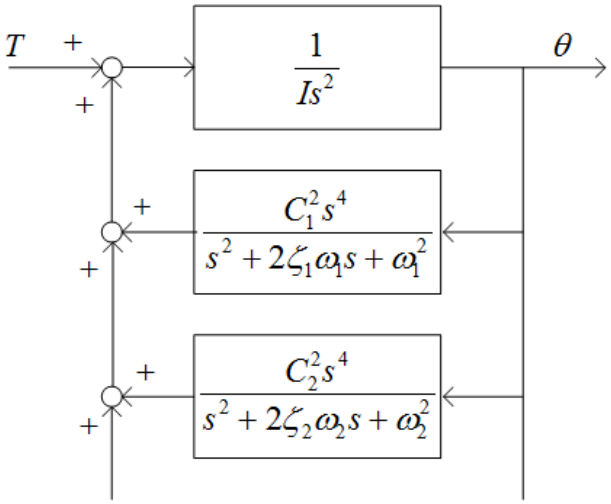

Figure 9-1: Constrained mode model

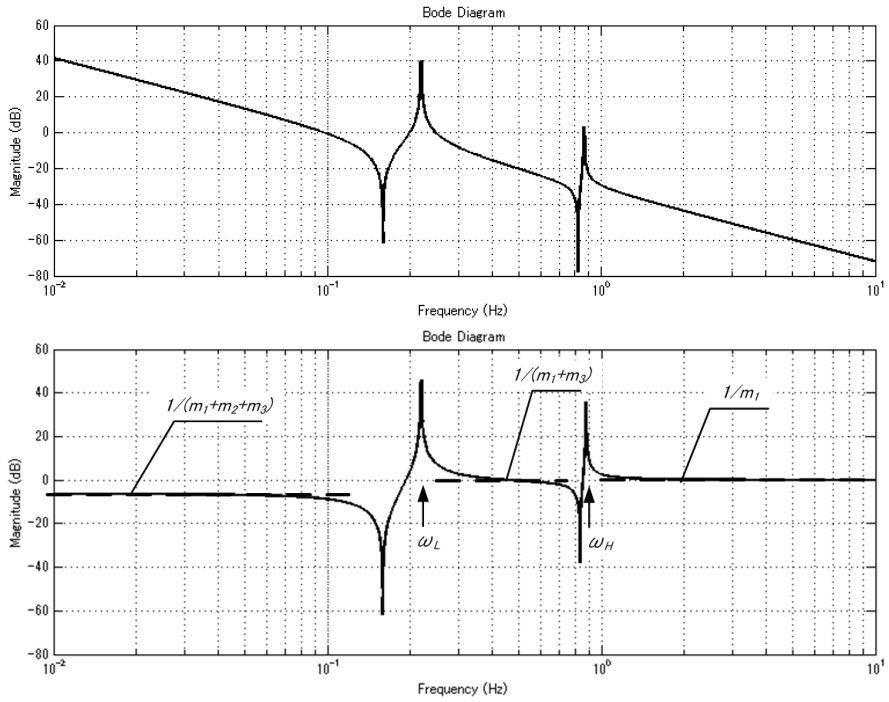

Figure 9-2: Gain of input torque to angle (top) and angular acceleration (bottom) (two-mode system: $m_1 = m_2 = k_1 = 1, m_3 = 0.1, k_2 = 2.76$)

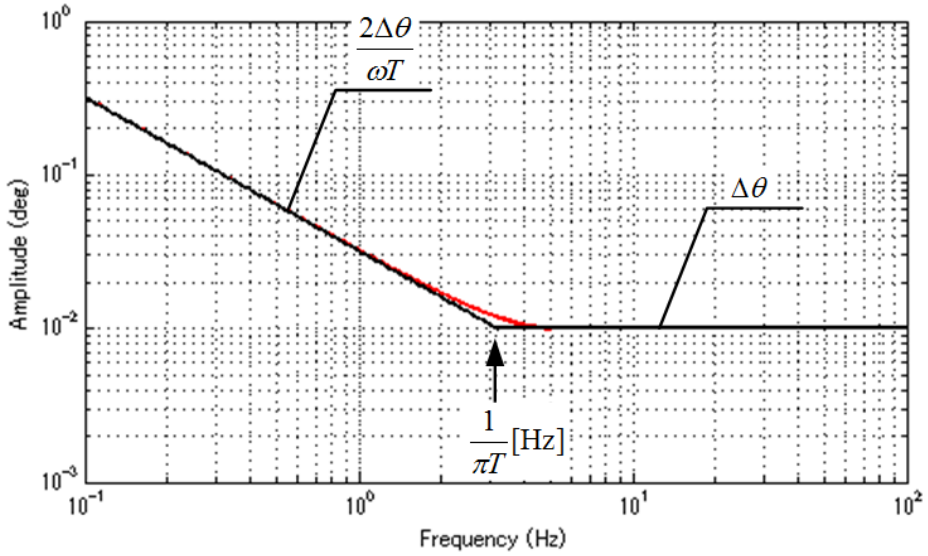

Figure 9-3: Allowable angle spectrum (red: exact, black: approximation) at $\Delta\theta$=0.01 deg (0-p), T=0.1 s

$$\max|\tau| \leq \begin{cases} \dfrac{2I\Delta\theta}{QT}\omega & \text{for} \quad \omega < \dfrac{2}{T} \\ \dfrac{I\Delta\theta}{Q}\omega^2 & \text{for} \quad \dfrac{2}{T} \leq \omega \end{cases} \tag{9.4}$$

where, Q is resonance magnification, and $\Delta\theta$ is given as 0-to-peak.

Going back to the concept for higher agility, the level and the slope of the allowable force at the frequency higher than the known low-mode frequency is given in frequency domain from a required pointing stability accuracy as shown in Fig. 9-5. The allowable input torque for the generalized pointing stability requirement can be approximated as,

$$\text{AllowableForce} = \begin{cases} \dfrac{2I\Delta\theta}{QT}\omega & (+20\text{dB/dec}) \quad \text{for} \quad \omega_L < \omega < \dfrac{2}{T} \\ \dfrac{I\Delta\theta}{Q}\omega^2 & (+40\text{dB/dec}) \quad \text{for} \quad \dfrac{2}{T} \leq \omega \end{cases} \tag{9.5}$$

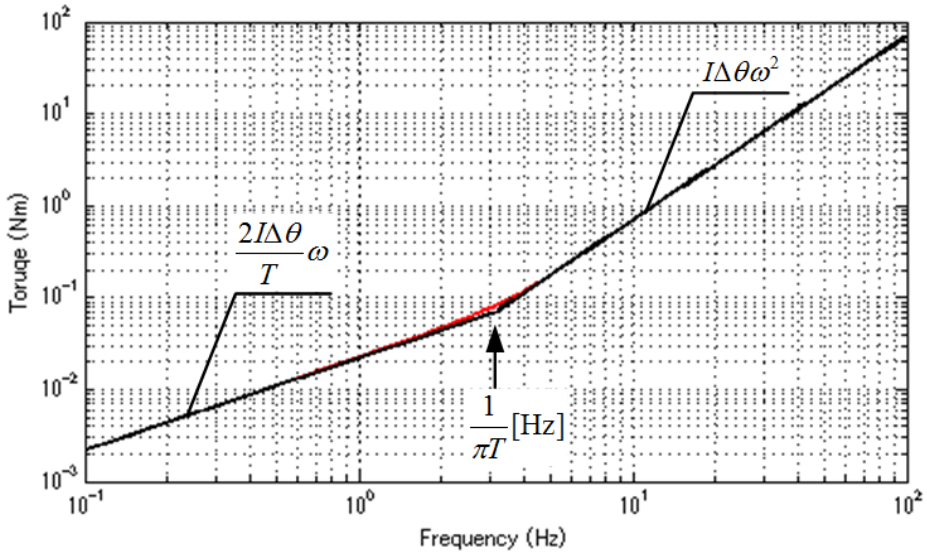

Figure 9-4: Allowable torque spectrum (red: exact, black: approximation) at $\Delta\theta$=0.01 deg (0-p), T=0.1 s

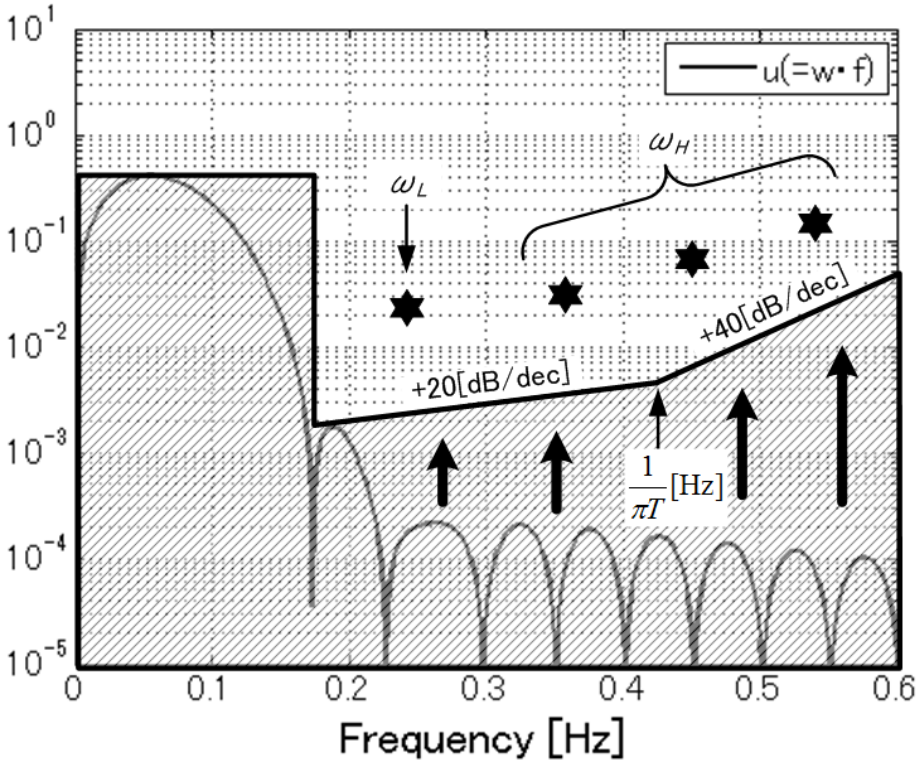

Figure 9-5: Concept for high agility

THIS PAGE INTENTIONALLY LEFT BLANK

Appendix A

Formulations of Conventional Input Shapers

Each section of this Appendix shows the formulation of each conventional method which is discussed in this thesis.

A.1 ZV shaper

The earliest appearance of an input shaper which meets the constraints of the zero vibration (ZV) shaper was in the method of posicast control developed by O. J. M. Smith in the late 1950s [20, 21]. Singer and Seering proposed an input shaper which was derived from constraint equations [22]. Generalized impulse response with amplitude A_j is given by

$$y_j(t) = A_j \frac{\omega}{\sqrt{1-\zeta^2}} e^{-\zeta\omega(t-t_j)} \sin\left(\omega\sqrt{1-\zeta^2}\,(t-t_j)\right) \tag{A.1}$$

where ω is the undamped natural frequency of the plant, ζ is the damping ratio of the plant, t is time, and t_j are the times at which the j-th impulses occur. Using the trigonometric relation, multi-impulse responses are superposed as

$$
\begin{aligned}
&y_1(t) + y_2(t) + y_3(t) + \cdots + y_N(t) \\
&= B_1 \sin(\alpha t + \phi_1) + B_2 \sin(\alpha t + \phi_2) + B_3 \sin(\alpha t + \phi_3) + \cdots + B_N \sin(\alpha t + \phi_N) \\
&= A_{amp} \sin(\alpha t + \psi)
\end{aligned}
\tag{A.2}
$$

where

$$
\begin{aligned}
B_j &= A_j \frac{\omega}{\sqrt{1-\zeta^2}} e^{-\zeta\omega(t-t_j)} \\
\alpha &= \omega\sqrt{1-\zeta^2} \\
\phi_j &= -\omega\sqrt{1-\zeta^2} t_j \\
\psi &= \tan^{-1}\left(\frac{\sum_{j=1}^{N} B_j \sin\phi_j}{\sum_{j=1}^{N} B_j \cos\phi_j}\right)
\end{aligned}
$$

The amplitude of vibration for a multi-impulse input is given by

$$
A_{amp} = \sqrt{\left(\sum_{j=1}^{N} B_j \cos\phi_j\right)^2 + \left(\sum_{j=1}^{N} B_j \sin\phi_j\right)^2} \tag{A.3}
$$

Elimination of vibration after the input has ended requires that the expression for A_{amp} equals to zero at the time of the input ends, t_N. This is true if both squared terms in (A.3) are independently zero, yielding

$$
\begin{aligned}
&\sum_{j=1}^{N} A_j e^{-\zeta\omega(t_N - t_j)} \sin\left(\omega\sqrt{1-\zeta^2} t_j\right) = 0 \\
&\sum_{j=1}^{N} A_j e^{-\zeta\omega(t_N - t_j)} \cos\left(\omega\sqrt{1-\zeta^2} t_j\right) = 0
\end{aligned}
\tag{A.4}
$$

Considering the two-impulse case ($N = 2$), zero vibration (ZV) shaper can be calculated from (A.4) based on the assumptions that $N = 2$, and 0 for the time of the first impulse (t_1) as follows,

$$
\begin{bmatrix} A_j \\ t_j \end{bmatrix} = \begin{bmatrix} A_1 & A_1 e^{-\frac{\zeta}{\sqrt{1-\zeta^2}}\pi} \\ 0 & 0.5T \end{bmatrix} \tag{A.5}
$$

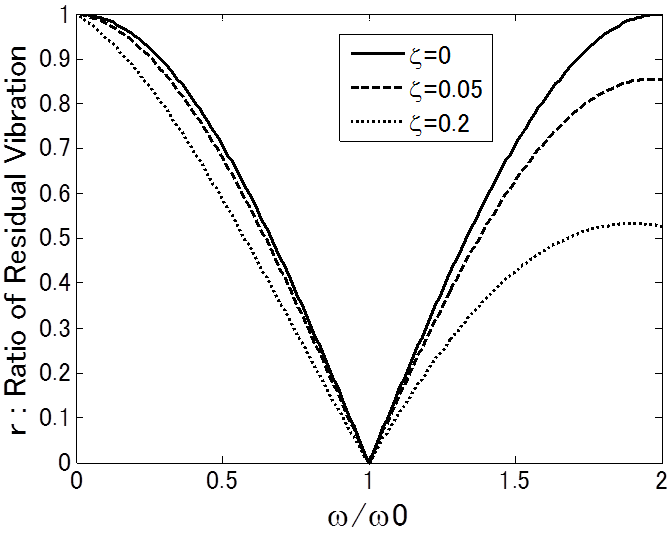

Figure A-1: Residual Vibration vs. Frequency Error (ZV shaper).

where

$$T = \frac{2\pi}{\omega\sqrt{1-\zeta^2}}$$

is the period of the damped vibration.

In order to quantify the residual vibration level for a system, sensitivity curves are calculated as plots of residual vibration vs. system frequency shown in Fig. A-1, here the maximum amplitude of the residual vibration after the input has ended as a percentage of a total amplitude of impulse responses is calculated by

$$r(\omega) = \frac{A_{amp}}{\sum_{j=1}^{N} A_j \frac{\omega}{\sqrt{1-\zeta^2}}} \tag{A.6}$$

Figure A-1 shows that the ZV shaper is robust for a frequency variation of less than ±3 percent if acceptable residual vibration of less than 5 percent is required.

A.2 ZVD shaper

Singer and Seering proposed an input shaper with robustness against modeling errors [22, 48]. In order to increase the robustness of the ZV shaper under variations

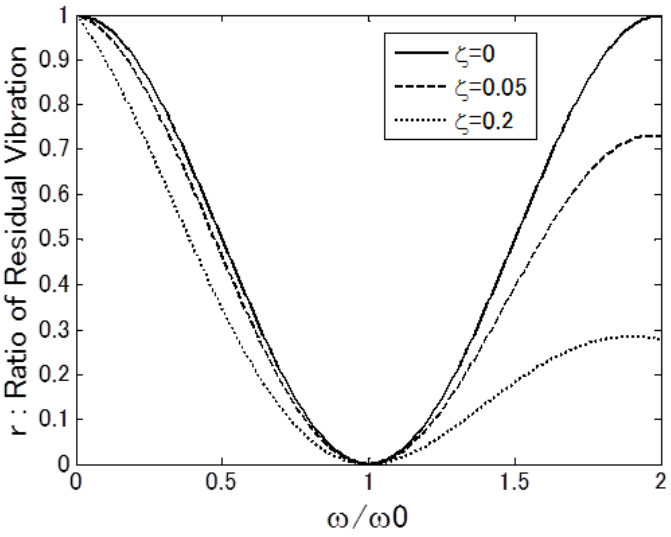

Figure A-2: Residual Vibration vs. Frequency Error (ZVD shaper).

of the system natural frequency, a new constraint can be added by the derivatives of (A.4) with respect to frequency ω, yielding

$$\begin{aligned} \sum_{j=1}^{N} A_j t_j e^{-\zeta\omega(t_N - t_j)} \cos\left(\omega\sqrt{1-\zeta^2}t_j\right) = 0 \\ \sum_{j=1}^{N} A_j t_j e^{-\zeta\omega(t_N - t_j)} \sin\left(\omega\sqrt{1-\zeta^2}t_j\right) = 0 \end{aligned} \tag{A.7}$$

Considering the three-impulse case ($N = 3$), zero vibration and derivative (ZVD) shaper can be calculated from (A.4) and (A.7) based on the assumptions that $N = 3$, and 0 for the time of the first impulse (t_1) as follows,

$$\begin{bmatrix} A_j \\ t_j \end{bmatrix} = \begin{bmatrix} A_1 & 2A_1 e^{-\frac{\zeta}{\sqrt{1-\zeta^2}}\pi} & A_1 e^{-2\frac{\zeta}{\sqrt{1-\zeta^2}}\pi} \\ 0 & 0.5T & T \end{bmatrix} \tag{A.8}$$

The corresponding sensitivity curves calculated by (A.6) is shown as Fig. A-2. Figure A-2 shows that the ZVD shaper is robust for a frequency variation of less than ± 14 percent if acceptable residual vibration of less than 5 percent is required.

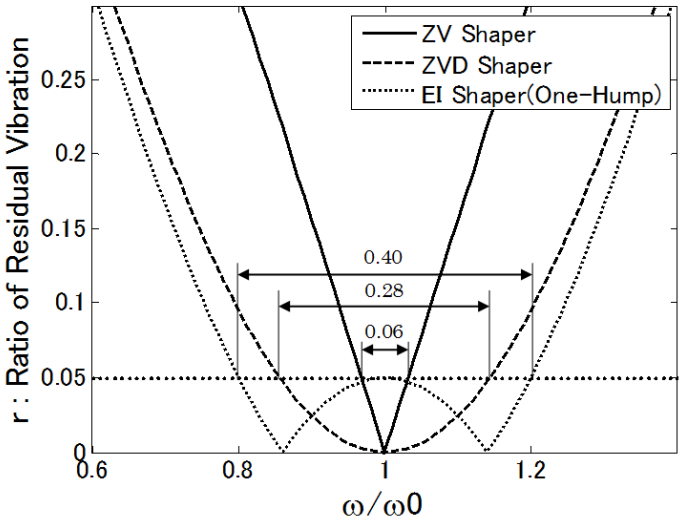

Figure A-3: Residual Vibration vs. Frequency Error (EI shaper).

A.3 EI shaper

Singhose et al. proposed an alternate robustness constraint which generates more insensitivity by abandoning the requirement of zero residual vibration at the modeling frequency i.e. $\omega/\omega_0 = 1$ [23]. By limiting the residual vibration to some small value, V, rather than forcing it to zero, the robustness can be improved without increasing the shaper duration. Shapers designed with this approach are called extra-insensitive (EI) shaper. The EI shaper for undamped systems is

$$\begin{bmatrix} A_j \\ t_j \end{bmatrix} = \begin{bmatrix} \frac{1+V}{4} & \frac{1-V}{2} & \frac{1+V}{4} \\ 0 & 0.5T & T \end{bmatrix} \tag{A.9}$$

Figure A-3 compares the sensitivity curves for ZVD shaper and one-hump EI shaper when $V = 5\%$. The EI shapers result in low levels of vibration over a wider range of frequencies than the ZVD shapers, the one-hump EI shaper is robust for a frequency variation of less than ± 20 percent if acceptable residual vibration of less than 5 percent is required, although less than ± 14 percent frequency variation is allowed for ZVD shapers.

A.4 Zero Vibration Time-Optimal Control

The methods mentioned in the Appendix A.1 to A.3 focused on vibration reduction and did not care about time optimal viewpoint. Liu and Wie proposed an approach for computing time-optimal control inputs for uncertain flexible spacecraft's rest-to-rest maneuver with constant-force actuators [30, 31].

Consider a linear model of flexible spacecraft and a bang-bang input with $(2n-1)$ switches described by

$$M\ddot{x} + Kx = Gu \tag{A.10}$$

where x is a generalized displacement vector, M a mass matrix, K a stiffness matrix, G a control input distribution matrix, and u a control input vector.

In this section, we consider a case with a scalar control input $u(t)$ described by

$$-1 \leq u \leq 1 \tag{A.11}$$

(A.10) can be transformed into the decoupled modal equations:

$$\begin{aligned} &\ddot{y}_1 + \omega_1^2 y_1 = \phi_1 u \\ &\ddot{y}_2 + \omega_2^2 y_2 = \phi_2 u \\ &\vdots \\ &\ddot{y}_n + \omega_n^2 y_n = \phi_n u \end{aligned} \tag{A.12}$$

where y_i is the i-th modal coordinate, ω_i the i-th modal frequency, ϕ_i the i-th modal shape, and n the number of modes considered in control design.

The problem is to determine the control input that minimizes the performance index

$$J = \int_0^{t_f} dt = t_f \tag{A.13}$$

subject to (A.11) and (A.12) and given boundary conditions.

The time-optimal control problem of a linear controllable system has a unique solution, which is bang-bang control with a finite number of switches [54]. For a spring-

mass dynamical system with n degrees of freedom, the time-optimal bang-bang solution for a rest-to-rest maneuver has, in most cases, (*2n-1*) switches [55], and the solution is symmetric about $t_f/2$ the middle point of the maneuver. A bang-bang control input with (*2n-1*) switches can be then described as

$$u(t) = \sum_{j=0}^{2n} B_j u_s(t - t_j) \tag{A.14}$$

where B_j is the magnitude of a unit step function $u_s(t)$ at t_j.

Consider the rest-to-rest maneuvering boundary conditions for the rigid-body mode motion, we have the following rest-to-rest maneuvering constraint for rigid-body mode of $y_1(t)$,

$$\frac{\phi_1}{2} \sum_{j=0}^{2n} (t_f - t_j)^2 B_j - y_1(t_f) = 0 \tag{A.15}$$

Substituting (A.14) into the i-th modal equation and solving for the time response for $t \geq t_f$ where $u = 0$, we get

$$\begin{aligned} y_i(t) &= -\frac{\phi_i}{\omega_i^2} \sum_{j=0}^{2n} B_j \cos \omega_i (t - t_j) \\ &= -\frac{\phi_i}{\omega_i^2} \left[\cos \omega_i (t - t_n) \sum_{j=0}^{2n} B_j \cos \omega_i (t_j - t_n) \right. \\ &\qquad \left. + \sin \omega_i (t - t_n) \sum_{j=0}^{2n} B_j \sin \omega_i (t_j - t_n) \right] \;\; ; \;\; i = 2, \cdots, n \end{aligned} \tag{A.16}$$

Consider the symmetry of bang-bang input that is symmetric about the midmaneuver time t_n, the 2^{nd} term of (A.16) will be zero and we have the following flexible mode constraints for no residual structural vibration [i.e. $y_i(t) = 0$ for $t \geq t_f$]:

$$\sum_{j=0}^{2n} B_j \cos \omega_i (t_j - t_n) = 0 \;\; ; \;\; i = 2, \cdots, n \tag{A.17}$$

Example 1

Consider an example shown in Fig. 2-1, the modal equations are obtained by decoupling as follows,

$$\begin{aligned} \ddot{y}_1 &= \frac{u}{2} \\ \ddot{y}_2 + \omega_2^2 y_2 &= \frac{u}{2} \end{aligned} \tag{A.18}$$

where $\omega_2 = \sqrt{2}$ rad/s is the nominal flexible mode frequency.
The boundary conditions for a rest-to-rest maneuver are given as

$$\begin{aligned} y_1(0) = y_2(0) &= 0 \\ \dot{y}_1(0) = \dot{y}_2(0) &= 0 \\ y_1(t_f) = y_2(t_f) &= 1 \\ \dot{y}_1(t_f) = \dot{y}_2(t_f) &= 0 \end{aligned} \tag{A.19}$$

Solving the time-optimal control problem subject to constraints of (A.15) and (A.17) with boundary conditions of (A.19) and applying the symmetry about $t_2 (= t_f/2)$, we have the time-optimal bang-bang control input as

$$\begin{aligned} u(t) \;=\; & u_s(t) - 2u_s(t - 1.00268) + 2u_s(t - 2.10893) \\ & -2u_s(t - 3.21518) + u_s(t - 4.21786) \end{aligned} \tag{A.20}$$

The shaped command and responses were shown in Fig. A-4.

A.5 Robust Zero Vibration Time-Optimal Control

Liu and Wie proposed a time-optimal controller of constant-force actuators with robustness against modeling errors [30, 31]. Consider the symmetry of bang-bang input that is symmetric about the midmaneuver time t_n into (A.16), and taking the derivative of the equation with respect to i-th modal frequency ω_i, we get

$$\frac{dy_i(t)}{d\omega_i} = \frac{\phi_i}{\omega_i^2} \cos\omega_i \left(t - \frac{t_f}{2} \right) \sum_{j=0}^{2n} B_j \left(t_j - \frac{t_f}{2} \right) \sin\omega_i \left(t_j - \frac{t_f}{2} \right) \;\; ; \;\; i = 2, \cdots, n \tag{A.21}$$

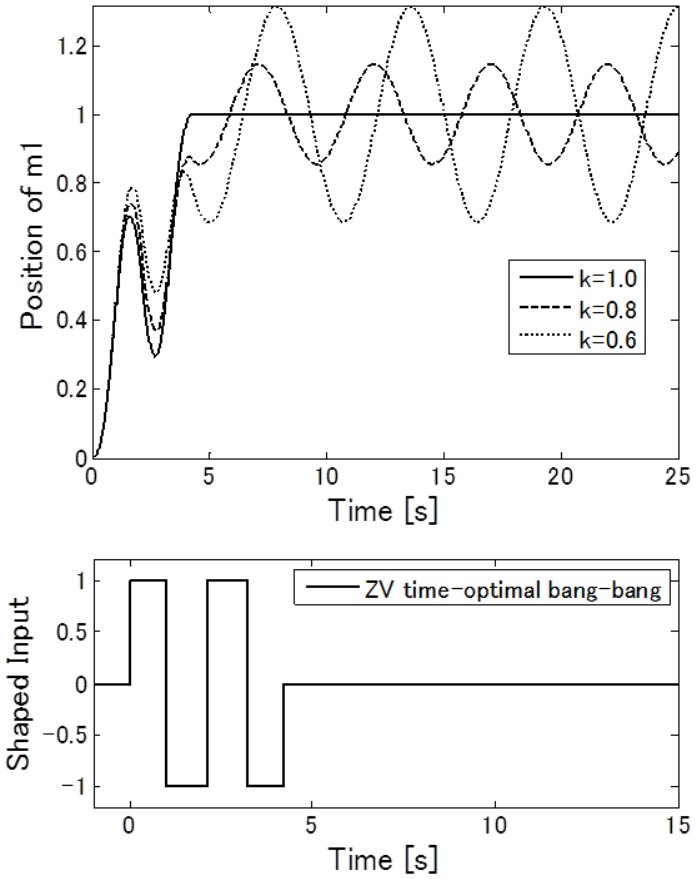

Figure A-4: Shaped command and responses of ZV Time-Optimal shaper

Letting $dy_i(t)/d\omega_i = 0$ for all $t \geq t_f$, we have

$$\sum_{j=0}^{2n} B_j \left(t_j - \frac{t_f}{2}\right) \sin\omega_i \left(t_j - \frac{t_f}{2}\right) = 0 \; ; \quad i = 2, \cdots, n \tag{A.22}$$

which is called the first-order robustness constraints.

Similarly, taking the derivative of (A.16) r_i times with respect to ω_i results in r_i-th order robustness constraints for each structural mode as follows:

$$\sum_{j=0}^{2n} B_j \left(t_j - \frac{t_f}{2}\right)^m \sin\omega_i \left(t_j - \frac{t_f}{2}\right) = 0 \; ; \quad \begin{matrix} i = 2, \cdots, n \\ m = 1, 3, \cdots \leq r_i \end{matrix} \tag{A.23}$$

$$\sum_{j=0}^{2n} B_j \left(t_j - \frac{t_f}{2}\right)^m \cos\omega_i \left(t_j - \frac{t_f}{2}\right) = 0 \; ; \quad \begin{matrix} i = 2, \cdots, n \\ m = 2, 4, \cdots \leq r_i \end{matrix} \tag{A.24}$$

Example 2

Consider an example shown in Fig. 2-1, the modal equations and the boundary conditions are same as Example 1 ((A.18) and (A.19)).

Solving the time-optimal control problem subject to constraints of (A.15), (A.17) and the first-order robustness constraints of (A.22) with boundary conditions of (A.19) and applying the symmetry about $t_2 (= t_f/2)$, we have the time-optimal bang-bang control input as

$$\begin{aligned} u(t) \;\; = \;\; & u_s(t) - 2u_s(t - 0.7124) + 2u_s(t - 1.6563) - 2u_s(t - 2.9330) \\ & + 2u_s(t - 4.2097) - 2u_s(t - 5.1536) + u_s(t - 5.8660) \end{aligned} \tag{A.25}$$

The shaped command and responses were shown in Fig. A-5.

A.6 Low-pass Filter

Conventional low-pass filters such as Butterworth, Chebyshev, and elliptic etc. can be applied to shape the input to reduce excitation energy at higher frequencies.

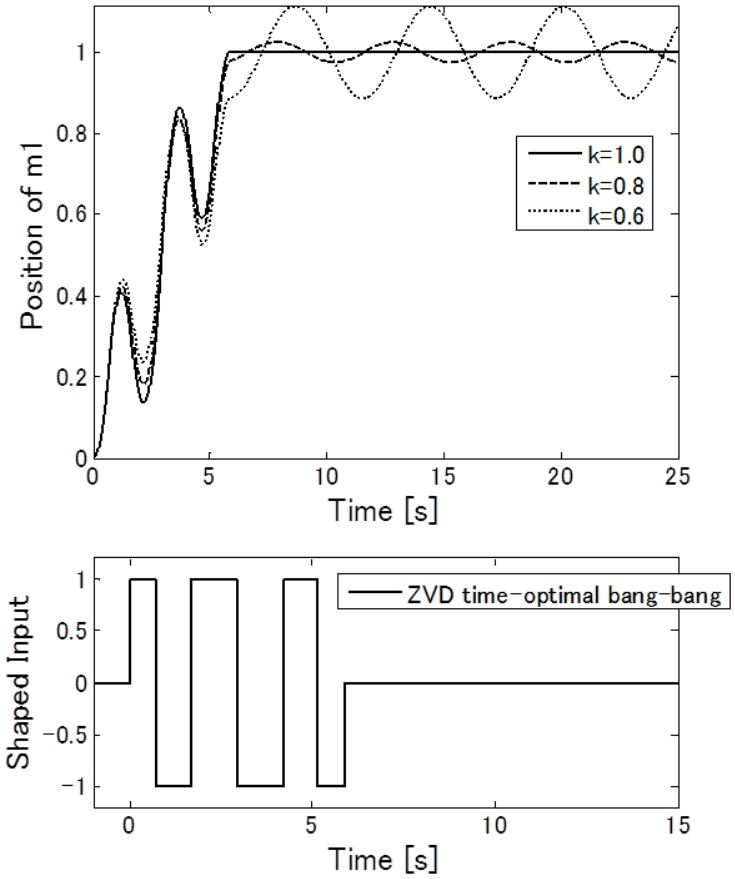

Figure A-5: Shaped command and responses of ZVD Time-Optimal shaper

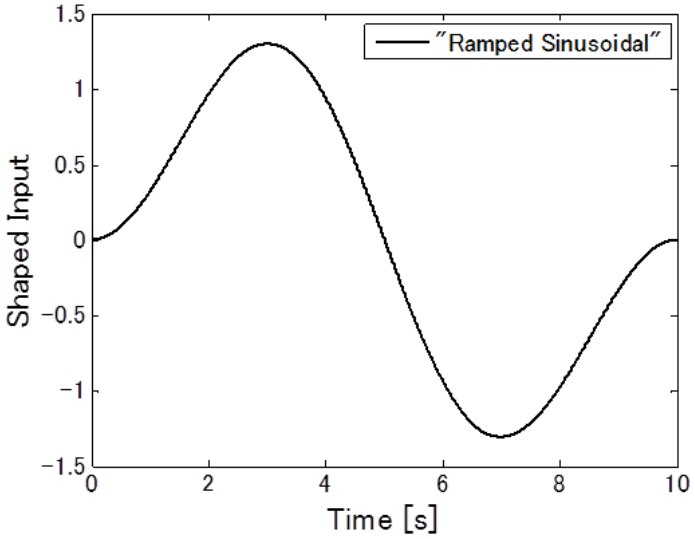

Figure A-6: Ramped Sinusoidal Curve

A.7 Sinusoidal Curve

Meckl and Seering proposed S-curve input functions from either versine functions or ramped sinusoids [35, 36, 37]. A ramped sinusoidal curve, shown in Fig. A-6, can be used as a characteristic function for a rest-to-rest maneuver since the smooth transitions in slope at the beginning and end tend to reduce excitation energy at higher frequencies. The fundamental ramped sinusoidal function and its harmonics as derived in [35, 37] are selectively added to approximate a square wave in order to achieve a swift maneuver. A 15-term series of ramped sinusoidal curves are shown in Fig. A-7.

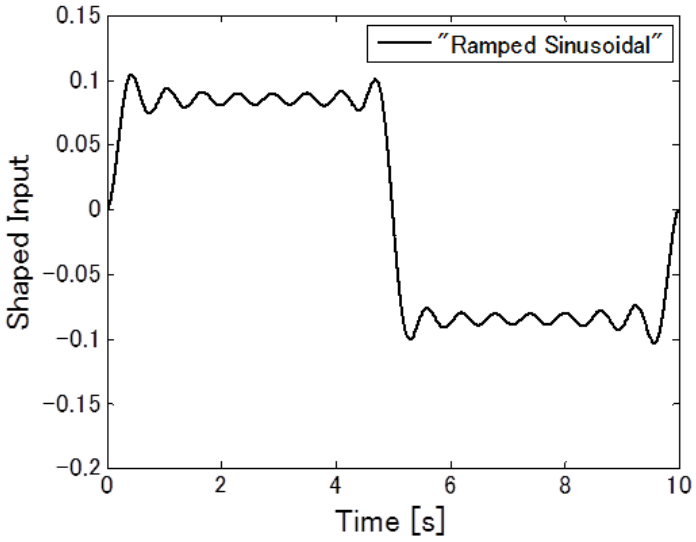

Figure A-7: 15-Term Ramped Sinusoidal Curve

THIS PAGE INTENTIONALLY LEFT BLANK

Appendix B

Time-Optimal Bang-bang Control for Two-mode System

This section presents time-optimal profiler for the two-mode system. The results can be used as theoretically maximum maneuver distances for the two-mode system.

For one rigid mode and $N-1$ oscillating modes, where N is the number of lumped masses, a minimum of $2(N-1)+1 = 2N-1$ switches is necessary to bring the system to rest [37]. Therefore the two-mode system requires, at least, five switches for rest-to-rest motions. Those switch times must be determined in order to uniquely define the forcing function. Such a determination is much simpler to make if the three-mass system is broken into its modal components. The modal equations can be used to derive expressions for the five switch times in terms of a given maneuver duration t_{mnv}. Since the resultant forcing function can be considered as a sum of step functions each delayed in time and alternating in sign and since the system is linear, the total response is simply the sum of responses for each step. Referring to the lower mode differential equation

$$\ddot{\eta}_2 + \omega_L^2 \eta_2 = 1 \tag{B.1}$$

$$\eta_2(0) = 0, \quad \dot{\eta}_2(0) = 0$$

and solving gives

$$\eta_2(t) = \frac{1}{\omega_L^2}\left(1 - \cos\omega_L t\right) \tag{B.2}$$

This expression gives the response to a single step. With the switch times numbered in ascending order for increasing time $\left(t_i = \left[\begin{array}{ccccccc} 0 & t_1 & t_2 & t_3 & t_4 & t_5 & t_{mnv} \end{array}\right]\right)$, the total response at time $t' > t_{mnv}$ is given by

$$\begin{aligned}\eta_2(t') = \tfrac{1}{\omega_L^2}\{&(1-\cos\omega_L t') - 2\left(1-\cos\omega_L\left(t'-t_1\right)\right) + 2\left(1-\cos\omega_L\left(t'-t_2\right)\right)\\ &- 2\left(1-\cos\omega_L\left(t'-t_3\right)\right) + 2\left(1-\cos\omega_L\left(t'-t_4\right)\right)\\ &- 2\left(1-\cos\omega_L\left(t'-t_5\right)\right) + \left(1-\cos\omega_L\left(t'-t_{mnv}\right)\right)\}\end{aligned} \tag{B.3}$$

where $\eta_2(t') = 0$ for all time $t'(> t_{mnv})$ implies that no more oscillation occurs at the end of the move. Simplifying the $\eta_2(t') = 0$ yields:

$$\begin{aligned}&\cos\omega_L t'\left\{1 - 2\cos\omega_L t_1 + 2\cos\omega_L t_2 - 2\cos\omega_L t_3 + 2\cos\omega_L t_4 - 2\cos\omega_L t_5 + \cos\omega_L t_{mnv}\right\}\\ &+\sin\omega_L t'\left\{-2\sin\omega_L t_1 + 2\sin\omega_L t_2 - 2\sin\omega_L t_3 + 2\sin\omega_L t_4 - 2\sin\omega_L t_5 + \sin\omega_L t_{mnv}\right\} = 0\end{aligned} \tag{B.4}$$

For this to be true for all t', both expressions in brackets must be zero. Thus,

$$1 - 2\cos\omega_L t_1 + 2\cos\omega_L t_2 - 2\cos\omega_L t_3 + 2\cos\omega_L t_4 - 2\cos\omega_L t_5 + \cos\omega_L t_{mnv} = 0 \tag{B.5}$$

$$-2\sin\omega_L t_1 + 2\sin\omega_L t_2 - 2\sin\omega_L t_3 + 2\sin\omega_L t_4 - 2\sin\omega_L t_5 + \sin\omega_L t_{mnv} = 0 \tag{B.6}$$

The same result follows for the higher mode, with ω_L replaced by ω_H:

$$1 - 2\cos\omega_H t_1 + 2\cos\omega_H t_2 - 2\cos\omega_H t_3 + 2\cos\omega_H t_4 - 2\cos\omega_H t_5 + \cos\omega_H t_{mnv} = 0 \tag{B.7}$$

$$-2\sin\omega_H t_1 + 2\sin\omega_H t_2 - 2\sin\omega_H t_3 + 2\sin\omega_H t_4 - 2\sin\omega_H t_5 + \sin\omega_H t_{mnv} = 0 \tag{B.8}$$

The symmetry conditions of the switch times are given as

$$\begin{aligned} t_3 &= t_{mnv}/2\\ t_4 &= t_{mnv} - t_2\\ t_5 &= t_{mnv} - t_1\end{aligned} \tag{B.9}$$

Substituting (B.9) into (B.5) and (B.6), the both equations will be equivalent each other. The same result follows for the higher mode equations ((B.7) and (B.8)).

Thus, the constrained time optimization problem for the two-mode system can be formulated as

$$\begin{aligned} &-2\sin\omega_L t_1 + 2\sin\omega_L t_2 - 2\sin\left(\omega_L t_{mnv}/2\right) \\ &+2\sin\omega_L\left(t_{mnv} - t_2\right) - 2\sin\omega_L\left(t_{mnv} - t_1\right) + \sin\omega_L t_{mnv} = 0 \end{aligned} \tag{B.10}$$

$$\begin{aligned} &-2\sin\omega_H t_1 + 2\sin\omega_H t_2 - 2\sin\left(\omega_H t_{mnv}/2\right) \\ &+2\sin\omega_H\left(t_{mnv} - t_2\right) - 2\sin\omega_H\left(t_{mnv} - t_1\right) + \sin\omega_H t_{mnv} = 0 \end{aligned} \tag{B.11}$$

These simultaneous nonlinear equations, two equations for two unknowns (t_1 and t_2), can be solved numerically.

Solving (B.10) and (B.11) numerically for the given maneuver duration t_{mnv}= 6 s, the time-optimal bang-bang control input is obtained as

$$\begin{aligned} u(t) &= u_s(t) - 2u_s(t - 1.7238) + 2u_s(t - 2.3285) - 2u_s(t - 3.0) \\ &+2u_s(t - 3.6715) - 2u_s(t - 4.2762) + u_s(t - 6.0) \end{aligned} \tag{B.12}$$

where u_s is step function.

Figure B-1 shows responses of a full acceleration and deceleration command in which large residual vibrations after the maneuvers are confirmed, whereas Fig. B-2 shows responses of the time-optimal bang-bang input for two-mode system in which no residual vibration is confirmed at exact value, i.e. k_2=0.67.

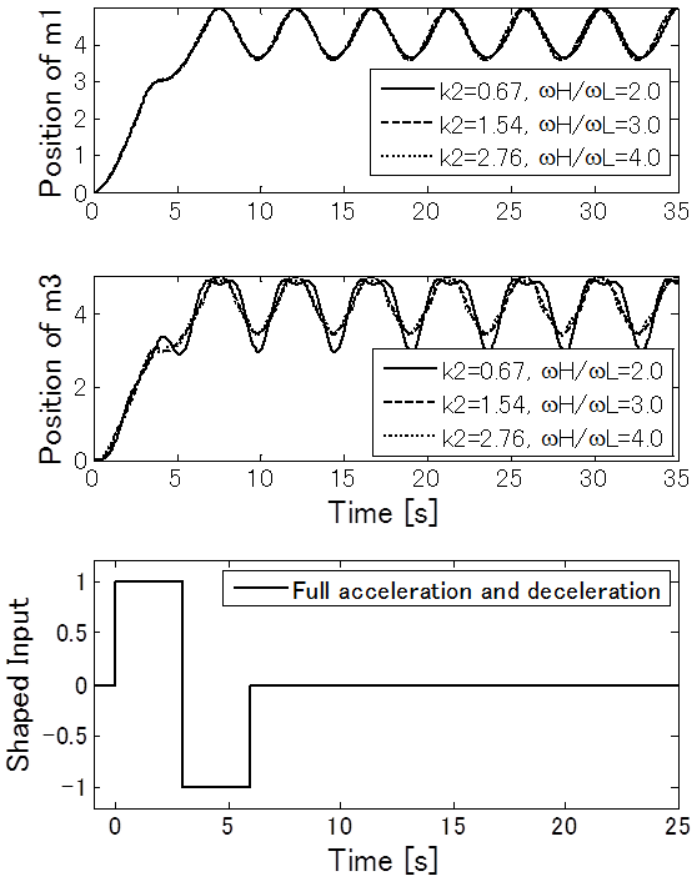

Figure B-1: Responses of a full acceleration and deceleration input at three values of stiffness k_2 of the unknown high-frequency mode. Top: positions of mass m_1. Middle: positions of mass m_3. Bottom: input command.

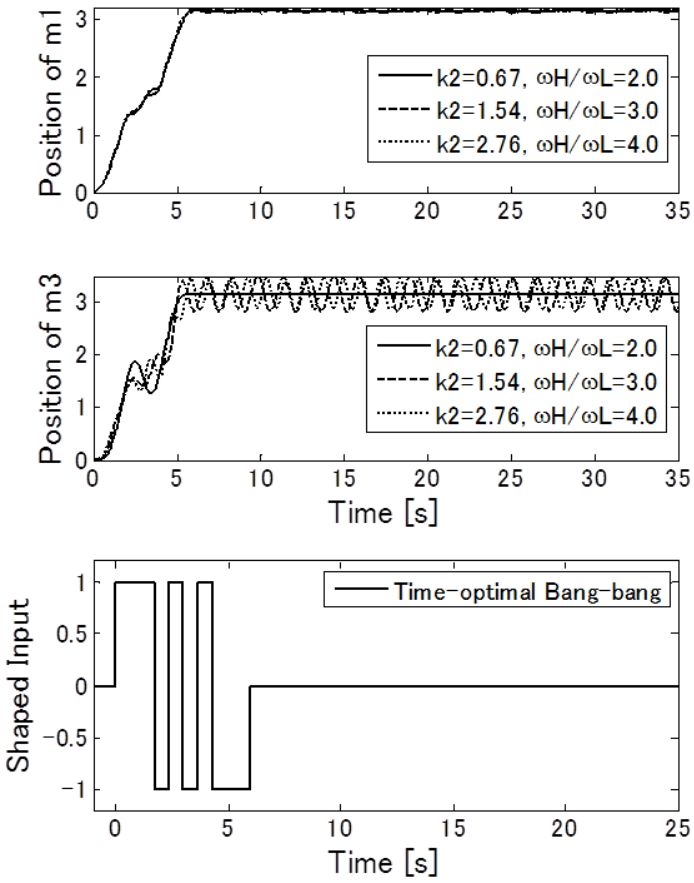

Figure B-2: Responses of time-optimal bang-bang input for two-mode system at three values of stiffness k_2 of the unknown high-frequency mode. Top: positions of mass m_1. Middle: positions of mass m_3. Bottom: input command.

THIS PAGE INTENTIONALLY LEFT BLANK

Appendix C

Trade-Off of Window Functioning Methods

In this Appendix, window functioning methods are compared in relation to Section 7.4. Trade-off of those window functioning methods when combined into sinc function with weighted harmonics is made to find a better method which realizes preferable frequency characteristic and higher agility.

C.1 Sinc Function with Weighted Harmonics Without Window Function

The input torque profile of the sinc function with weighted harmonics without window function, or equivalently rephrased as "windowed by rectangular window function," which has been introduced in Section 7.4 is given as,

$$u(t) = \begin{cases} A \sum_{j=1}^{L} A_j \cdot f_j(t) & \text{for} \quad 0 \leq t \leq t_{mnv} \\ 0 & \text{for} \quad t < 0, t_{mnv} < t \end{cases} \tag{C.1}$$

where A is a constant to determine the amplitude of the input torque profile, A_j and $f_j(t)$ are defined in Section 7.4.

Figure C-1 shows the waveform of (C.1), and Fig C-2 shows its jerk. It is confirmed

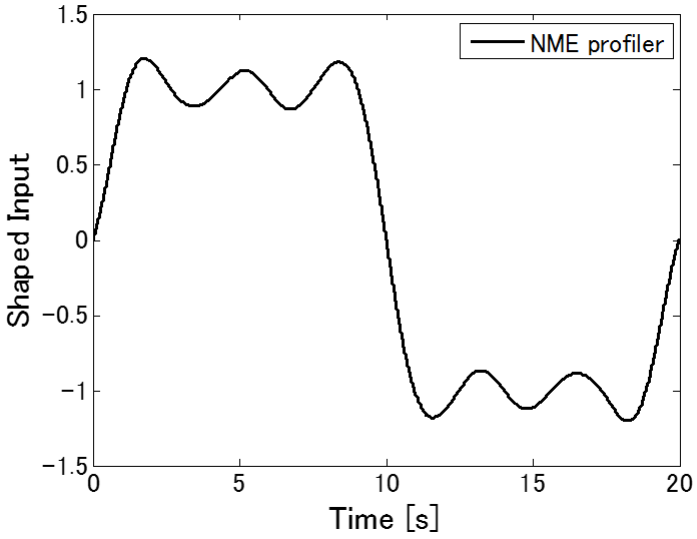

Figure C-1: Shaped input before windowing at $L = 5$ (T_s=10 s)

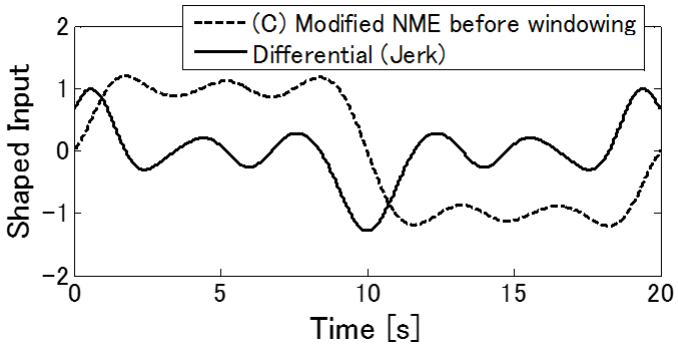

Figure C-2: Jerk of shaped input before windowing at $L = 5$ (T_s=10 s)

that the jerk begins and ends at nonzero values. This should be considered for controller design, because actual actuator h.as some delay time at rise and decay.

C.2 Sinc Function with Weighted Harmonics Windowed before Rectangular Fitting

Another input command, sinc function with weighted harmonics-type, is introduced and compared in this section. Hamming window is applied to each order harmonics, then weighted sum is fitted to the rectangular waveform by the minimization problem,

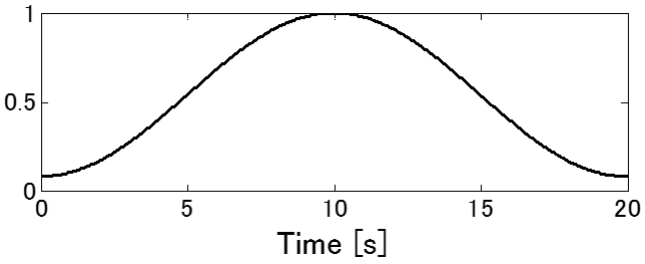

Figure C-3: Hamming window (T_s=10 s)

i.e. equivalent procedure derived in Section 7.4.

$$u(t) = A\, w(t) \sum_{j=1}^{L} A_j \cdot f_j(t) \tag{C.2}$$

where

A: Constant which determines amplitude of input torque

$w(t)$: Hamming window function

The window function $w(t)$ is the Hamming window, which is shown in Fig. C-3 and expressed as

$$w(t) = \begin{cases} 0.54 + 0.46 \cos\left\{ \dfrac{2\pi}{t_{mnv}} \left(t - \dfrac{t_{mnv}}{2} \right) \right\} & \text{for} \quad 0 \le t \le t_{mnv} \\ 0 & \text{for} \quad t < 0, t_{mnv} < t \end{cases} \tag{C.3}$$

The harmonics after windowing from 1^{st} to 5^{th} order are shown in Fig. C-4 when T_s is 10 s. If the windowed harmonics could be added so that the resulting function approximates a square wave, the equivalent procedure introduced in Section 7.4 can be applied hereafter.

A least-squares approximation to the square wave can be constructed by minimizing the square of the error between the desired square wave of height F and a finite sum of weighted harmonics from 1^{st} to L^{th} order. The weighting coefficients A_j can be determined by the minimization problem given as

$$\int_0^{T_f/2} \left[F - w(t) \sum_{j=1}^{L} A_j f_j(t) \right]^2 dt + \int_{T_f/2}^{T_f} \left[-F - w(t) \sum_{j=1}^{L} A_j f_j(t) \right]^2 dt = \min . \tag{C.4}$$

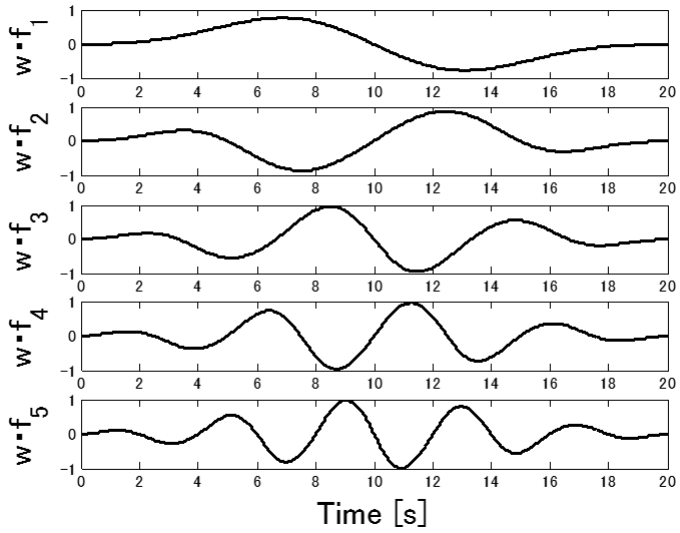

Figure C-4: Harmonics after windowing at $j = 1$ to 5 (T_s=10 s)

where T_f is a maneuver duration and $T_f = 2T_s$. Differentiating with respect to A_i,

$$\int_0^{T_f/2} \left[F - w(t) \sum_{j=1}^{L} A_j f_j(t) \right] w(t) f_i(t) dt - \int_{T_f/2}^{T_f} \left[F + w(t) \sum_{j=1}^{L} A_j f_j(t) \right] w(t) f_i(t) dt = 0 \tag{C.5}$$

where $i = 1, 2, \cdots, L$, and rearranging gives:

$$\sum_{j=1}^{L} A_j \underbrace{\int_0^{T_f} w^2(t) f_j(t) f_i(t) dt}_{I_{ij}} = F \underbrace{\left[\int_0^{T_f/2} w(t) f_i(t) dt - \int_{T_f/2}^{T_f} w(t) f_i(t) dt \right]}_{I_i}, \ (i = 1, 2, \cdots, L) \tag{C.6}$$

The resulting matrix expression to solve for the A_i is

$$\begin{bmatrix} I_{11} & I_{12} & \cdots & I_{1L} \\ I_{21} & I_{22} & \cdots & I_{2L} \\ \vdots & \vdots & & \vdots \\ I_{L1} & I_{L2} & \cdots & I_{LL} \end{bmatrix} \begin{bmatrix} A_1 \\ \vdots \\ \vdots \\ A_L \end{bmatrix} = F \begin{bmatrix} I_1 \\ I_2 \\ \vdots \\ I_L \end{bmatrix} \tag{C.7}$$

where

$$I_{ij} = \int_0^{T_f} w^2(t) f_j(t) f_i(t) dt \tag{C.8}$$

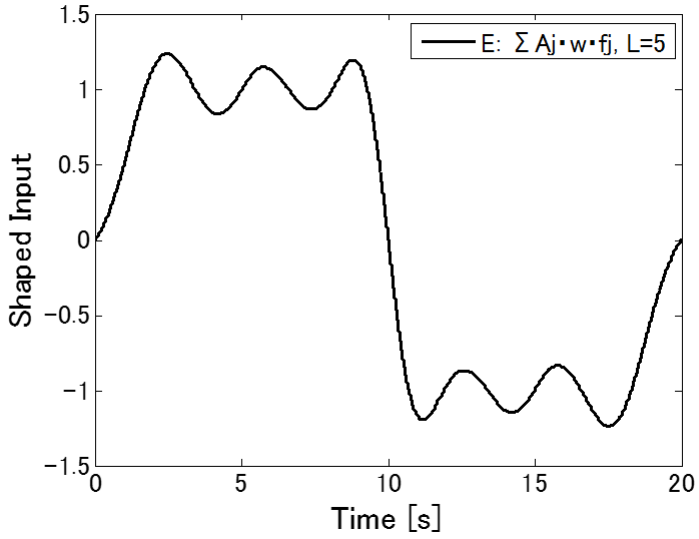

Figure C-5: Shaped input after windowing at $L = 5$ (T_s=10 s)

$$I_i = \int_0^{T_f/2} w(t) f_i(t) dt - \int_{T_f/2}^{T_f} w(t) f_i(t) dt \tag{C.9}$$

Thus, the weighting coefficients A_j are given by

$$[A_j] = F\,[I_{ij}]^{-1}\,[I_i] \tag{C.10}$$

Figure C-5 shows input torque waveform at $L = 5$.

C.3 Trade-Off of Window Functioning Method in Sinc Function with Weighted Harmonics

Input command of the windowed profiler introduced in Appendix C.2 and response of two-mode system are shown in Fig. C-6. For each shaper discussed in this Appendix, Table C.1 lists the duration and residual vibration (peak-to-peak) of the two-mode system for $k_2 = 0.188$, 0.318, 0.67, 1.54, and 2.76 and Table C.2 lists the duration and residual vibration (peak-to-peak) of the single-mode system for $k = 1.0$, 0.8, and 0.6.

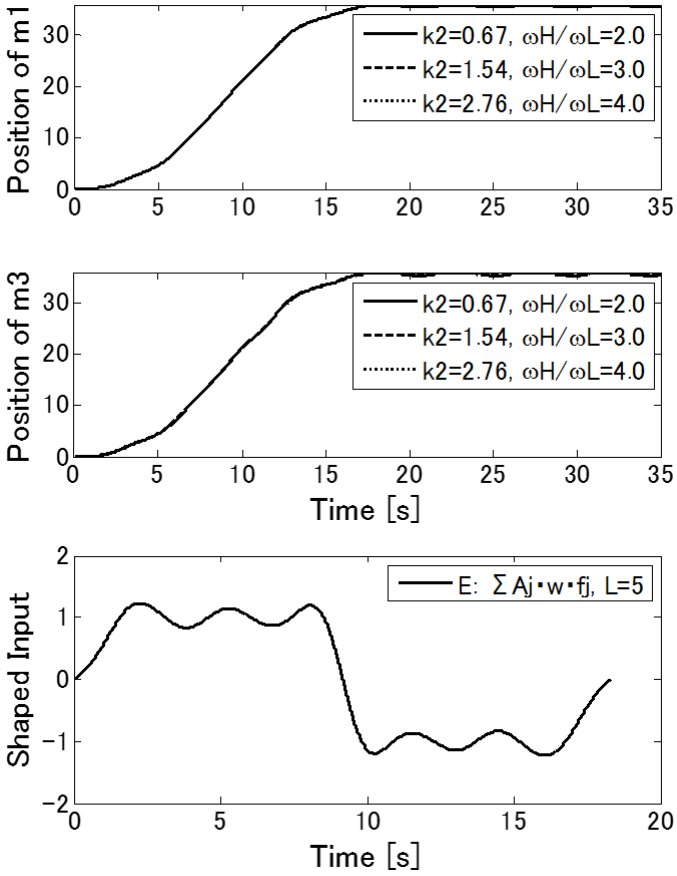

Figure C-6: Shaped command and responses of harmonics after windowing at $L = 5$ and three values of stiffness k_2 in two-mode system

It is confirmed that the maneuver distances are slightly longer in sinc with harmonics without window function (or rectangular function), and the residual vibrations are basically smaller in sinc with harmonics without window function.

FFTs plots of sinc with harmonics without window and that with window and ramped sinusoids at $L = 1$ are shown in Fig. C-7 and those of at $L = 5$ are shown in Fig. C-8. The differences are confirmed as follows:

- The sinc function with harmonics WITHOUT window shows slightly lower boundary frequency compared to other two profilers.
- The sidelobes of the sinc function with harmonics WITH/WITHOUT window are -40[dB/dec] whereas -60[dB/dec] for ramped sinusoids.

Table C.1: Comparison of simulation results for maneuver durations and vibrations of mass m_1 for smooth controllers (Two-Mode System).

	Maneuver distance	Vibration of m_1 (peak-to-peak)				
		$k_2 = 0.188$ (2^{nd} harm. of t_{mnv} =10s)	$k_2 = 0.318$ (5^{th} harm. of t_{mnv} =18s)	$k_2 = 0.67$ (ω_H/ω_L =2.0)	$k_2 = 1.54$ (ω_H/ω_L =3.0)	$k_2 = 2.76$ (ω_H/ω_L =4.0)
Ramped sine (L=1, 18s)	19.31	0.12%	0.42%	0.50%	0.52%	0.53%
Ramped sine (L=5, 18s)	28.05	1.66%	3.35%	1.75%	1.66%	1.62%
Ramped sine (L=15, 18s)	31.24	1.81%	1.47%	0.41%	0.42%	0.37%
NME (L=1)	17.28/15.25/14.71	0.04%	0.08%	0.09%	0.09%	0.09%
Sinc with harmonics (L=5)	37.42/33.04/31.87	2.73%	1.04%	0.19%	0.11%	0.08%
Sinc with windowed harmonics (L=5)	33.91/29.92/28.88	1.80%	2.42%	1.23%	1.13%	1.10%

Note:

- The durations of the all types of NME profilers are 19.875 s when k_2 is 0.188, 18.674 s when k_2 is 0.318, and 18.340 s when k_2 is 0.67/1.54/2.76.
- X/Y/Z shown in the column of maneuver distance mean that X is maneuver distance when k_2=0.188, Y is when k_2=0.318, and Z is when k_2=0.67, 1.54, 2.76.

Table C.2: Comparison of simulation results for maneuver durations and vibrations of mass m_1 for smooth controllers (Single-Mode System).

	Maneuver distance	Vibration of m_1 (peak-to-peak)		
		Exact (k=1)	k=0.8 (10.6% Low)	k=0.6 (22.5% Low)
Ramped sine (L=1, 18s)	19.31	0.51%	0.39%	1.40%
Ramped sine (L=5, 18s)	28.05	0.91%	5.75%	9.67%
Ramped sine (L=15, 18s)	31.24	0.03%	3.16%	8.76%
NME (L=1, 17.772 s)	13.82	0.10%	0.11%	1.43%
Sinc with harmonics (L=5)	29.92	0.22%	4.49%	9.41%
Sinc with windowed harmonics (L=5)	27.11	1.46%	6.43%	9.55%

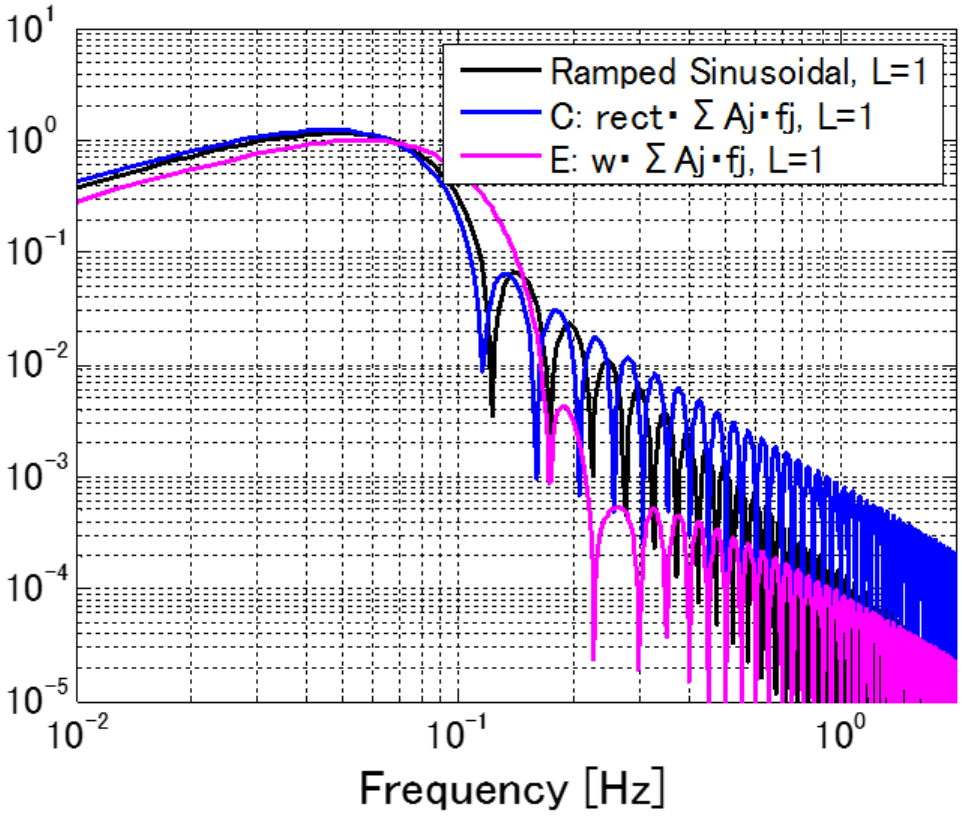

Figure C-7: FFTs of shaped input of ramped sinusoids (black), sinc with harmonics without window (blue), and sinc with harmonics with window (pink) at $L = 1$ (T_s=10 s)

- The boundary frequency of the sinc function with harmonics WITH window is higher than others, but spectrum in higher frequency is lower than others.

Thus, in this thesis, the sinc function with weighted harmonics WITHOUT window (or rectangular window) has been chosen in Section 7.4 as the profiler for better balanced solutions of maneuver distance and residual vibration.

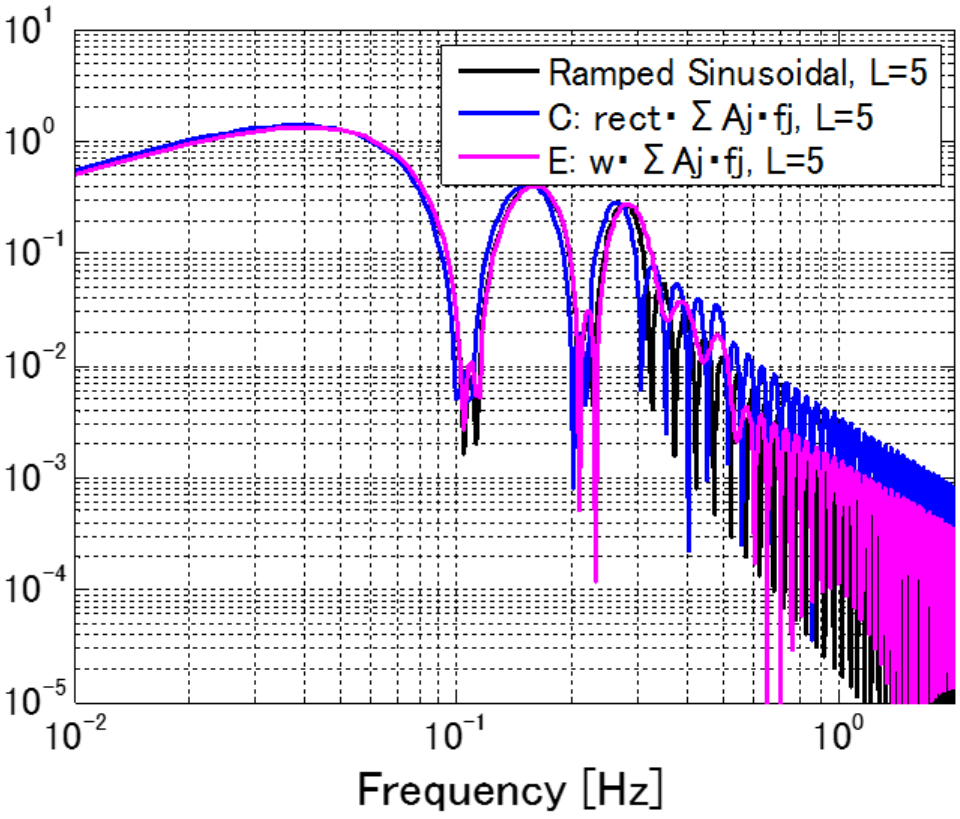

Figure C-8: FFTs of shaped input of ramped sinusoids (black), sinc with harmonics without window (blue), and sinc with harmonics with window (pink) at $L = 5$ (T_s=10 s)

THIS PAGE INTENTIONALLY LEFT BLANK

Appendix D

Experimental Verification

Experimental test to verify the effectiveness of the proposed NME profiler and the modified NME profiler presented in Section 7.2 have been performed by Nakamura [49, 50] using test module with simplified flexible structures. The test configuration is shown in Fig. D-1.

Transfer functions of the test module and mathematical model are shown in Fig. D-2. Three flexible modes are confirmed. Residual vibrations versus maneuver duration based on the test results are shown in Fig. D-3 in case of nominal parameters and Fig. D-4 in case of frequency modeling errors on the second and third flexible modes (Note that no frequency errors are considered for the first flexible mode). The tests are performed on the NME profiler, modified NME profiler presented in Section 7.2, SMART (Structural Vibration Minimized Acceleration Trajectory), and shaped bang-bang. The SMART which was designed for hard disk controller [56] is a smooth type profiler to minimize the jerk of the position profiler. The shaped bang-bang is made by convolving the three ZV shaper designed for three measured flexible modes and bang-bang command. The SMART shows the largest residual vibrations in a wide range of maneuver duration. The shaped bang-bang shows small residual vibrations however that is because the frequencies for ZV shapers are well adjusted to the measured data. The NME profiler is confirmed to show the intended performances. The modified NME profiler shows some improvement for shorter maneuver durations compared to the NME profiler, using ZV shaper designed based on the measured frequency. If

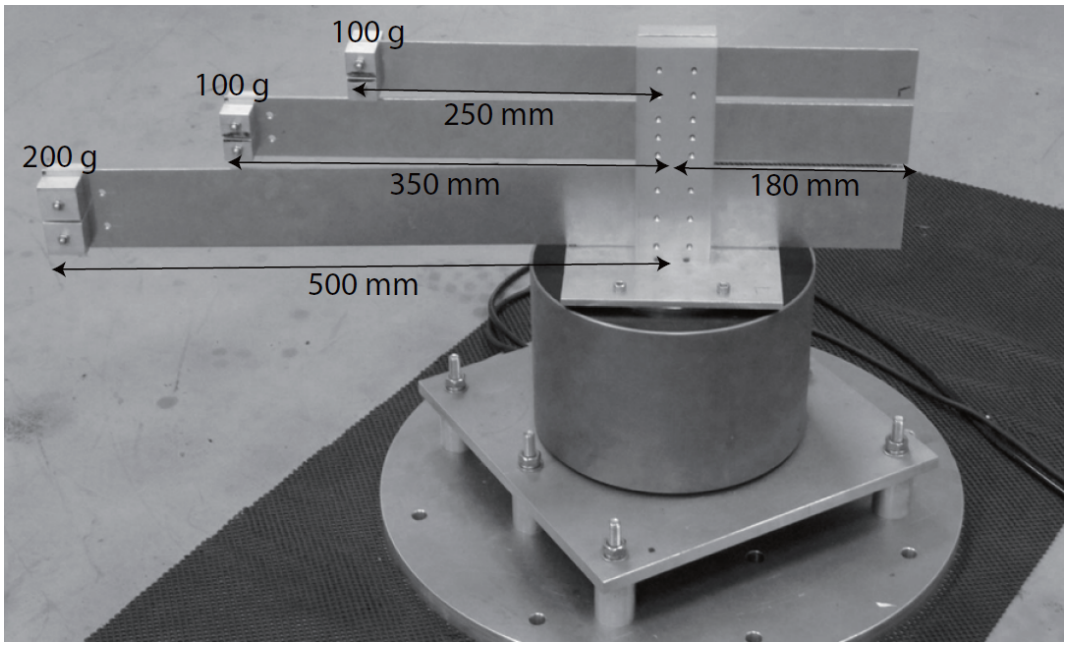

Figure D-1: Test module with simplified flexible structures [49]

a modeling error on the first flexible mode is considered, residual vibrations of the modified NME profiler would be larger.

The effectiveness of the proposed NME profiler and the modified NME profiler presented in Section 7.2 from the viewpoint of theoretical frequency separation has been confirmed in this way.

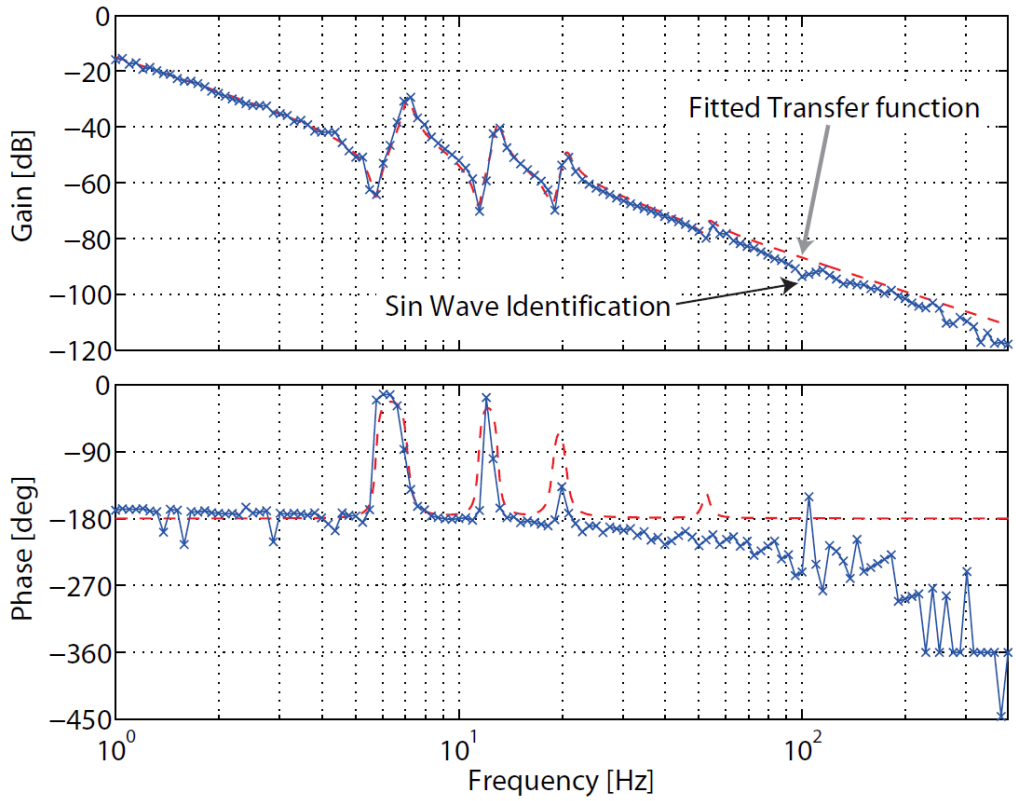

Figure D-2: Transfer function of test module (blue solid line) and mathematical model (red broken line) [49]

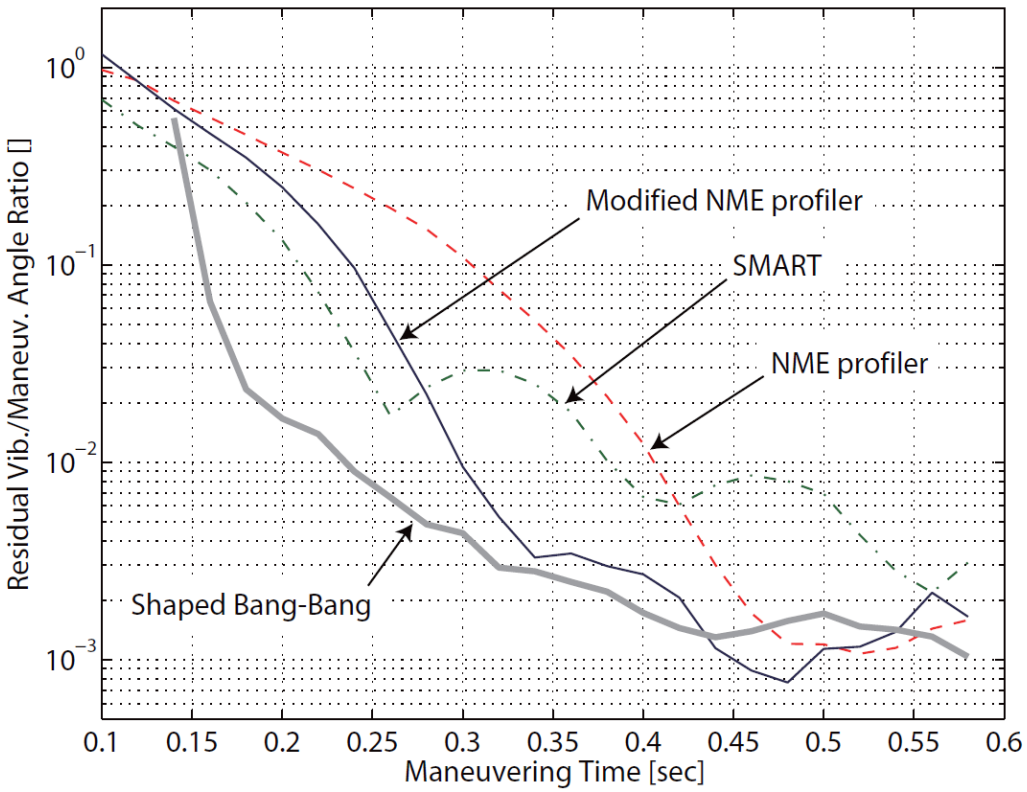

Figure D-3: Residual vibration vs. maneuver duration [49]

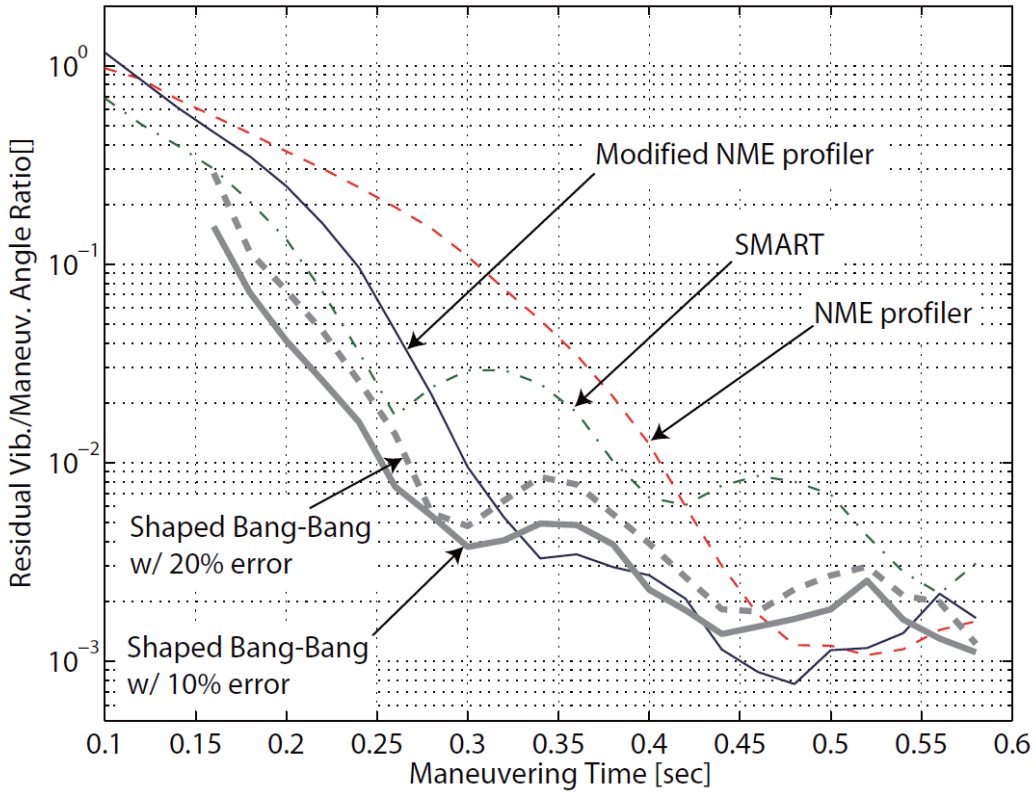

Figure D-4: Residual vibration vs. maneuver duration with frequency errors [49]

THIS PAGE INTENTIONALLY LEFT BLANK

Appendix E

Dynamics Characterization Test of Control Moment Gyro for ASTRO-G

In this Appendix, summary of dynamics characterization test which has been performed as a part of ASTRO-G ACS design work is presented. The experimental verification test is to identify dynamical characteristics of the CMG have been performed using engineering model. The test configuration is shown in Fig. E-1.

Examples of test data are shown in Figs. E-2 to E-4 which show measured data and those errors of gimbal angle, rate, and wheel speed respectively. Red line shows commanded date and blue line shows measured data. Test for repeating rest-to-rest maneuver motion are also conducted as shown in Figs. E-5 to E-7. Then, the measured date have been compared to those of mathematical model as shown in Figs. E-8 and E-9 to verify the validity of mathematical model. Green line shows data by mathematical model. The green line shows worse behavior of gimbal motion. The verification of the mathematical model of ASTRO-G has been successfully done by this way.

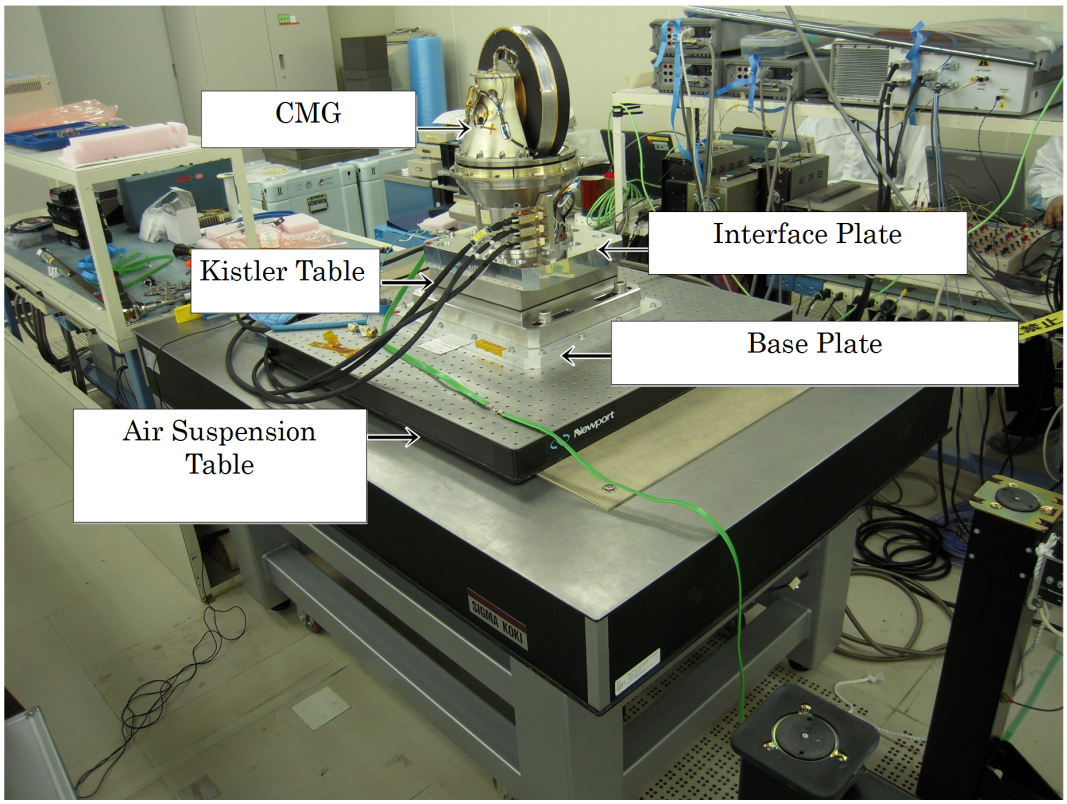

Figure E-1: CMG dynamics characterization test configuration

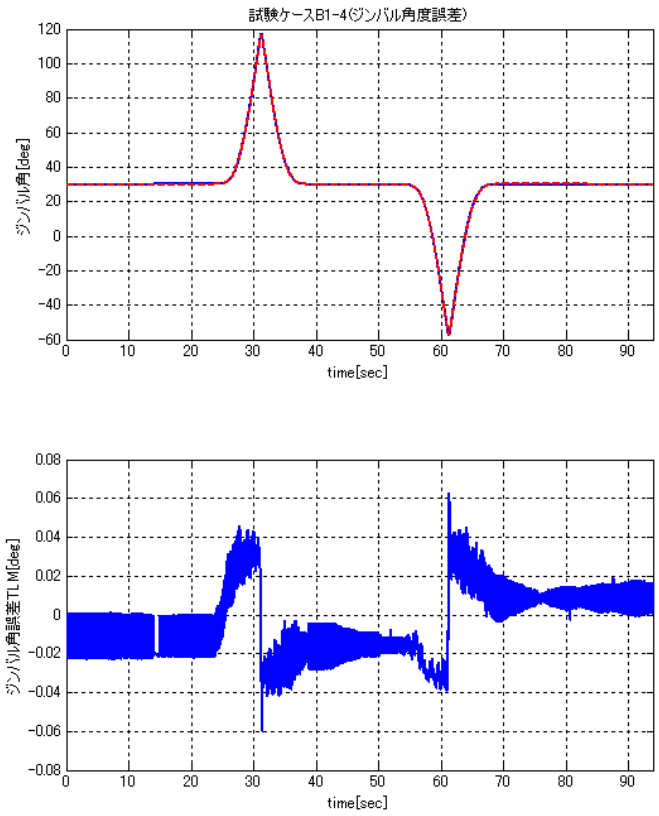

Figure E-2: Top: gimbal angle, bottom: gimbal angle error

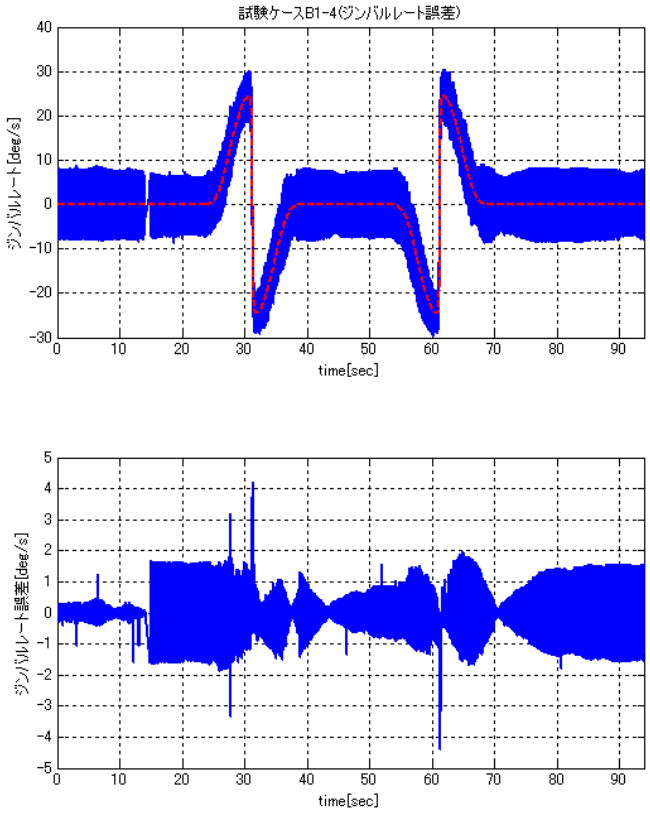

Figure E-3: Top: gimbal rate, bottom: gimbal rate error

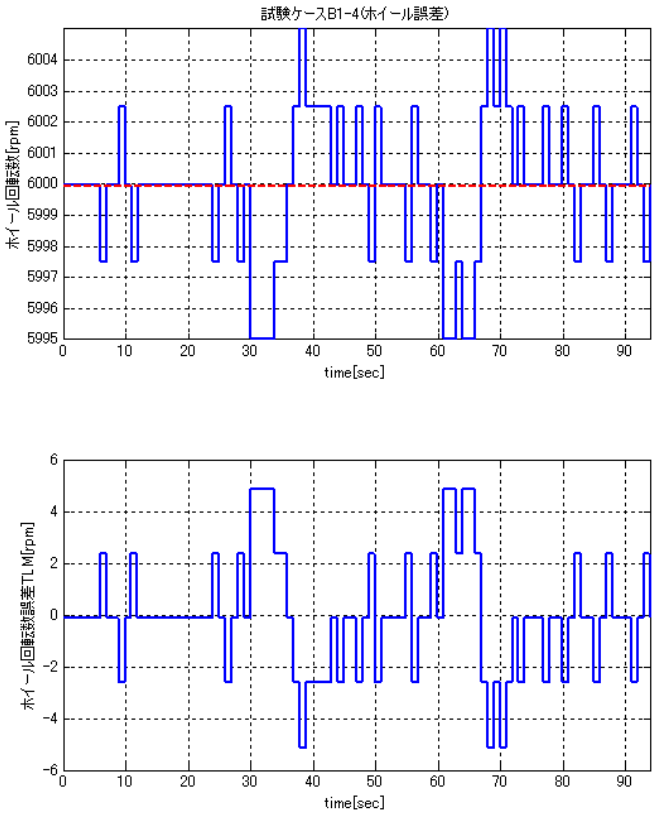

Figure E-4: Top: wheel speed, bottom: wheel speed error

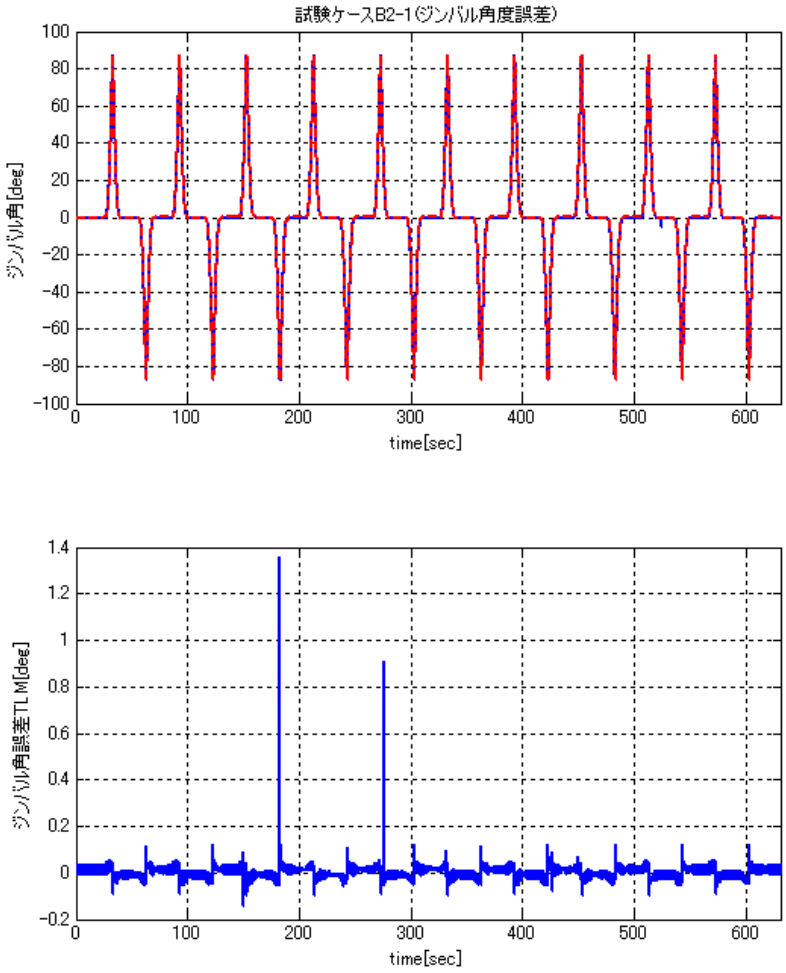

Figure E-5: Top: gimbal angle, bottom: gimbal angle error

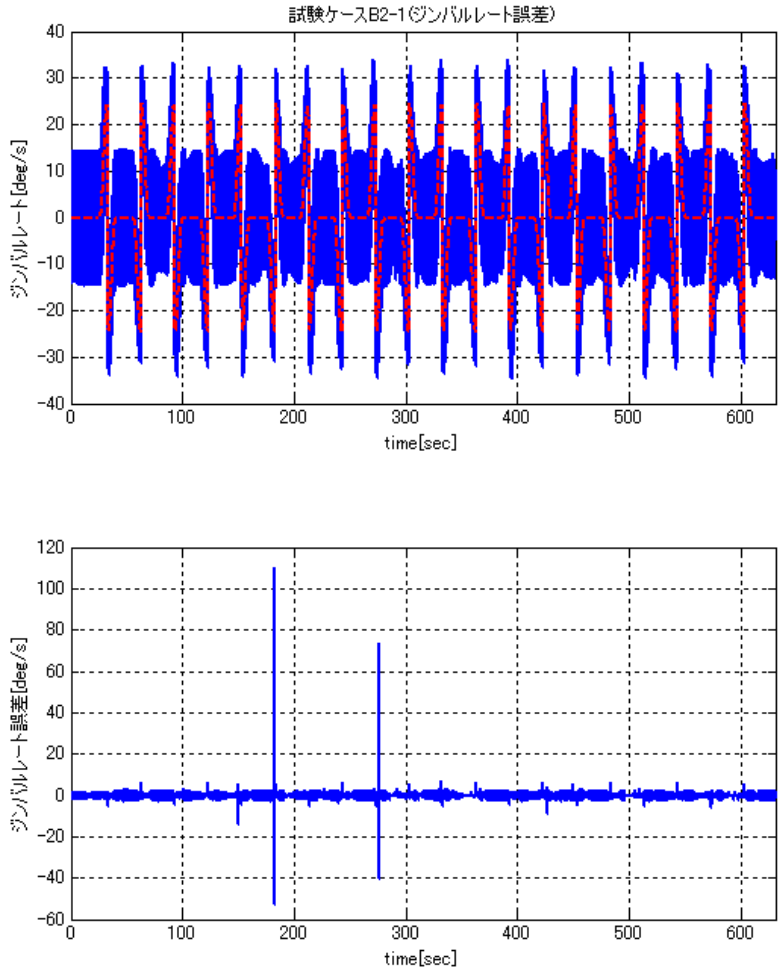

Figure E-6: Top: gimbal rate, bottom: gimbal rate error

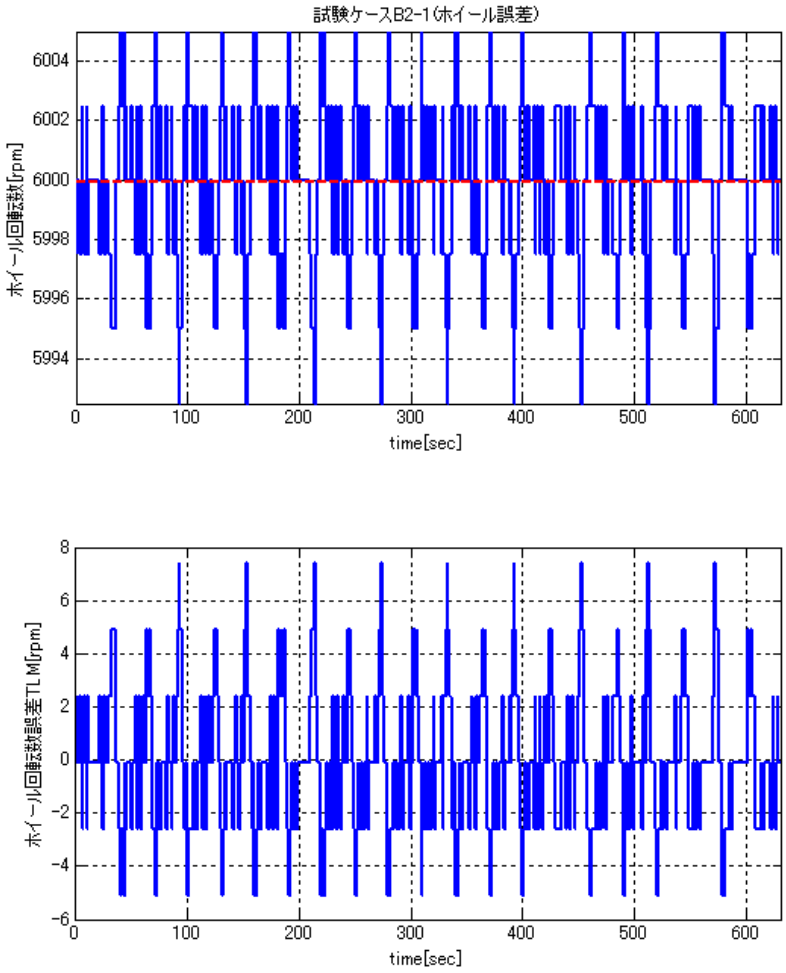

Figure E-7: Top: wheel speed, bottom: wheel speed error

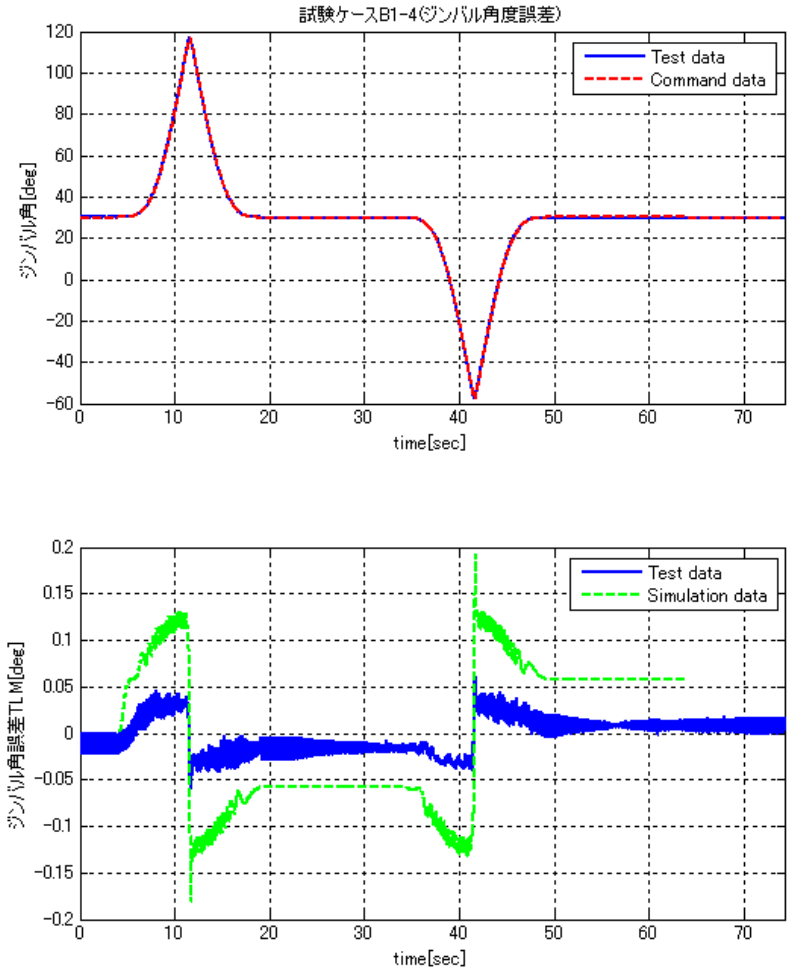

Figure E-8: Top: gimbal angle, bottom: gimbal angle error

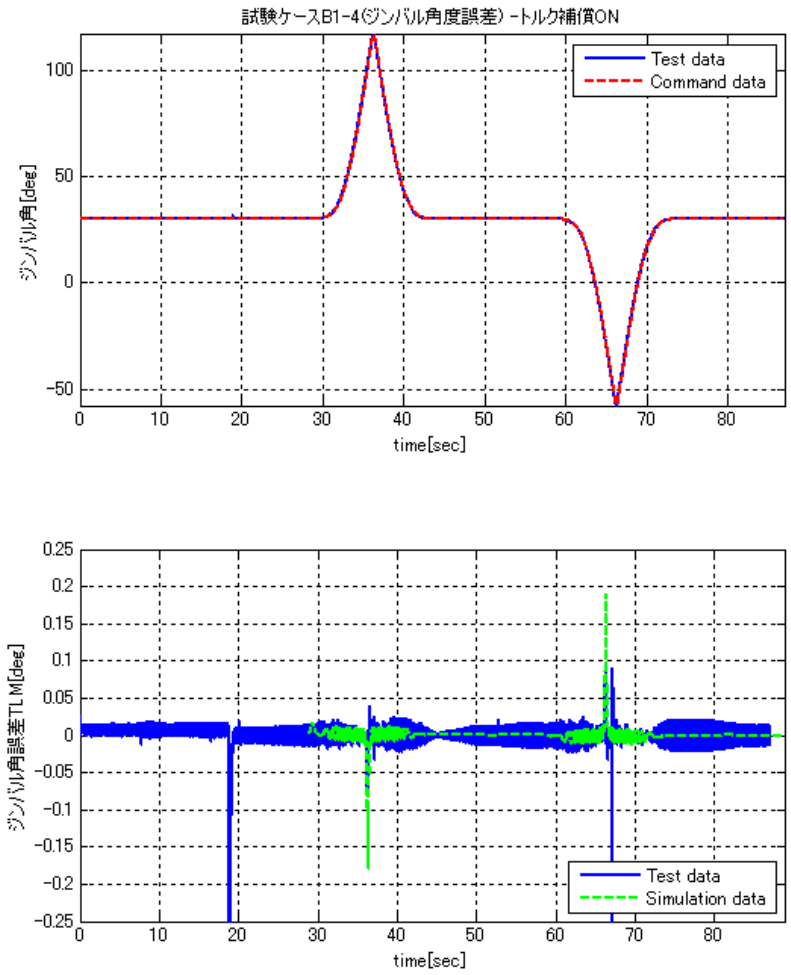

Figure E-9: Top: gimbal angle, bottom: gimbal angle error

Bibliography

[1] T. Kamiya, K. Maeda, T. Hashimoto, and S. Sakai. 柔軟構造物用姿勢マヌーバ時における姿勢制御データ生成方法、及びそれを適用した姿勢制御装置, Nov. 2007. Japan Patent No. JP2007302142.

[2] T. Kamiya, K. Maeda, T. Hashimoto, and S. Sakai. Attitude control data creating method, and attitude control system applying the method, Sep. 2009. U.S. Patent No. US20090218449.

[3] T. Kamiya, K. Maeda, T. Hashimoto, and S. Sakai. Attitude control data creating method, and attitude control system applying the method, May 2012. U.S. Patent No. US8186627.

[4] T. Kamiya, K. Maeda, T. Hashimoto, and S. Sakai. Attitude control data creating method, and attitude control device applying the method, Nov. 2007. Canada Patent No. CA2651814.

[5] T. Kamiya, K. Maeda, T. Hashimoto, and S. Sakai. Attitude control data creating method, and attitude control device applying the method, Feb. 2009. Europe Patent No. EP2022718.

[6] T. Kamiya, K. Maeda, T. Hashimoto, and S. Sakai. Attitude control data creating method, and attitude control device applying the method, Nov. 2007. PCT Patent No. WO2007132793.

[7] B. Girouart and I. Sebbad. Performances of the pleiades-hr agile attitude control system. In *Proceedings of ESA International conference 5th, Spacecraft guidance, navigation and control systems*, pages 497–500, 2003.

[8] A. Thieuw and H. Marcille. Pleiades-hr cmgs-based attitude control system design, development status and performances. In *Proceedings of 17th IFAC Symposium on Automatic Control in Aerospace*, volume 17, pages 834–839, 2007.

[9] P. Damilano. Pleiades high resolution satellite : A solution for military and civilian needs in metric-class optical observation. In *Proceedings of 15th Annual/USU Conference on Small Satellites*, 2001.

[10] T. Kida, I. Yamaguchi, Y. Chida, and T. Sekiguchi. On-orbit robust control experiment of flexible spacecraft ets-vi. *Journal of Guidance, Control, and Dynamics*, 20(5):865–872, 1997.

[11] T. Kasai, K. Komatsu, and M. Sano. Modal parameter identification of controlled structures. *Journal of Guidance, Control, and Dynamics*, 20(1):184–186, 1997.

[12] T. Nagashio, T. Kida, T. Ohtani, and Y. Hamada. Design and flight test results of robust attitude controller for the ets-viii spacecraft. In *Proceedings of the 18th IFAC World Congress*, volume 18, pages 5154–5159, 2011.

[13] T. Ohtani, Y. Hamada, T. Nagashio, and T. Kida. Robust attitude control using mu-synthesis for the large flexible satellite ets-viii. *Journal of Space Technology and Science*, 25(1):27–40, 2009.

[14] T. Kamiya, K. Maeda, and N. Ogura. Preshaping profiler for flexible spacecraft rest-to-rest maneuvers. In *IFAC Proceedings of 17th IFAC Symposium on Automatic Control in Aerospace*, pages 283–288. MIT Press, Cambridge, MA, 2007.

[15] T. Kamiya, N. Ogura, K. Maeda, and S. Sakai. Preshaping profiler for astro-g rest-to-rest maneuvers. *Journal of Space Technology and Science*, 25(1):41–47, 2009.

[16] T. Kamiya, K. Maeda, and N. Ogura. Flexible spacecraft rest-to-rest maneuvers with cmgs parallel gimbal arrangement. In *Proceedings of AIAA Guidance, Navigation, and Control Conference*, volume 9, pages 6025–6036, 2009.

[17] T. Kamiya, N. Ogura, and Y. Haruna. Preshaping profiler for astro-g rest-to-rest maneuvers. In *Proceedings of the 7th International ESA Conference on Guidance, Navigation and Control Systems*, 2008.

[18] T. Nakamura, N. Bando, S. Sakai, and H. Saito. Agile and robust attitude control system for vsop-2 satellite astro-g. In *Proceedings of the 10th International Workshop on Advanced Motion Control*, pages 578–583, 2008.

[19] T. Nakamura, N. Bando, S. Sakai, and H. Saito. Vibration suppression effect of translational motion control for asymmetric flexible satellite. In *Proceedings of the 11th International Workshop on Advanced Motion Control*, pages 667–672, 2010.

[20] O. J. M. Smith. Posicast control of damped oscillatory systems. In *Proceedings of the IRE*, volume 45, pages 1249–1255, 1957.

[21] O. J. M. Smith. *Feedback Control Systems*, pages 331–345. McGraw-Hill Book Inc., 1958.

[22] Neil C. Singer and Warren P. Seering. Preshaping command inputs to reduce system vibration. *ASME Journal of Dynamic Systems, Measurement, and Control*, 112(1):76–82, 1990.

[23] W. Singhose, W. Seering, and N. Singer. Residual vibration reduction using vector diagrams to generate shaped inputs. *Journal of Mechanical Design*, 116(2):654–659, 1994.

[24] W. Singhose, W. Seering, , and N. Singer. Time-optimal negative input shapers. *ASME J. of Dynamic Systems, Measurement, and Control*, 119(2):198–205, 1997.

[25] W. Singhose, L. Porter, T. Tuttle, and N. Singer. Vibration reduction using multi-hump input shapers. *ASME J. of Dynamic Systems, Measurement, and Control*, 119(2):320–326, 1997.

[26] David P. Magee and Wayne J. Book. Filtering schilling manipulator commands to prevent flexible structure. In *Proceedings of American Control Conference*, volume 3, pages 2538–2542, 1994.

[27] William E. Singhose, Neil C. Singer, and Warren P. Seering. Design and implementation of time-optimal negative input shapers. In *ASME WINTER ANNUAL MEETING*, pages 151–7, 1994.

[28] William Earl Singhose. *Command Generation for Flexible Systems*. Massachusetts Institute of Technology, Department of Mechanical Engineering, 1997.

[29] T. Singh and S. R. Vadali. Input-shaped control of three-dimensional maneuvers of flexible spacecraft. *Journal of Guidance, Control, and Dynamics*, 16(6):1061–1068, 1993.

[30] Q. Liu and B. Wie. Robust time-optimal control of uncertain flexible spacecraft. *Journal of Guidance, Control, and Dynamics*, 15(3):597–604, 1992.

[31] B. Wie and Q. Liu. Comparison between robustified feedforward and feedback for achieving parameter robustness. *Journal of Guidance, Control, and Dynamics*, 15:935–943, 1992.

[32] W. Singhose, S. Derezinski, and N. Singer. Extra-insensitive input shapers for controlling flexible spacecraft. *Journal of Guidance, Control, and Dynamics*, 19(2):385–391, 1996.

[33] P. H. Meckl, P. B. Arestides, and M. C. Woods. Optimized s-curve motion profiles for minimum residual vibration. In *American Control Conference, 1998. Proceedings of the 1998*, pages 2627–2631. IEEE Publ., Piscataway, NJ, 1998.

[34] R. Eloundou and W. Singhose. Justification for using step-function reference commands: Comparison to s-curves. In *2nd IFAC Conference on Mechatronic Systems*, volume 5, pages 25–30. Elsevier, Amsterdam, 2002.

[35] P. H. Meckl and W. P. Seering. Experimental evaluation of shaped inputs to reduce vibration for a cartesian robot. *J. Dynam. Systems, Measurement, and Control*, 112(2):159–165, 1990.

[36] P. H. Meckl and W. P. Seering. Minimizing residual vibration for point-to-point motion. *Journal of Vibration, Acoustics, Stress and Reliability in Design*, 107(4):378–382, 1985.

[37] P.H. Meckl. *Minimizing Residual Vibration of a Linear System Using Appropriately Shaped Forcing Functions*. Massachusetts Institute of Technology, Department of Mechanical Engineering, 1984.

[38] R. L. Farrenkopf. Optimal open-loop maneuver profiles for flexible spacecraft. *Journal of Guidance and Control*, 2(6):491–498, 1979.

[39] C. J. Swigert. Shaped torque techniques. *Journal of Guidance and Control*, 3(5):460–467, 1980.

[40] P.H. Meckl. *Control of Vibration in Mechanical Systems Using Shaped Reference Inputs*. Massachusetts Institute of Technology, Department of Mechanical Engineering, 1988.

[41] M.J. Bell. *Near-minimum-time Three-dimensional Maneuvers of Rigid and Flexible Spacecraft*. Texas A & M University, 1993.

[42] N. C. Singer, W. E. Singhose, and W. P. Seering. Comparison of filtering methods for reducing residual vibration. *European Journal of Control*, 5(2–4):208–218, 1999.

[43] W. Singhose. Command shaping for flexible systems: A review of the first 50 years. *International Journal of Precision Engineering and Manufacturing*, 10(4):153–168, 2009.

[44] W. Singhose, R. Eloundou, and J. Lawrence. Command generation for flexible systems by input shaping and command smoothing. *Journal of Guidance, Control, and Dynamics*, 33(6):1697–1707, 2010.

[45] K. Grosser, J. Fortgang, and W. Singhose. Limiting high mode vibration and rise time in flexible telerobotic arms. In *Proceedings of Conf. on Systemics, Cybernetics, and Informatics*, 2000.

[46] K. Grosser and W. Singhose. Command generation for reducing perceived lag in flexible telerobotic arms. *JSME International Journal*, 43:755–761, 2000.

[47] T. Kamiya, K. Maeda, and S. Sakai. Comparison of preshaping profilers for reducing residual vibrations after rest-to-rest maneuvers. *Journal of Guidance, Control, and Dynamics*, 37(TBD):TBD–TBD, 2014. [In press].

[48] N. C. Singer. *Residual Vibration Reduction in Computer Controlled Machines*. Massachusetts Institute of Technology, Department of Mechanical Engineering, 1989.

[49] T. Nakamura. *Control System Design for Agile Attitude Maneuver of Flexible Satellite*. Department of Electrical Engineering and Information Systems of the Graduate School of Engineering, The University of Tokyo, 2010.

[50] T. Nakamura, N. Bando, S. Sakai, and H. Saito. 柔軟衛星の高速な姿勢変更のための制振指令値設計. 日本航空宇宙学会論文集 = *Journal of the Japan Society for Aeronautical and Space Sciences*, 58(682):309–315, nov 2010.

[51] Y. Nakamura and H. Hanafusa. Inverse kinematic solutions with singularity robustness for robot manipulator control. *Journal of Dynamic Systems, Measurement, and Control*, 108(3):163–171, 1986.

[52] T. Saito, K. Maeda, K. Ninomiya, and T. Hashimoto. Rate-profiler based minimum-time control for spacecraft attitude maneuver. In *Proceedings of 15th IFAC Symposium on Automatic Control in Aerospace*, pages 83–88, 2001.

[53] T. Kamiya, T. Kurii, and Y. Kawakatsu. Microvibration management and pointing stability analysis of selene satellite. In *Proceedings of 16th IFAC Symposium on Automatic Control in Aerospace*, volume 1, pages 141–148, 2004.

[54] H. Hermes and J. LaSalle. *Functional analysis and time optimal control*. Mathematics in Science and Engineering. Elsevier Science, 1969.

[55] G. Singh, P. T. Kabamba, and N. H. McClamroch. Planar, time-optimal, rest-to-rest slewing maneuvers of flexible spacecraft. *Journal of Guidance, Control, and Dynamics*, 12:71–81, 1989.

[56] Y. Mizoshita, S. Hasegawa, and K. Takaishi. Vibration minimized access control for disk drives. *Magnetics, IEEE Transactions on*, 32(3):1973–1978, 1996.